Microstructure, Crystallographic Orientation, and Electrochemical Response of 420 Martensitic Stainless Steel

by

Salar Salahi

A Thesis Submitted to the

School of Graduate Studies

in partial fulfillment of the requirements for the degree of

Doctor of Philosophy

Faculty of Engineering and Applied Science

Memorial University of Newfoundland

May 2022

St. John's   Newfoundland

Abstract

Although the corrosion performance of the 420 martensitic stainless steel has been investigated from the electrochemical perspective, the impact of process-induced metallurgical factors such as secondary phase formation, grain distribution, and crystallographic orientation on the corrosion performance of the alloy is not thoroughly disclosed. This thesis aims to understand the correlation between the microstructure, crystallographic orientation, and electrochemical response of the 420 martensitic stainless steel (420MSS) fabricated by various manufacturing techniques. The corrosion resistance of 420 MSS decreased with increasing the deformation level in both uniaxial tension and cold rolling processes. Increasing the level of uniaxial tension in 420 martensitic stainless steel enlarged the size of sensitized regions along the matrix-coarse chromium carbide precipitates interface, providing more susceptible areas to pitting initiation and propagation. As the cold rolling level increased, higher fraction of fragmented precipitates formed in the microstructure, provoking the micro-galvanic coupling, and deteriorating the corrosion resistance. On the other hand, the microstructural characterization of the wire arc additive manufactured 420 MSS revealed the formation of a martensitic matrix with residual delta ferrite and retained austenite as a result of complex thermal history. Localized corrosion attacks were primarily detected adjacent to the delta ferrite phase, regardless of the implemented interlayer temperature during the fabrication process. Through the post-fabrication heat treatment, the corrosion morphology of the annealed sample was characterized by severe pitting due to the high susceptibility of the ferritic matrix-carbide interface to pitting. The electrochemical performance of the quench and tempered (Q&T) sample was significantly improved, ascribed to the elimination of the chromium-depleted regions adjacent to the delta ferrite phase and enhanced protectiveness of the passive film on the alloy's surface. Following the characterization of the interfacial bonding region between the wire arc additive manufactured 420 MSS part and the wrought 420 MSS, the formation of four distinct microstructural regions, including (i) far heat-affected zone (HAZ), (ii) close HAZ, (iii) partially melted zone (PMZ), and (iv) fusion zone was disclosed. The electrochemical response of the interfacial bonding region revealed intense degradation close to the PMZ and fusion zone, potentially ascribed to the formation of several distinctive microstructural regions with high susceptibility to localized corrosion attacks. The onset of localized corrosion attack in the interfacial bonding region mainly was initiated along the primary austenite grain boundaries (PAGBs), where segregation of chromium carbides was detected. Similarly, the interface of 420 MSS substrate and a repairing track of PH 13-8Mo stainless steel, fabricated by a wire arc additive manufacturing process, revealed severe deterioration on the electrochemical response possibly attributed to the formation of highly populated fine chromium-rich carbides. The corrosion onset was initiated at the carbide/matrix interface in the close HAZ and PMZ regions, where chromium depleted regions adjacent to the carbides intensified the micro-galvanic coupling effect.

Acknowledgment

First and foremost, I would like to thank my supervisor, Dr. Ali Nasiri, for his outstanding guidance, immense knowledge contribution, patience, and motivation throughout my Ph.D. study. I am indebted to him for his continual encouragement and support to carry out the current research.

Besides my supervisor, I would like to thank the rest of my supervisory committee: Dr. Susan Caines, and Dr. Lorenzo Moro, for their insightful comments and encouragement to widen my research from various perspectives.

Last but not least, I would like to thank my amazing parents, my sister, and all my friends for supporting me spiritually throughout this journey. None of this would have been possible without their love, patience, and support.

Table of Content

List of Tables

List of Figures

11

List of Abbreviations and Symbols

AF	Acicular Ferrite
AM	Additive Manufacturing
APP	Anodic Potentiodynamic Polarization
B	Bainite
BM	Base Metal
C	Capacitance
CE	Counter Electrode
C_{eff}	Passive Film Capacitance
CMT	Cold Metal Transfer
CPE	Constant Phase Element
CPE_{cath}	Constant Phase Element of The Cathodic Phase
CPE_{dl}	Constant Phase Element of The Double Layer
CPE_{oxide}	Constant Phase Element of The Oxide Layer
CPE_{p}	Constant Phase Element of The Passive Layer
CPE_{pit}	Constant Phase Element of The Pitting
CRPs	Cu-Enriched Particles
C_{SC}	Space Charge Capacitance
D	Particle Size
d	Grain Size
DBTT	Ductile to Brittle Transition Temperature
dl	Double Layer
DLF	Direct Laser Fabrication
DMLS	Direct Metal Laser Sintered
D_{ox}	Steady-State Passive/Oxide Layer Thickness
DRX	Dynamic Recrystallization
DSC	Differential Scanning Calorimetry
E	Applied Potential
e	Electron Charge
EBSD	Electron Backscattered Diffraction
$E_{corr.}$	Corrosion Potential
EDX	Energy Dispersive X-ray
E_{FB}	Flat Band Potential
EIS	Electrochemical Impedance Spectroscopy
$E_{pit.}$	Pitting Potential
ε_{r}	Relative Dielectric Constant
F	Polygonal Ferrite
f''_{m}	Maximum Frequency

FESEM	Field Emission Scanning Electron Microscope
FIB	Focused Ion Beam
f_{max}	Maximum Measured Frequency
FSP	Friction Stir Processing
GB	Grain Boundary
GMA	Gas Metal Arc
GMAW	Gas Metal Arc Welding
GP	Guinier–Preston
GTA	Gas Tungsten Arc
HAGB	High Angle Grain Boundaries
HAZ	Heat Affected Zone
HIP	Hot Isostatic Pressing
H-M	Hsu And Mansfield's Model
ICHAZ	Inter-Critical Heat Affected Zone
$I_{Corr.}$	Corrosion Current Density
IGC	Intergranular Corrosion
IPF	Inverse Pole Figure
k	Boltzmann's Constant
LAGB	Low Angle Grain Boundaries
LBM	Laser Beam Melting
LBZ	Localized Brittle Zones
LMD	Laser Metal Deposition
L-PBF	Laser-Powder Bed Fusion
MA	Martensite-Austenite
MP	Melt Pool
n	Dispersion Coefficient
N_A	Acceptance Density
ND	Donor Density
NDT	Non-Destructive Testing
OCP	Open Circuit Potential
PDM	Point Defect Model
PF	Pole Figure
P-L	Power-Law Model
R_{ct}	Double Layer Resistance
RE	Reference Electrode
RE	Solidification Rate
R_{el}	Electrolyte Resistance
R_{oxide}	Oxide Layer Resistance
Rp	Passive Layer Resistance
R_{pit}	Pitting Resistance
R_{pol}	Polarization Resistance

R_s	Ohmic Drop Resistance
SDAS	Secondary Dendrite Arm Spacing
SEC	Simplified Equivalent Circuit
SEM	Scanning Electron Microscopy
SLM	Selective Laser Melting
S-S	Simple Substitution Model
STEM	Scanning Transmission Electron Microscopy
STEM-BF	STEM in Bright-Field Mode
STT	Surface Tension Transfer
SZ	Stir Zone
TEM	Transmission Electron Microscopy
TMAZ	Thermo-Mechanically Affected Zone
WAAM	Wire Arc Additive Manufacturing
W_{pit}	Warburg Diffusion Element
XRD	X-Ray Diffraction
YS	Yield Strength
α	Dispersion Coefficient
β_A	Anodic Slope
β_C	Cathodic Slope
δ	Passive Layer Thickness
ε	Dielectric Constant
ε_0	Vacuum Permittivity
θ	Apparent Contact Angle
θ_e	Intrinsic Contact Angle
λ	Dendrite Arm Spacing
ρ_δ	The Resistivity at the Maximum Thickness of the Passive Layer
ω	Angular Frequency
$\omega^{"}_m$	Angular Frequency

Chapter 1

Introduction

1. Background

Stainless steels (SS) are widely used in various areas, including daily kitchenware application to critical industries such as automotive, marine, and aerospace sectors, due to their high mechanical performance and acceptable corrosion resistance [1,2]. Based on the dominant microstructural phase at room temperature, stainless steels are subdivided into four major groups: ferritic, austenitic, martensitic, and austenoferritic (duplex) stainless steels [3]. Adding alloying elements such as chromium, nickel, carbon, molybdenum, nitrogen, and aluminum can significantly impact stainless steel's mechanical properties and electrochemical performance. Among stainless steels, martensitic stainless steels (MSS) and specially AISI420 MSS are more favorable for application in the offshore industry compared to their counterparts, potentially due to their high corrosion performance at harsh corrosive environments along with their reasonable price [4].

From the electrochemical aspect, the high corrosion resistance of the 420 martensitic stainless steel is generally related to passivation ability and its resistance to environmental degradation [5]. The passivation behavior of the stainless steel is often characterized by the formation of an oxide layer on the surface; generally, chromium oxide (Cr_2O_3) film, which highly depends on the concentration of the Cr element in the alloy and is required to be higher than 11 wt.%. For the AISI 420 MSS with high chromium concentration (~13 wt.%), it is well documented that an intact and thick passive film would form on the alloy's surface, leading to high electrochemical stability and corrosion response when exposed to corrosive environments [6]. It should be noted that the

chromium can only contribute to the electrochemical stability of 420 MSS in a Fe-Cr solid solution system, and the impact of other types of the chromium-based microconstituents in corrosion response of 420 MSS can be the matter of discussion [7,8].

Unlike their austenitic counterpart, martensitic stainless steel can be subjected to various heat treatment techniques [9,10]. In most cases, surface modification of the MSS is conducted through ion implantation, laser surface melting, or plasma nitriding, and enhancement in surface corrosion performance is reported compared to the bulk core in various corrosion environments [11–13]. Multiple types of corrosive environments can be used for evaluating the corrosion performance of the martensitic stainless steel, such as artificial ocean water with 3.5 wt.% of NaCl at room temperature, low concentration H_2SO_4 solutions, and combined HCl+HF acidic environments [8,14]. Moreover, different electrochemical measurements can be performed to quantify the corrosion response of the martensitic stainless steel in both direct and alternative current regimes (AC and DC) [15]. Open circuit potential (OCP), immersion tests, and potentiodynamic polarization measurements are carried out to characterize the general corrosion behavior of the MSS [16].

On the other hand, to quantify the electrical resistance (impedance) of the metal/solution interface (passive film), electrochemical impedance spectroscopy (EIS) measurements are generally performed over various frequencies [15]. The experimental data gathered from the EIS measurements are often compared to the fitted data using an equivalent electric circuit [14,17]. The semiconductor behavior of the formed passive film for the martensitic stainless steels is characterized with Mott-Schottky measurements in a few studies [18–20].

Following the electrochemical testing, several studies have made attempts to capture micrograph images of the corroded regions of martensitic stainless steels to characterize the surface

morphology for various corrosion mechanisms by implementing optical microscopy [8], scanning electron microscopy (SEM)[17,21], confocal laser scanning microscopy [7], and the X-ray photoelectron spectroscopy (XPS) techniques [22].

It is well documented that the corrosion mechanism of the 420 martensitic stainless steels, fabricated by conventional techniques such as hot rolling and forging, involves the initiation and propagation of pitting corrosion, which mainly occurs in the presence of anions such as chloride and a major oxidizing element such as oxygen [23–25]. Although generally, the stability of the oxide layer on the surface of the martensitic stainless are strong, in the presence of the chloride or other aggressive anions, the localized iron dissolution can occur where the iron anions lose their passivity at a specific potential called pitting potential [26,27]. If exposed to the corrosive environment for a more extended period, this can lead to the propagation of these pitting sites, forming major deep pitting mostly elongated toward the gravity direction [28,29], as illustrated in Figure 1.1.
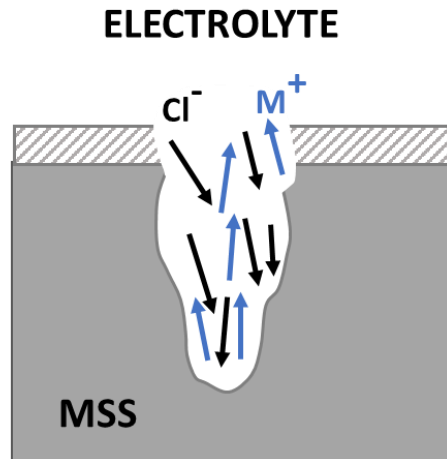
Figure. 1. 1. Partial reactions in pitting corrosion

Dissolution of iron inside a pit is expected to be faster than the passive film, due to the lower surface area of the pit with anodic behavior, compared to the extensive surface area in the cathodic

passive film [30]. This anode to cathode surface ratio is a significant factor determining the pitting potential of the martensitic stainless steels. It is highly dependent on the chemical composition of the corrosive media, microstructural features of the martensitic stainless steel, and its surface tribology [6,31]. Several studies have characterized the pitting potential of the martensitic stainless steels in different electrolytes [8,17,18,32]. Most of these studies focus on implementing experimental techniques such as polarization graphs and potential steps to identify the pitting potential [17,33].

Another area of concern in previous literature is the re-passivation ability of this alloy. Through the pitting corrosion, metastable pitting can occur on the sample's surface, while the recurrence of the passive film formation can constantly sustain the electrochemical stability of the passive film [34,35]. Re-passivation can frequently occur through the corrosion mechanism of martensitic stainless steels, hindering the complete pitting corrosion [35]. However, the re-passivation ability can be voided in certain circumstances where the stability of the passive film deteriorates due to the increase in corrosive anions or higher exposed PH, leading to de-passivated behavior of the surface.

Although most of the corrosion studies on martensitic stainless steel have been devoted to the characterization of pitting corrosion, several studies have found other major corrosion mechanisms such as intergranular corrosion and crevice corrosion governing the electrochemical response of their studied alloys [36–38]. In the case of intergranular corrosion, the microstructural features of the martensitic stainless steels, especially at the grain boundaries and interfaces, have been studied. The micro constituents formation at the grain boundaries can highly localize the corrosion behavior of the alloy depending on the nature of the formed particle [17]. Moreover, the crevice performance of 420 martensitic stainless steel is also thoroughly investigated in another study by Marcelin et

al. [39], where a significant decrease in corrosion resistance is observed when the medium is increasingly confined. The data obtained in the bulk electrolytes were used to determine the critical conditions in the thin-layer cell which impede the re-passivation of the MSSs.

2. Technical Background

In order to better understand the current thesis's structure and realize how the experimental procedure, results gathering, and discussion sections were developed, a technical background on the applied experiments herein, material fabrication techniques, and the implemented data analysis methods is required. First, a brief introduction to used material fabrication techniques, i.e., plastic deformation and additive manufacturing, will be provided. Subsequently, the applied experimental procedures will be elaborated, i.e., microstructural characterization techniques and electrochemical testing methods.

2.1. Uniaxial Tension

In chapter two of the current thesis, the uniaxial tension has been implemented to form strain-induced plastic deformation on the studied 420 MSS sample. Hence, understanding the plastic deformation mechanism through the uniaxial tensile is vital for this study. In this section, the fundamentals of the uniaxial tensile test have been thoroughly discussed, and the experimental procedure to measure the stress-strain curve is described.

In daily used English, force refers to a push or pull. In basic engineering, force (F) is defined as an interaction between two bodies or between a body and its surroundings. The force may be defined as stress, which characterizes the force's intensity on a force per unit area basis. The linked quantity, I,e., strain describes the ensuing deformation generated by the stress. When the stress and strain are modest enough, we often find that they are directly proportional, and the proportionality constant is referred to as the elastic modulus [40]. The force of equal size but the opposing direction

applied to the ends of a body is described as tension [41]. The stress is symbolized by the Greek letter sigma and is defined as the ratio of force to the cross-sectional area of the body:

$$stress, (\sigma) = \frac{F}{A} \tag{1}$$

The Pascal (Pa) is the SI unit of stress, which equals newton per square meter (N/m2). The strain is the fractional change in length induced by the stress, which is the ratio of the elongation length to the original length. Because length and elongation are measured in the same units, strain is a dimensionless quantity [40,42]. We may represent the strain mathematically as follows:

$$strain, (\varepsilon) = \frac{\Delta L}{L} \tag{2}$$

A component defined as in equilibrium condition is eighter at rest or traveling with constant velocity (along a straight path at constant speed). A part is considered to be in equilibrium if any forces do not act on it or it is under numerous forces such that its vector sum is zero [40]. Equilibrium is defined as the sum of net forces equaling zero, corresponding to Newton's first rule of motion. There are an unlimited number of methods to apply stress to a body; however, for material testing purposes, loading types have been simplified into four primary groups, i.e., short-term static loading, static loading for an extended period, repeated loading, and dynamic loading. Through the uniaxial tensile testing, the maximum load is delivered gradually and sustained. It is maintained for a sufficient period throughout testing to measure the mechanical strength of the tested sample. Long-term static testing, performed at various temperatures, is implemented to determine materials' creep and tensile strength in different service conditions [40,41].

The material undergoes an elastic deformation region through the first stage of the uniaxial tensile testing, where the applied strain is reversible. Elasticity is the characteristic of materials that allows them to revert to their original shape and size after being deformed. Reversible elastic deformations are when the energy used during deformation is stored as elastic strain energy and recovered

entirely upon load release. The material's elastic limit is the highest stress that may occur before permanent deformation occurs. The material's behavior through the elastic deformation zone is linear, and elasticity (E) can be mathematically correlated to the stress (σ) and strain (ε) values using the Hook's law [43]:

$$\sigma = E\varepsilon \tag{3}$$

The permanent shape change in material occurs through plastic deformation. Plasticity is the material's characteristics that allow them to transform in shape permanently when exposed to stress values higher than the material elastic limit. Theoretically, elastic deformation refers to a change in the distance between atoms or molecules. In contrast, plastic deformation refers to a change in their relative positions over time that eventually leads to failure [44]. This permanent rearrangement occurs mainly via displacements of the atoms inside the crystal lattice in metals and other crystalline materials [45].

The uniaxial tensile test is perhaps the most helpful material characterization procedure. It measures the force necessary to elongate a test specimen by increasing force until it cracks. The tensile test in a uniaxial manner determines many critical material characteristics, including elasticity, plasticity, and ultimate tensile strength (UTS). Most notably, it creates stress-strain curves, which represent the mechanical characteristics of a material [46]. An expanded plastic deformation zone forms for the ductile materials with high deformability, as shown in Figure 1. 2. As the tensile test progresses, the stress and strain curve exhibit a linear behavior until it reaches the proportional yield limit. The elastic modulus, or Youngs's modulus, is the slope of the curve up to this point. The stress value hits the top yield point, or elastic limit, at which the metal's behavior changes from elastic to plastic. Before reaching the ultimate tensile strength, a nonlinear stress-strain curve forms in the uniform plastic deformation region, referred to as the strain

hardening zone, indicating the dislocations of atoms and permanent displacement [40,47]. Beyond the ultimate tensile strength point, the stress value decreases due to necking, resulting in a final fracture of the specimen. If the applied stress (and hence strain) is less than the elastic limit, both stress and strain will revert to zero when the load is removed. However, if the elastic limit is surpassed, only the elastic strain is restored; the plastic strain is permanently established. Since a permanent deformation is generally undesired in a mechanical component, it is preferable to design parts with estimated service stress that is less than the elastic limit by an acceptable factor of safety [47,48].
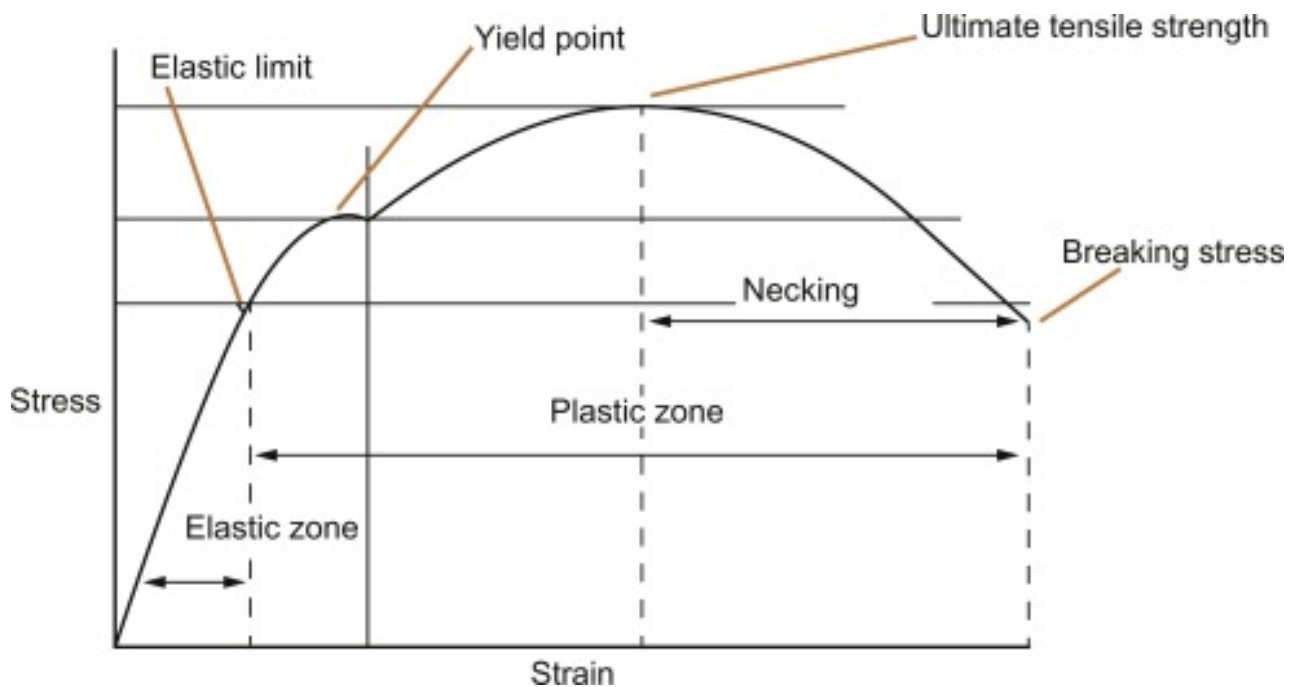
Figure. 1. 2. Stress-strain curve for a ductile material [47,49].

2.2. Cold Rolling

Rolling is extensively used in the automobile industry to manufacture high-strength sheet metal [50]. Chapter 3 of the current thesis implements the cold rolling procedure to apply plastic deformation to the samples. Hence, understanding how the rolling process is conducted on the 420

MSS samples is essential. In the conventional rolling process, a sheet of metal is compressed between two rollers [47,51], constructed of high-strength materials while spinning on opposing sides, as shown in Figure. 1. 3a. The detailed illustration of the rolling process is shown in Figure 1. 3b.
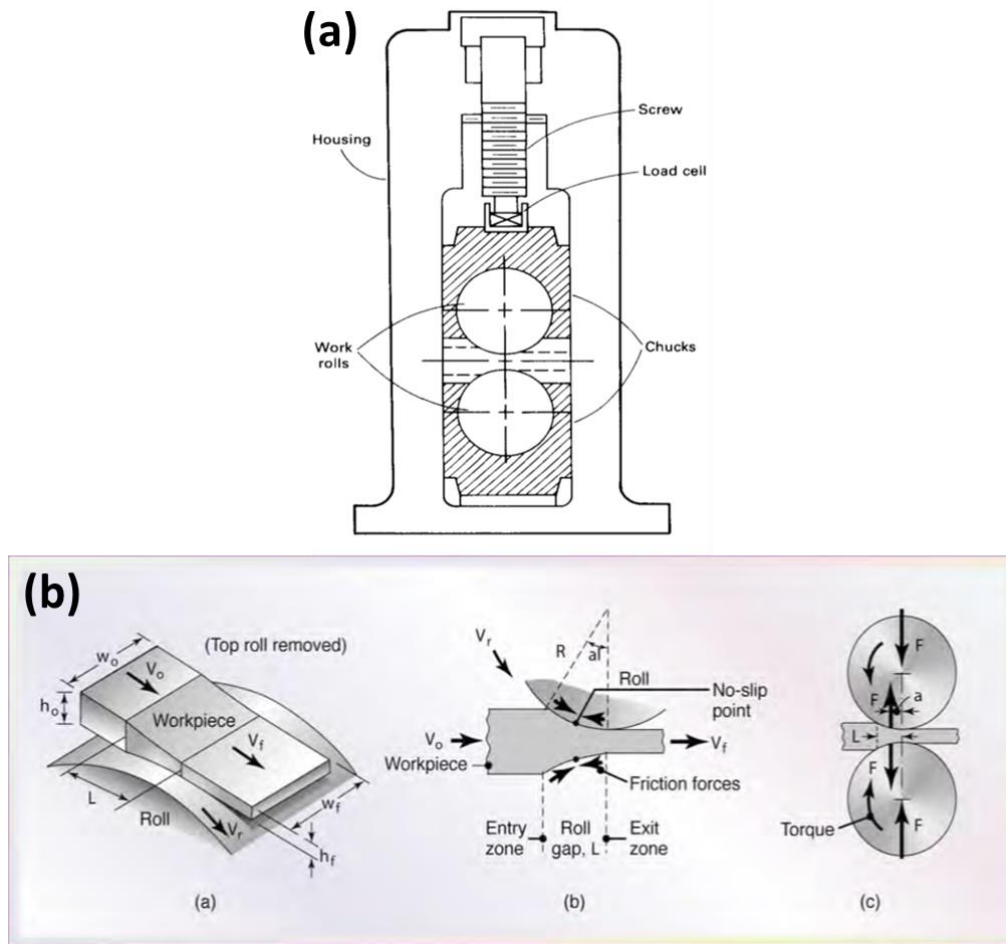
Figure. 1. 3. (a) Schematic illustration of a conventional rolling machine (b) detailed illustration of the rolling process [51].

2.3. Crystallographic Orientation and Texture

Each grain in a structure has a unique crystallographic orientation. Individual grains establish a preference orientation (texture) due to deformation and recrystallization processes such as rolling, solidification, and heat treatment cycles. A set of grains with the same crystallographic orientation is predicted to generate a crystallographic texture [51]. The crystallographic orientation or texture

is a microstructural characteristic that contributes significantly to a crystalline material's microstructure. Historically, this characteristic or component of microstructure was studied separately, but it is now considered an intrinsic element of microstructure. This has occurred primarily as a result of the widespread usage of electron backscatter diffraction (EBSD. Three-dimensional techniques have aided this comprehension, such as serial sectioning and mapping using synchrotron radiation [52].

Technically, a grain's orientation is defined by a rotation and quantified using three vectors. Historically, the study of texture was centered on examining pole figures as determined by X-ray (or neutron) diffraction. Still, new texture representation and determination techniques have been frequently employed in recent years [52,53]. EBSD under the scanning electron microscope (SEM) (see Fig. 1. 4) has become a widely used approach for characterizing microstructures due to its simplicity and ability to quantify various microstructural properties, including texture.

While the diffraction patterns from metals were initially gathered in the 1960s, Dingley *et al.* [54] primarily applied the pattern acquisition technique for the low-light TV cameras. They opened a widespread interest in the method, leading to the development of commercially available systems. The use of EBSD in combination with the FEG-SEM system is a more recent breakthrough, and the resulting improvement in spatial resolution has broadened the scope of EBSD application [52]. In general, the hardware for EBSD acquisition consists of a sensitive CCD camera and an image processing system for pattern averaging and background removal. The EBSD acquisition program is used to manage data collection, solve diffraction patterns, and store data [52,55]. Before performing any experiment, the various software segment the diffraction patterns using a variety of approaches. The distinctive interplanar angles of the low-index peaks are utilized to identify the peaks and derive their orientation automatically. EBSD is performed on a specimen inclined

between 60 and 70 degrees from the horizontal, and data points are acquired by rostering the beam over the sample. These data points may be displayed as pixels to create an orientation map. Because the beam deviates from the optic axis during a scan, absolute orientation errors are introduced at very low magnifications, and beam defocusing owing to the sharply tilted sample may result in a loss of spatial resolution [52,56]. As a result of these considerations, beam scanning is often confined to smaller regions. A stationary electron beam is employed to eliminate these problems when measuring more extensive areas. The specimen is moved relative to the beam using stage stepping motors controlled by the EBSD software.
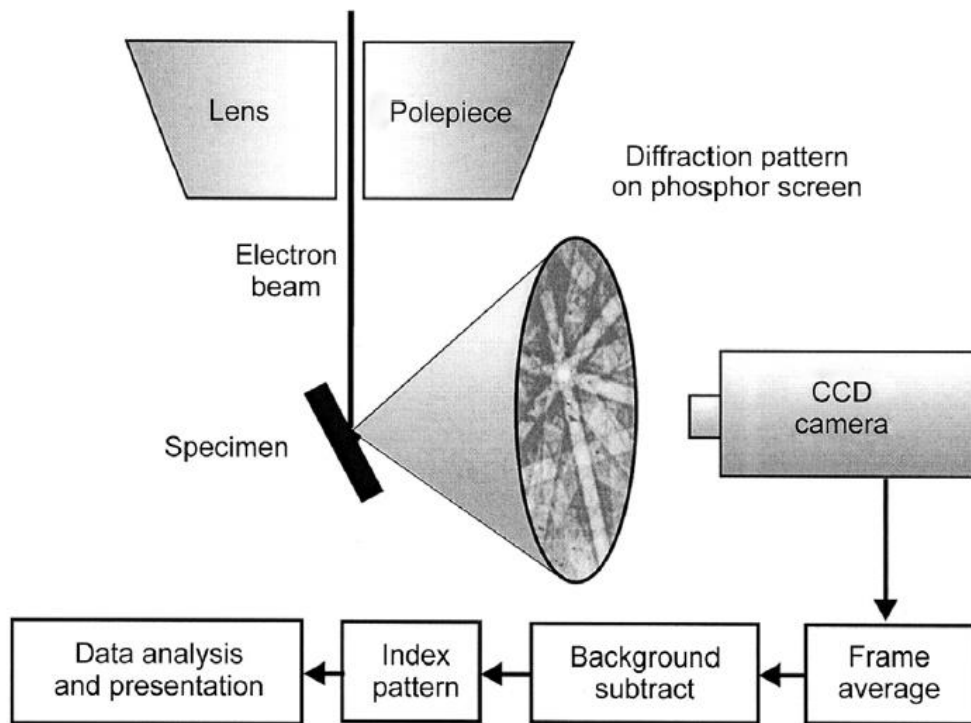
Figure. 1. 4. Schematic illustration of a conventional EBSD detector in an SEM [52,55].

To explain texture, we must first understand that a correct rotation determines the orientation of a crystal concerning a reference frame. Thus, we may quantify texture using rotational mathematics [57]. Polycrystalline materials exhibit various directions within a single sample, necessitating

statistical techniques' quantification of orientation distributions. A Cartesian axis, as shown in

Figure 1. 5 primarily used to correlate between the individual grain and bulk material.
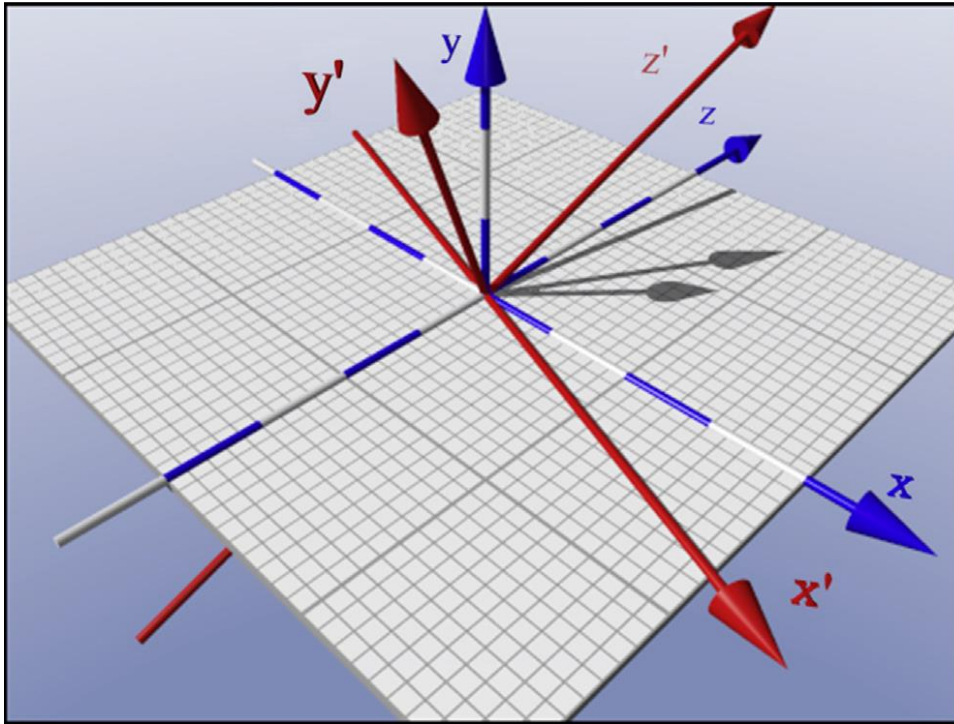
Figure. 1. 5. Illustration of a definition of orientation based on a pair of Cartesian frames[52].

For texture analysis, a pole figure is a projection (usually stereographic or equal area) of the density

variation of a specified crystallographic plane normal to sample space. The term "sample space"

refers to a frame of reference defined by the sample and in which the axes (x,y, and z-axis)

correspond to a set of directions in the material. These directions have referred to the forming

process, for example, the drawing direction in wires or the rolling direction in rolled sheets, or the

film normal in thin films (with x and y determined by directions in the base metal). Figure 1. 5.

illustrates idealized pole figures for drawn wire and rolled sheets [55].
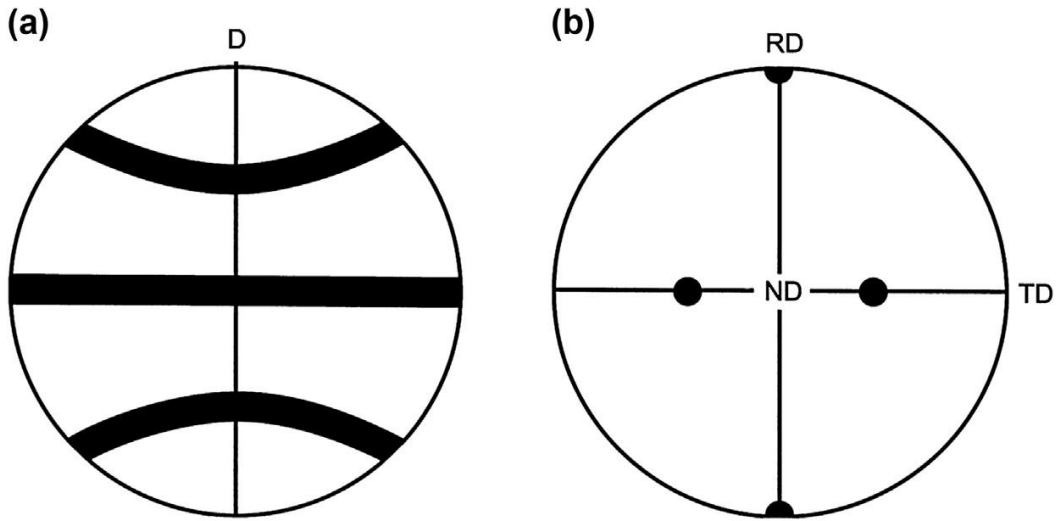
Figure. 1. 6. (100) plane pole figures for (a) wire with <110> fiber texture, (b) rolled sample with {110}<001> texture[52].

As another illustrative technique to show the texture formation, the inverse pole figure (IPF) is a projection (usually stereographic or uniform area) of the density variation along a specified sample direction in crystal space. The term "crystal space" refers to a frame of reference defined by an orthonormal set of axes that correspond to a group of directions in the crystal. An IPF is especially advantageous for deformation operations such as wire drawing or extrusion that need just a single axis specification due to its cylindrical symmetry [52,53]. For cubic structures such as BCC and FCC, the frequency with which a given crystallographic direction corresponds to the specimen axis is displayed in a single standard stereographic triangle, as shown in Figure. 1. 7. Inverse pole figures may also represent rolling textures, although, two or often three independent plots are displayed in this case, one for each of the primary rolled directions, i.e., ND, RD (and TD if required)[52].
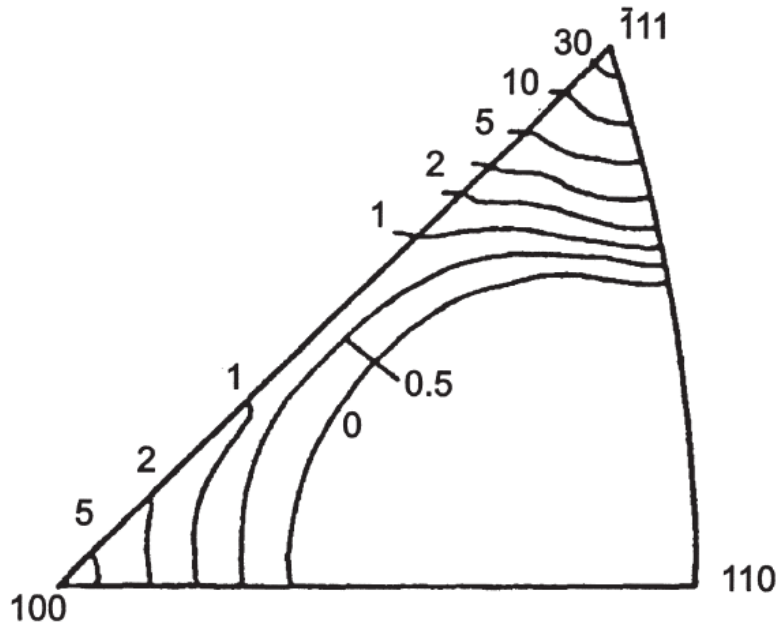
Figure. 1. 7. Inverse pole figure for cold drawn aluminium wire [58].

2.4. Additive Manufacturing

The growing additive manufacturing (AM) technique, which was initially pioneered by Charles W. Hull [59] and first used in the manufacturing of rapid prototypes (RP) in the 1980s, has been extensively embraced in the recent decade for the manufacturing of complicated metallic components [60]. In contrast to typical manufacturing techniques, AM employs a layer-by-layer deposition process, enabling the fabrication of near-net-shape items without supporting equipment or materials [61–63]. Previous research has classified metallic AM methods according to the applied heat sources, including laser, electron beam, and arc [64–66]. A schematic illustration of the categorized additive manufacturing techniques is represented in Figure. 1. 8. Additionally, AM technologies are classified into powder bed fusion (PBF) and direct energy deposition (DED) procedures depending on the deposition processes used [67]. While the metal powder is used as the feedstock material for PBF, powder, and wire are used as feedstock materials for DED. The PBF technique is intended to enhance near-net-shape production and product complexity. At the

same time, the DED approach is frequently used to rapidly manufacture big components with a simpler design, high mechanical qualities, and a regulated microstructure [68]. Wire arc additive manufacturing (WAAM) is a DED technique that utilizes an electric arc or plasma as the heat source and a wire as the feedstock material, as illustrated in Figure 1.9. WAAM hardware typically comprises a welding torch placed on a multi-axis robotic arm or a CNC machine, a welding power supply, and an accompanying wire feeding system. As the wire is fed into the electric arc at a regulated pace, it melts and deposits either on the base plate, generating the first deposited layer or on previously deposited layers [69].
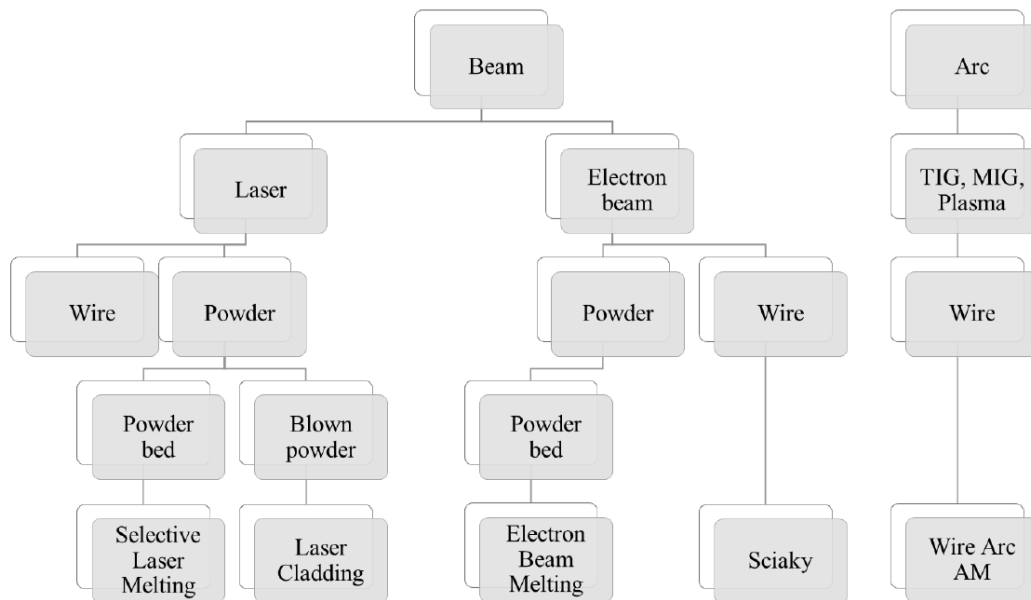
Figure. 1. 8. Different Metal Additive Manufacturing processes [70].
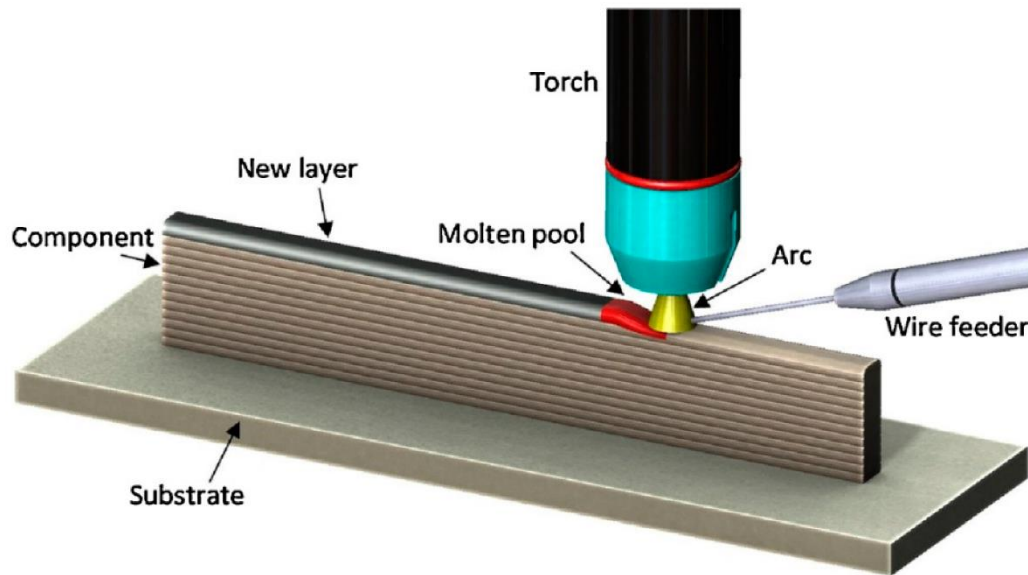
Figure. 1. 9. Schematic representation of a WAAM system [71].

Recently, the manufacturing industry has paid close attention to the WAAM technology due to its ability to produce large-scale parts at a significantly higher deposition, lower equipment cost, and shorter lead time when compared to laser-based and electron beam-based AM processes [72–74]. However, WAAM parts are subjected to a complex thermal treatment during the deposition process, resulting in changes to the part's localized metallurgical characteristics due to frequent heating and cooling. As a result, the microstructural properties of the manufactured WAAM components are highly localized, influencing their mechanical performance and corrosion resistance [73,75,76].

The use of WAAM technology to manufacture a variety of non-ferrous alloys, including titanium alloys, aluminum alloys, nickel-based alloys, and various intermetallic compounds, has received considerable attention [77–80]. Ferrous alloys, particularly stainless steels, which are the most commonly used materials in modern industry, were also chosen as feedstock materials for component fabrication using the WAAM. Wang *et al.* [69] used the WAAM to produce 316L stainless steel in various arc modes and at a constant deposition rate. They explored the mechanism

and effect of process parameters on manufacturing process stability, microstructures, and mechanical response. Caballero *et al.* [81] investigated the impact of process variables such as shielding gas, deposition path, and post-fabrication heat treatment on the microstructure and mechanical properties of WAAM 17-4 PH stainless steel and demonstrated that the required tensile properties could be achieved by solution treatment at 1040 °C for 30 min followed by aging at 480 °C for 1 h. Feng *et al.* [82] proposed an innovative and highly efficient process for fabricating Cr-Ni stainless steel components using a double-wire feed and plasma arc additive manufacturing (DWF-PAM) process and investigated the process's superior characteristics in terms of bead appearance, microstructure, and mechanical properties. Finally, Zhang *et al.* [83] used a tungsten inner gas wire arc additive manufacturing (TIG-WAAM) approach with an integrated wire feeder and continuous liquid transfer mode to fabricate a super duplex stainless steel (ER2594) with an exceptional combination of mechanical qualities and corrosion resistance. The application of the WAAM for the fabrication of martensitic stainless steel will be elaborated in the upcoming chapters comprehensively.

2.5. Electrochemical Testing

A metal-electrolyte contact undergoes at least two electrochemical reactions through electrochemical testing, oxidation, and reduction. Since corrosion is an electrochemical process, it is obvious that electrochemical methods may be utilized to examine corrosion reactions and processes. This section discusses electrochemical corrosion testing principles, the fabrication of electrodes for electrochemical polarisation research, and the many electrochemical techniques available for laboratory investigations of corrosion events [84,85].

The fundamental premise underlying all electrochemical approaches is the mixed potential theory that uniform corrosion occurs when anodic and cathodic reactions occur in a consistent state of

change in terms of location and time for the separate processes [85]. It is not required for corrosion to appear under this idea to presuppose the existence of local anodes and cathodes. Nonetheless, it has often been said that corrosion happens when local anodes and cathodes are created, even though uniform corrosion occurrence is impossible in this situation. Numerous electrochemical methods characterize the laboratory corrosion performance and corrosion monitoring of in-service metallic components. Table 1.1 summarizes the electrochemical testing suggested by the National Association of Corrosion Engineers (NACE) for corrosion analysis of metallic components [84,85].

Table1. 1. Electrochemical corrosion testing techniques [85].

Category	Test method
No applied signal	Open circuit or corrosion potential
	Dissimilar metal corrosion (galvanic corrosion)
	Electrochemical noise analysis
Small-signal polarization	Polarization resistance (linear polarization)
	Electrochemical impedance spectroscopy
Large-signal polarization	Potentiostatic and galvanostatic polarization
	Potentiodynamic and Galvano dynamic polarization
Scanning electrode techniques	Current scans
	Potential scans

Open circuit potential (OCP) measurement is the simplest electrochemical test to perform, but it provides the least information about the underlying mechanism. No external electrochemical signal is used while measuring OCP. To determine corrosion potential (E_{corr}) in an OCP measurement, a stable reference electrode, such as an SCE, a high-impedance voltmeter, or suitable recording equipment is required. Corrosion potential can also be determined by observing

the potentiostat's digital display and recording the potential output value as a function of exposure time on a strip chart recorder. Open-circuit potential rises as passivity improves for passive samples, but OCP frequently drops as localized corrosion occurs [85,86]. Figure 1. 10 shows the OCP values versus monitoring times for several alloys.
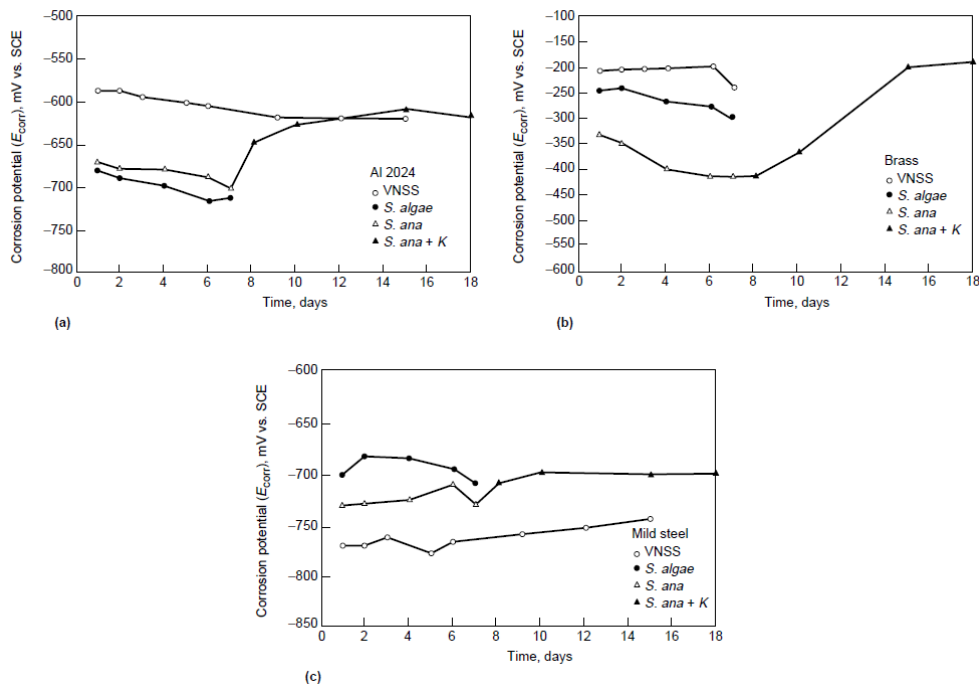
Figure. 1. 10. OCP values versus time for (a) Al 2024, (b) brass, and (c) mild steel exposed to artificial seawater [86]

The applied potential is modulated across a broad range in large-signal polarization experiments using either a series of applied potential steps or a continuous potential rate change. Additionally, a succession of current steps or a continually changing current may be used; however, these approaches are less common. Due to the possibility that polarization across a broad potential range may result in permanent changes to the sample surface characteristics, it is usually not practical to repeat a large-signal polarization test on the same sample [84,85,87]. Figure 1.11 shows the implemented setup for polarization measurement and most other electrochemical testings.
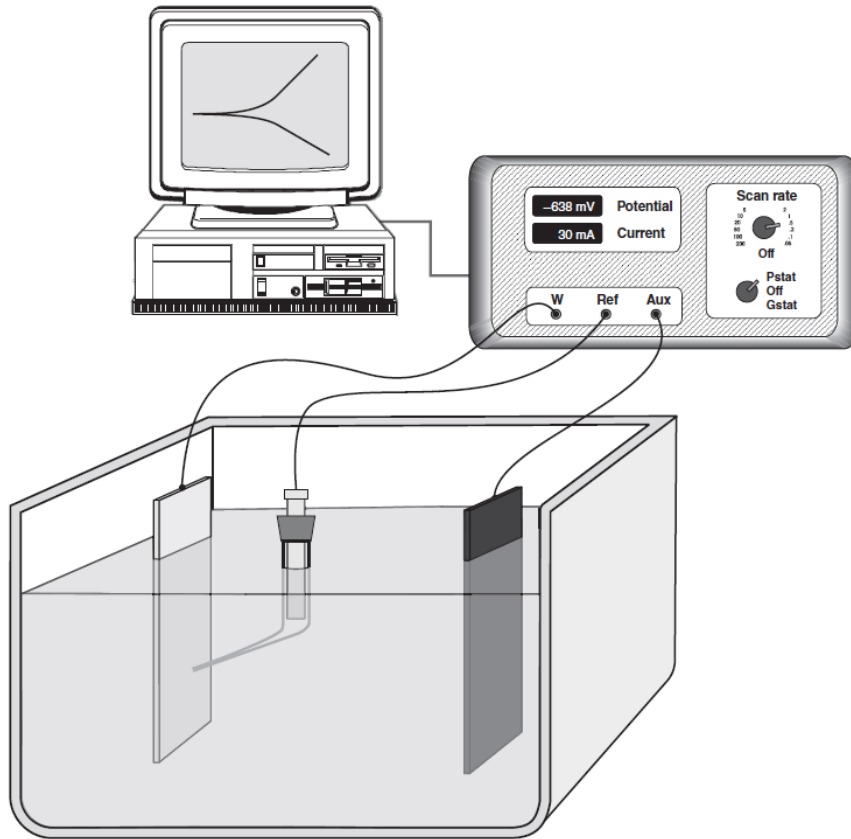
Figure. 1. 11. Electrochemical instrumentation to carry out potentiodynamic measurements [84].

A full polarization curve is made up of a cathodic and anodic component. The cathodic region of the polarization curve offers information on the kinetics of the reduction reaction(s) that occur in a given system. The anodic portion of the polarization curve has distinct characteristics heavily dependent on the metal-electrolyte combination [85]. Typically, a charge-transfer-controlled area occurs around the corrosion potential. Passive metals exhibit an active-passive transition at potentials higher than corrosion potential, followed by a passive area and an oxygen evolution region. When the pitting potential (E_{pit}) is surpassed, a significant rise in current occurs in the passive zone[85,88].

The information related to the kinetics of the corrosion reactions can be calculated from the polarization curves in the Tafel area, in which the connection between the applied potential (E_{appl}) and the measured current density (i) can be measured for anodic reactions using the equation below [85]:

$$E_{appl} = E_{corr} + \beta_a \log \left({i}/{i_{corr}} \right) \tag{4}$$

And for the cathodic region:

$$E_{appl} = E_{corr} - \beta_c \log \left({i}/{i_{corr}} \right) \tag{5}$$

where β is Tafel cathodic or anodic slope; the corrosion current density (i_{corr}) can be calculated using equations 4 and 5 by extrapolating the Tafel lines to $E_{appl}=E_{corr}$ at the corrosion current density value, as shown in Figure 1.12 [84,85].
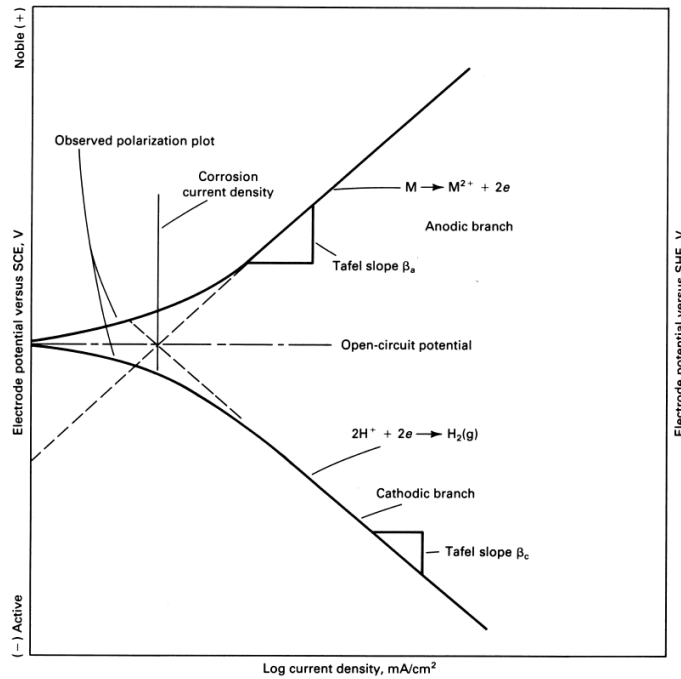
Figure. 1. 12. Theoretical Tafel curve, showing the Tafel extrapolation technique [85].

Electrochemical impedance spectroscopy (EIS) is collected as a function of the frequency of an applied alternating current signal at a defined potential. Typically, a wide frequency range must

be examined to acquire the whole impedance spectrum. This frequency range is often extended from 100 kHz, to 1 mHz in most corrosion experiments. Lower frequency measurements are very time demanding. Typically, impedance measurements are calculated using a three-electrode system, but it is also feasible to utilize a two-electrode system using the same material for both electrodes. A notable benefit of EIS over other electrochemical methods is detecting characteristics with extremely tiny amplitude signals without appreciably affecting them. To estimate the polarisation resistance (R_p), the EIS findings must be evaluated in conjunction with an interface model. Among the several equivalent circuits developed to model electrochemical interactions in a passive fil of materials, only a handful apply to a uniformly corroding system [84,85]. The first circuit is the simplest equivalent circuit for describing the interface between metal and electrolyte, as shown in Figure 1. 13.
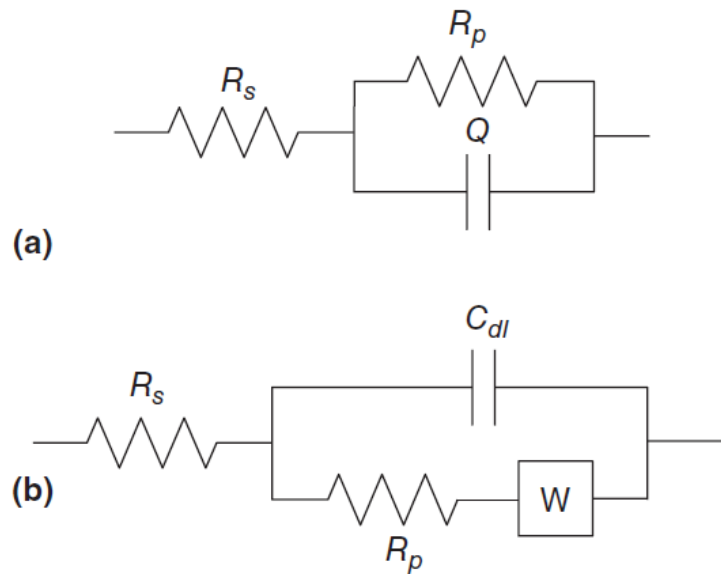
Figure. 1. 13. The equivalent circuit (EC) models suggested for analyzing the EIS results in (a) simple representation of the interface and (b) one time constant with diffusion [84].

The electrochemical behavior of a passive film using the EIS measurements can be interpreted using the equation below [84]:

$$Z(\omega) = R_s + \frac{R_p}{1+(j\omega R_p c_{dl})^\beta} \tag{6}$$

where R_s is the solution resistance, R_p is the polarization resistance, ω is the frequency, and C_{dl} is the double layer capacitance [84,85,89]. For example, the electrochemical behavior and corrosion resistance of a passive film for a 430 stainless steel in a solution containing 0.005 M sulfuric acid and 0.495 M sodium sulfate is presented using Nyquist and Bode plots as shown in Figure 1.14. The detailed description of EIS measurements and how the Bode and Nyquist plots are interpreted will be elaborated on in the upcoming chapters.
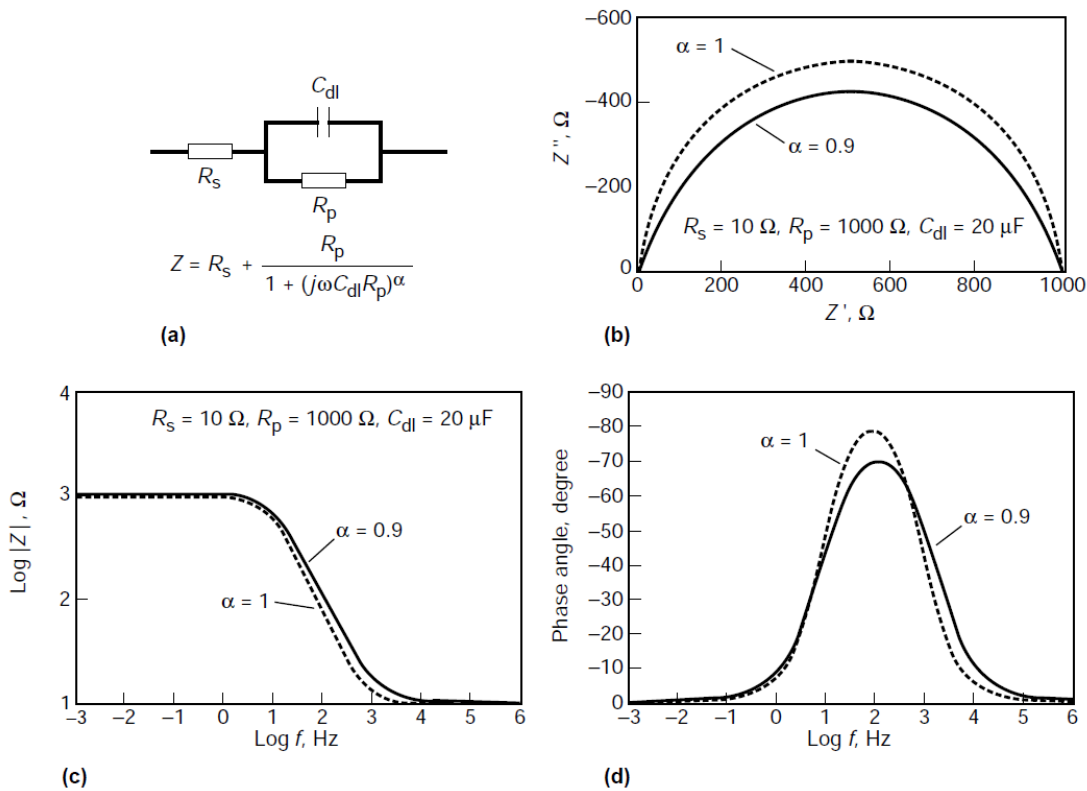
Figure. 1. 14. (a) Equivalent circuit (b) the Nyquist plot (c) Bode plot of impedance magnitude vs. frequency (d) Bode plot of the negative phase angle vs. frequency for a 430 stainless steel in a solution containing 0.005 M sulfuric acid and 0.495 M sodium sulfate.

3. Motivation and Research objectives

Most of the previous studies have mainly characterized the corrosion response of the 420 martensitic stainless steel from the electrochemical perspective [7,8]. It is well known that the corrosion performance of the martensitic stainless steels is governed by both electrochemical and metallurgical factors [7,8,17,90]. From the microstructure perspective, the corrosion performance of martensitic stainless steel is impacted by various factors, including grain size distribution, inclusion and secondary phase formation, surface roughness, residual stress, and elemental segregation [91–93]. Therefore, process-induced microstructure features can lead to distinct corrosion performance in adverse and favorable ways.

Unlike their austenitic counterparts, MSSs can be heat-treated, significantly influencing the secondary phase formation and corrosion performance [8,94]. Although upon cooling from quenching treatments, a fully martensitic structure is expected for 420 MSS, unwanted micro-constituents can form due to high alloying elements and the uncontrolled cooling regimes [7,8]. Undissolved chromium-rich carbides generally remain at the structure upon insufficient quenching at low temperatures or low exposure times [34]. On the other hand, unwanted retained austenite and residual delta ferrite can form at room temperature through fast cooling rates [95]. Carbides can also develop in the microstructure of the 420 MSS through tempering heat treatments [8]. The contribution of each metastable particle to the corrosion performance of the 420 MSS under various heat treatment conditions is a fascinating subject to investigate.

Moreover, although the impact of deformation-induced microstructure on the corrosion performance of the most ferritic, austenitic, and duplex steels has been investigated thoroughly in previous literature [96–99], there is no study covering the impact of deformation on the electrochemical response of the martensitic stainless steels such as AISI 420 MSS. Plastic

deformation can lead to a significant change in the grain rearrangements and the texture of the materials [100,101]. Hence, it can be interesting to study the impact of the deformation-induced crystallographic orientation on corrosion resistance. Variation in the residual stress caused by plastic deformation and characterizing its influence on the electrochemical response of the 420 MSS is another aspect that requires more attention herein [102].

On the other hand, as the demand for material consumption increases and the supplies remain limited, the invention and implementation of new fabrication techniques become crucial [103]. Newly developed fabrication techniques such as metal additive manufacturing (AM) with the ability to fabricate customized parts with low waste rates can be promising resolutions to the existing gaps and deficiencies in design and manufacturing [104]. On the other hand, AM provides a fast solution for on-site manufacturing, where accessibility to the conventional manufacturing techniques is limited, which can be a great option for fabrication adaption for the post-covid era, considering the current disruption in most manufacturing supply chains [105].

As one of the most promising additive manufacturing techniques for fabrication of large-scale metallic parts, wire arc additive manufacturing (WAAM) can be implemented for layer by layer manufacturing of martensitic stainless steels [106]. In a WAAM process, generally, a robotic arm carries an arc welding torch as the energy source and the metal wire as the feedstock material to fabricate each layer [77]. Layer by layer deposition strategy and high heat rate in each deposition cycle leads to complex thermal history experienced by the fabricated parts in different zones [107]. This can lead to unique microstructural features in components deposited with the WAAM process compared to the conventional fabrication techniques [108]. Some of these microstructural features potentially can be unfavorable for the electrochemical stability of the alloy [109], indicating the importance of the post-fabrication heat treatment to improve the corrosion response [110]. Hence,

characterizing the corrosion performance of the deposited parts and correlating the impact of the observed distinct microstructural features with corrosion performance is essential. Moreover, through the deposition of each layer, the heat dissipation path can have a specific concurrence with the deposition direction leading to the formation of strong texture in the microstructure [107]. Therefore, the crystallographic orientation of the as-printed parts and its influence on the corrosion should be investigated.

On the other hand, wire arc additive manufacturing has excellent potential as an alternative technique for remanufacturing and restoring failed components [111]. The localized restoration of failed 420 MSS parts can be implemented through the deposition of an automated repairing track by applying a similar ER420 wire material or an alternative alloy with better mechanical and electrochemical performance. Hence, the microstructural features and the corrosion performance of the 420 MSS repairing track and the interfacial region between the substrate and the repairing track, fabricated by the WAAM process, should be thoroughly investigated. Therefore, this thesis aims to answer the following questions:

1. What is the impact of the plastic deformation on the corrosion performance of the AISI 420 martensitic stainless steel?

2. What is the impact of the crystallographic orientation and grain distribution on the electrochemical performance of the 420 martensitic stainless steel?

3. What is the impact of the secondary phase formation on the microstructure and corrosion performance of the as-printed wire arc additive manufactured 420 martensitic stainless steels?

4. What is the true impact of the post-fabrication heat treatment on the microstructure and corrosion performance of the wire arc additive manufactured 420 martensitic stainless steel?

5. How can the wire arc additive manufacturing be applied as a restoration technique for 420 MSS, and what is the impact of microstructural factors on the corrosion performance of the interfacial bonding region of a repairing track?

Focusing on these questions, current thesis investigates the impact of the process-induced microstructural and crystallographic orientation on the electrochemical performance of the 420 martensitic stainless steel.

4. Organization of the thesis

The current thesis is prepared in a manuscript format (paper-based). Overall, the research outcome of the present dissertation has been published in four peer-reviewed journal papers as a first author, four peer-reviewed journals as the second or third author, three conference papers as a first author, and five conference papers as second or third author. Two journal papers are submitted and under review as well. The details of each publication are listed below:

<u>Journal Papers:</u>

1) **Salar Salahi,** , Mostafa Kazemipour, and Ali Nasiri. "Effect of Uniaxial Tension-Induced Plastic Strain on the Microstructure and Corrosion Behavior of 13Cr Martensitic Stainless Steel." *Corrosion* 76, no. 12 (2020): 1122-1135.

2) **Salar Salahi,** , Mostafa Kazemipour, and Ali Nasiri. "Effects of microstructural evolution on the corrosion properties of AISI 420 martensitic stainless steel during cold rolling process." *Materials Chemistry and Physics* 258 (2021): 123916.

3) **Salar Salahi,** , Mahya Ghaffari, Alireza Vahedi Nemani, and Ali Nasiri. "Effects of Secondary-Phase Formation on the Electrochemical Performance of a Wire Arc Additive

Manufactured 420 Martensitic Stainless Steel under Different Heat Treatment Conditions." *Journal of Materials Engineering and Performance* (2021): 1-12.

4) **Salar Salahi,** , Alireza Vahedi Nemani, Mahya Ghaffari, Jonas Lunde, and Ali Nasiri. "On microstructure, crystallographic orientation, and corrosion properties of wire arc additive manufactured 420 martensitic stainless steel: Effect of the inter-layer temperature." *Additive Manufacturing* 46 (2021): 102157.

5) Mostafa Kazemipour , **Salar Salahi**, and Ali Nasiri. "Box-Behnken Design Approach Toward Predicting the Corrosion Response of 13Cr Stainless Steel." *Corrosion* 76, no. 4 (2020): 356-365.

6) Alireza Vahedi Nemani, , Mahya Ghaffari, **Salar Salahi**, Jonas Lunde, and Ali Nasiri. "Effect of interpass temperature on the formation of retained austenite in a wire arc additive manufactured ER420 martensitic stainless steel." *Materials Chemistry and Physics* 266 (2021): 124555.

7) Alireza Vahedi Nemani, Mahya Ghaffari, **Salar Salahi**, and Ali Nasiri. "Effects of post-printing heat treatment on the microstructure and mechanical properties of a wire arc additive manufactured 420 martensitic stainless steel part." *Materials Science and Engineering: A* 813 (2021): 141167.

8) Jonas Lunde, Mostafa Kazemipour, **Salar Salahi**, and Ali Nasiri. "Wire Arc Additive Manufacturing of AISI 420 Martensitic Stainless Steel: On As-Printed Microstructure and Mechanical Properties." *Journal of Materials Engineering and Performance* 30, no. 12 (2021): 9181-9191.

Conference papers:

1) Jonas Lunde , Mostafa Kazemipour, Salar Salahi, and Ali Nasiri. "Microstructure and Mechanical Properties of AISI 420 Stainless Steel Produced by Wire Arc Additive Manufacturing." In *TMS 2020 149th Annual Meeting & Exhibition Supplemental Proceedings*, pp. 413-424. Springer, Cham, 2020.

2) Mostafa Kazemipour , Jonas Halvorsen Lunde, **Salar Salahi**, and Ali Nasiri. "On the Microstructure and Corrosion Behavior of Wire Arc Additively Manufactured AISI 420 Stainless Steel." In *TMS 2020 149th Annual Meeting & Exhibition Supplemental Proceedings*, pp. 435-448. Springer, Cham, 2020.

3) **Salar Salahi,** , Mostafa Kazemipour, , and Ali Nasiri. " Effect of Crystallographic Orientation on the Corrosion Behavior of 13Cr Stainless Steel." In *NACE INTERNATIONAL, Northern Area Western Conference, Calgary, Alberta*, December, 2020.

4) Kazemipour, Mostafa, **Salar Salahi**, and Ali Nasiri. " Investigation on the synergistic effect of environmental conditions on the corrosion behavior of 13Cr stainless steel."

In *NACE INTERNATIONAL, Northern Area Western Conference, Calgary, Alberta*, December 2020.

5) **Salar Salahi,** , Mostafa Kazemipour, , and Ali Nasiri. " Effect of Crystallographic Orientation on the Corrosion Behavior of 13Cr Stainless Steel." In *Canadian Society for Mechanical Engineering and CFD Society of Canada International Congress* , June, 2019.

6) Mostafa Kazemipour , **Salar Salahi** , and Ali Nasiri. " On the Influence of the Environmental Factors on Corrosion Behavior of 13Cr Stainless Steel Using Box-Behnken Design." In *Canadian Society for Mechanical Engineering and CFD Society of Canada International Congress,* June 2019.

7) **Salar Salahi,** , Mahya Ghaffari, Alireza Vahedi Nemani, and Ali Nasiri. " Microstructural Evolution and Electrochemical Performance of the Interfacial Region between a Wrought and a Wire Arc Additive Manufactured 420 Martensitic Stainless Steel." *60th Conference of Metallurgists, Halifax*, August 2021.

8) Mahya Ghaffari , **Salar Salahi,** , Alireza Vahedi Nemani, and Ali Nasiri. " Effects of Columnar Grain Growth and Inhomogeneous Microstructure on the Anisotropic Mechanical Properties of a Wire Arc Additive Manufactured pH 13-8Mo Martensitic Stainless Steel." *60th Conference of Metallurgists, Halifax*, August 2021.

9) Alireza Vahedi Nemani, Mahya Ghaffari**,** , **Salar Salahi** , and Ali Nasiri. " On the Hardening and Subsequent Tempering of a Wire Arc Additive Manufactured 420 Martensitic Stainless Steel." *60th Conference of Metallurgists, Halifax*, August 2021.

10) Jonas Lunde, **Salar Salahi**, Ali Nasiri. " The Effects of Tempering Time on the Microstructure and Corrosion Behavior of Wire Arc Additively Manufactured 420 Martensitic Stainless Steel." *60th Conference of Metallurgists, Halifax*, August 2021.

Submitted Journal Papers:

1)   **Salar Salahi** , Mahya Ghaffari, Alireza Vahedi Nemani, and Ali Nasiri. " Microstructural Evolution and Electrochemical Performance of the Interfacial Region between a Wrought and a Wire Arc Additive Manufactured 420 Martensitic Stainless Steel." *Submitted to the Journal of Materials Characterization*.

2)   **Salar Salahi** , Mahya Ghaffari, Alireza Vahedi Nemani, and Ali Nasiri. " Electrochemical Performance of the Interfacial Region between an AISI 420 and a Wire Arc Additive Manufactured PH 13–8Mo Martensitic Stainless Steel *" Submitted to the Journal of Additive Manufacturing.*

Chapter 2 examines the impact of uniaxial tension on the microstructure and corrosion behavior of the AISI 420 martensitic stainless steel (also known as 13Cr martensitic stainless steel).

Chapter 3 characterizes the effect of the cold rolling on the microstructure and corrosion performance of the AISI 420 martensitic stainless steel.

Chapter 4 examines the impact of interlayer temperature on the microstructure, crystallographic orientation, and corrosion response of the 420 martensitic stainless parts fabricated by wire arc additive manufacturing technique.

Chapter 5 characterized the impact of the two different heat treatment processes on the corrosion response of the as-printed 420 MSS samples fabricated by the wire arc additive manufacturing process.

In chapter 6, the feasibility of applying the wire arc additive manufacturing as a restoration technique for AISI 420 martensitic stainless steel and the microstructure and corrosion performance of the interfacial region between the substrate 420 MSS deposited layer is investigated.

Chapter 7 examines the microstructural evolution, crystallographic orientation, and electrochemical response of the interfacial region between a 420 MSS and a PH 13–8Mo martensitic stainless steel repairing track fabricated by the wire arc additive manufacturing technique.

References:

[1]   R.K. Gupta, N. Birbilis, The influence of nanocrystalline structure and processing route on corrosion of stainless steel: a review, Corros. Sci. 92 (2015) 1–15.
[2]   K.H. Lo, C.H. Shek, J.K.L. Lai, Recent developments in stainless steels, Mater. Sci. Eng. R Reports. 65 (2009) 39–104.
[3]   A.J. Sedriks, Corrosion of stainless steel, 2, (1996).
[4]   Y. Zhao, W. Liu, T. Zhang, Z. Sun, Y. Wang, Y. Fan, B. Dong, Assessment of the correlation between M23C6 precipitates and pitting corrosion resistance of 0Cr13 martensitic stainless steel, Corros. Sci. (2021) 109580.

[5]   K. Morshed-Behbahani, N. Zakerin, P. Najafisayar, M. Pakshir, A survey on the passivity of tempered AISI 420 martensitic stainless steel, Corros. Sci. 183 (2021) 109340.

[6]   A. Dalmau, C. Richard, A. Igual–Muñoz, Degradation mechanisms in martensitic stainless steels: Wear, corrosion and tribocorrosion appraisal, Tribol. Int. 121 (2018) 167–179.

[7]   C.J. Scheuer, F.A.A. Possoli, P.C. Borges, R.P. Cardoso, S.F. Brunatto, AISI 420 martensitic stainless steel corrosion resistance enhancement by low-temperature plasma carburizing, Electrochim. Acta. 317 (2019) 70–82.

[8]   K.H. Anantha, C. Ornek, S. Ejnermark, A. Medvedeva, J. Sj, Correlative Microstructure Analysis and In Situ Corrosion Study of AISI 420 Martensitic Stainless Steel for Plastic Molding, 164 (2017) 85–93. https://doi.org/10.1149/2.0531704jes.

[9]   N.A. Akeel, V. Kumar, O. Zaroog, Impact of the Heat Treatment Process on the Properties of Stainless Steel Material, Solid State Technol. 64 (2021) 1461–1471.

[10]   J. Singh, S.K. Nath, Effects of cyclic heat treatment on microstructure and mechanical properties of 13% Cr-4% Ni martensitic stainless steel, J. Mater. Eng. Perform. 29 (2020) 2478–2490.

[11]   S.P. Brühl, R. Charadia, S. Simison, D.G. Lamas, A. Cabo, Corrosion behavior of martensitic and precipitation hardening stainless steels treated by plasma nitriding, Surf. Coatings Technol. 204 (2010) 3280–3286.

[12]   Y. Van Ingelgem, I. Vandendael, D. Van den Broek, A. Hubin, J. Vereecken, Influence of laser surface hardening on the corrosion resistance of martensitic stainless steel, Electrochim. Acta. 52 (2007) 7796–7801.

[13]   J.-P. Hirvonen, D. Rück, S. Yan, A. Mahiout, P. Torri, J. Likonen, Corrosion resistance of N-, Cr- or Cr+ N-implanted AISI 420 stainless steel, Surf. Coatings Technol. 74 (1995) 760–764.

[14]   X. Lü, F. Zhang, X. Yang, J. Xie, G. Zhao, Y. Xue, Corrosion performance of high strength 15Cr martensitic stainless steel in severe environments, J. Iron Steel Res. Int. 21 (2014) 774–780.

[15]   L. Hamadou, L. Aïnouche, A. Kadri, S.A.A. Yahia, N. Benbrahim, Electrochemical impedance spectroscopy study of thermally grown oxides exhibiting constant phase element behaviour, Electrochim. Acta. 113 (2013) 99–108. https://doi.org/https://doi.org/10.1016/j.electacta.2013.09.054.

[16]   P. Fathi, M. Mohammadi, X. Duan, A.M. Nasiri, A Comparative Study on Corrosion and Microstructure of Direct Metal Laser Sintered AlSi10Mg_200C and Die Cast A360.1 Aluminum, J. Mater. Process. Technol. 259 (2018) 1–14. https://doi.org/https://doi.org/10.1016/j.jmatprotec.2018.04.013.

[17]   K.H. Anantha, C. Örnek, S. Ejnermark, A. Medvedeva, J. Sjöström, J. Pan, Correlative microstructure analysis and in situ corrosion study of AISI 420 martensitic stainless steel for plastic molding applications, J. Electrochem. Soc. 164 (2017) C85.

[18]   H. Luo, Q. Yu, C. Dong, G. Sha, Z. Liu, J. Liang, L. Wang, G. Han, X. Li, Influence of the aging time on the microstructure and electrochemical behaviour of a 15-5PH ultra-high strength stainless steel, Corros. Sci. 139 (2018) 185–196. https://doi.org/https://doi.org/10.1016/j.corsci.2018.04.032.

[19]   A. Fattah-Alhosseini, M.A. Golozar, A. Saatchi, K. Raeissi, Effect of solution concentration on semiconducting properties of passive films formed on austenitic stainless steels, Corros. Sci. 52 (2010) 205–209.

[20]   S. Ningshen, U.K. Mudali, V.K. Mittal, H.S. Khatak, Semiconducting and passive film properties of nitrogen-containing type 316LN stainless steels, Corros. Sci. 49 (2007) 481–496.

[21]   P. Corengia, G. Ybarra, C. Moina, A. Cabo, E. Broitman, Microstructure and corrosion behaviour of DC-pulsed plasma nitrided AISI 410 martensitic stainless steel, Surf. Coatings Technol. 187 (2004) 63–69.

[22]   G. Fierro, G.M. Ingo, F. Mancia, XPS investigation on the corrosion behavior of 13Cr-Martensitic stainless steel in CO2-H2S-Cl− environments, Corrosion. 45 (1989) 814–823.

[23]   Y. Zhou, Y. Zuo, The inhibitive mechanisms of nitrite and molybdate anions on initiation and propagation of pitting corrosion for mild steel in chloride solution, Appl. Surf. Sci. 353 (2015) 924–932.

[24]   J. Bhandari, F. Khan, R. Abbassi, V. Garaniya, R. Ojeda, Modelling of pitting corrosion in marine and offshore steel structures–A technical review, J. Loss Prev. Process Ind. 37 (2015) 39–62.

[25]   S. Marcelin, N. Pébère, S. Régnier, Electrochemical characterisation of a martensitic stainless steel in a neutral chloride solution, Electrochim. Acta. 87 (2013) 32–40.

[26]   S. Pahlavan, S. Moazen, I. Taji, K. Saffar, M. Hamrah, M.H. Moayed, S.M. Beidokhti, Pitting corrosion of martensitic stainless steel in halide bearing solutions, Corros. Sci. 112 (2016) 233–240.

[27]   I. Taji, M.H. Moayed, M. Mirjalili, Correlation between sensitisation and pitting corrosion of AISI 403 martensitic stainless steel, Corros. Sci. 92 (2015) 301–308.

[28]   X. Lei, Y. Feng, J. Zhang, A. Fu, C. Yin, D.D. Macdonald, Impact of reversed austenite on the pitting corrosion behavior of super 13Cr martensitic stainless steel, Electrochim. Acta. 191 (2016) 640–650.

[29]   Y.Z. Li, X. Wang, G.A. Zhang, Corrosion behaviour of 13Cr stainless steel under stress and crevice in 3.5 wt.% NaCl solution, Corros. Sci. 163 (2020) 108290.

[30]   Z.F. Yin, M.L. Yan, Z.Q. Bai, W.Z. Zhao, W.J. Zhou, Galvanic corrosion associated with SM 80SS steel and Ni-based alloy G3 couples in NaCl solution, Electrochim. Acta. 53 (2008) 6285–6292.

[31]   C. Andrade, P. Garcés, I. Martínez, Galvanic currents and corrosion rates of reinforcements measured in cells simulating different pitting areas caused by chloride attack in sodium hydroxide, Corros. Sci. 50 (2008) 2959–2964.

[32]   S.K. Bonagani, V. Bathula, V. Kain, Influence of tempering treatment on microstructure and pitting corrosion of 13 wt.% Cr martensitic stainless steel, Corros. Sci. (2018). https://doi.org/10.1016/j.corsci.2017.12.012.

[33]   A.F. Candelaria, C.E. Pinedo, Influence of the heat treatment on the corrosion resistance of the martensitic stainless steel type AISI 420, J. Mater. Sci. Lett. 22 (2003) 1151–1153.

[34]   G. Wei, S. Lu, S. Li, K. Yao, H. Luan, X. Fang, Unmasking of the temperature window and mechanism for "loss of passivation" effect of a Cr-13 type martensite stainless steel, Corros. Sci. 177 (2020) 108951.

[35]   J. Jun, T. Li, G.S. Frankel, N. Sridhar, Corrosion and repassivation of Super 13Cr stainless steel in artificial 1D pit electrodes at elevated temperature, Corros. Sci. 173 (2020) 108754.

[36]   S.S.M. Tavares, F.J. Da Silva, C. Scandian, G.F. Da Silva, H.F.G. De Abreu, Microstructure and intergranular corrosion resistance of UNS S17400 (17-4PH) stainless steel, Corros. Sci. 52 (2010) 3835–3839.

[37]   R. Singh, I. Chattoraj, A. Kumar, B. Ravikumar, P.K. Dey, The effects of cold working on sensitization and intergranular corrosion behavior of AISI 304 stainless steel, Metall. Mater. Trans. A. 34 (2003) 2441–2447.

[38]   J.M. Aquino, C.A. Della Rovere, S.E. Kuri, Intergranular corrosion susceptibility in supermartensitic stainless steel weldments, Corros. Sci. 51 (2009) 2316–2323.

[39]   S. Marcelin, N. Pébère, S. Régnier, Electrochemical investigations on crevice corrosion of a martensitic stainless steel in a thin-layer cell, J. Electroanal. Chem. 737 (2015) 198–205.

[40]   E. Stange, Thermography and tensile tests of steel samples. Study of material properties and internal friction effects, (2018).

[41]   D. Roylance, Stress-strain curves, Massachusetts Inst. Technol. Study, Cambridge. (2001).

[42]   R. Janco, B. Hucko, Introduction to Mechanics of Materials: Part II, (2014).

[43]   J. Rychlewski, On Hooke's law, J. Appl. Math. Mech. 48 (1984) 303–314.

[44]   J. Lubliner, Plasticity theory, Courier Corporation, 2008.

[45]   C. Teodosiu, Large Plastic Deformation of crystalline aggregates, Springer, 1997.

[46]   P.J.N. Pells, Uniaxial strength testing, in: Rock Test. Site Charact., Elsevier, 1993: pp. 67–85.

[47]   W.D. Callister, Fundamentals of materials science and engineering, Wiley London, 2000.

[48]   W.D. Callister, Mechanical properties of metals, Mater. Sci. Eng. an Introd. (1994).

[49]   J.P. Singh, S. Verma, Woven Terry Fabrics: Manufacturing and Quality Management, Woodhead Publishing, 2016.

[50]   S. Salem, Alloyed steel intended for hot rolling mill rolls, Met. Sci. Heat Treat. 35 (1993) 657–659.

[51]   S. Salahi, Low temperature behavior of ZK60 magnesium alloy after thermo-mechanical

processing, (2017).

[52]   F.J. Humphreys, M. Hatherly, Recrystallization and related annealing phenomena, Elsevier, 2012.

[53]   S. Suwas, R.K. Ray, Crystallographic texture of materials, Springer, 2014.

[54]   D.J. Dingley, V. Randle, Microtexture determination by electron back-scatter diffraction, J. Mater. Sci. 27 (1992) 4545–4566.

[55]   F.J. Humphreys, M. Hatherly, Chapter 15 - Control of Recrystallization, in: F.J. Humphreys, M. Hatherly (Eds.), Recryst. Relat. Annealing Phenom. (Second Ed., Second Edi, Elsevier, Oxford, 2004: pp. 469–505. https://doi.org/https://doi.org/10.1016/B978-008044164-1/50019-0.

[56]   Y. Huang, F.J. Humphreys, Subgrain growth and low angle boundary mobility in aluminium crystals of orientation {110}〈001〉, Acta Mater. 48 (2000) 2017–2030. https://doi.org/https://doi.org/10.1016/S1359-6454(99)00418-8.

[57]   D. Rowenhorst, A.D. Rollett, G.S. Rohrer, M. Groeber, M. Jackson, P.J. Konijnenberg, M. De Graef, Consistent representations of and conversions between 3D rotations, Model. Simul. Mater. Sci. Eng. 23 (2015) 83501.

[58]   W.B. Hutchinson, B.J. Duggan, M. Hatherly, Development of deformation texture and microstructure in cold-rolled Cu–30Zn, Met. Technol. 6 (1979) 398–403.

[59]   T. Horii, S. Kirihara, Y. Miyamoto, Freeform fabrication of superalloy objects by 3D micro welding, Mater. Des. 30 (2009) 1093–1097.

[60]   J.F. Wang, Q.J. Sun, H. Wang, J.P. Liu, J.C. Feng, Effect of location on microstructure and mechanical properties of additive layer manufactured Inconel 625 using gas tungsten arc welding, Mater. Sci. Eng. A. 676 (2016) 395–405.

[61]   N. Li, J. Zhang, W. Xing, D. Ouyang, L. Liu, 3D printing of Fe-based bulk metallic glass composites with combined high strength and fracture toughness, Mater. Des. 143 (2018) 285–296.

[62]   M. Bambach, I. Sizova, Hot working behavior of selective laser melted and laser metal deposited Inconel 718, in: AIP Conf. Proc., AIP Publishing, 2018: p. 170001.

[63]   M. Bambach, I. Sizova, F. Silze, M. Schnick, Hot workability and microstructure evolution of the nickel-based superalloy Inconel 718 produced by laser metal deposition, J. Alloys Compd. 740 (2018) 278–287.

[64]   Z. Yang, M. Zhang, Z. Zhang, A. Liu, R. Yang, S. Liu, A study on diamond grinding wheels with regular grain distribution using additive manufacturing (AM) technology, Mater. Des. 104 (2016) 292–297.

[65]   L.E. Murr, S.M. Gaytan, A. Ceylan, E. Martinez, J.L. Martinez, D.H. Hernandez, B.I. Machado, D.A. Ramirez, F. Medina, S. Collins, Characterization of titanium aluminide alloy components fabricated by additive manufacturing using electron beam melting, Acta Mater. 58 (2010) 1887–1894.

[66]   D. Yang, C. He, G. Zhang, Forming characteristics of thin-wall steel parts by double electrode GMAW based additive manufacturing, J. Mater. Process. Technol. 227 (2016) 153–160.

[67]   S. Moylan, E. Whitenton, B. Lane, J. Slotwinski, Infrared thermography for laser-based powder bed fusion additive manufacturing processes, in: AIP Conf. Proc., AIP, 2014: pp. 1191–1196.

[68]   T.D. Ngo, A. Kashani, G. Imbalzano, K.T.Q. Nguyen, D. Hui, Additive manufacturing (3D printing): A review of materials, methods, applications and challenges, Compos. Part B Eng. (2018). https://doi.org/10.1016/j.compositesb.2018.02.012.

[69]   L. Wang, J. Xue, Q. Wang, Correlation between arc mode, microstructure, and mechanical properties during wire arc additive manufacturing of 316L stainless steel, Mater. Sci. Eng. A. (2019). https://doi.org/10.1016/j.msea.2019.02.078.

[70]   M. Rafieazad, On microstructure and corrosion properties of the laser-powder bed fused (L-PBF) AlSi10Mg alloy, (2021).

[71]   Y. Kok, X.P. Tan, P. Wang, M.L.S. Nai, N.H. Loh, E. Liu, S.B. Tor, Anisotropy and heterogeneity of microstructure and mechanical properties in metal additive manufacturing: A critical review, Mater. Des. (2018). https://doi.org/10.1016/j.matdes.2017.11.021.

[72]   M. Ghaffari, A.V. Nemani, M. Rafieazad, A. Nasiri, Effect of solidification defects and HAZ softening on the anisotropic mechanical properties of a wire arc additive-manufactured low-carbon low-

alloy steel part, JOM. 71 (2019) 4215–4224.

[73]   M. Rafieazad, M. Ghaffari, A.V. Nemani, A. Nasiri, Microstructural evolution and mechanical properties of a low-carbon low-alloy steel produced by wire arc additive manufacturing, Int. J. Adv. Manuf. Technol. 105 (2019) 2121–2134.

[74]   A.V. Nemani, M. Ghaffari, A. Nasiri, Comparison of microstructural characteristics and mechanical properties of shipbuilding steel plates fabricated by conventional rolling versus wire arc additive manufacturing, Addit. Manuf. 32 (2020) 101086.

[75]   Z. Wang, A.M. Beese, Effect of chemistry on martensitic phase transformation kinetics and resulting properties of additively manufactured stainless steel, Acta Mater. 131 (2017) 410–422.

[76]   L. Costa, R. Colaço, T. Réti, A.M. Deus, R. Vilar, Tempering effects in steel parts produced by additive fabrication using laser powder deposition, Proc. VR@ P. (2003) 249.

[77]   B. Wu, Z. Pan, D. Ding, D. Cuiuri, H. Li, J. Xu, J. Norrish, A review of the wire arc additive manufacturing of metals: properties, defects and quality improvement, J. Manuf. Process. 35 (2018) 127–139. https://doi.org/10.1016/j.jmapro.2018.08.001.

[78]   S.W. Williams, F. Martina, A.C. Addison, J. Ding, G. Pardal, P. Colegrove, Wire+ arc additive manufacturing, Mater. Sci. Technol. 32 (2016) 641–647.

[79]   C. Shen, Z. Pan, Y. Ma, D. Cuiuri, H. Li, Fabrication of iron-rich Fe–Al intermetallics using the wire-arc additive manufacturing process, Addit. Manuf. 7 (2015) 20–26.

[80]   A. Vahedi Nemani, M. Ghaffari, A. Nasiri, On the Post-Printing Heat Treatment of a Wire Arc Additively Manufactured ER70S Part, Materials (Basel). 13 (2020) 2795.

[81]   A. Caballero, J. Ding, S. Ganguly, S. Williams, Wire+ Arc Additive Manufacture of 17-4 PH stainless steel: Effect of different processing conditions on microstructure, hardness, and tensile strength, J. Mater. Process. Technol. 268 (2019) 54–62.

[82]   Y. Feng, B. Zhan, J. He, K. Wang, The double-wire feed and plasma arc additive manufacturing process for deposition in Cr-Ni stainless steel, J. Mater. Process. Technol. 259 (2018) 206–215.

[83]   X. Zhang, K. Wang, Q. Zhou, J. Ding, S. Ganguly, G. Marzio, D. Yang, X. Xu, P. Dirisu, S.W. Williams, Microstructure and mechanical properties of TOP-TIG-wire and arc additive manufactured super duplex stainless steel (ER2594), Mater. Sci. Eng. A. 762 (2019) 138097.

[84]   P.R. Roberge, Handbook of corrosion engineering, McGraw-Hill Education, 2019.

[85]   F. Mansfeld, Electrochemical methods of corrosion testing, ASM Handb. 13 (2003) 446–462.

[86]   A. Nagiub, F. Mansfeld, Evaluation of microbiologically influenced corrosion inhibition (MICI) with EIS and ENA, Electrochim. Acta. 47 (2002) 2319–2333.

[87]   M. Kazemipour, M. Mohammadi, E. Mfoumou, A.M. Nasiri, Microstructure and Corrosion Characteristics of Selective Laser-Melted 316L Stainless Steel: The Impact of Process-Induced Porosities, JOM. 71 (2019) 3230–3240. https://doi.org/10.1007/s11837-019-03647-w.

[88]   R.G. Kelly, J.R. Scully, D. Shoesmith, R.G. Buchheit, Electrochemical techniques in corrosion science and engineering, CRC Press, 2002.

[89]   D. Wallinder, J. Pan, C. Leygraf, A. Delblanc-Bauer, EIS and XPS study of surface modification of 316LVM stainless steel after passivation, Corros. Sci. 41 (1998) 275–289.

[90]   G. Chakraborty, C.R. Das, S.K. Albert, A.K. Bhaduri, V. Thomas Paul, G. Panneerselvam, A. Dasgupta, Study on tempering behaviour of AISI 410 stainless steel, Mater. Charact. 100 (2015) 81–87. https://doi.org/https://doi.org/10.1016/j.matchar.2014.12.015.

[91]   A.H. Ettefagh, S. Guo, J. Raush, Corrosion performance of additively manufactured stainless steel parts: A review, Addit. Manuf. 37 (2021) 101689.

[92]   V. Venegas, F. Caleyo, T. Baudin, J.H. Espina-Hernandez, J.M. Hallen, On the role of crystallographic texture in mitigating hydrogen-induced cracking in pipeline steels, Corros. Sci. 53 (2011) 4204–4212.

[93]   S.S. Chouthai, K. Elayaperumal, Texture dependence of corrosion of mild steel after cold rolling, Br. Corros. J. 11 (1976) 40–43.

[94]   K. Morshed-Behbahani, P. Najafisayar, M. Pakshir, M. Shahsavari, An electrochemical study on the effect of stabilization and sensitization heat treatments on the intergranular corrosion behaviour of

AISI 321H austenitic stainless steel, Corros. Sci. 138 (2018) 28–41.

[95]	J. Lunde, M. Kazemipour, S. Salahi, A. Nasiri, Microstructure and Mechanical Properties of AISI 420 Stainless Steel Produced by Wire Arc Additive Manufacturing BT - TMS 2020 149th Annual Meeting & Exhibition Supplemental Proceedings, in: Springer International Publishing, Cham, 2020: pp. 413–424.

[96]	J. Lv, W. Guo, T. Liang, The effect of pre-deformation on corrosion resistance of the passive film formed on 2205 duplex stainless steel, J. Alloys Compd. 686 (2016) 176–183.

[97]	H. Luo, H. Su, G. Ying, C. Dong, X. Li, Effect of cold deformation on the electrochemical behaviour of 304L stainless steel in contaminated sulfuric acid environment, Appl. Surf. Sci. 425 (2017) 628–638.

[98]	T. Malkiewicz, S. Rudnik, Deformation of non-metallic inclusions during rolling of steel, J. Iron Steel Inst. 201 (1963) 33.

[99]	X. Feng, X. Lu, Y. Zuo, N. Zhuang, D. Chen, The effect of deformation on metastable pitting of 304 stainless steel in chloride contaminated concrete pore solution, Corros. Sci. 103 (2016) 223–229.

[100]	B.R. Kumar, R. Singh, B. Mahato, P.K. De, N.R. Bandyopadhyay, D.K. Bhattacharya, Effect of texture on corrosion behavior of AISI 304L stainless steel, Mater. Charact. 54 (2005) 141–147.

[101]	D. Lindell, R. Pettersson, Crystallographic effects in corrosion of austenitic stainless steel 316L, Mater. Corros. 66 (2015) 727–732.

[102]	A. Ben Rhouma, H. Sidhom, C. Braham, J. Lédion, M.E. Fitzpatrick, Effects of surface preparation on pitting resistance, residual stress, and stress corrosion cracking in austenitic stainless steels, J. Mater. Eng. Perform. 10 (2001) 507–514.

[103]	G.S. San, I.N. Pujawan, Remanufacturing of the short life-cycle products, Oper. Supply Chain Manag. An Int. J. 7 (2014) 13–22.

[104]	D. Thomas, Costs, benefits, and adoption of additive manufacturing: a supply chain perspective, Int. J. Adv. Manuf. Technol. 85 (2016) 1857–1876.

[105]	E. Larrañeta, J. Dominguez-Robles, D.A. Lamprou, Additive manufacturing can assist in the fight against COVID-19 and other pandemics and impact on the global supply chain, 3D Print. Addit. Manuf. 7 (2020) 100–103.

[106]	Z. Lyu, Y.S. Sato, S. Tokita, Y. Zhao, J. Jia, A. Wu, Microstructural evolution in a thin wall of 2Cr13 martensitic stainless steel during wire arc additive manufacturing, Mater. Charact. 182 (2021) 111520.

[107]	J. Ge, J. Lin, H. Fu, Y. Lei, R. Xiao, A spatial periodicity of microstructural evolution and anti-indentation properties of wire-arc additive manufacturing 2Cr13 thin-wall part, Mater. Des. 160 (2018) 218–228. https://doi.org/10.1016/j.matdes.2018.09.021.

[108]	P.P. Nikam, D. Arun, K.D. Ramkumar, N. Sivashanmugam, Microstructure characterization and tensile properties of CMT-based wire plus arc additive manufactured ER2594, Mater. Charact. 169 (2020) 110671. https://doi.org/https://doi.org/10.1016/j.matchar.2020.110671.

[109]	Y. Zhang, F. Cheng, S. Wu, Improvement of pitting corrosion resistance of wire arc additive manufactured duplex stainless steel through post-manufacturing heat-treatment, Mater. Charact. 171 (2021) 110743.

[110]	X. Fang, H. Li, X. Li, K. Huang, L. Zhang, B. Lu, Effect of post heat treatment on the microstructure and mechanical properties of wire-arc additively manufactured A357 alloy components, Mater. Lett. 269 (2020) 127674. https://doi.org/https://doi.org/10.1016/j.matlet.2020.127674.

[111]	M. Ghaffari, A.V. Nemani, A. Nasiri, Interfacial bonding between a wire arc additive manufactured 420 martensitic stainless steel part and its wrought base plate, Mater. Chem. Phys. (2020) 123199.

Chapter 2

Effect of Uniaxial Tension-Induced Plastic Strain on the Microstructure and Corrosion Behavior of 13Cr Martensitic Stainless Steel [1]

Preface

A version of this paper has been published in the journal of CORROSION. I am the initial and corresponding author of the current article. In this chapter, along with co-authors Dr. Ali Nasiri and Mostafa Kazemipour, I investigated the effect of uniaxial tension on the microstructure and corrosion behavior of the 13Cr martensitic stainless steel. I prepared the methodology, experimental procedure, formal analysis, and the original and revised versions of the manuscript based on the reviewers' and coauthors' feedback and comments. The co-authors of this work, Dr. Ali Nasiri and Mostafa Kazemipour, helped me in idea conceptualization, experiment design, supervision, and editing of the manuscript.

---

[1] Salar Salahi, , Mostafa Kazemipour, and Ali Nasiri. "Effect of Uniaxial Tension-Induced Plastic Strain on the Microstructure and Corrosion Behavior of 13Cr Martensitic Stainless Steel." Corrosion 76, no. 12 (2020): 1122-1135.

Abstract

This study is aimed to understand the correlation between the manufacturing process-induced plastic deformation, microstructure, and corrosion behavior of a 13Cr martensitic stainless-steel tubing material (UNS S42000). Comparisons were made between the microstructure, crystallographic orientation, and corrosion performance of a texture free heat-treated sample and uniaxially tensioned samples to the elongations of 5% and 22%. Cyclic potentiodynamic polarization (CPP) tests and electrochemical impedance spectroscopy (EIS) were performed on all samples in aerated 3.5 wt.% NaCl electrolyte at room temperature. Overall, the corrosion resistance of the samples was found to decrease with increasing the deformation level. A more stable and higher corrosion potential and pitting potential values with a better stability of the passive film were derived for the non-deformed sample, whereas the 5% and 22% elongated samples exhibited lower corrosion and pitting potential values and were characterized by having a less stable passive layer. All samples consistently revealed micro-pits formation on the lath boundaries where high concentration of chromium carbide precipitates was detected. Increasing the level of plastic strain in 13Cr stainless steel was found to enlarge the size of sensitized regions along the matrix-coarse chromium carbide precipitates interface, providing more susceptible regions to initiation and propagation of pitting.

1.   Introduction

Due to the increased development of deep hot wells and their extremely harsh and corrosive environments, the applications of corrosion resistant martensitic stainless steels (MSS) have been increased drastically considering their economic benefit with a price nearly half of its duplex stainless steels counterparts [1]. The use of MSS tubing is not only limited to sweet water applications, but also has been expanded to numerous sour service applications [2]. 13Cr MSS is one of the most commonly used Oil Country Tubular Goods (OCTG) materials, particularly as tubing and casing, providing an optimal combination of mechanical strength and corrosion resistance due to its high content of Chromium (13 wt.%) [3].

The corrosion behavior of stainless steels is influenced by a combination of electrochemical and metallurgical factors governing the initiation, propagation, and stabilization of a specific type of localized corrosion attack, known as pitting corrosion [4]. Therefore, understanding the fabrication process-induced microstructural features on the corrosion response and electrochemical stability of the stainless steel is quite important to be able to predict possible unforeseen failures of the components in service conditions as a result of corrosion [5]. The fabrication process of martensitic stainless steels typically involves warm or cold deformation of the annealed material followed by applying post-deformation heat treatment cycles (commonly a hardening cycle followed by tempering), leading to the formation of different types of precipitates embedded in a ferritic/martensitic matrix [6]. While annealing leads to the formation of localized large spherical carbides in the microstructure, the hardening and its subsequent tempering form undissolved carbides along with fine precipitated carbides. Anantha *et al.* [7] reported that the martensitic transformation associated with the hardening of MSS can be accompanied with the formation of undissolved carbides, unwanted retained austenite, and possibly a low volume fraction of the ferrite phase. On the other hand,

although the carbide dissolution can be accelerated by increasing austenitizing temperature, the resultant austenite grain coarsening during the austenitization can potentially lead to the stability of some volume fraction of austenite at room temperature (so-called retained austenite), deteriorating the mechanical properties of the alloy [6]. The attained martensitic phase from the hardening cycle is characterized by high hardness and strength with extremely low ductility. Accordingly, Barlow and Du Toit [8] recommended the application of the tempering process to improve the toughness and ductility of the alloy and to relieve the residual stresses induced by the martensitic transformation.

Each of the individual constituents in the microstructure of MSS, *i.e.* carbides, retained austenite, ferrite, and martensite phases can effectively change the mechanical properties of the alloy, among which the formation and volume fraction of chromium carbides have the primary impacts [9]. Lula [5] also reported that chromium can contribute to the corrosion resistance of the martensitic stainless steels only in solid solution form. Therefore, the volume fraction of dissolved carbides in the matrix during austenitizing and carbide precipitation through tempering can highly influence the corrosion behavior of MSS [10]. The adopted heat treatment cycles and the carbon content of the alloys in the MSS family should be precisely chosen for any structural applications that require high resistance to corrosion [11,12].

Extensive studies have been conducted to characterize the mechanical properties of MSS and to discuss the effect of tempering conditions on the microstructure and corrosion properties. Lu *et al.*[13] studied the effect of tempering temperature on the corrosion properties of 13Cr stainless steel alloy and reported a higher corrosion resistance for samples tempered at 300 °C relative to the samples tempered at 500 °C due to the sensitization of the matrix adjacent to the chromium carbide precipitates. Anantha *et al.*[7] analyzed the effect of various types of precipitates in the microstructure on the localized corrosion behavior of the AISI 13Cr

martensitic stainless steel and reported that regions adjacent to the carbides are less noble due to the formation of chromium depleted zones at the periphery of the chromium carbides.

Despite all existing literature studying the impacts of post-fabrication thermal cycles on the corrosion properties of 13Cr MSS, the possible influence of other manufacturing process-induced structural modifications, such as plastic deformation, on the corrosion response of the alloy remains unknown. Applying plastic deformation, which commonly occurs during forming operation of the component, can drastically affect the mechanical properties and microstructural characteristics of the alloys [14,15]. In terms of mechanical properties, plastic deformation positively contributes to the strength and hardness of the metals by the formation and slipping of dislocations, resulting in a higher dislocation density in the structure (strain-hardening)[16,17]. Differently, plastic deformation can deteriorate the mechanical properties of the alloys by producing inclusions, causing the elongation of the particles and precipitates, leading to their breakage or rupture of their interface from the matrix[16,18].

The applied plastic deformation during cold working can further modify the microstructure and grain orientation drastically by turning a texture free microstructure into a strongly textured one after deformation. For tempered martensitic stainless steels, possessing a body-centered cubic (BCC) crystal structure, the cold worked texture mainly composes of a nearly perfect normal direction (ND) fiber and two other components, centered at {001}<110> and {112}<110>, which lie along the deformation direction [19]. The major component of the deformation texture in BCC materials is almost independent of compositional and processing parameters [20,21]. Venegas *et al.*[22] in a recent study on the API X46 steel, showed that the high density of grains with preferred orientation of {111}//ND (corresponding to the grains with their (111) plane parallel to the normal direction (ND)) increased the corrosion resistance. A study by Verdeja *et al.* [23] revealed that the effect of texture on the corrosion properties is

significantly dependent on the slip system. For instance, the crystallographic textures associated with {110}//ND and {332}//ND reduce the sensitivity to corrosion in ferritic-pearlite steels, while {001}//ND and {112}//ND textures have the opposite effect. On the other hand, the composition and thickness of the passive layers in stainless steels can be modified by cold working [24,25]. Consequently, the electrochemical stability of the passive layer on the stainless steel can potentially change. Favorable passivation was observed for the rolled 304 stainless steel due to the formation of a thicker passive film, whereas for a high nitrogen 30Cr15Mo1N stainless steel, a passive layer with a less protective nature was reported to form after deformation [25,26].

Previous studies exhibit relatively contradictory results in case of establishing a relationship between cold rolling and corrosion resistance. Barbucci *et al.* [27] noticed the increase of the passive current in acidic medium by increasing the level of deformation in 304 stainless steel. Chandra *et al.* [28] and Liang *et al.* [29] analyzed the effect of plastic deformation on the pitting potential, as a criterion to understand the corrosion resistance of samples against the pitting, and revealed that its effect is not as significant as the effect of chloride concentration or exposed media. Regarding the impact of cold deformation on corrosion current density and repassivation potential, irregular trends were reported, highly dependent on the composition of studied stainless steels and the concentration of chloride in the medium[30,31].

To the best of the authors' knowledge, no study has been done to characterize the effect of plastic deformation on the corrosion properties of MSS. Characterizing the impact of plastic deformation associated with the manufacturing process on the corrosion properties of the alloy is extremely vital to be able to oversee the components' integrity and remaining life after a long service life, especially in harsh environments. In particular, the effect of plastic deformation on both grains' orientation and distribution of precipitates and the resultant

corrosion behavior are required to be investigated. It is found that the galvanic potential difference between the micro-constituents and their surrounding matrix can provoke micro-galvanic coupling and deteriorate the corrosion performance [32,33]. However, the impact of plastic deformation on the micro-galvanic corrosion between the precipitate and its surrounding matrix is not also well understood. The present study is aimed to focus on these gaps by investigating the relationship between various cold deformation levels, microstructure, and corrosion properties in 13Cr martensitic stainless steel.

2. Experimental Procedure

2.1. Sample Preparation

A 13Cr martensitic stainless steel (UNS S42000) with the measured chemical composition summarized in Table 2.1 was used in this study. The material of the study was sectioned from a long tube that was austenitized at 1020 °C for 30 min in a vacuum furnace, followed by rapid cooling. The material was then hot deformed and tempered at 250 °C, followed by cooling in air.

To induce various plastic deformation levels in the samples and create a microstructure containing a stronger texture, the samples were plastically deformed under uniaxial tension at the strain rate of 10^{-3} s^{-1} up to the elongations of 5% and 22% (approximately fracture elongation). The samples for electrochemical experiments were cut from the center of the uniaxially tensioned samples. The sample preparation steps followed by the corrosion testing are illustrated schematically in Figure 2.1.

Table 2. 1. The measured chemical composition of 13Cr stainless steel used in this study (all data in wt.%)

C	Cr	Mn	Mo	P	S	Si	Cu	Al	Co	Fe
0.22	13.23	0.48	0.03	0.014	0.002	0.39	0.027	0.08	0.018	Bal.
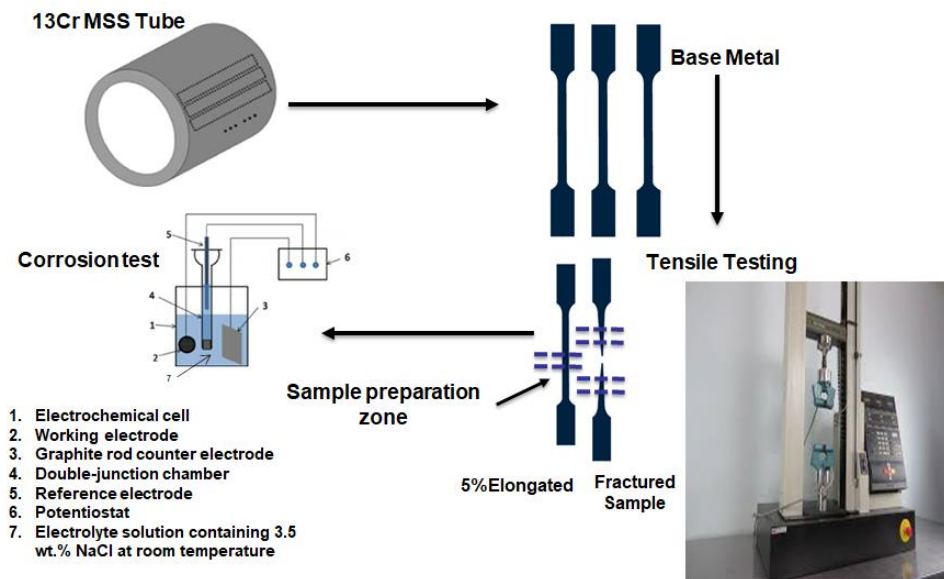
Figure 2. 1. Schematic of the sample preparation procedure for the subsequent corrosion testing.

2.2. Electrochemical Analysis

The exposed surface of the samples was cold mounted into an epoxy resin, ground using 500 grit sandpaper, and ultrasonically cleaned in acetone, followed by polishing to a mirror-like finish using alumina suspension up to 0.02 μm. To avoid crevice corrosion along the sample-epoxy interface, the edges between the sample and the epoxy were coated using a masking lacquer. All electrochemical measurements in this study were performed in aerated 3.5 wt.% NaCl solution. The solution's temperature was maintained at 25±0.5 °C using a temperature-controlled water bath. A standard three-electrode cell set-up, containing a graphite rod as the counter electrode, a saturated Ag/AgCl electrode as the reference electrode, and the 13Cr stainless steel specimen as the working electrode, was used. The open circuit potential (OCP) was monitored for one hour prior to each test. Cyclic potentiodynamic polarization (CPP) tests were performed at a scanning rate of 0.5 mV/s, commencing at -0.2 V *vs* OCP. The EIS measurements were conducted over the frequency range of 100 kHz to 10 mHz with a signal

amplitude of 10 mV. The CPP and EIS experiments for each condition were repeated at least 3 times to ensure the reproducibility of the results.

2.3. Microstructural Characterization

To reveal the microstructural characteristics of the samples, samples were cut and mounted in an epoxy resin from both the non-deformed sample and the gauge length of the deformed samples. The mounted samples were prepared following standard grinding and polishing procedures for the MSS materials. Villella's reagent was used for etching of the polished surfaces. Microstructural features of the samples were revealed using a FEI MLA 650F scanning electron microscope (SEM) equipped with a high throughput Bruker energy dispersive X-ray (EDX) analytical system and an HKL EBSD system. EBSD analysis was also performed on polished samples to acquire crystallographic orientation micrographs (inverse pole figures (IPF)), pole figures (PF), and grain boundary maps. EBSD data points with a confidence index (CI) lower than 0.01 were not included in the analysis. Channel 5 software was used to process and analyze the EBSD data. X-ray diffraction (XRD) analysis was also performed at 40 kV and 35 mA with an aperture of 2 mm over a diffraction angle range of 40°-90° with a step size of 0.01° using a Rigaku Ultima IV X-ray diffractometer with Cu-k$_\alpha$ radiation (λ = 1.54056 Å). Peak positions of index data were compared with those obtained from the standard powder diffraction file (PDF) cards.

3. Results

3.1. Mechanical Properties Characterization

Figure 2.2 shows the engineering stress-elongation diagram along with the hardness variation of the alloy at different levels of plastic strain. Accordingly, the base metal revealed the yield strength (YS) of 365±6 MPa and ultimate tensile strength (UTS) of 769±4 MPa. The elongation value at the initiation of the homogenous plastic deformation (the yield point) was around

1±0.15% and the onset of the inhomogeneous plastic deformation (UTS point) was at ~10±0.20%. As depicted in Figure 2. 2, the plastically deformed samples for the purpose of electrochemical testing were prepared from 5% elongated and the fractured samples possessing the largest possible plastic strain.

The variation of Vickers hardness data indicates that by increasing the deformation level from 5% to 22%, the hardness increases from 245±1 HV to 280±1 HV, attributed to the increased level of strain hardening in the alloy.
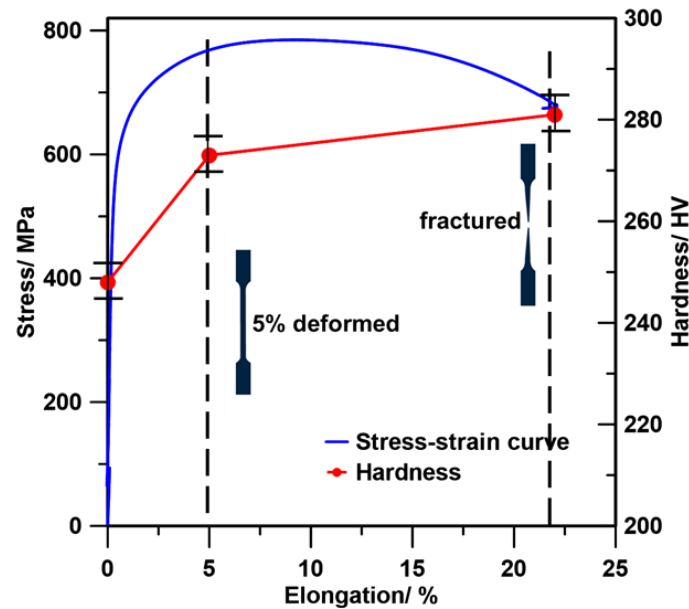
Figure 2. 2. The stress-elongation curve and the variation of hardness values at different strain levels, indicating the degree of plastic deformation in the deformed samples prior to the corrosion testing

3.2. Microstructure Characterization

Figure 2.3 shows the XRD spectra for all samples. Three peaks corresponding to the martensite phase (M) were observed for the three samples in angles ranging from 40° to 90°, indicating martensite as the dominant phase in the microstructure. Anantha et al. [7] have also detected peaks corresponding to the formation of retained austenite and undissolved carbides in the XRD spectra. However, none of those phases were detected on the XRD spectra herein, plausibly due to their drastically lower volume fraction as compared to the martensite phase.
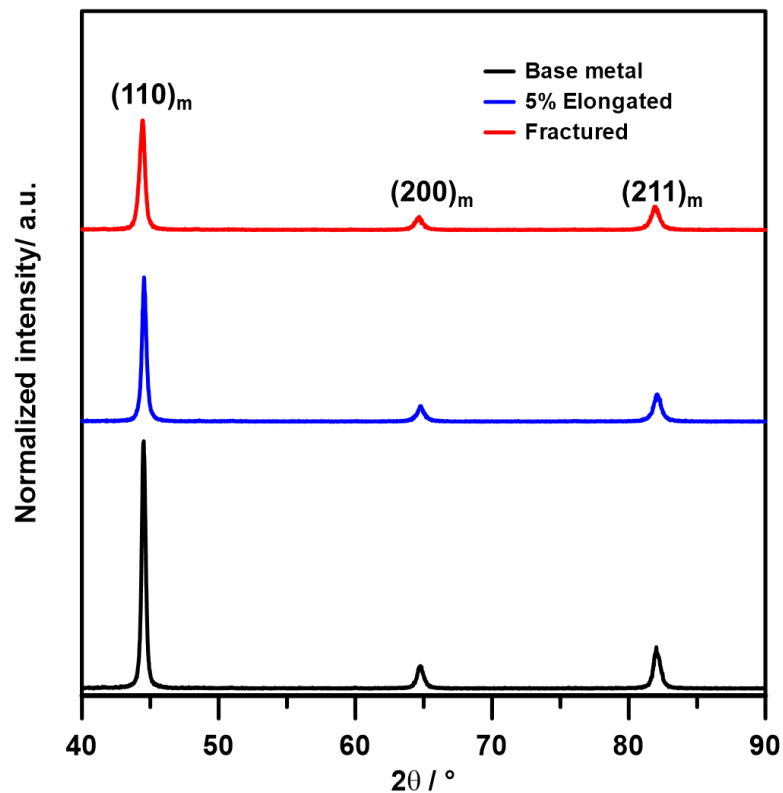
Figure 2. 3. The XRD results showing the presence of the martensite phase.

Figures 2.4 and 2.5 illustrate the SEM micrographs taken from the prepared samples at different deformation levels. As shown in Figures. 2. 4a and 4b, the non-deformed base metal sample exhibited a high-volume fraction of precipitates embedded in a matrix of martensite lathes

originated from the hierarchical tempered martensite. Precipitates were mainly coarse carbides distributed homogenously in the Fe matrix and mostly within the lath boundaries along with fine intra-lath carbides with the diameter of nearly 200 nm propagated through laths possibly generated during the tempering process. The geometry of coarse inter-lath precipitates is nearly round-shaped, while the fine precipitates have capsule-like shapes [7]. Analogous to the non-deformed sample, the 5% elongated sample revealed a high-volume fraction of coarse carbides along with intra-lath carbides in the matrix, shown in Figure 2. 5a. The EDX elemental mapping of the microstructure (Figures 2. 5b and 5c) revealed higher concentration of chromium and carbon for the precipitates, where Fe was depleted (Figure 2. 5d), indicating the chromium carbide nature of the formed precipitates. No high concentration for the other alloying elements was observed indicating no further enrichment or depletion. The fractured samples (Figures 2. 4c and 4d) showed the distribution of both inter-lath and intra-lath carbides. As shown in Figures 2. 4c and 4d, the formation of micro-cracks along the larger precipitates-matrix interface and in some cases breakage of the large precipitates were detected at the high plastic strain of 22%.
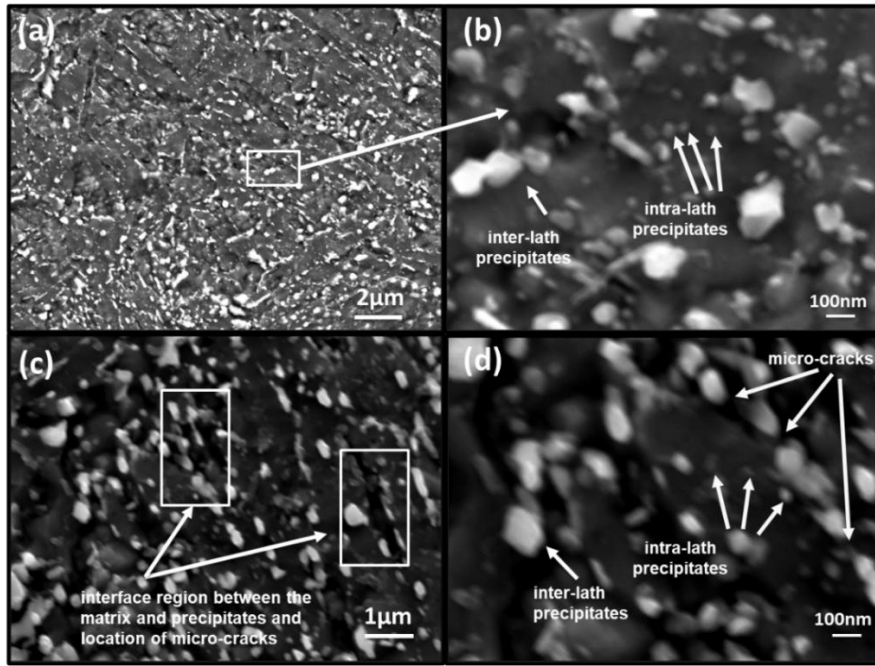
Figure 2. 4. SEM micrographs of the (a) base metal, (b) higher magnification of the enclosed area in (a), (c) fractured sample (d) fractured sample at a higher magnification.
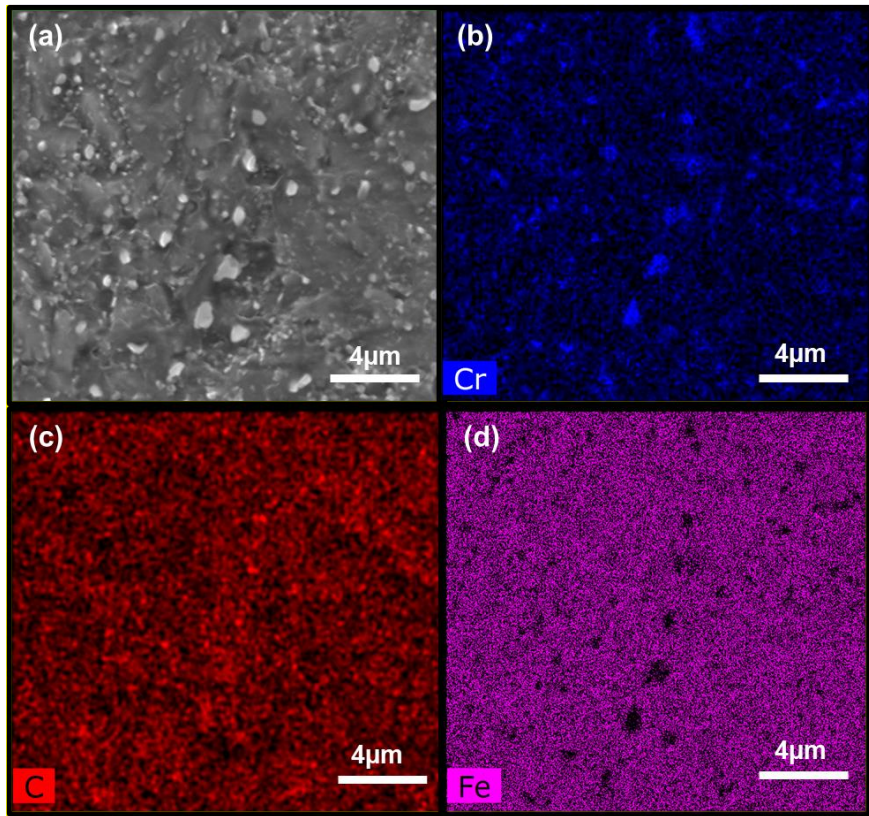
Figure 2. 5. (a) The SEM micrograph of the 5% elongated sample, and its corresponding EDX elemental mapping showing (b) chromium concentration, (c) carbon concentration, and (d) iron concentration.

Figure 2.6 shows the inverse pole figures (IPFs) from the microstructure of the non-deformed base metal, the 5% elongated sample, and the fractured sample, revealing an extremely finer structure (average lath size < 1 µm) in all samples. Slight refinement was detected in the samples after fracture. The average lath size in the non-deformed base metal was 0.79 µm, and it decreased to 0.76 µm and 0.64 µm for the 5% deformed and fractured samples, respectively. It is reported that the refinement during the cold deformation is resulted from the elongation and breakage of the grains [34,35]. Similarly, Ueji *et al.* [36] observed the grain refinement of low carbon steel during cold deformation by rolling and ascribed the formation of ultra-fine-grained structure to the characteristics of the martensite starting structure. Bracke *et al.* [37] investigated the effect of cold deformation on the texture and microstructure of the austenitic Fe–Mn–C alloy and reported that the mechanism behind grain refinement was based on the nucleation and growth of the recrystallized state in an energetically homogeneous microstructure.

In MSS, the deformation mechanism is controlled by grain boundaries hardening due to the dislocation pile up and precipitate fragmentation [8,38]. The quality of Kikuchi patterns of EBSD results can be affected by the deformation level due to the formation of microcracks, grain and precipitate fragmentation, the density of slip line, twinning, and the formation of deformation-induced martensitic phase [39,40]. However, the quality of IPF results herein was not found to be affected by the increased deformation level in the alloy
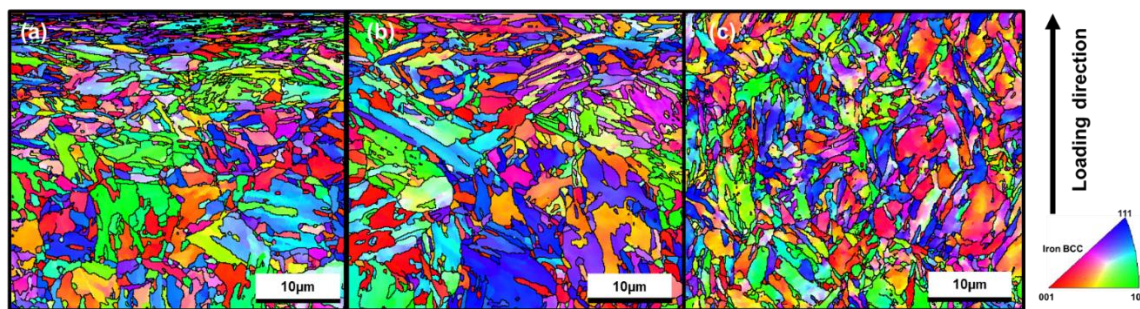
Figure 2. 6. EBSD inverse pole figure and grain boundaries maps of the (a) non-deformed base metal, (b) 5% elongated sample, and (c) fractured sample.

Figure 2.7 exhibits the distribution of high-angle grain boundaries (HAGBs), medium-angle grain boundaries (MAGBs), also known as coincidence site lattice (CSL) boundaries, and low-angle grain boundaries (LAGBs) in all samples. While the fraction of LAGBs is nearly the same for the base metal and the 5% elongated sample, a high fraction of LAGBs was observed in the fractured samples. LAGBs represent low energy boundaries and are known to be less susceptible to corrosion attack [41]. The fraction of HAGBs remains relatively constant in all samples with various deformation levels. It is reported that the high frequency of MAGBs can improve the corrosion resistance, while consequent discontinuity of the random boundaries (HAGBs) can deteriorate the corrosion properties [41,42].

The pole figures of the samples obtained from the EBSD data are shown in Figure 2.8. The active slip planes in the BCC materials are generally {110} and {111} families of planes while the {100} planes are responsible for phase transformation textures [43]. They also mentioned that the uniaxial deformation, such as tension, generally leads to the formation of a fiber type texture. The uniaxial deformation of BCC alloys leads to the formation of {110} fiber texture after cold deformation [44]. The {110} and {111} pole figures for the base metal (Figure 2.8a) show random textures with an intermediate intensity along the generated poles. The 5% elongated sample revealed a texture component aligned with the direction normal to the loading direction (LD) for the {111} planes. The fractured sample depicted a strong texture for the {110} plane with one pole concentrated along the direction normal to the loading direction. A

more random texture for the {111} planes approximately aligned with the loading direction was also detected for the fractured sample. An analogous texture distribution in BCC steels is reported during the rolling process, revealing a strong texture component for the close-packed planes of {110}[45]. According to Kumar *et al.* [46] and Phadnis *et al.* [25], the presence of a texture component in close-packed crystallographic planes parallel to the sample surface can improve the corrosion properties.
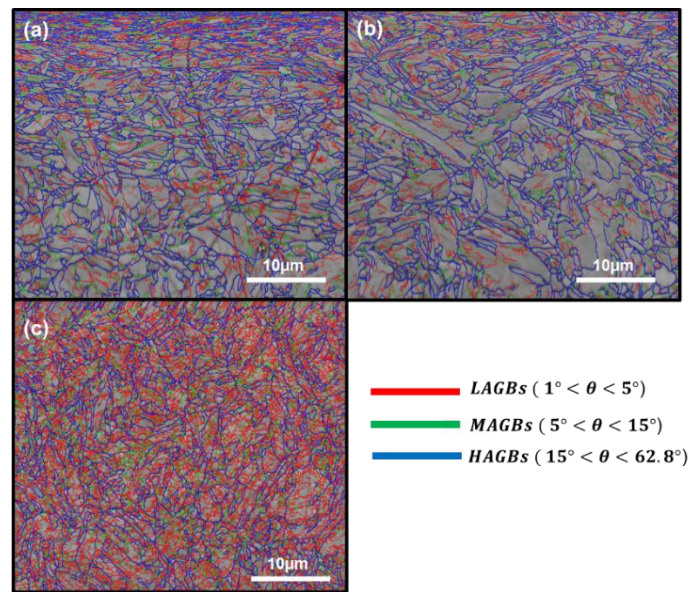
Figure 2. 7. EBSD grain boundary maps showing the distribution of HAGBs, MAGBs, and LAGBs in the (a) non-deformed base metal, (b) 5% elongated sample, and (c) fractured sample.
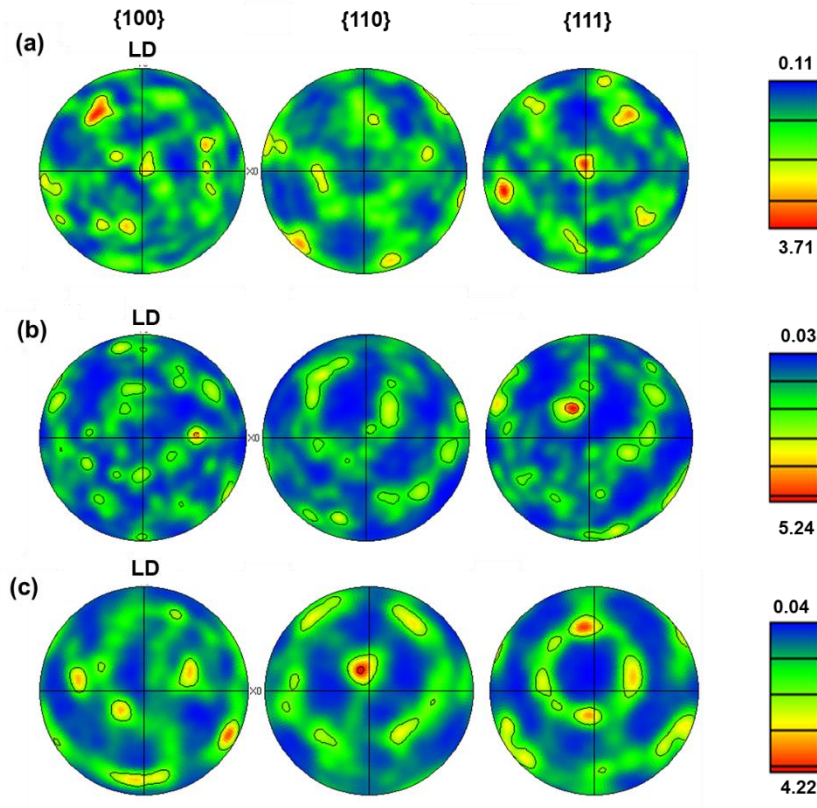
Figure 2. 8. Pole figures (PFs) for the (a) non-deformed base metal, (b) 5% elongated sample, and (c) fractured sample.

3.3. Corrosion Results

The open-circuit potential (OCP) trends for all samples are displayed in Figure 2.9. A slight fluctuation of OCP was recorded for the base metal from the onset through the whole measurement. Anantha *et al.* [7]showed that fluctuation of the OCP represents a continuous occurrence of metastable localized corrosion (pitting) during the OCP monitoring. Fluctuations with lower intensity were also recorded for the 5% elongated and fractured samples exhibiting few peaks during the OCP monitoring. The presence of fluctuations hindered measuring the exact value for the OCP, however, the average OCP value for the base metal was ~ -0.11 $V_{Ag/AgCl}$, while it decreases to -0.17 $V_{Ag/AgCl}$ and -0.20 $V_{Ag/AgCl}$ for the 5% deformed and fractured samples, respectively, showing a deterioration in the stability of the passive film by increasing the degree of plastic deformation in the sample. It is well established that the OCP has a close relationship with the density and integrity of the passive film [47]. A nobler value

for the OCP indicates better passivation state of the stainless steel attributed to the existence of a higher quality and denser passive film on the sample's surface. Hence, the measured lower OCP values for the deformed samples reveal their inferior passive film stability as compared to the non-deformed base metal. It is shown that the decrease in the OCP value can be also correlated to the decrease in the thickness of the passive film [47].
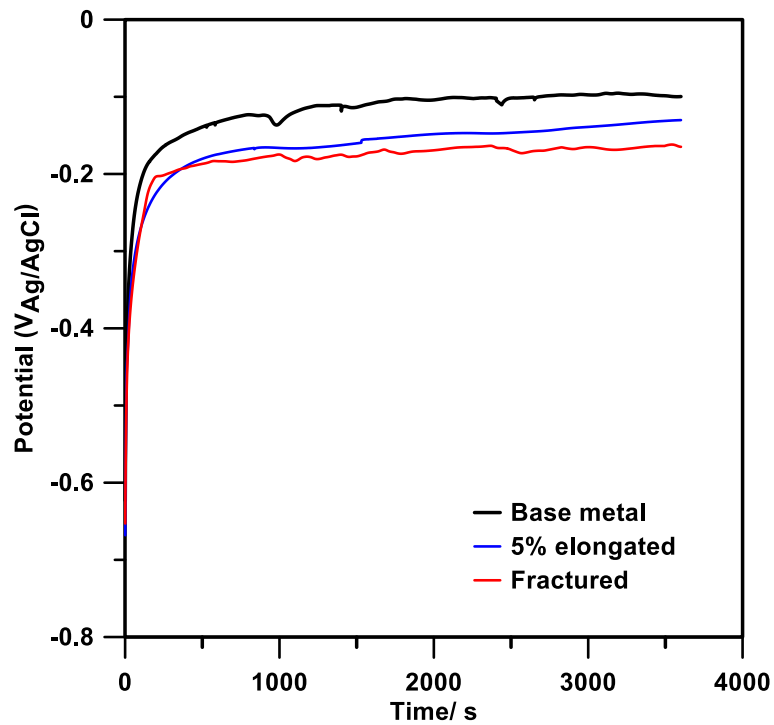
Figure 2. 9. The open-circuit potential (OCP) values over time for all studied samples.

To study the electrochemical behavior of all samples, CPP testing in aerated 3.5 wt.% NaCl solution at 25 °C was conducted and the results are shown in Figure 2.10. The values for the corrosion current density (i_{corr}) corrosion potential (E_{corr}), passive current density (i_p), pitting potential (E_{pit}), anodic and cathodic Tafel slope (β_a and β_c) were extracted from the graphs and are summarized in Table 2. 2. The CPP graphs of samples revealed that by increasing the level of deformation , corrosion current density is slightly increasing, as outlined in Table 2. 2. It can be seen that E_{corr} is relatively the same for the 5% elongated and fractured samples (~ -164

mV$_{Ag/AgCl}$ and -171 mV$_{Ag/AgCl}$, respectively), while it decreases to -199 mV$_{Ag/AgCl}$ for the base metal. It is also observed that anodic resistance is decreased by increasing the level of deformation. Moreover, the i$_p$ value slightly increased by increasing the deformation level from 0.103 µAcm^{-2} for the non-deformed base metal to 0.134 µAcm^{-2} for the fractured sample. The passive current density is a criterion corresponding to the mobility of the chromium into the solution and indicates the protective characteristic of the passive film during the passivation process[48,49]. A higher passive current density indicates a higher mobility of the chromium to the solution and lower enrichment of the chromium at the passive state, suggesting a less protective nature for the passive film. The pitting potential of 154 mV$_{Ag/AgCl}$ was recorded for the base metal. The pitting potential was decreased to 134.3 mV$_{Ag/AgCl}$ for the 5% elongated sample and to 45 mV$_{Ag/AgCl}$ for the fractured sample. The measured lower pitting potential value for the fractured sample is in good agreement with the OCP results, exhibiting lower stability of the passive film on the severely deformed sample, leading to its lower corrosion resistance against pitting corrosion. These results are in good agreement with the findings of Luo *et al*. [50] and Barbucci *et al.* [27], on different grades of stainless steel.
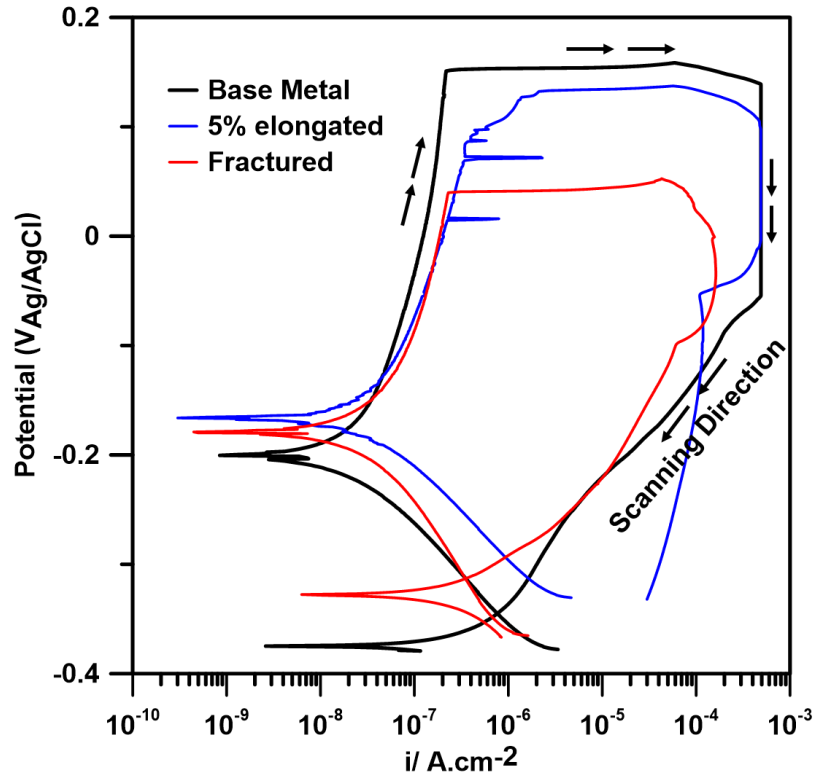
Figure 2. 10. The cyclic potentiodynamic polarization curves for the 13Cr stainless steel in aerated 3.5 wt. % NaCl solution at room temperature.

Table 2. 2 .The electrochemical parameters extracted from the polarization graphs of the non-deformed and deformed 13Cr stainless steel material.

Sample	i_{corr} (μA cm^{-2})	E_{corr} (mV$_{Ag/AgCl}$)	i_p (μA cm^{-2})	E_{pit} (mV$_{Ag/AgCl}$)	β_a (mV decade^{-1})	β_c (mV decade^{-1})
Base metal	0.011$\pm$0.0008	-199$\pm$27	0.103$\pm$0.003	154$\pm$24	121$\pm$2.2	-90$\pm$7.3
5% Elongated	0.013$\pm$0.0005	-164$\pm$17	0.125$\pm$0.004	134$\pm$19	115$\pm$2.4	-89$\pm$6.4
Fractured	0.018$\pm$0.0003	-171$\pm$19	0.131$\pm$0.004	45$\pm$13	117$\pm$1.6	-122$\pm$9.1

The EIS measurements were implemented to characterize the effect of cold deformation on the electrochemical behavior of the passive film in a solution containing 3.5 wt.% NaCl at room temperature. Figure 2. 11a shows the effect of uniaxial tension deformation on the Nyquist plots of 13Cr martensitic stainless steel. Similar capacitive loops were observed in all Nyquist plots, confirming the consistency of the corrosion mechanism in all samples regardless of the level of plastic deformation. It is shown that the diameter of the capacitive semicircle is related to the corrosion resistance [51]. The larger diameter of the semicircle is associated with the

higher corrosion resistance of the passive film. Hence, the large diameter of semicircle for the base metal indicates its higher corrosion resistance, consistent with the obtained OCP and CPP results. The effect of uniaxial tension on the Bode plots of 13Cr martensitic stainless steel is illustrated in Figure 2. 11b. For a wide range of frequencies, linear behavior is observed for log $|Z|$ over log f, and constant phase angle θ near -80° is recorded, confirming the formation of a stable passive film on the surface in solution containing 3.5 wt.% NaCl. According to plots of impedance magnitude vs. frequency, polarization resistance ($R_p = R_1 + R_2$) can be obtained in low-frequency levels, while solution resistance (R_s) is expressed at the high-frequency region and middle-frequency regions of the plots are showing CPE_1 and CPE_2.
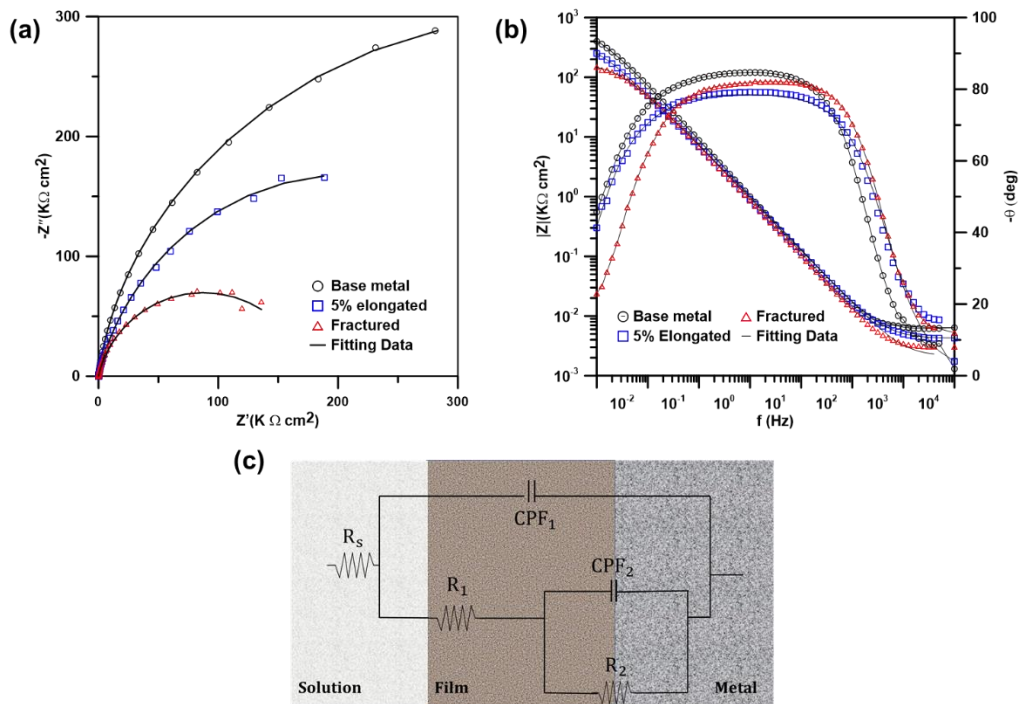
Figure 2. 11 (a) Nyquist plots and (b) Bode plots obtained from 13Cr stainless steel with different deformation level in aerated 3.5 wt.% NaCl electrolyte at room temperature, (c) schematic representation of the physical model and the equivalent circuit model used to describe the EIS data.

The schematic representation of the interface between the formed passive layer and the stainless steel substrate is shown in Figure 2.11c. Various equivalent circuit (EC) models have been adopted to interpret the impedance spectra results in stainless steels [52]. In this study,

the EIS spectra data were modeled and fitted using the two times constant EC model (shown in Figure 2. 11c). Although the EIS plots do not exhibit a clear two-times constants behavior, the fitted EC model was found to increase the fitting accuracy significantly. The formation of a thin passive layer on the surface of various grades of stainless steel can lead to the overlap of two-time constants, making it difficult to distinguish between the characteristics of the passive oxide layer/electrolyte interface and the passive oxide layer [53,54]. Freire *et al.* [55] and Kocijan *et al.* [52] have stated that the non-ideal capacitance response of the interface requires the usage of constant phase element (CPE). In order to address the micro or nano surface inhomogeneities, such as surface roughness, porosity, grain boundaries, and impurities at stainless steel surface, CPE was used instead of a perfect capacitance. The impedance of a CPE ($Z(\omega)$) can be calculated using [56]:

$$Z(\omega) = Z_0^{-1} . (i\omega)^{-n} \tag{1}$$

where Z_0 is the admittance magnitude of CPE, ω is the angular frequency, and n is the CPE exponent. The n factor is between 0 to 1. In the EC model, R_s is the NaCl solution resistance, R_1 and R_2 are the passive film and charge transfer resistances, and CPE_1 and CPE_2 are the capacitance of the passive film and the double layer capacitance, respectively. The detailed fitting parameters of the obtained EIS results are listed in Table 2.3. The values for the R_1 and R_2 decreased by increasing the deformation level, indicating lower protective effect of passive film at high deformation levels. The values of the CPE_1 and CPE_2 for deformed samples are higher than base non-deformed samples, which is an indication of more defects in the passive film for deformed samples. The n_1 and n_2 valuers are relatively near to 1 and exhibit a reasonable capacitive behavior of the passive film layer for all samples.

Table 2. 3.The fitted electrochemical parameters for the obtained impedance spectra.

Sample	R_s (Ωcm^2)	CPE_1 ($\Omega^{-1}cm^{-2}s^n$)	n_1	R_1(Ωcm^2)	CPE_2 ($\Omega^{-1}cm^{-2}s^n$)	n_2	R_2 (Ωcm^2)	$\sum \chi^2$
Base metal	3.62±0.02	$1.00\times10^{-5}\pm10^{-6}$	0.93±0.01	$1.02\times10^6\pm10^2$	$1.517\times10^{-5}\pm10^{-6}$	0.77±0.01	$4.65\times10^6\pm10^2$	1.32×10^{-4}
5% Elongated	3.43±0.04	$5.22\times10^{-5}\pm10^{-6}$	0.87±0.01	$2.22\times10^5\pm10^2$	$2.25\times10^{-5}\pm10^{-6}$	0.87±0.02	$1.23\times10^6\pm10^2$	1.27×10^{-4}
Fractured	3.64±0.07	$4.42\times10^{-5}\pm10^{-6}$	0.87±0.01	$1.03\times10^5\pm10^2$	$1.85\times10^{-5}\pm10^{-6}$	0.98±0.01	$1.32\times10^5\pm10^2$	1.54×10^{-4}

4. Discussion

4.1.Effect of Grains Orientation on the Corrosion Behavior

To understand the corrosion mechanism in stainless steels, the dominant factor(s) controlling the protective passive film stability needs to be investigated. The integrity and density of the passive layer directly impact the evolution of the corrosion potential[47]. On this context, It has been shown that the deformation process can potentially deteriorate the integrity and the thickness of the passive film, leading to the reduced corrosion potential of the surface [39,47]. Such detrimental effect of the applied plastic deformation on the electrochemical stability of the surface is in good agreement with the results presented herein. Although the measured lower pitting corrosion resistance and passive layer resistance in the deformed samples in this study are clearly attributed to the decreased stability of the passive film, the factors that contribute to such instability in the passive film need to be further elaborated.

The microstructural analysis of the samples confirmed a slight refinement for the fractured samples. It is well known that finer structures provide larger boundary areas, and since most of the precipitates form along the boundaries, it can consequently lead to an increased galvanic coupling over the entire microstructure exposed to the corrosive electrolyte. The SEM micrographs of the fractured sample after the CPP testing (Figures 2.12a and 2.12b) depict randomly distributed large pits, in addition to micro-pits that were detected at higher

magnifications. These micro-pits correspond to the onset location of larger pits, initially formed during either the meta-stable (E < E_{pit}) or stable pitting (E = E_{pit}) initiation state, and gradually grow to larger pits during the cyclic polarization test. Interestingly, the larger pits seem to be propagated along the loading direction (Figure 2.12a). The propagation of growing pits with comet-shaped morphology is usually caused by the aggressive local chemistry of the environment resulting from the growing pit, which flows downwards due to gravity [57–59]. The alignment of the loading direction and the pits propagation direction in the studied samples is attributed to the coincidental alignment of the loading direction and the direction of gravity during the potentiodynamic testing.

Studying the locations of micro-pits can provide substantial information regarding the driving force for the initiation of pitting in deformed samples. The micro-pits locations for the base metal, 5% elongated, and fractured samples are shown in Figure 2.13. The locations of micro-pits were found to be nearly the same for the deformed and non-deformed samples and were detected near the lath boundaries where the inter-lath carbides are mainly concentrated.

Although the general impact of the grain boundaries on the plastic deformation of materials is discussed thoroughly, the effect of grain boundaries on the electrochemical stability of the surface is highly complex [60,61]. In this study, the severely deformed sample showed a higher volume fraction of LAGBs relative to that of the base metal and the 5% deformed sample. Ren et al. [62] reported that a high volume fraction of LAGBs can lead to corrosion properties enhancement. On the other hand, Tan et al. [63] claimed that the corrosion behavior is also affected by the fraction of CSL boundaries in the microstructure. In general, grain boundaries are considered as high diffusion paths, and their low energies can hinder high-speed diffusion. Due to the low energies of the low-Σ CSL boundaries, the diffusivity is reduced along these grain boundaries, resulting in a grain boundary diffusivity that is very close to the bulk

diffusivity [64]. Thus, a relatively uniform bulk diffusivity is expected to occur in the sample without cold deformation, promoting the formation of a homogenous and continuous chromium oxide passive film. The fraction of CSL boundaries in the deformed samples remained relatively constant in this study, thereby its effect is not a dictating factor in controlling the corrosion mechanism. Analogously, the contribution from LAGBs was not a determining factor in dictating the electrochemical response of the deformed samples studied herein, considering their impaired corrosion properties as compared to the non-deformed base metal.

In addition to the grain boundaries distribution, the preferential texture of certain crystallographic planes aligned with the exposed surface of the sample can further contribute to the electrochemical stability of the surface. It is reported that the high-density close-packed crystal planes possess better corrosion properties and better passivation and re-passivation characteristics [65]. The close-packed plane for the metals with BCC crystal structure is {110} plane. Among the studied samples herein, the fractured sample revealed the strongest {110} texture parallel with the sample's surface. However, the degraded electrochemical properties of this sample imply that the formed texture component in this sample cannot be the dominant factor in controlling its corrosion behavior. The pitting resistance of stainless steels are also affected by the texture formation in low index planes of {100} and {111}. Shahryari et al. [66] reported that {100} and {111} planes were less prone to pitting corrosion initiation for 316L austenitic stainless steel, although the overall impact of the texture on the corrosion properties of the alloy was reported to be insignificant. In the current study, the base metal exhibited relatively stronger texture components in the {100} and {111} planes as compared to the fractured sample. However, the small differences in the intensity of the pole figures between the base metal and fractured samples along with the stronger texture in the {110} planes for the fractured sample leads to a complex effect of the texture on the corrosion performance of

the alloy, making it relatively complicated to interpret the correlations between the crystallographic orientations and corrosion behavior of the samples.
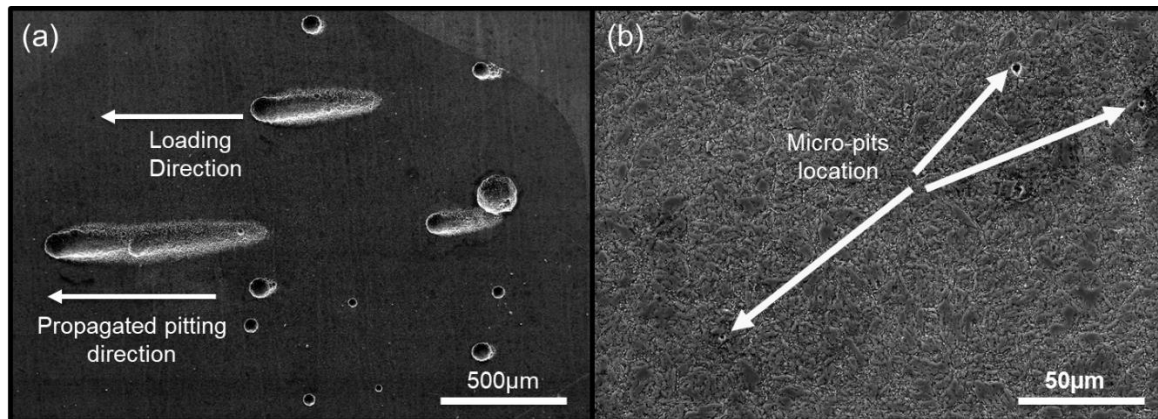
Figure 2. 12. SEM micrographs of the fractured sample after CPP testing indicating (a) the pitting propagation direction and (b) micro-pits locations.
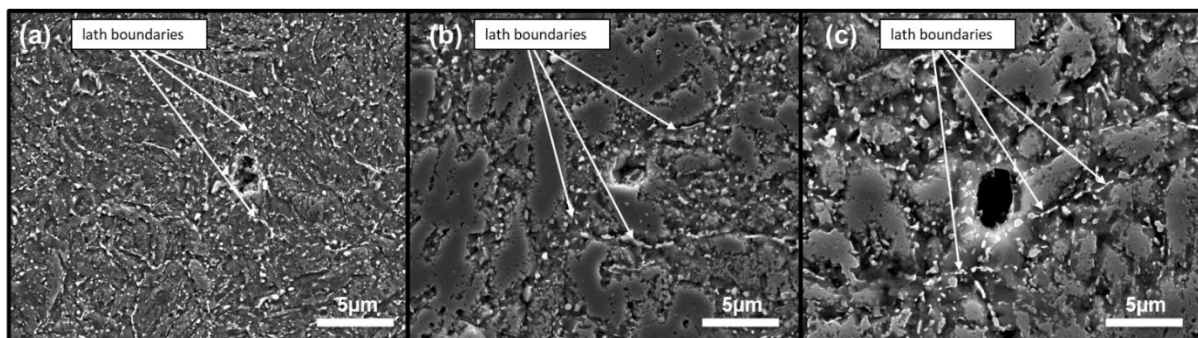
Figure 2. 13. SEM micrographs taken from the surface micro-pits after CPP testing of the (a) base metal, (b) 5% elongated sample, and (c) fractured sample.

4.2. Effect of Precipitation on the Corrosion Behavior

Considering previous studies on the effect of precipitates, particularly carbides, on the corrosion behavior of stainless steels, it is frequently reported that in most cases, the matrix phase is electrochemically less noble than the precipitates [7,67]. It is stated that the interface between the matrix and the precipitates is more susceptible to localized corrosion attack [35,67]. The high potential difference between the matrix and the embedded constituents can accelerate the micro-galvanic coupling, in which the matrix acts as a local anode and the carbides as the local cathode [68]. Figure 2.14 shows the SEM micrographs of the fractured

and 5% elongated samples after CPP testing and their corresponding elemental maps for chromium concentration. The intensity of pitting on the surface of the fractured sample after the CPP testing was found to be much higher than that of the 5% elongated sample (compare Figure 2. 14a to Figure 2. 14c). The chromium concentration maps taken from the fractured and 5% elongated samples after cyclic polarization testing (Figures 2. 14b and 14d, respectively) revealed high concentration of chromium inside the elongated comet-shaped pits or on the side of circular pits, suggesting the preferential dissolution of Fe from the surface of the alloy into the electrolyte, while chromium element, which primarily exists in the form of Cr-carbide precipitates, does not seem to leach from the surface. The higher magnification SEM micrographs taken from the corroded surfaces of the studied samples shown in Figure 2. 13 also confirmed the onset of corrosion pits from the carbides-matrix interface. The microstructure of the non-deformed and deformed samples showed the random distribution of coarse carbides. It is reported that the existence of larger carbides surrounded by more expanded sensitized regions (Cr-depleted zones) in the structure provokes the pitting susceptibility of the alloy [69,70].

The SEM micrographs of the samples (Figures 2. 4 and 2. 5) confirmed that the fractured sample contained relatively finer precipitates generated through the fragmentation of coarser undissolved brittle carbides during severe plastic deformation of the sample. Breakage of a coarse carbide precipitate surrounded by an expanded sensitized region into smaller precipitates also splits the large sensitized region into smaller sensitized zones, each adjacent to the finer precipitates. Consequently, the number of susceptible locations to stable pitting on the surface increases.

The potential difference between the precipitates and matrix can stimulate micro-galvanic coupling and act as the main driving force for corrosion [7]. However, the galvanic coupling is

not only affected by the magnitude of potential difference but also the distance between the anodic and cathodic sites can affect the severity of the corrosion drastically. Uniaxial tension can lead to the breakage of the carbides and decrease the distance between the precipitates, leading to a provoked micro-galvanic coupling effect at higher deformation levels [71]. Furthermore, it was observed that the applied plastic strain to the matrix under uniaxial tension leads to the formation of a more expanded interface region between the matrix and inter-lath carbides (Figures 2. 4c and 4d). The expanded interface region provides a larger chromium depleted zone that can further accelerate the formation and propagation of pitting if the chromium concentration decreases to lower than 11 wt.%. Figures 2. 15a and 15b show the SEM micrographs taken from the interface regions between the matrix and inter-lath carbide particles in the base metal and fractured samples along with their corresponding EDX line scanning across the depicted arrows (Figures 2. 15c and 15d). A sudden decrease in chromium concentration adjacent to the precipitates is observed in both the fractured and base metal samples, making the precipitate-matrix interface region prone to pitting corrosion. The EDX line scanning results revealed a more expanded interface regions ($a_1 + a_2$) between the matrix and carbide (chromium-depleted zones) for the fractured sample relative to the base metal. A larger interface with a low concentration of chromium (near 11 wt.%) is less resistant to corrosion and is prone to initiation and propagation of micro-pits. Hence, the possibility of initiation and propagation of pitting in deformed 13Cr stainless steel samples is higher than the non-deformed base metal, leading to the deterioration of the corrosion resistance of the alloy.
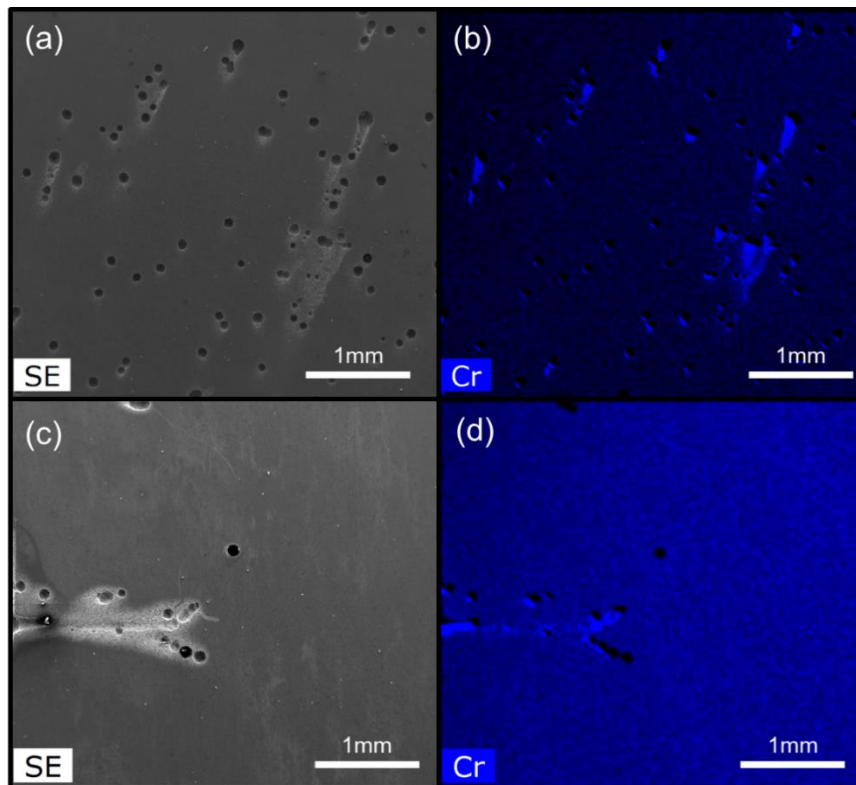
Figure 2. 14. The SEM micrographs from the samples after cyclic polarization tests and their corresponding Cr concentration maps: (a,b) the fractured sample, and (c,d) the 5% elongated sample.

5. Conclusions

In this study, the effects of plastic deformation on the microstructure and corrosion behavior of 13Cr martensitic stainless steel are investigated. Samples with deformation levels of 5% and 22% (fracture elongation) were prepared using uniaxial tensile testing, and their microstructure and corrosion properties were investigated thoroughly and compared with the non-deformed base metal. The fractured sample revealed a high fraction of LAGBs with a strong {110} texture, while the 5% elongated and the non-deformed base metal samples showed lower densities of LAGBs, possessing a weaker {110} texture. A more stable and higher corrosion potential value was measured for the base sample, indicating better stability of the passive film on its surface, whereas the 5% elongated and deformed samples showed lower corrosion potential values over time with a higher fluctuation of their OCP values. From the CPP test results, a higher pitting potential value was detected for the base metal, consistent with the

trends of OCPs. EIS results also revealed a higher capacitive resistance for the non-deformed sample.

The corrosion morphology of the samples after the CPP testing revealed the formation of micro-pits primarily along the lath boundaries where a high concentration of chromium carbide precipitates was observed. The interface region between the matrix and coarse chromium carbides was found to be more susceptible to localized pitting corrosion. The sensitized regions at the periphery of the precipitates were found to be elongated under the uniaxial tension, leading to a higher fraction of susceptible regions to initiation and propagation of pitting in deformed samples. Consequently, the corrosion resistance of the alloy was found to deteriorate by increasing the applied plastic strain in the sample.
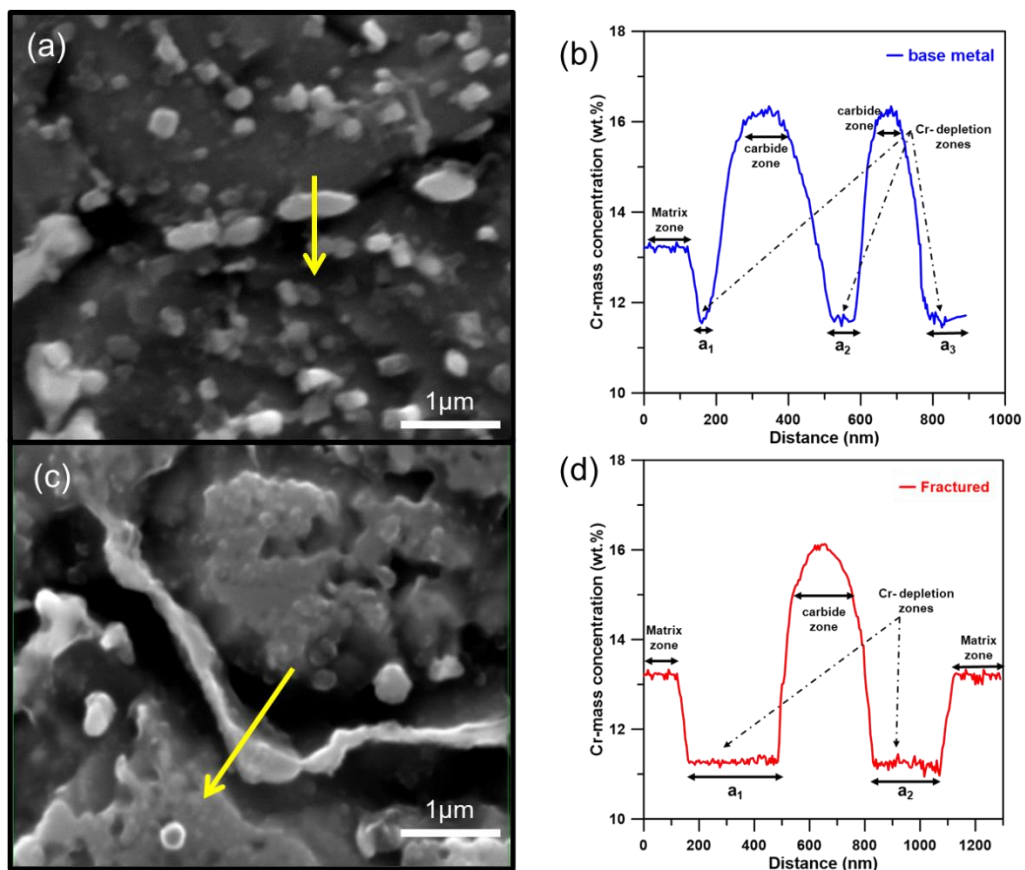
Figure 2. 15. The SEM micrographs taken from the matrix-carbide precipitates interface and their corresponding Cr composition line scan analysis results across the arrows shown on the SEM images for (a,b) the non-deformed base metal and (c,d) the fractured sample.

References

[1]   G. Bellingham, P. Peng, Scholar (26), Pudendal Nerve Blockade. (2003) 7786-7787. doi:10.1163/_q3_SIM_00374.

[2]   H. Eriksson, S. Bernhardsson, The applicability of duplex stainless steels in sour environments, Corrosion. 47 (1991) 719–727.

[3]   S. Hashizume, Y. Minami, Y. Ishizawa, Corrosion resistance of martensitic stainless steels in environments simulating carbon dioxide gas wells, Corrosion. 54 (1998) 1003–1011.

[4]   B. Baroux, Further insights on the pitting corrosion of stainless steels, Corros. Mech. Theory Pract. (1995) 265–309.

[5]   R.A. Lula, Stainless steel, (1985).

[6]   A.N. Isfahany, H. Saghafian, G. Borhani, The effect of heat treatment on mechanical properties and corrosion behavior of AISI420 martensitic stainless steel, J. Alloys Compd. 509 (2011) 3931–3936.

[7]   K.H. Anantha, C. Ornek, S. Ejnermark, A. Medvedeva, J. Sj, Correlative Microstructure Analysis and In Situ Corrosion Study of AISI 420 Martensitic Stainless Steel for Plastic Molding, 164 (2017) 85–93. doi:10.1149/2.0531704jes.

[8]   L.D. Barlow, M. Du Toit, Effect of austenitizing heat treatment on the microstructure and hardness of martensitic stainless steel AISI 420, J. Mater. Eng. Perform. 21 (2012) 1327–1336.

[9]   C.G. De Andrés, L.F. Alvarez, V. López, J.A. Jiménez, Effects of carbide-forming elements on the response to thermal treatment of the X45Cr13 martensitic stainless steel, J. Mater. Sci. 33 (1998) 4095–4100.

[10]   A. Rajasekhar, G.M. Reddy, T. Mohandas, V.S.R. Murti, Influence of austenitizing temperature on microstructure and mechanical properties of AISI 431 martensitic stainless steel electron beam welds, Mater. Des. 30 (2009) 1612–1624.

[11]   M. Sarikaya, B.G. Steinberg, G. Thomas, Optimization of Fe/Cr/C base structural steels for improved strength and toughness, Metall. Trans. A. 13 (1982) 2227–2237.

[12]   M. Sarikaya, A.K. Jhingan, G. Thomas, Retained austenite and tempered martensite embrittlement in medium carbon steels, Metall. Trans. A. 14 (1983) 1121–1133.

[13]   S.-Y. Lu, K.-F. Yao, Y.-B. Chen, M.-H. Wang, X. Liu, X. Ge, The effect of tempering temperature on the microstructure and electrochemical properties of a 13 wt.% Cr-type martensitic stainless steel, Electrochim. Acta. 165 (2015) 45–55.

[14]   H. Hänninen, J. Romu, R. Ilola, J. Tervo, A. Laitinen, Effects of processing and manufacturing of high nitrogen-containing stainless steels on their mechanical, corrosion and wear properties, J. Mater. Process. Technol. 117 (2001) 424–430.

[15]   S.S. Hecker, M.G. Stout, K.P. Staudhammer, J.L. Smith, Effects of strain state and strain rate on deformation-induced transformation in 304 stainless steel: Part I. Magnetic measurements and mechanical behavior, Metall. Trans. A. 13 (1982) 619–626.

[16]   J. Friedel, Dislocations: International Series of Monographs on Solid State Physics, Elsevier, 2013.

[17]   E. Rozovsky, W.C. Hahn, B. Avitzur, The behavior of particles during plastic deformation of metals, Metall. Trans. 4 (1973) 927–930.

[18]   T. Malkiewicz, S. Rudnik, Deformation of non-metallic inclusions during rolling of steel, J. Iron Steel Inst. 201 (1963) 33.

[19]   S. Suwas, R.K. Ray, Crystallographic texture of materials, Springer, 2014.

[20]   B.T. Lu, Z.K. Chen, J.L. Luo, B.M. Patchett, Z.H. Xu, Pitting and stress corrosion cracking behavior in welded austenitic stainless steel, Electrochim. Acta. 50 (2005) 1391–1403. doi:10.1016/j.electacta.2004.08.036.

[21]   D. Raabe, K. Lücke, Rolling and annealing textures of bcc metals, in: Mater. Sci. Forum, Trans Tech Publ, 1994: pp. 597–610.

[22]   V. Venegas, F. Caleyo, T. Baudin, J.H. Espina-Hernandez, J.M. Hallen, On the role of crystallographic texture in mitigating hydrogen-induced cracking in pipeline steels, Corros. Sci. 53 (2011) 4204–4212.

[23] J.I. Verdeja, J. Asensio, J.A. Pero-Sanz, Texture, formability, lamellar tearing and HIC susceptibility of ferritic and low-carbon HSLA steels, Mater. Charact. 50 (2003) 81–86.

[24] F. Navai, Effects of tensile and compressive stresses on the passive layers formed on a type 302 stainless steel in a normal sulphuric acid bath, J. Mater. Sci. 30 (1995) 1166–1172.

[25] S. V Phadnis, A.K. Satpati, K.P. Muthe, J.C. Vyas, R.I. Sundaresan, Comparison of rolled and heat treated SS304 in chloride solution using electrochemical and XPS techniques, Corros. Sci. 45 (2003) 2467–2483.

[26] X. Feng, X. Lu, Y. Zuo, N. Zhuang, D. Chen, The effect of deformation on metastable pitting of 304 stainless steel in chloride contaminated concrete pore solution, Corros. Sci. 103 (2016) 223–229.

[27] A. Barbucci, G. Cerisola, P.L. Cabot, Effect of cold-working in the passive behavior of 304 stainless steel in sulfate media, J. Electrochem. Soc. 149 (2002) B534–B542.

[28] N. Chandra, D.K. Singh, M. Sharma, R.K. Upadhyay, S.S. Amritphale, S.K. Sanghi, Synthesis and characterization of nano-sized zirconia powder synthesized by single emulsion-assisted direct precipitation, J. Colloid Interface Sci. 342 (2010) 327–332.

[29] C. Liang, C. Cao, N. Huang, Electrochemical behavior of 304 stainless steel with electrodeposited niobium as PEMFC bipolar plates, Int. J. Miner. Metall. Mater. 19 (2012) 328–332.

[30] B. Mazza, P. Pedeferri, D. Sinigaglia, A. Cigada, G.A. Mondora, G. Re, G. Taccani, D. Wenger, Pitting Resistance of Cold-Worked Commercial Austenitic Stainless Steels in Solution Simulating Seawater, J. Electrochem. Soc. 126 (1979) 2075–2081.

[31] L. Peguet, B. Malki, B. Baroux, Influence of cold working on the pitting corrosion resistance of stainless steels, Corros. Sci. 49 (2007) 1933–1948.

[32] D.B. Blücher, J.-E. Svensson, L.-G. Johansson, M. Rohwerder, M. Stratmann, Scanning Kelvin Probe Force Microscopy A Useful Tool for Studying Atmospheric Corrosion of MgAl Alloys In Situ, J. Electrochem. Soc. 151 (2004) B621–B626.

[33] V. Guillaumin, P. Schmutz, G.S. Frankel, Characterization of corrosion interfaces by the scanning Kelvin probe force microscopy technique, J. Electrochem. Soc. 148 (2001) B163–B173.

[34] S. Baldo, I. Mészáros, Effect of cold rolling on microstructure and magnetic properties in a metastable lean duplex stainless steel, J. Mater. Sci. 45 (2010) 5339–5346.

[35] C. Örnek, D.L. Engelberg, SKPFM measured Volta potential correlated with strain localisation in microstructure to understand corrosion susceptibility of cold-rolled grade 2205 duplex stainless steel, Corros. Sci. 99 (2015) 164–171.

[36] R. Ueji, N. Tsuji, Y. Minamino, Y. Koizumi, Ultragrain refinement of plain low carbon steel by cold-rolling and annealing of martensite, Acta Mater. 50 (2002) 4177–4189.

[37] L. Bracke, K. Verbeken, L. Kestens, J. Penning, Microstructure and texture evolution during cold rolling and annealing of a high Mn TWIP steel, Acta Mater. 57 (2009) 1512–1524.

[38] Y. Cao, H. Di, R.D.K. Misra, X. Yi, J. Zhang, T. Ma, On the hot deformation behavior of AISI 420 stainless steel based on constitutive analysis and CSL model, Mater. Sci. Eng. A. 593 (2014) 111–119.

[39] H. Luo, X. Wang, C. Dong, K. Xiao, X. Li, Effect of cold deformation on the corrosion behaviour of UNS S31803 duplex stainless steel in simulated concrete pore solution, Corros. Sci. 124 (2017) 178–192.

[40] S.S.M. Tavares, M.R. Da Silva, J.M. Pardal, H.F.G. Abreu, A.M. Gomes, Microstructural changes produced by plastic deformation in the UNS S31803 duplex stainless steel, J. Mater. Process. Technol. 180 (2006) 318–322.

[41] S. Kobayashi, R. Kobayashi, T. Watanabe, Control of grain boundary connectivity based on fractal analysis for improvement of intergranular corrosion resistance in SUS316L austenitic stainless steel, Acta Mater. 102 (2016) 397–405.

[42] M. Shimada, H. Kokawa, Z.J. Wang, Y.S. Sato, I. Karibe, Optimization of grain boundary character distribution for intergranular corrosion resistant 304 stainless steel by twin-induced grain boundary engineering, Acta Mater. 50 (2002) 2331–2341.

[43] V. Randle, O. Engler, Introduction to texture analysis: macrotexture, microtexture and orientation mapping, CRC press, 2014.

[44] S. Suwas, R. Kumar Ray, Crystallographic texture og materials, Springer, London, 2014.

[45] S.H. Lee, D.N. Lee, Analysis of deformation textures of asymmetrically rolled steel sheets, Int. J. Mech. Sci. 43 (2001) 1997–2015.

[46] B.R. Kumar, R. Singh, B. Mahato, P.K. De, N.R. Bandyopadhyay, D.K. Bhattacharya, Effect of texture on corrosion behavior of AISI 304L stainless steel, Mater. Charact. 54 (2005) 141–147.

[47] D. Song, A. Ma, W. Sun, J. Jiang, J. Jiang, D. Yang, G. Guo, Improved corrosion resistance in simulated concrete pore solution of surface nanocrystallized rebar fabricated by wire-brushing, Corros. Sci. 82 (2014) 437–441.

[48] R. Kirchheim, B. Heine, H. Fischmeister, S. Hofmann, H. Knote, U. Stolz, The passivity of iron-chromium alloys, Corros. Sci. 29 (1989) 899–917.

[49] B. Heine, R. Kirchheim, Dissolution rates of iron and chromium and Fe☐ Cr☐ alloys in the passive state, Corros. Sci. 31 (1990) 533–538.

[50] H. Luo, H. Su, G. Ying, C. Dong, X. Li, Effect of cold deformation on the electrochemical behaviour of 304L stainless steel in contaminated sulfuric acid environment, Appl. Surf. Sci. 425 (2017) 628–638.

[51] C.-N. Cao, On the impedance plane displays for irreversible electrode reactions based on the stability conditions of the steady-state—I. One state variable besides electrode potential, Electrochim. Acta. 35 (1990) 831–836.

[52] A. Kocijan, D.K. Merl, M. Jenko, The corrosion behaviour of austenitic and duplex stainless steels in artificial saliva with the addition of fluoride, Corros. Sci. 53 (2011) 776–783.

[53] M. Serdar, L.V. Žulj, D. Bjegović, Long-term corrosion behaviour of stainless reinforcing steel in mortar exposed to chloride environment, Corros. Sci. 69 (2013) 149–157.

[54] M. Talha, C.K. Behera, S. Kumar, O. Pal, G. Singh, O.P. Sinha, Long term and electrochemical corrosion investigation of cold worked AISI 316L and 316LVM stainless steels in simulated body fluid, RSC Adv. 4 (2014) 13340–13349.

[55] L. Freire, M.J. Carmezim, M.G.S. al Ferreira, M.F. Montemor, The passive behaviour of AISI 316 in alkaline media and the effect of pH: A combined electrochemical and analytical study, Electrochim. Acta. 55 (2010) 6174–6181.

[56] D. Wallinder, J. Pan, C. Leygraf, A. Delblanc-Bauer, EIS and XPS study of surface modification of 316LVM stainless steel after passivation, Corros. Sci. 41 (1998) 275–289.

[57] H.H. Uhlig, Corrosion and Corrosion Control, 1971, Sangyo-Tosyo Corp. (n.d.) 185.

[58] W. Schwenk, Theory of stainless steel pitting, Corrosion. 20 (1964) 129t-137t.

[59] K. Wu, W.-S. Jung, J.-W. Byeon, In-situ monitoring of pitting corrosion on vertically positioned 304 stainless steel by analyzing acoustic-emission energy parameter, Corros. Sci. 105 (2016) 8–16.

[60] A. Cao, Y. Wei, E. Ma, Grain boundary effects on plastic deformation and fracture mechanisms in Cu nanowires: Molecular dynamics simulations, Phys. Rev. B. 77 (2008) 195429.

[61] X. Sauvage, G. Wilde, S. V Divinski, Z. Horita, R.Z. Valiev, Grain boundaries in ultrafine grained materials processed by severe plastic deformation and related phenomena, Mater. Sci. Eng. A. 540 (2012) 1–12.

[62] X. Ren, K. Sridharan, T.R. Allen, Effect of grain refinement on corrosion of ferritic–martensitic steels in supercritical water environment, Mater. Corros. 61 (2010) 748–755.

[63] L. Tan, X. Ren, K. Sridharan, T.R. Allen, Corrosion behavior of Ni-base alloys for advanced high temperature water-cooled nuclear plants, Corros. Sci. 50 (2008) 3056–3062.

[64] L. Tan, X. Ren, K. Sridharan, T.R. Allen, Effect of shot-peening on the oxidation of alloy 800H exposed to supercritical water and cyclic oxidation, Corros. Sci. 50 (2008) 2040–2046.

[65] S.S. Chouthai, K. Elayaperumal, Texture dependence of corrosion of mild steel after cold rolling, Br. Corros. J. 11 (1976) 40–43.

[66] A. Shahryari, J.A. Szpunar, S. Omanovic, The influence of crystallographic orientation distribution on 316LVM stainless steel pitting behavior, Corros. Sci. 51 (2009) 677–682.

[67] C. Örnek, D.L. Engelberg, An experimental investigation into strain and stress partitioning of duplex stainless steel using digital image correlation, X-ray diffraction and scanning Kelvin probe force microscopy, J. Strain Anal. Eng. Des. 51 (2016) 207–219.

[68] F. Navai, O. Debbouz, AES study of passive films formed on a type 316 austenitic stainless-steels in a stress field, J. Mater. Sci. 34 (1999) 1073–1079.

[69] O. Yevtushenko, D. Bettge, S. Bohraus, R. Bäßler, A. Pfennig, A. Kranzmann, Corrosion behavior of steels for CO2 injection, Process Saf. Environ. Prot. 92 (2014) 108–118.

[70] S. Sharafat, N.M. Ghoniem, P.I.H. Cooke, R.C. Martin, F. Najmabadi, K.R. Schultz, C.P.C. Wong, T. Team, Materials selection criteria and performance analysis for the TITAN-II reversed-field-pinch fusion power core, Fusion Eng. Des. 23 (1993) 201–217.

[71] G.S. Frankel, J.R. Scully, C. V Jahnes, Repassivation of pits in aluminum thin films, J. Electrochem. Soc. 143 (1996) 1834–1840.

Chapter 3

Effects of Microstructural Evolution on the Corrosion Properties of AISI 420 Martensitic Stainless Steel during Cold Rolling Process[2]

Preface

The original version of this manuscript has already been published in the Journal of Materials Chemistry and Physics. I am the first and the corresponding author of the current work. In this chapter, I and my colleagues, Dr. Ali Nasiri and Mostafa Kazemipour, investigated the impact of microstructural evolution on the corrosion response of the AISI 420 martensitic stainless steel after the cold rolling process. I was responsible for preparing methodology, experimental testing, result gathering, and drafting of the original manuscript. Subsequently, I revised the paper based on my colleagues' initial comments and the peer-review process. The co-authors contributed to the conceptualizing, project administration, supervision, and review & editing of the manuscript

---

[2] Salahi, Salar, Mostafa Kazemipour, and Ali Nasiri. "Effects of microstructural evolution on the corrosion properties of AISI 420 martensitic stainless steel during cold rolling process." Materials Chemistry and Physics 258 (2021): 123916.

Abstract

In this study, the impacts of plastic deformation induced by compressive stresses on the evolution of the microstructure and the resultant corrosion properties of AISI 420 martensitic stainless steel (MSS) are investigated. With multiple applications in downhole environments, AISI 420 martensitic stainless steel was chosen, and cold rolling was implemented to develop preferentially textured samples of this alloy. The non-deformed samples of the base metal were cold-rolled to the deformation levels of 25% and 50%. The performed corrosion analysis herein confirmed a more stable passive layer and a higher corrosion resistance for the base metal, while the 25% and 50% rolled samples exhibited higher susceptibility to localized pitting corrosion. A detailed study of the corrosion morphology of all samples revealed the preferential pitting at the regions with a high fraction of fragmented carbides. As the deformation level increases, a higher fraction of fragmented precipitates forms in the microstructure, provoking the micro-galvanic coupling and deteriorating the corrosion resistance.

1. Introduction

Cold deformation as a step in the manufacturing process is commonly applied in the fabrication of many engineering components and alloys, including stainless steels. One of the most frequently used stainless steel families in highly corrosive environments, such as in marine and downhole, is martensitic stainless steel and, in particular, 13Cr (AISI420) stainless steel, owing to its excellent combination of high strength, good corrosion resistance, and reasonable cost for high-volume and large-scale applications.

Corrosion properties of martensitic stainless steels (MSS), similar to the other grades of stainless steels, are highly dependent on the quality and the thickness of the formed oxide passive layer, which is primarily composed of iron, chromium, and oxygen elements [1,2], covering the entire surface of the component. Based on the exposed environment, the atomic percent ratio of the Fe/Cr in the passive layer can change between 1.5 (in the aerated solution) to 7.2 (in contact with air), affecting the corrosion resistance of the MSS due to the changes in the structure and the formation mechanism of the passive layer [3,4]. The increase in the chromium content of the stainless steel is associated with the formation of a more stable and thicker passive layer on the material, leading to its enhanced corrosion resistance [5,6]. The structure of the protective passive layer in the MSS is also reported to be dependent on the exposed thermal history and its formation kinetics [7,8]. Thermal treatments of the MSSs are usually accompanied by a hardening process to enhance the mechanical performance of the steel in service [9]. These thermal treatments normally contain a cycle of austenitization treatment up to a temperature in which the matrix completely transforms into the austenite followed by relatively rapid quenching at cooling rates higher than 0.25 $K.s^{-1}$ in order to achieve a fully martensitic structure [10–12]. The high cooling rates ($\gg$10 $K.s^{-1}$) associated with the quenching process can lead to the stabilization of retained

97

austenite and δ-ferrite in the microstructure at room temperature [9,11,13–15]. On the other hand, due to their insufficient dissolution during the austenitization or their formation during the quenching process, inter-lath carbides can coexist along with the martensite phase [16]. The hardening treatment is usually followed by a tempering process to enhance the toughness and formability of the alloy and to relieve the residual stresses associated with the martensitic transformation, leading to the formation of fine newly precipitated carbides in the martensite matrix [9]. Variations in the volume fraction of inter-lath carbides, fine intra-lath carbides, retained austenite, and δ-ferrite can all significantly influence the mechanical performance and corrosion properties of the heat-treated MSSs [9,14,15]. While the formation of large inter-lath carbides can intensify the selective corrosion attack [16], the high volume fraction of the retained austenite is reported to improve the pitting corrosion of the MSSs [15].

In addition to the thermal treatments, applying plastic deformation can also have a drastic impact on the final microstructure of the material, and subsequently, on its mechanical properties and corrosion performance. Several electrochemical and metallurgical factors are involved in controlling the corrosion mechanism of cold-deformed stainless steels [17,18]. The major studies on this context have been focused on the austenitic stainless steels family [19–21]. It is reported that the cold deformation could change the composition of the passive film, leading to the formation of CrO_3 and metal Ni species in the passive film of 304L stainless steel after cold deformation, while the Ni-oxide was detected to form after applying more severe plastic deformation [22,23]. From the crystallographic perspective, applying cold-deformation to austenitic stainless steels can lead to the formation of preferential texture aligned with the loading direction [21,24]. If this alignment leads to the re-arrangement of the high density close-packed crystallographic planes parallel to the loading direction, it can potentially enhance the corrosion

properties of the alloy due to the formation of a more stable passive layer on its surface [19,25]. As an example, the formation of Cr-rich passive layer on 304L austenitic stainless steel, cold-rolled to 66% reduction, possessing a high density of close-packed planes parallel to the specimen's surface, was reported to enhance the pitting potential of the alloy [19]. However, the effect of texture is minimized at lower deformation levels due to the lower density of close-packed planes aligned with the rolling direction (RD) [26]. At lower deformation levels, the effect of deformation-induced residual stress on the corrosion properties of the alloy becomes more dominant [19]. As another deformation-induced microstructural modification in austenitic stainless steels, continuous strain hardening during deformation can provoke the strain-induced martensitic transformation, causing the increased fraction of $\acute{\alpha}$-martensite phase in the alloy, which can detrimentally affect the corrosion performance of the alloy [27]. At lower deformation levels, the corrosion mechanism of austenitic stainless steel is controlled both by the degree of residual stress and the fraction of $\acute{\alpha}$-martensite phase in the alloy [20].

It is also expected that during cold deformation, a change in the fraction of low-$\sum$ coincident site lattice (CSL) boundaries occur, directly impacting the corrosion properties. Low-$\sum CSL$ boundaries are low energy boundaries with less susceptibility to impurity [28,29]. High-$\sum CSL$ boundaries and random boundaries are known to be fast diffusion paths [30]. Differently, the low energy level of Low-$\sum CSL$ boundaries hinders the fast diffusion, leading to the grain boundaries diffusivity very similar to the bulk diffusivity [30]. A more uniform diffusivity inside the grains and along the grain boundaries can significantly enhance the formation of a uniform passive layer with improved corrosion resistance [31]. Several studies have reported that the fraction of Low-$\sum CSL$ boundaries decreases by increasing the deformation level [22,32].

An increase in the fraction of the Low-$\sum 3^n$ *CSL* boundaries was reported by West *et al*. [33] to improve the inter-lath stress corrosion cracking resistance of 316L stainless steel alloy.

For the MSSs, although there is a potential difference between the precipitated carbides and the matrix, the highest potential contrast has been reported between the carbide particles and the interface of matrix and carbides [16]. Such potential difference can accelerate the micro-galvanic coupling in which the interface and the carbides act as the local anode and local cathode, respectively, consequently deteriorating the corrosion properties of the alloy [34,35]. The microstructure of AISI 420 martensitic stainless steel commonly possesses two types of constituents, including the coarse chromium-carbide particles embedded along the grain boundaries with spherical shapes, produced commonly during the post-annealing heat treatment, and the nano-scale intra-lath precipitates of chromium carbides, formed within the lath martensitic structure during the tempering process [16]. Coarse carbides significantly contribute to the corrosion of alloy due to their high potential difference with the matrix, while the contribution of nano-scale carbides is rarely investigated. Therefore, characterizing the constituents' evolution during plastic deformation of the alloy and elucidating their effects on the corrosion performance are of vital importance.

While several studies have concentrated on characterizing the passive layer properties along with the effect of texture and grain boundaries on the corrosion performance of deformed steels [22,36–38], there is no study on characterizing the effect of micro-constituents' evolution during cold deformation on the localized corrosion behavior of martensitic stainless steels. A comprehensive study on the evolution of these secondary phases during deformation and their effects on the corrosion performance of the alloy can enlighten the dominating factors that control the corrosion mechanism in this family of stainless steels. In this study, the impacts of cold rolling-

induced plastic deformation on the microstructural evolution and the resultant corrosion response

of the AISI420 martensitic stainless steel are thoroughly investigated and compared with those of

the non-deformed sample.

2. Experimental Procedure

2.1.Sample Preparation

The chemical composition of AISI420 martensitic stainless steel used in this study is summarized

in Table 3.1. To induce plastic deformation and to create a textured microstructure, as-tempered

samples with a thickness of 5 mm were plastically deformed through the rolling process. The

reduction in thickness was adjusted to 0.125 mm in each rolling pass and respectively 10 and 20

passes were used to prepare two sets of samples, one with 25% and the other with 50% total

reduction in the thickness.

Table 3. 1. The measured chemical composition of AISI 420 stainless steel used in this study (wt.%).

C	Cr	Mn	Mo	P	S	Si	Cu	Al	Co	Fe
0.22	13.23	0.48	0.03	0.014	0.002	0.39	0.027	0.08	0.018	Bal.

2.2.Microstructural Characterization

To characterize the microstructural evolution of both the base plate and cold-rolled samples,

samples were cut and mounted in an epoxy resin. Standard grinding and polishing procedures for

stainless steels were applied for sample preparation. To reveal the microstructure, the polished

surfaces were etched using Villella's reagent. An FEI MLA 650F scanning electron microscope

(SEM) equipped with a Bruker energy dispersive X-ray (EDX) system was used to characterize the

microstructural characteristics. An HKL EBSD detector was also utilized to obtain the

crystallographic orientation features of polished surfaces, including inverse pole figures (IPF), pole

figures (PF), and martensitic lath boundaries maps using the step size of 0.4 µm. Post-processing

of the raw EBSD data was performed using Channel 5 software. To characterize the existing phases in the microstructure, X-ray diffraction (XRD) analysis was conducted with Cu-K$_\alpha$ source (λ=1.5406 Å) at 40 kV and 35 mA using an aperture of 2 mm over a diffraction angle range of 10° to 90° with a step size of 0.01°.

2.3. Electrochemical Analysis

Before the electrochemical testing, all samples were cold mounted into an epoxy resin to limit the exposed area of the sample to only one face, while a wire was connected to the backside of the sample through the resin, providing the electrical connection during the electrochemical tests. The samples for electrochemical analysis were then ground using 500 grit SiC sandpaper, cleaned ultrasonically in acetone, and were polished to a mirror-like finish using a 0.02 µm alumina suspension at the final step. To avoid crevice corrosion along the sample-epoxy interface, the edges between the sample and the epoxy were coated using a masking lacquer. The electrochemical measurements were performed in aerated 3.5 wt.% NaCl solution. A temperature-controlled water bath was used to maintain the temperature of the solution at 25±0.5 °C. The used three-electrode cell setup contained a graphite rod as the counter electrode, a saturated silver-silver chloride (Ag/AgCl) electrode as the reference electrode, and the AISI 420 stainless steel as the working electrode. Before each test, the open circuit potential (OCP) was monitored for an hour for stabilization. The potentiodynamic polarization tests were performed at the scanning rate of 0.5 mV/s commencing at –0.2 V *versus* OCP. The electrochemical impedance spectroscopy (EIS) tests were also conducted over a frequency range from 100 kHz to 10 mHz with a signal amplitude of 10 mV after 1 h and 120 h of immersion time. Mott-Schottky measurements were performed at the frequency of 1000 Hz in the potential ranging from -1000 to 1000 mV$_{Ag/AgCl}$ with an amplitude of 10 mV. To avoid the variation in passive layer thickness, the scanning rate of 50 mV/step was

applied. All electrochemical experiments were repeated at least three times to verify the reliability of the results.

3. Results

3.1. Microstructure Characterization

The acquired XRD spectra for all samples are shown in Figure. 3.1. Peaks associated with the martensite phase (M) were detected for the rolled and base metal samples in diffraction angles ranging from 10° to 90°. All samples similarly demonstrate the highest intensity peak for $(110)_M$ plane at 44°, followed by $(211)_M$ and $(200)_M$ peaks with lower intensities at 82° and 64°, respectively. As the rolling percentage increased, the intensities of detected peaks were found to increase, while their corresponding full-width at half maximum (FWHM) decreased, indicating the enhancement of crystallite size[39–42]. No clear peaks were identified corresponding to the formation of precipitates and retained austenite plausibly due to their significantly lower volume fraction as compared to the martensite phase. The obtained XRD data allows the calculation of both grain diameter (crystallite size) and dislocation density for samples. The pure diffraction line profile can be used to calculate the crystallite size and the lattice strain value [39]. This "pure" line profile is calculated by subtracting the instrumental broadening factor from the experimental line profile, as follows [39]:

$$\beta = \delta(2\theta) = B\left(1 - \frac{b^2}{B^2}\right)(rad) \tag{1}$$

where δ is the dislocation density, 2θ is the diffraction angle, B and b are the breadths of the same Bragg peak from the XRD spectra, which is used as the FWHM (β) [40]. Scherrer equation can be applied to calculate the average diameter of the crystallites (crystal size) [39]:

$$L = \frac{D\lambda}{\beta \cos\theta} \qquad (2)$$

where D is the shape factor and is approximately equal to unity, L is the crystal size, θ is the Bragg angle, and λ is the wavelength of the used X-ray (for Cu-K$_\alpha$ radiation = 1.54056 Å).

Using another method known as Cauchy [40], an appropriate equation to separate the crystallite size and lattice strain can be developed, presuming that the crystallite size and strain line profiles are both considered to be Cauchy[40]:

$$\beta \cos\theta = \frac{\lambda}{L} + 4e \sin\theta \qquad (3)$$

where L and e are the crystallite size and strain, respectively. The crystallite size from Cauchy equation can be estimated from the ordinate-intersection and slope of the $\beta \cos\theta$ versus $\sin\theta$ graph.

The dislocation density of the base metal and the rolled samples can be defined as the length of dislocation lines per unit volume (δ) and calculated using the following equation [43]:

$$\delta = \frac{1}{L^2} \qquad (4)$$

The calculated values for the dislocation density (δ), based on the Sherrer and Cauchy equations for the (110), (200), and (211) intensity peaks on the XRD spectra, are summarized in Table 3.2 for the studied samples herein. Expectedly, the rolled samples exhibited remarkably higher dislocation densities as compared to the base metal, deducted from the Sherrer and Cauchy models, ascribed to the multiplication and rearrangement of dislocations during the applied rolling process [42,44] .
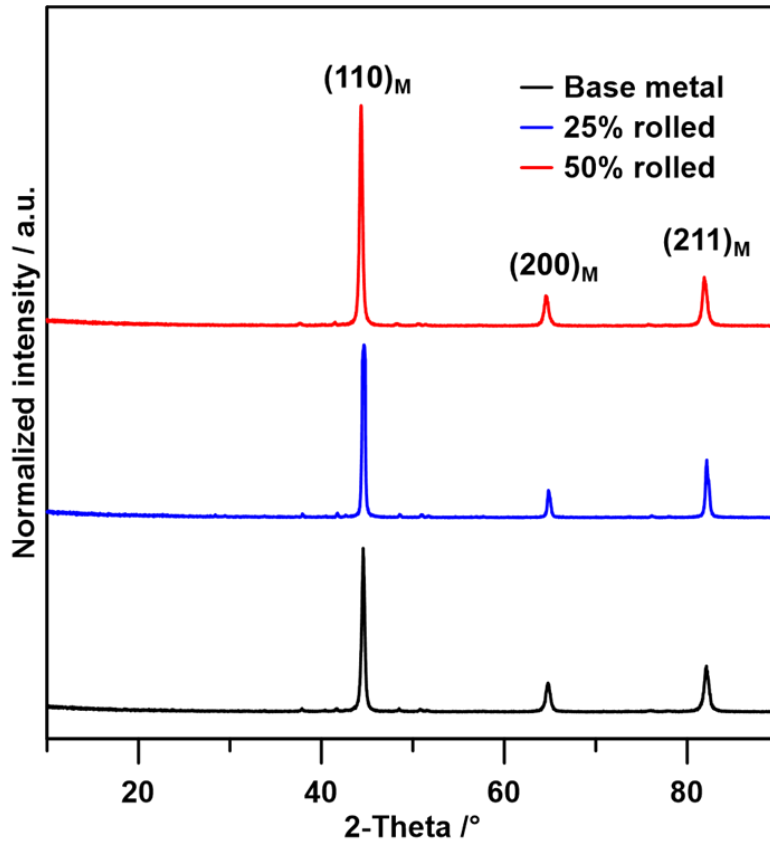
Figure 3. 1. The XRD results of the non-deformed base metal, 25%, and 50% rolled samples.

Table 3. 2 .Calculated dislocation density (δ) for the base metal and the rolled samples using Sherrer and Cauchy equations.

Sample	$\delta/1.nm^{-2}$ (Scherrer)			$\delta/1.nm^{-2}$ (Cauchy)		
	(110)	(200)	(211)	(110)	(200)	(211)
Base metal	0.003	0.49	0.01	0.03	0.54	0.01
25% rolled	0.06	2.56	0.92	0.07	2.68	1.06
50% rolled	0.07	2.97	0.98	0.09	3.84	1.26

Figure. 3.2 shows the SEM micrographs taken from the microstructure of the base metal, 25%, and 50% rolled samples, along with their corresponding EDX elemental maps for Fe, Cr, Mn, and C elements. A relatively high-volume fraction of precipitates was detected in each sample. The EDX elemental maps show a high concentration for Chromium and Manganese for precipitates, where iron is depleted in all samples. The elemental mapping also reveals a considerable concentration of carbon in the precipitates (Figure. 3. 2e, j, o), indicating the chromium carbide

origin of the existing precipitates containing Mn in solid solution form. The chromium carbide precipitates are relatively large (micro-scale) with a round shape and distributed homogeneously in the matrix and more accumulated along the grain boundaries (inter-lath sites) of the matrix, formed during the tempering heat treatment. The fraction and geometry of the carbides were found to remain constant after cold rolling. Furthermore, the precipitates' fragmentation (breakage of carbide particles) was detected in the 25% rolled samples, as indicated by arrows in Figure. 3. 2f. The fraction of fragmentation was found to increase in the 50% rolled samples. Generally, the larger particles of carbides were found to be more susceptible to fragmentation, leading to the formation of intercept voids between them.
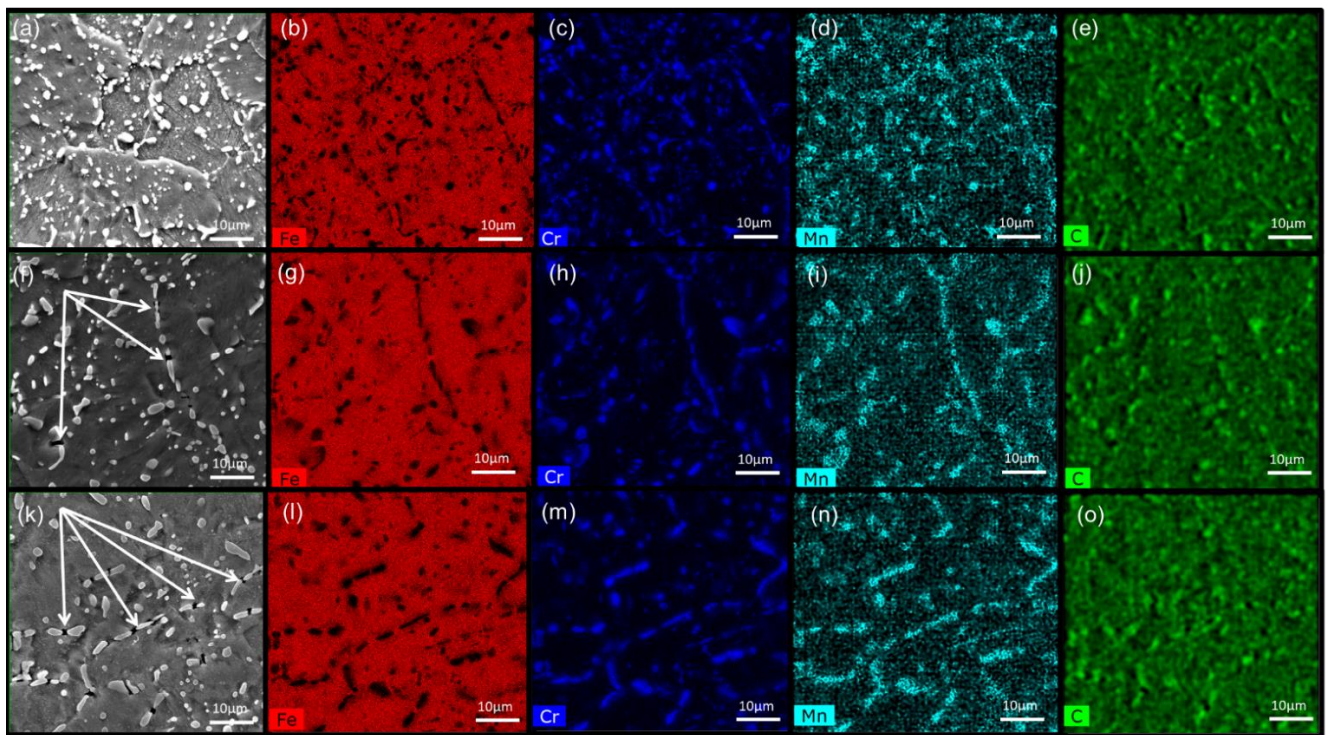
Figure 3. 2. SEM micrographs taken from the (a) base metal, (f) 25% rolled sample, (k) 50% rolled sample along with their corresponding elemental maps for (b-e) base metal, (g-i) 25% rolled, and (l-o) 50% rolled samples.

The SEM micrographs at higher magnification (Figures. 3. 3b and 3d) also revealed the existence of nanoscale precipitates in the microstructure embedded in the martensitic matrix.

Similarly, these fine intra-lath precipitates with capsule-like morphology are assumed to have chromium carbide origins, commonly formed during the tempering process [16].
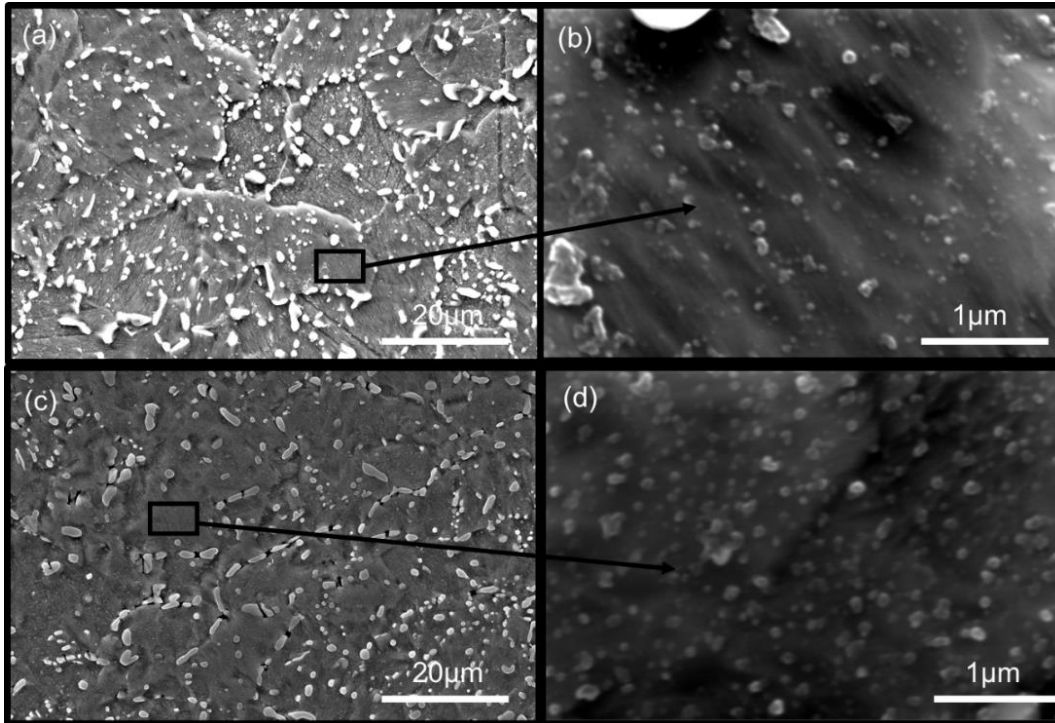
Figure 3. 3. SEM micrographs of the (a) base metal and (c) 50% rolled sample. Higher magnification SEM micrographs showing the formation of nano-scale precipitates in the (b) base metal and (d) 50% rolled sample.

The obtained inverse pole figures (IPF) maps of the base metal, 25%, and 50% rolled samples are shown in Figure. 3. 4. Finer martensitic lath structure was observed after the cold rolling as the average lath size of the base metal was measured to be 6.44 µm, while the lath size of the 25% and 50% rolled samples decreased to 3.67 µm and 1.95 µm, respectively. All the samples exhibited a bimodal lath structure with relatively large laths surrounded by martensitic laths with a size of lower than 1 µm (Figure. 3. 4d-f). The 50% rolled sample illustrated the highest fraction of laths with a size smaller than 1 µm (68%), while the base metal exhibited a wider distribution of lath size. The grain refinement during the cold deformation is reported to be attributed to the elongation and

breakage of the grains along with the nucleation and growth of grains in a homogenous microstructure [35,45,46].
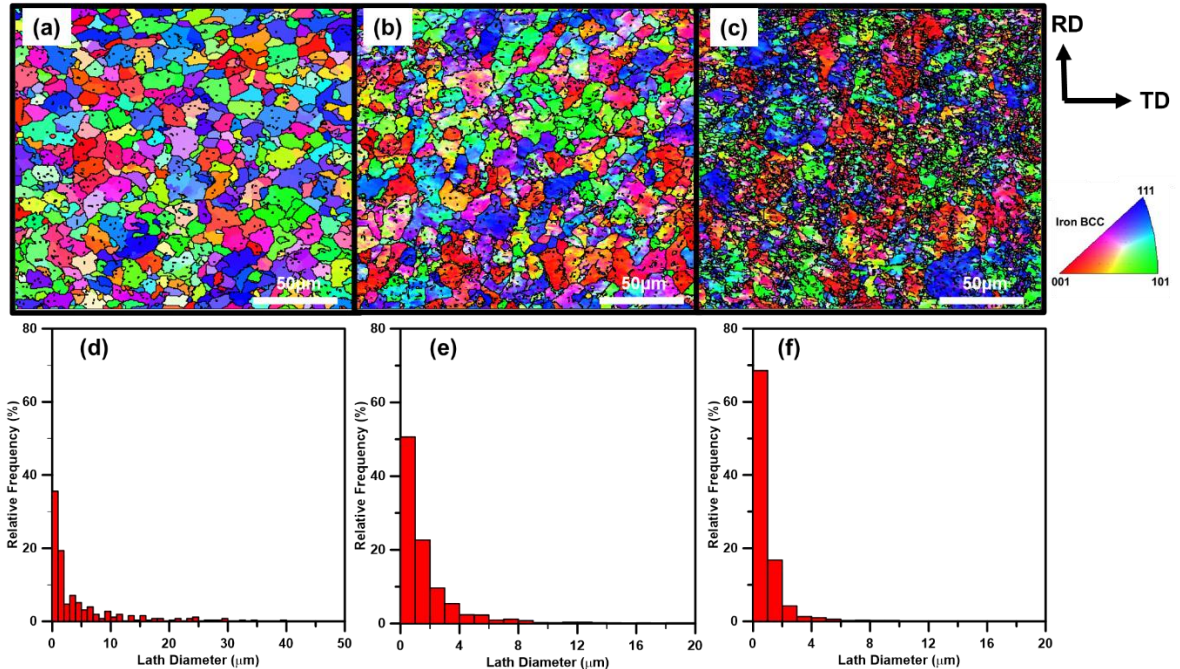
Figure 3. 4. The EBSD inverse pole figure maps of the (a) base metal, (b) 25% rolled, and (c) 50% rolled samples. The martensitic lath size distribution plots for the (d) base metal, (e) 25% rolled, and (f) 50% rolled samples

It is worth noting that the quality of Kikuchi patterns obtained from the EBSD analysis is highly dependent on the formation of voids, microcracks, and precipitates fragmentation [22,47]. In this study, the quality of the IPF results for the 50% rolled sample was found to decrease due to the high fraction of precipitates fragmentation between the fractured precipitates, resulting in the acquisition of a higher percentage of zero solutions during the EBSD measurement.

Distribution of high angle grain boundaries (HAGBs), medium angle grain boundaries (MAGBs), and low angle grain boundaries (LAGBs) for the base metal and rolled samples are exhibited in Figure. 3. 5. The base metal revealed a high fraction of HAGBs and a very low fraction of MAGBs and LAGBs. The 25% rolled sample exhibits a higher fraction of LAGBs and MAGBs

relative to the base metal sample, whereas the 50% rolled sample contained the highest fraction of LAGBs and a lower fraction of MAGBs as compared to the 25% rolled sample. Therefore, by increasing the percent deformation, the fraction of LAGBs increases. Low angle grain boundaries possess a lower level of energy and can hinder a fast diffusion-controlled process [28].
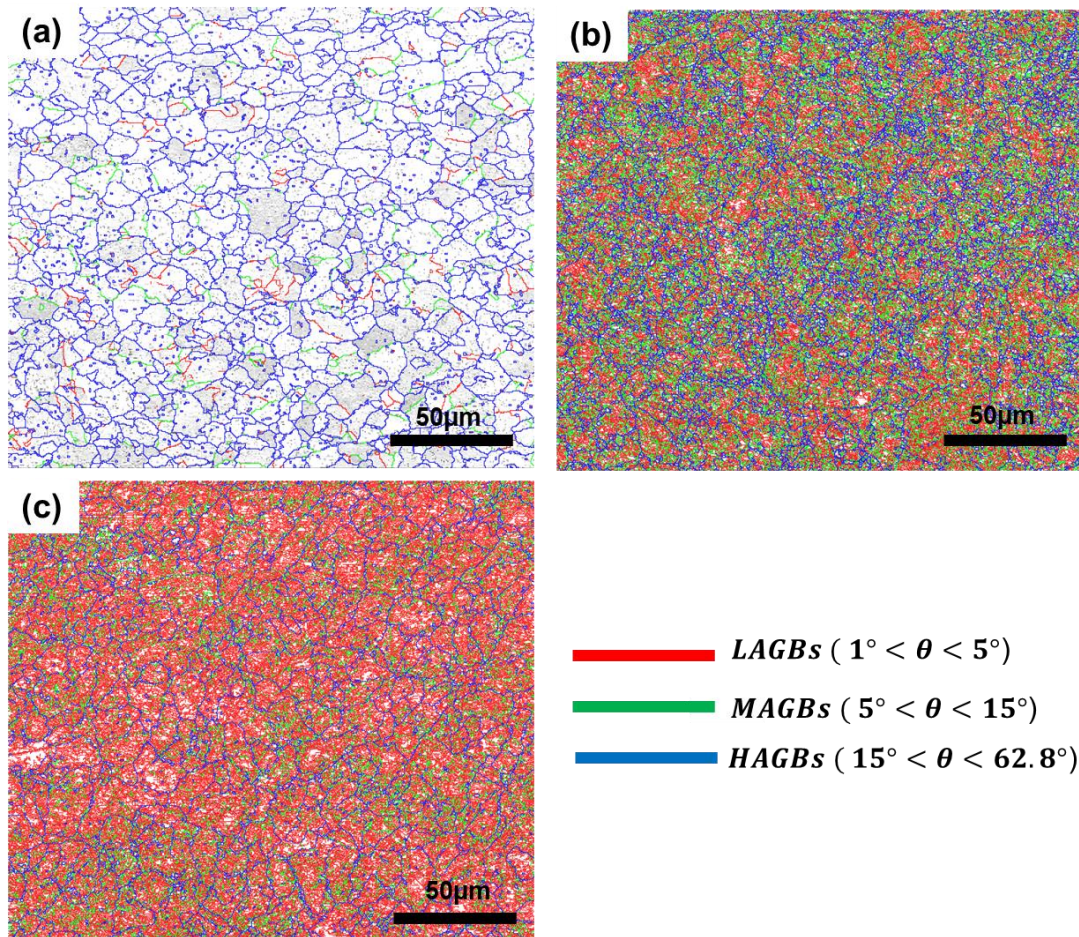
Figure 3. 5. EBSD grain boundaries maps showing the distribution of HAGBs, MAGBs, and LAGBs in the (a) base metal, (b) 25% rolled, and (c) 50% rolled samples

The pole figures of the samples calculated from the EBSD data are illustrated in Figure. 3. 6. Tempered martensitic stainless steel with body-centered cubic (BCC) crystallographic structure is known to possess a texture composed of perfect normal direction (ND) fiber and two other components lying on the deformation direction [48,49]. The active plane families in the BCC

structure are generally {110} and {111}, while the {100} planes can show strong texture resulted from solidification and phase transformation activities, such as heat treatment. As shown in Figure. 3. 6a, the base metal shows strong texture components in the {100} plane, which can be attributed to the phase transformation during high-temperature heat treatment of the base plate [50]. The hot-rolling process has been reported to give rise to {111}<110> (on the RD fiber) texture component, while the cold deformation leads to the formation of {111}<112> texture component on the ND fiber [50]. Strong {111} texture component aligned with the ND was observed for the 50% rolled sample.
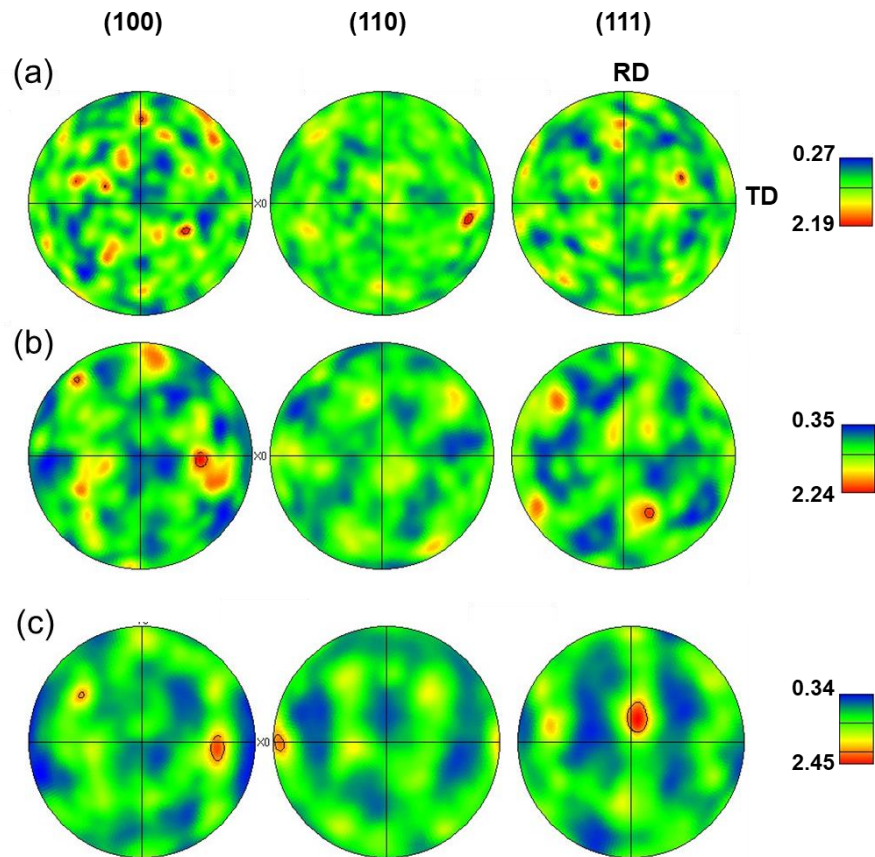
Figure 3. 6. EBSD pole figure maps of the (a) base metal, (b) 25% rolled, and (c) 50% rolled samples.

3.2. Corrosion Results

3.2.1. *Open circuit potential results*

Open circuit potential (OCP) variations over 1 h of immersion time in aerated 3.5 wt.% NaCl

solution for all studied samples are illustrated in Figure. 3. 7. Fluctuations in the OCP were

observed over the monitoring time due to the continuous occurrence of metastable pitting corrosion

during the testing [16]. Samples demonstrated relatively stable OCP values approximately after

700 s. The stabilized OCP value was found to decrease by increasing the deformation level. The

average OCP value for the base metal was recorded as -96$\pm$7.50 mV$_{Ag/AgCl}$, while it reduced to -

111$\pm$8.25 mV$_{Ag/AgCl}$ and -126$\pm$9.50 mV$_{Ag/AgCl}$ for the 25% and 50% rolled samples, respectively.

The reduction of the measured OCP value for the rolled samples implies the deterioration of the

passive layer integrity and density [51]. As the deformation level increases, the passive film

stability for the deformed samples seems to decrease, leading to less noble values for OCP.
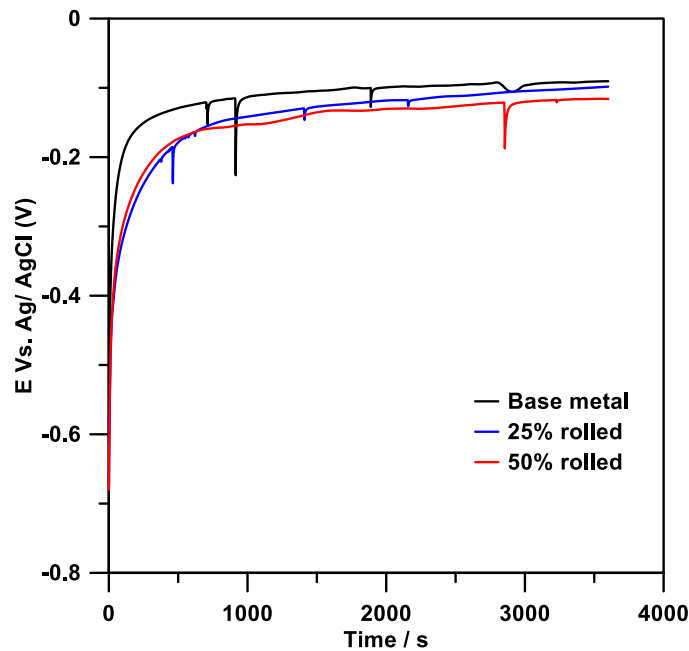
Figure 3. 7. The OCP values over the immersion time for AISI420 martensitic stainless-steel
samples in aerated 3.5 wt.% NaCl at room temperature.

3.2.2. Potentiodynamic polarization results

The potentiodynamic polarization measurements were conducted in aerated 3.5 wt.% NaCl solution to characterize the electrochemical performance of the prepared samples. The obtained results at 25°C are shown in Figure. 3. 8. The deducted parameters from the polarization graphs, *i.e.* corrosion potential (E_{corr}), pitting potential (E_{pit}), cathodic slope (β_c), and anodic slope (β_a) are summarized in Table 3. 3. It is observed that E_{corr} decreases with increasing the deformation level, suggesting a general weakening of the corrosion resistance in the NaCl solution for the rolled samples. The obtained lowest corrosion potential value for the 50% rolled sample is in good agreement with the OCP results.

Table 3. 3. Polarization parameters deducted from the polarization graphs for all studied samples.

Sample	E_{corr} (mV$_{Ag/AgCl}$)	E_{pit} (mV$_{Ag/AgCl}$)	β_c (mV decade $^{-1}$)	β_a (mV decade $^{-1}$)
Base metal	-125 ± 8.25	138 ± 11.25	-91 ± 3.20	114 ± 2.40
25% rolled	-133 ± 7.25	91 ± 9.50	-97 ± 2.30	118 ± 2.30
50% rolled	-143 ± 8.50	37 ± 8.25	-113 ± 1.40	127 ± 1.20

The anodic branch of the polarization graphs revealed fluctuations due to the formation of metastable pits during the transition from the corrosion potential to the pitting potential. A wide passive region was observed for all samples, regardless of the percent cold deformation of the sample. Analogous to the corrosion potential trend, the pitting potential values were decreased with increasing the deformation level. While the pitting potential of the base metal is ~138 mV$_{Ag/AgCl}$, it decreased to ~91 mV$_{Ag/AgCl}$ for 25% rolled sample and to ~37 mV$_{Ag/AgCl}$ for 50% rolled sample.
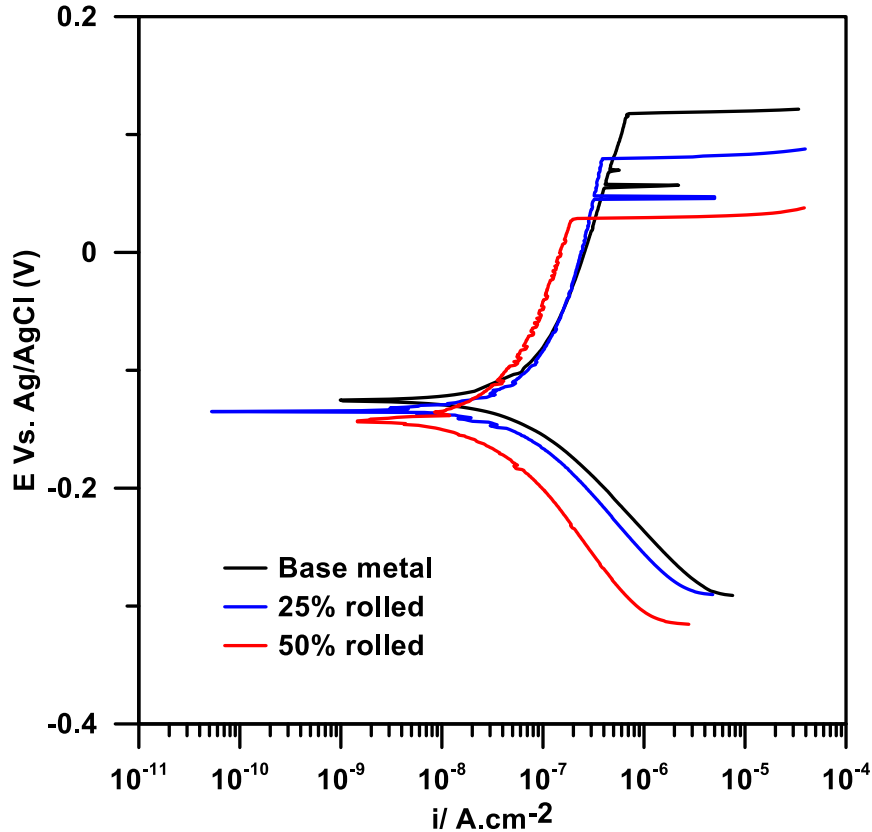
Figure 3. 8. Potentiodynamic polarization curves for AISI420 stainless steel in aerated 3.5 wt.% NaCl solution at room temperature.

3.2.3.   Electrochemical impedance spectroscopy results

To further characterize the electrochemical behavior of the passive film on the rolled samples versus the base metal, the EIS measurements were conducted in aerated 3.5 wt.% NaCl electrolyte at room temperature. Figures. 3. 9a and 9b show the effect of cold rolling on the Nyquist and Bode plots of AISI 420 martensitic stainless steel after 1 h of immersion in the aerated 3.5% NaCl solution. The trend of capacitive loops for the base metal and the rolled samples were nearly the same, suggesting no change in the corrosion mechanism stemmed from the cold rolling. A large semi-circle diameter was observed for the Nyquist plot of the base metal sample relative to the 25% and 50% rolled samples indicating a higher corrosion resistance of the passive film for the

113

base metal after 1 h of immersion. Figure. 3. 9b shows the Bode plots of the base metal and the rolled samples after 1 h of immersion. The Bode plots revealed more linearity with the slope near -1 for the impedance module *vs* frequency of the base metal, having a constant phase angle value near -80° over a wider frequency range (~ 0.1-100 Hz), indicating a more stable passive film formation on the surface of the base metal as compared to the deformed samples. By increasing the degree of deformation, the linearity of $\log|Z|$ *vs* $\log f$ and the maximum phase angle and its stability range were found to diminish.

In order to characterize the electrochemical stability of the passive film formed on the samples' surfaces over time, EIS experiments were also conducted after 120 h of immersion time in the solution. At longer immersion time, the radius of the Nyquist curves (Figure. 3. 9c) was found to significantly reduce as compared to the results after 1 h of immersion time (Figure. 3. 9a), accompanied by an intense drop in the Bode plots to lower impedance and phase angle values at medium to low frequency ranges. These observations indicate a continuous deterioration in the electrochemical stability of the surfaces by increasing of the immersion time. The detected reduction in the absolute value of the impedance after 120 h with respect to that after 1 h affirms the intense dissolution of the passive layer into the solution over time. The EIS spectra of the samples after 120 h revealed the same trend between the studied samples as the trend detected at 1 h of immersion time, showing a higher passive layer stability for the base metal and reduced stability for the deformed samples. The Bode plots exhibited a steady reduction in the absolute values of impedance and phase angles in the low- to medium-frequency range by the increase in the rolling level.
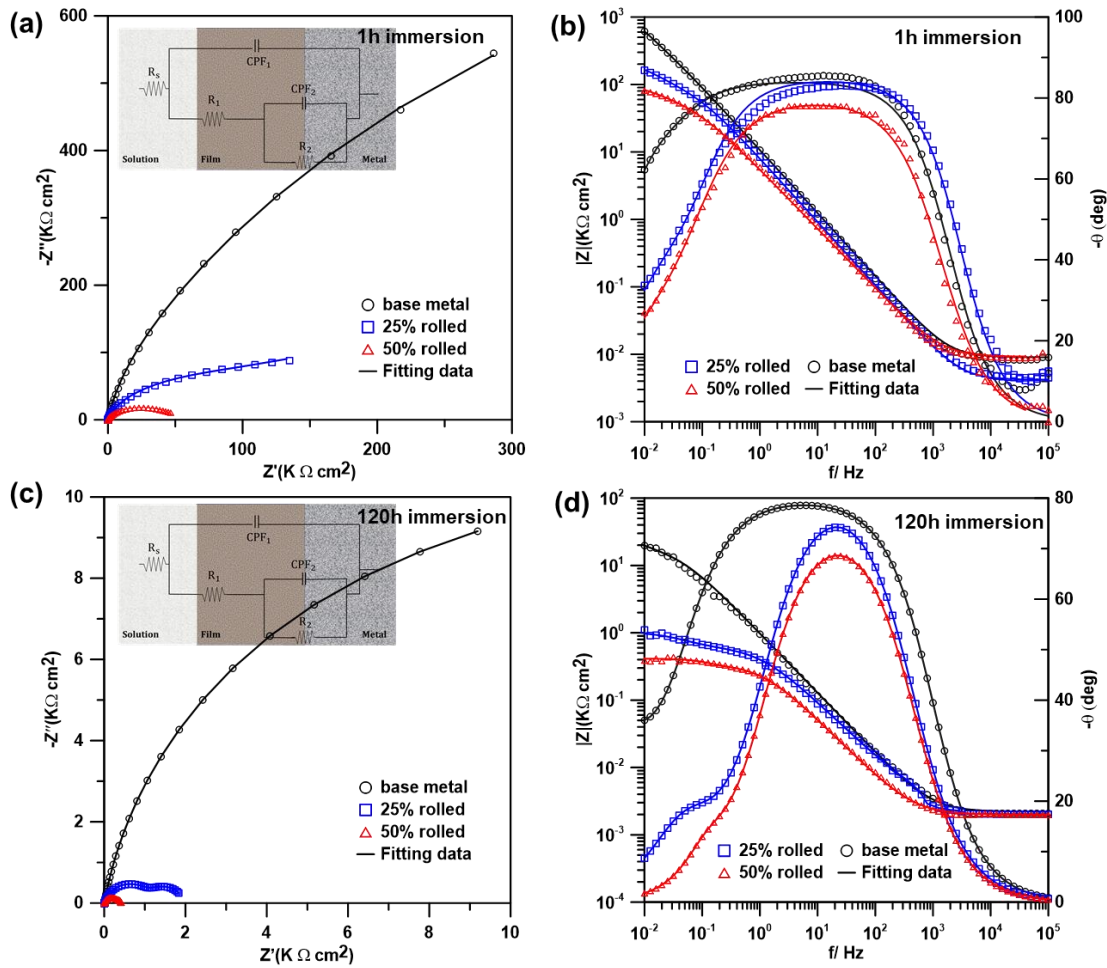
Figure 3. 9. (a) Nyquist plots and Bode plots obtained from the 420 AISI stainless steel with different deformation levels in aerated 3.5 wt.% NaCl electrolyte at room temperature: (a) and (b) after 1 h of immersion time, (c) and (d) after 120 h of immersion time.

Previous studies have suggested several equivalent circuit (EC) models for interpreting the impedance spectra in stainless steel [35]. In this study, the EIS data were modeled and fitted using the EC shown in Figure. 3. 9a and c (commonly employed for stainless steel [52,53]). In this EC model, constant phase element (CPE) was used to characterize the non-ideal capacitance response of the interface and to address the micro or nano surface inhomogeneities, such as surface roughness, porosity in grain boundaries, and impurities [54,55]. The impedance value of the CPE can be defined using [55]:

$$Z_{CPE} = [Y_0(j\omega)^n]^{-1} \tag{5}$$

where Y_0 is a frequency-independent constant (*CPE* constant), $j = -(1)^{1/2}$, ω is the angular frequency, and *n* is the fractional exponent of the *CPE*, representing the surface irregularities. The EC model consists of three resistors, representing the solution resistance (R_s), passive film resistance (R_1), and charge transfer resistance (R_2), and two constant phase elements, corresponding to the capacitance of the passive film (CPE_1) and double layer capacitance (CPE_2). The detailed fitting parameters of the obtained EIS results are listed in Table 3. 4. For all samples, n_1 values were obtained between 0.91-0.93, whereas n_2 values were between 0.70-0.86. Chi-square (χ^2) values below 1.67×10^{-4} revealed good accordance between the EIS data and the fitted values. After 1 h of immersion time, the passive layer resistance and the charge transfer resistance values (R_1 and R_2, respectively) were found to decrease drastically by increasing the deformation level, indicating the reduced protective nature of the passive film at higher deformation levels in the samples immersed for 1 hour. A similar trend was detected at longer immersion time of 120 h. On the other hand, the values of the CPE_1 and CPE_2 for the deformed samples were higher than those of the base metal, suggesting the formation of a more defected passive film on the deformed samples. The samples immersed for 120 h revealed significantly lower values for R_1 and R_2 and higher values for CPE_1 and CPE_2, as compared to the samples immersed for only 1 h, suggesting the formation of a more stable passive film at the intial immersion time. For all samples, the general passive layer resistance was found to be lower than their corresponding charge transfer resistance, confirming that uniform corrosion is the dominating corrosion mechanism at the OCP. This is consistent with the observed clear passive region for all samples in Figure. 3. 9.

Table 3. 4.The fitted electrochemical parameters for the EIS spectra.

Immersion Time (h)	Sample	R_s (Ωcm²)	CPE_1 (Ω⁻¹cm⁻²sⁿ)	n_1	R_1 (Ωcm²)	CPE_2 (Ω⁻¹cm⁻²sⁿ)	n_2	R_2 (Ωcm²)	$\sum \chi^2$
1	Base metal	17.03	1.03×10^{-5}	0.924	1.52×10^6	5.87×10^{-6}	0.865	1.70×10^6	1.54×10^{-4}
	25% rolled	18.23	4.45×10^{-5}	0.962	5.00×10^5	9.62×10^{-6}	0.734	9.27×10^5	1.34×10^{-4}
	50% rolled	17.46	2.57×10^{-4}	0.922	6.52×10^4	5.91×10^{-5}	0.702	8.89×10^4	1.67×10^{-4}
120	Base metal	17.40	4.36×10^{-5}	0.88	8.87×10^4	1.93×10^{-4}	0.76	3.49×10^4	1.45×10^{-4}
	25% rolled	17.56	7.57×10^{-5}	0.85	4.45×10^3	1.25×10^{-3}	0.85	1.35×10^3	1.34×10^{-4}
	50% rolled	17.65	4.23×10^{-4}	0.85	1.58×10^3	4.74×10^{-3}	0.99	2.93×10^2	1.13×10^{-4}

3.2.4. Mott-Schottky analysis

Semiconducting properties of the samples in aerated 3.5 wt.% NaCl solution at room temperature were measured using the Mott-Schottky approach. Figure. 3. 10 shows the obtained Mott-Schottky plots for 420 MSS at various deformation levels. According to the Mott-Schottky theory, the measured electrode capacitance (C) and the applied potential (E) can lead to the following relationship [22,56]:

$$\frac{1}{C^2} = \frac{1}{C_H^2} + \frac{1}{C_{SC}^2} = \frac{1}{C_H^2} + \frac{2}{e.N_q.\varepsilon.\varepsilon_0}(E - E_{FB} - \frac{kT}{e})$$ (6)

where C_H is the Helmholtz capacitance, C_{SC} is the space charge capacitance of the passive film, N_q is the doping density, ε is the relative dielectric constant for the passive layer ($\varepsilon = 15.6$ for stainless steel), ε_0 is the vacuum permittivity, k is Boltzmann's constant (8.16×10^{-5} eV/K), e is the electron charge (1.6×10^{-19} C), E_{FB} is the flat band potential, and T is the absolute temperature. The value of kT/e can be very negligible. The values for the N_q and E_{FB} can be calculated by using the slope and intercept with the potential axis of the C^{-2} vs E linear portion curves [22].

As shown in Figure. 3. 10, the Mott-Schottky curves (the electrode capacitance vs the applied potential) for all samples have two straight zones with positive and negative slopes. The potential

plateau region, where the flat bond potential (E_{FB}) is recorded, separates the positive and negative slopes. The base metal sample and the rolled ones showed the same semiconducting behavior, demonstrating the p-n heterojunction. The n-type semiconductor behavior is suggested for the region with a positive slope, which is an indication of vacancies caused by oxygen [22,57]. The p-type semiconductor behavior occurs in the negative slope region, indicating that the cation vacancies are the major defects in the passive film layer [57]. According to the electron band theory of solids, if the number of electrons in the conduction band of an oxide is more than the number of holes in valence band, the oxide passive layer is considered to be an n-type semiconductor, such as Fe_2O_3, ZnO, TiO_2, V_2O_5 and MoO_3. Conversely, when the number of holes in the valence band of an oxide is higher than the number of electrons in its conduction band, the oxide layer is considered to be a p-type semiconductor, such as Cu_2O, NiO, and Cr_2O_3 [58]. It has been reported that different passive oxide layers formed on stainless steel illustrate different semiconductor properties, determined by the predominant defects existing in the passive film [59]. For Fe–Cr based alloys (such as MSS 420 alloy), it is often assumed that the semiconducting behavior reflects the duplex characteristic of their surface passive films, with an inner region of film essentially comprised of Cr_2O_3 and an outer region mainly composed of Fe_2O_3 [60]. Thus, the positive slope of the Mott-Schottky curve illustrates an n-type semiconductor behavior that is characteristic of Fe_2O_3, containing oxygen vacancies as donor states [61]. The negative slope, in the higher potential range, results from the electrochemical behavior of a p-type semiconductor, ascribed to the presence of Cr_2O_3 in the inner oxide layers, containing metal vacancies as acceptor states [61]. While the transformation from the p-type to n-type semiconductor occurs at nearly the same potential value (E ≈ -0.5 $V_{Ag/AgCl}$) for the 25% and 50% rolled samples, the base metal transition was found to occur at a lower potential value (E ≈ -0.73 $V_{Ag/AgCl}$). This confirms the more

protective nature of the formed passive film on the base metal, which is in good agreement with the results obtained from other electrochemical experiments. It should be also noted that a p-type semiconductor behavior (negative slope on the Mott- Schottky curves) was observed for the samples at potential values higher than 0.2 $V_{Ag/AgCl}$. In this potential region, no direct correlation between the semiconducting properties and defects concentration can be established primarily due to instability of the passive layer at such high potential range (see the polarization graphs in Figure. 3. 8)[62,63].

Only one donor level was observed for the samples. Table 3. 5 presents the calculated values of donor density (N_D), acceptor density (N_A), and E_{FB} based on equation 2 and the slope of the Mott-Schottky curves. The base metal showed a lower value for the E_{FB}, while the E_{FB} value remained nearly the same for the 25% and 50% rolled samples. The N_D and N_A values for the base metal and the rolled samples are in the order of 10^{17}-10^{18} cm^{-3} magnitude, indicating the formation of a highly disordered passive film on all samples [64]. As shown in Table 3. 5, by increasing the rolling-induced deformation percentage, both the N_D and N_A values (defect densities) increase. A higher donor and acceptor density can reduce the stability of the passive film and increase the electrochemical reactions occurring at the interface of the electrolyte and the metal [22,57]. The N_D value can also feature the adsorption affinity of the Cl$^-$ ions in the passive film, representing the pit nucleation susceptibility of the passive film [65–67]. Thus, the rolled samples represent easier adsorption of the chloride ions on their passive film, and concomitantly, an easier reaction between chloride ions and the oxygen vacancies in the passive film [65,66].

Table 3. 5. Effect of rolling deformation on the semiconducting properties of the passive film formed on AISI420 MSS.

Sample	N_D (10^{18} cm^{-3})	N_A (10^{18} cm^{-3})	E_{FB} (mV$_{Ag/AgCl}$)
Base metal	0.89	5.12	-670
25% rolled	1.18	5.44	-550
50% rolled	1.32	5.78	-550
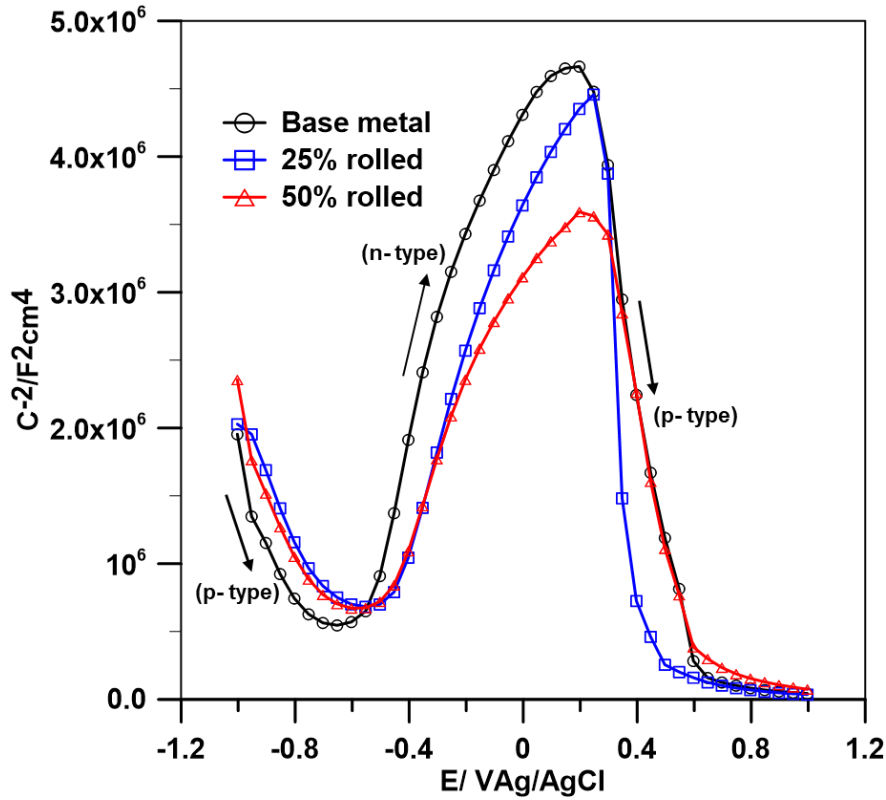
Figure 3. 10. The Mott-Schottky curves of the passive films formed on the AISI 420 stainless steel at different deformation levels in aerated 3.5 wt.% NaCl solution.

4. Discussion

4.1. Effect of grain orientation and passive layer formation on the corrosion behavior

Based on the EBSD inverse pole figure data, a slight refinement in the martensite lath size was detected for the rolled samples, and as the rolling percentage increased, the refinement was intensified. The grain refinement can potentially deteriorate the corrosion performance in stainless steels due to the formation of larger grain boundary areas [22,57], where commonly the precipitates

or secondary phases with different electrochemical potentials relative to the matrix tend to accumulate, leading to an increased galvanic coupling over the entire microstructure exposed to the corrosive electrolyte. a

Characterizing the micro-pit locations in the microstructure is also vital to understand the corrosion mechanism in the rolled samples as well as the dominating factors that control the severity of the corrosion attack. These micro-pits form during the initial stage of the corrosion and transform into the propagated pitting spots during the stabilization stage. A change in the location of pitting initiation was observed in the cold-rolled samples. The micro-pits on the base metal were formed near the martensitic lath boundaries where a high concentration of inter-lath carbides were detected (Figure. 3. 11a-11c), while the pitting initiation on the 25% and 50% rolled samples were observed on the locations where the carbide fragmentation started due to the applied plastic deformation during rolling (Figure. 3. 11d-11i). Chromium depletion along the interface between the fragmented particles can lead to the initiation of pittings, stimulated by the potential difference between the gap zone (the fragmented area) and the brittle carbides.
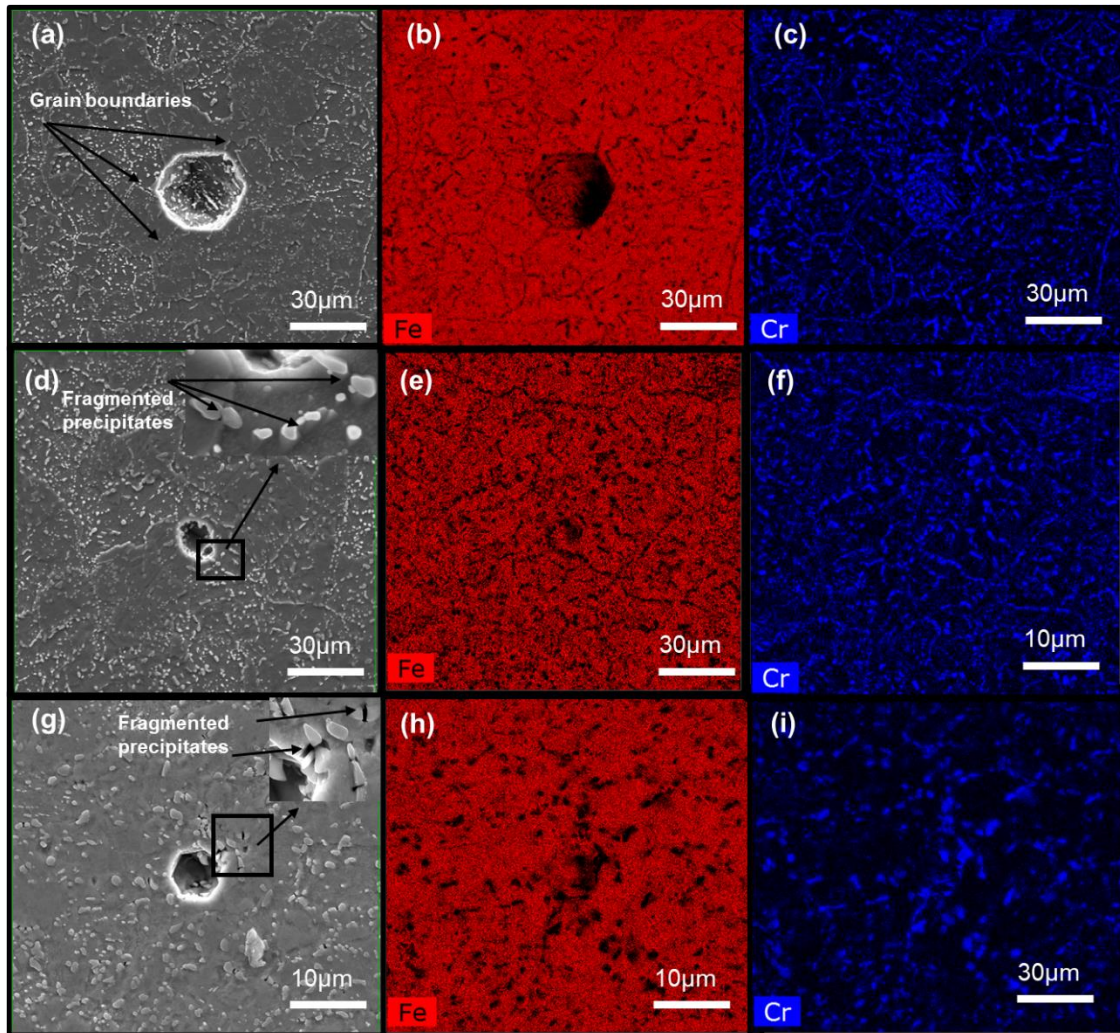
Figure 3. 11. SEM images from the formed micro-pits after polarization testing on the (a) base metal, (b) and (c) the corresponding EDX elemental maps taken from (a), (d) 25% rolled sample, (e) and (f) EDX elemental maps taken from (d), (g) 50% rolled sample, (h) and (i) EDX elemental maps taken from (g).

The obtained martensitic lath boundary maps from all samples studied herein confirmed the highest fraction of LAGBs for the 50% rolled samples. While the grain boundaries are considered as fast diffusion paths, the LAGBs have low energy and can hinder the fast diffusion [22]. Hence, a high fraction of LAGBs in the structure can keep the grain boundary diffusivity very close to the bulk diffusivity, leading to the formation of a more uniform oxide layer, and consequently enhancing the corrosion performance. Such contribution from LAGBs was not a determining factor in dictating the electrochemical response of the rolled samples studied herein, considering

their impaired corrosion properties as compared to the non-deformed base metal. On the other hand, it is known that the high-density close-packed crystal planes that are aligned with the exposed surface of the sample to a corrosive electrolyte possess better corrosion properties and better passivation and re-passivation characteristics [25]. The close-packed plane for the metal with BCC crystal structure is {110} plane. Among the studied samples herein, the base metal sample revealed the strongest {110} texture aligned with the TD (Figure. 3. 6a). This can be counted as a contributing factor towards better corrosion performance of the base metal relative to the rolled samples. However, the PF maps taken from this family of planes for all samples did not reveal a high intensity (strong texture component) or a significant difference in the intensity of the pole figures between the base metal and rolled samples. Therefore, the impact from the close-packed crystal planes cannot also be a dominant factor in controlling the corrosion behavior of the cold-rolled AISI420 MSS. Overall, the contributions from grain boundaries and grain misorientation (texture) were found not to be determining factors in dictating the electrochemical response of the rolled samples studied herein, as compared to the side effects stemming from the carbide particles' evolutions through the rolling process, further discussed in section 4.2.

On the other hand, it was noted that the dislocation density of the samples increased significantly after the rolling process, as reported in Table 3. 2. According to the Mott-Schottky analysis results, the doping concentration in the MSS 420 stainless steel increases as the rolling level increases. Higher doping concentration is known to increase the susceptibility of the passive film to localized corrosion attack [68]. The point defect model (PDM) suggests that the cation vacancies are generally formed at the interface of film and solution, while cation interstitials and oxygen vacancies are mostly generated at the metal/film interface and can lead to excessive growth

and break down of the passive layer [69]. Strain-induced dislocations can also participate in the passive layer formation at the metal/film interface as per the following reaction[68]:

$$M + T \rightarrow M + \frac{x}{2}V_{\ddot{O}} + xe'$$ (7)

where M represents the material (stainless steel in this study), $V_{\ddot{O}}$ is oxygen vacancy, e' is the transferred electron, and T is defined as the strain-induced dislocation existing at the metal/passive film interface. Based on this reaction, one mole of strain-induced dislocations (dislocation produced by rolling process here) can generate $\frac{x}{2}$ mole of oxygen vacancies at the passive film [70,71]. Therefore, the higher dislocation densities associated with the rolled samples can induce more oxygen vacancies in the passive film, deteriorating its protective nature and corrosion resistance [70]. In addition, the absorbed chloride ions through the passive film can replace the oxygen vacancies by generating cation vacancies [72]. Further diffusion of cation vacancies into the passive film can be accelerated by the formed dislocations during the rolling process, further facilitating the breakdown of the passive layer [72].

For stainless steels, a clear understanding of the corrosion mechanism is closely related to the passive film stability. In this context, it is reported that the integrity and thickness of the passive film can be affected adversely by a deformation process, leading to a reduced corrosion potential [22,51]. Such a detrimental effect of the applied plastic deformation on the electrochemical stability of the surface is consistent with the results presented herein. The deformed samples showed a lower pitting corrosion potential and lower passive layer and charge-transfer resistance, which is plausibly attributed to the decreased thickness of the passive film. The steady-state passive film thickness (L_{ss}) can be estimated based on the measured EIS data and using the parallel plate expression [73,74]:

$$L_{ss} = \frac{\varepsilon\varepsilon_0 A}{C_f} \tag{8}$$

where ε is the dielectric constant of the passive film (assumed to be equal to 15.6 for Cr_2O_3) [75], ε_0 is the vacuum permittivity (8.854×10^{-14} F cm^{-1}), C_f is the pure passive film capacitance, and A is the surface area of the corroded sample. The value for the C_f can be calculated using:

$$C_f = \frac{(Y_0 R_{ct})^{1/n}}{R_{ct}} \tag{9}$$

where Y_0 is the *CPE* constant, R_{ct} is the charge transfer resistance at the interface between the matrix and passive film (refers to the R_2 values in Table 3. 3), and n is the exponent related to pure passive film capacitance (n_1 values in Table 3. 3) [76–78]. The obtained thickness data and C_f values for samples are presented in Table 3. 6. It is shown that the thickness of the passive layer decreases by increasing the rolling percentage, indicating the lower stability of the passive layer at both immersion times of 1 h and 120 h, which is in good agreement with other electrochemical testing results obtained in this study. It should be noted that a significant decrease was observed in the thickness of the passive film for the samples immersed for a longer time (120 h), correlated to the gradual dissolution of the passive film into the solution over time.

Table 3. 6. The passive layer thickness (L_{ss}) and its pure capacitance for the base metal and the deformed samples.

Immersion Time (h)	Sample	C_f ($\Omega^{-1}cm^{-2}s^n$)	L_{ss} (nm)
1	Base metal	1.23×10^{-5}	67.1
	25% rolled sample	4.83×10^{-6}	57.2
	50% rolled sample	2.75×10^{-5}	38.2
120	Base metal	4.62×10^{-5}	18.0
	25% rolled sample	5.06×10^{-5}	5.4
	50% rolled sample	2.93×10^{-5}	3.5

4.2.Effect of precipitation on the corrosion behavior

Several studies on the corrosion behavior of AISI 420 MSS reported that the martensitic matrix in this alloy is electrochemically less noble than the existing inter-lath carbide precipitates, leading to the high susceptibility of the matrix-carbides interface to pitting corrosion attack [34,79]. Consequently, the potential difference between the interface and the carbide can provoke micro-galvanic coupling in which the carbide acts as the cathode and the interface as the anode [80]. Therefore, the pits are highly accumulated in the areas adjacent to the regions where a high concentration of chromium carbides (chromium-rich zone) form. Generally, large carbide particles are surrounded by chromium-depleted zones (along their interface with the matrix), where are highly susceptible to localized pitting corrosion and exhibit high anodic activities.

As discussed earlier, a high fraction of fragmented brittle carbide particles were detected in the rolled samples. The applied severe plastic deformation during rolling can break the coarser carbide particles into the finer precipitates. Breakage of a coarse carbide precipitate surrounded by an expanded sensitized region into smaller precipitates also splits the large sensitized region into smaller sensitized zones, encompassing the finer precipitates. As a consequence, the number of locations susceptible to meta-stable/stable pitting on the surface increases. However, the galvanic coupling is not only affected by the magnitude of the potential difference between the anode and the cathode, but also the distance between the anodic and cathodic sites can affect the severity of the corrosion drastically. Cold deformation can lead to the breakage of the carbides and decrease the distance between the precipitates, provoking the micro-galvanic coupling effect at higher deformation levels [81]. Figures. 3. 12a and 12c show the fragmented carbide particles in the 25% and 50% rolled samples, respectively, and Figures. 3. 12b and 12d characterize the chromium concentration change along the fragmented regions using the EDX line scanning analysis

technique. It was observed that the chromium concentration drops drastically in the regions between the fragmented precipitates. The region between the fractured precipitates with low chromium concentration acts as a local anode and intensifies the galvanic coupling effect, causing the increased susceptibility to corrosion in the rolled samples. While the pitting initiates near the martensitic lath boundaries containing large carbide precipitates in the base metal sample (Figure. 3. 11a), in the rolled samples, the Cr-depleted regions between the fragmented carbides further provoke the pits initiation (Figures. 3. 11b and 11c). As the number of fragmented regions increases by increasing the degree of rolling-induced plastic deformation, the pitting susceptibility escalates; resulting in the lowest corrosion resistance for the 50% rolled sample.
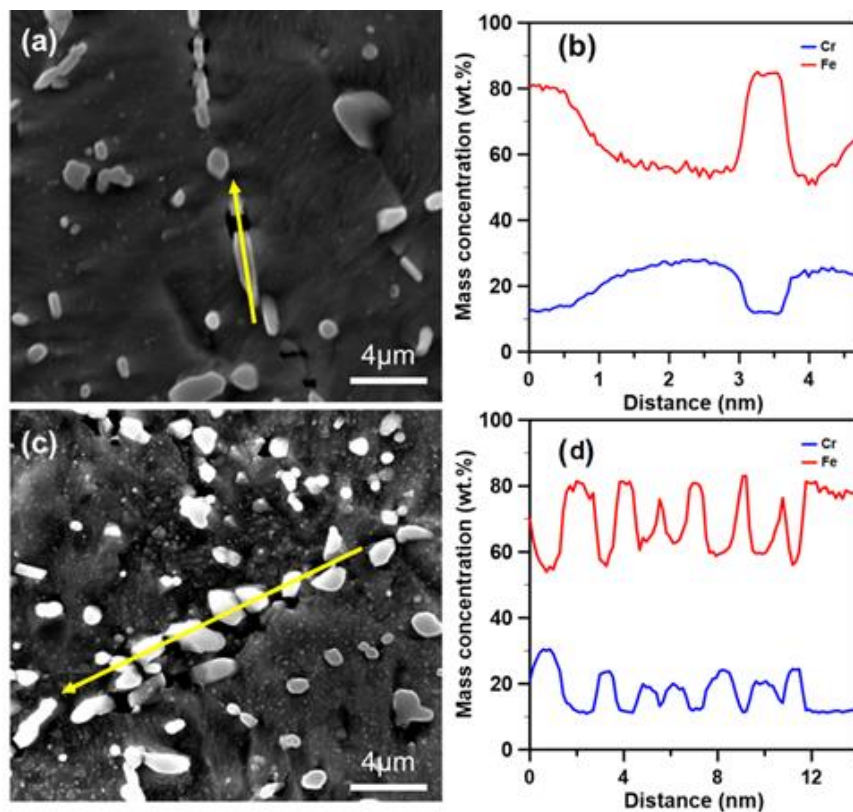
Figure 3. 12. The SEM micrographs taken from the (a) 25% rolled sample and (c) 50% rolled samples, the EDX line scanning results along the yellow arrow (b) shown in (a), and (d) shown in (c) across the fragmented precipitates.

5. Conclusions

In this study, the effect of cold rolling-induced plastic deformation on the microstructure and corrosion behavior of AISI 420 martensitic stainless steel was investigated. Two groups of deformed samples with the thickness reduction of 25% and 50% were prepared and their microstructure and corrosion properties were compared with the non-deformed base plate. The main conclusions drawn from this study are as follows:

1. From the microstructure point of view, the cold-rolling process led to a slight refinement in lath size (6.44 µm, 3.67 µm, and 1.95 µm as the average lath size of the base plate, the 25% and 50% deformed samples, respectively), the fragmentation of pre-existing large carbide precipitates (in particular in the 50% rolled sample), and increased fraction of LAGBs. The fraction of MAGBs was found to reduce from the 25% to 50% rolled sample.

2. The applied cold deformation also resulted in the formation of a stronger {111}<112> texture component aligned with the ND in the 50% rolled sample.

3. The polarization results confirmed the decrease of the corrosion potential, and the pitting potential values by increasing the deformation level of the samples, suggesting the reduced stability of the protective passive film on the deformed samples against both the uniform and pitting corrosion attacks.

4. Likewise, the EIS results revealed the formation of a more stable passive film on the surface of the base metal as compared to the deformed samples.

5. The Mott-Schottky analysis also indicated the increase of the passive film's donor density by increasing the rolling-induced deformation percentage in the alloy, representing easier adsorption of chloride ions, leading to the reduced stability of the passive film.

6. Among all different contributing factors to the corrosion performance of the alloy, the precipitates' fragmentation resulted from the cold deformation was found to be the controlling factor. The higher fraction of fragmented precipitates surrounded by an expanded Cr-depleted region provoked the micro-galvanic coupling effect at higher deformation levels, and caused the deterioration of the alloy's corrosion performance by increasing the deformation level.

References

[1]   C.-O. Olsson, D. Landolt, Passive films on stainless steels—chemistry, structure and growth, Electrochim. Acta. 48 (2003) 1093–1104.
[2]   C.J. Scheuer, F.A.A. Possoli, P.C. Borges, R.P. Cardoso, S.F. Brunatto, AISI 420 martensitic stainless steel corrosion resistance enhancement by low-temperature plasma carburizing, Electrochim. Acta. 317 (2019) 70–82.
[3]   S. Marcelin, N. Pébère, S. Régnier, Electrochemical characterisation of a martensitic stainless steel in a neutral chloride solution, Electrochim. Acta. 87 (2013) 32–40.
[4]   J.A.L. Dobbelaar, E.C.M. Herman, J.H.W. De Wit, The corrosion behaviour of iron-chromium alloys in 0.5 M sulphuric acid, Corros. Sci. 33 (1992) 765–778.
[5]   D. Hamm, C.-O. Olsson, D. Landolt, Effect of chromium content and sweep rate on passive film growth on iron–chromium alloys studied by EQCM and XPS, Corros. Sci. 44 (2002) 1009–1025.
[6]   K. Asami, K. Hashimoto, S. Shimodaira, An XPS study of the passivity of a series of iron—chromium alloys in sulphuric acid, Corros. Sci. 18 (1978) 151–160.
[7]   H. Zhang, Y.L. Zhao, Z.D. Jiang, Effects of temperature on the corrosion behavior of 13Cr martensitic stainless steel during exposure to CO_2 and Cl− environment, Mater. Lett. 59 (2005) 3370–3374.
[8]   A. Dalmau, C. Richard, A. Igual–Muñoz, Degradation mechanisms in martensitic stainless steels: Wear, corrosion and tribocorrosion appraisal, Tribol. Int. 121 (2018) 167–179.
[9]   A. Rajasekhar, G.M. Reddy, T. Mohandas, V.S.R. Murti, Influence of austenitizing temperature on microstructure and mechanical properties of AISI 431 martensitic stainless steel electron beam welds, Mater. Des. 30 (2009) 1612–1624.
[10]   L.D. Barlow, M. Du Toit, Effect of austenitizing heat treatment on the microstructure and hardness of martensitic stainless steel AISI 420, J. Mater. Eng. Perform. 21 (2012) 1327–1336.
[11]   C.G. De Andrés, L.F. Alvarez, V. López, J.A. Jiménez, Effects of carbide-forming elements on the response to thermal treatment of the X45Cr13 martensitic stainless steel, J. Mater. Sci. 33 (1998) 4095–4100.
[12]   A. LF, C. Garcia, V. Lopez, Continuous cooling transformations in martensitic stainless steels, ISIJ Int. 34 (1994) 516–521.

[13]   A.N. Isfahany, H. Saghafian, G. Borhani, The effect of heat treatment on mechanical properties and corrosion behavior of AISI420 martensitic stainless steel, J. Alloys Compd. 509 (2011) 3931–3936.

[14]   C.T. Kwok, H.C. Man, F.T. Cheng, Cavitation erosion and pitting corrosion behaviour of laser surface-melted martensitic stainless steel UNS S42000, Surf. Coatings Technol. 126 (2000) 238–255.

[15]   L. Pan, C.T. Kwok, K.H. Lo, Enhancement in hardness and corrosion resistance of AISI 420 martensitic stainless steel via friction stir processing, Surf. Coatings Technol. 357 (2019) 339–347.

[16]   K.H. Anantha, C. Ornek, S. Ejnermark, A. Medvedeva, J. Sj, Correlative Microstructure Analysis and In Situ Corrosion Study of AISI 420 Martensitic Stainless Steel for Plastic Molding, 164 (2017) 85–93. doi:10.1149/2.0531704jes.

[17]   B. Baroux, Further insights on the pitting corrosion of stainless steels, Corros. Mech. Theory Pract. (1995) 265–309.

[18]   L. Peguet, B. Malki, B. Baroux, Influence of cold working on the pitting corrosion resistance of stainless steels, Corros. Sci. 49 (2007) 1933–1948.

[19]   B.R. Kumar, R. Singh, B. Mahato, P.K. De, N.R. Bandyopadhyay, D.K. Bhattacharya, Effect of texture on corrosion behavior of AISI 304L stainless steel, Mater. Charact. 54 (2005) 141–147.

[20]   A.A. Lebedev, V. V Kosarchuk, Influence of phase transformations on the mechanical properties of austenitic stainless steels, Int. J. Plast. 16 (2000) 749–767.

[21]   S. V Phadnis, A.K. Satpati, K.P. Muthe, J.C. Vyas, R.I. Sundaresan, Comparison of rolled and heat treated SS304 in chloride solution using electrochemical and XPS techniques, Corros. Sci. 45 (2003) 2467–2483.

[22]   H. Luo, X. Wang, C. Dong, K. Xiao, X. Li, Effect of cold deformation on the corrosion behaviour of UNS S31803 duplex stainless steel in simulated concrete pore solution, Corros. Sci. 124 (2017) 178–192.

[23]   H. Luo, H. Su, G. Ying, C. Dong, X. Li, Effect of cold deformation on the electrochemical behaviour of 304L stainless steel in contaminated sulfuric acid environment, Appl. Surf. Sci. 425 (2017) 628–638.

[24]   C.L. McBee, J. Kruger, Nature of passive films on iron-chromium alloys, Electrochim. Acta. 17 (1972) 1337–1341.

[25]   S.S. Chouthai, K. Elayaperumal, Texture dependence of corrosion of mild steel after cold rolling, Br. Corros. J. 11 (1976) 40–43.

[26]   A. Ben Rhouma, H. Sidhom, C. Braham, J. Lédion, M.E. Fitzpatrick, Effects of surface preparation on pitting resistance, residual stress, and stress corrosion cracking in austenitic stainless steels, J. Mater. Eng. Perform. 10 (2001) 507–514.

[27]   P.E. Manning, D.J. Duquette, W.F. Savage, The effect of test method and surface condition on pitting potential of single and duplex phase 304L stainless steel, Corrosion. 35 (1979) 151–157.

[28]   S. Kobayashi, R. Kobayashi, T. Watanabe, Control of grain boundary connectivity based on fractal analysis for improvement of intergranular corrosion resistance in SUS316L austenitic stainless steel, Acta Mater. 102 (2016) 397–405.

[29]   M. Shimada, H. Kokawa, Z.J. Wang, Y.S. Sato, I. Karibe, Optimization of grain boundary character distribution for intergranular corrosion resistant 304 stainless steel by twin-induced grain boundary engineering, Acta Mater. 50 (2002) 2331–2341.

[30]   X. Ren, K. Sridharan, T.R. Allen, Effect of grain refinement on corrosion of ferritic–martensitic steels in supercritical water environment, Mater. Corros. 61 (2010) 748–755.

[31]   L. Tan, X. Ren, K. Sridharan, T.R. Allen, Corrosion behavior of Ni-base alloys for advanced high temperature water-cooled nuclear plants, Corros. Sci. 50 (2008) 3056–3062.

[32]   L. Zhang, J.A. Szpunar, R. Basu, J. Dong, M. Zhang, Influence of cold deformation on the corrosion behavior of Ni–Fe–Cr alloy 028, J. Alloys Compd. 616 (2014) 235–242.

[33]   E.A. West, G.S. Was, IGSCC of grain boundary engineered 316L and 690 in supercritical water, J. Nucl. Mater. 392 (2009) 264–271.

[34] C. Örnek, D.L. Engelberg, An experimental investigation into strain and stress partitioning of duplex stainless steel using digital image correlation, X-ray diffraction and scanning Kelvin probe force microscopy, J. Strain Anal. Eng. Des. 51 (2016) 207–219.

[35] C. Örnek, D.L. Engelberg, SKPFM measured Volta potential correlated with strain localisation in microstructure to understand corrosion susceptibility of cold-rolled grade 2205 duplex stainless steel, Corros. Sci. 99 (2015) 164–171.

[36] D. Lindell, R. Pettersson, Crystallographic effects in corrosion of austenitic stainless steel 316L, Mater. Corros. 66 (2015) 727–732.

[37] S. Krishnan, J. Dumbre, S. Bhatt, E.T. Akinlabi, R. Ramalingam, Effect of crystallographic orientation on the pitting corrosion resistance of laser surface melted AISI 304L austenitic stainless steel, (2013).

[38] R. Singh, I. Chattoraj, A. Kumar, B. Ravikumar, P.K. Dey, The effects of cold working on sensitization and intergranular corrosion behavior of AISI 304 stainless steel, Metall. Mater. Trans. A. 34 (2003) 2441–2447.

[39] R.A. Varin, J. Bystrzycki, A. Calka, Effect of annealing on the microstructure, ordering and microhardness of ball milled cubic (L12) titanium trialuminide intermetallic powder, Intermetallics. 7 (1999) 785–796.

[40] A.A. Al-Ghamdi, S.A. Khan, A. Nagat, M.S. Abd El-Sadek, Synthesis and optical characterization of nanocrystalline CdTe thin films, Opt. Laser Technol. 42 (2010) 1181–1186.

[41] M. Dongol, A. El-Denglawey, M.S. Abd El Sadek, I.S. Yahia, Thermal annealing effect on the structural and the optical properties of Nano CdTe films, Optik (Stuttg). 126 (2015) 1352–1357.

[42] M.R. Jandaghi, H. Pouraliakbar, Elucidating the microscopic origin of electrochemical corrosion and electrical conductivity by lattice response to severe plastic deformation in Al-Mn-Si alloy, Mater. Res. Bull. 108 (2018) 195–206.

[43] M. Dongol, A. El-Denglawey, A.F. Elhady, A.A. Abuelwafa, Structural properties of nano 5, 10, 15, 20-Tetraphenyl-21H, 23H-porphine nickel (II) thin films, Curr. Appl. Phys. 12 (2012) 1334–1339.

[44] T. Shintani, Y. Murata, Evaluation of the dislocation density and dislocation character in cold rolled Type 304 steel determined by profile analysis of X-ray diffraction, Acta Mater. 59 (2011) 4314–4322.

[45] S. Baldo, I. Mészáros, Effect of cold rolling on microstructure and magnetic properties in a metastable lean duplex stainless steel, J. Mater. Sci. 45 (2010) 5339–5346.

[46] R. Ueji, N. Tsuji, Y. Minamino, Y. Koizumi, Ultragrain refinement of plain low carbon steel by cold-rolling and annealing of martensite, Acta Mater. 50 (2002) 4177–4189.

[47] S.S.M. Tavares, M.R. Da Silva, J.M. Pardal, H.F.G. Abreu, A.M. Gomes, Microstructural changes produced by plastic deformation in the UNS S31803 duplex stainless steel, J. Mater. Process. Technol. 180 (2006) 318–322.

[48] S. Li, I.J. Beyerlein, M.A.M. Bourke, Texture formation during equal channel angular extrusion of fcc and bcc materials: comparison with simple shear, Mater. Sci. Eng. A. 394 (2005) 66–77.

[49] D. Raabe, K. Lücke, Rolling and annealing textures of bcc metals, in: Mater. Sci. Forum, Trans Tech Publ, 1994: pp. 597–610.

[50] S. Suwas, R.K. Ray, Crystallographic texture of materials, Springer, 2014.

[51] D. Song, A. Ma, W. Sun, J. Jiang, J. Jiang, D. Yang, G. Guo, Improved corrosion resistance in simulated concrete pore solution of surface nanocrystallized rebar fabricated by wire-brushing, Corros. Sci. 82 (2014) 437–441.

[52] M. Serdar, L.V. Žulj, D. Bjegović, Long-term corrosion behaviour of stainless reinforcing steel in mortar exposed to chloride environment, Corros. Sci. 69 (2013) 149–157.

[53] M. Talha, C.K. Behera, S. Kumar, O. Pal, G. Singh, O.P. Sinha, Long term and electrochemical corrosion investigation of cold worked AISI 316L and 316LVM stainless steels in simulated body fluid, RSC Adv. 4 (2014) 13340–13349.

[54] L. Freire, M.J. Carmezim, M.G.S. al Ferreira, M.F. Montemor, The passive behaviour of AISI 316

in alkaline media and the effect of pH: A combined electrochemical and analytical study, Electrochim. Acta. 55 (2010) 6174–6181.

[55]   D. Wallinder, J. Pan, C. Leygraf, A. Delblanc-Bauer, EIS and XPS study of surface modification of 316LVM stainless steel after passivation, Corros. Sci. 41 (1998) 275–289.

[56]   M.J. Carmezim, A.M. Simoes, M.F. Montemor, M.D.C. Belo, Capacitance behaviour of passive films on ferritic and austenitic stainless steel, Corros. Sci. 47 (2005) 581–591.

[57]   L. V Taveira, M.F. Montemor, M.D.C. Belo, M.G. Ferreira, L.F.P. Dick, Influence of incorporated Mo and Nb on the Mott–Schottky behaviour of anodic films formed on AISI 304L, Corros. Sci. 52 (2010) 2813–2818.

[58]   S.R. Morrison, Electrochemistry at semiconductor and oxidized metal electrodes, (1980).

[59]   S. Ningshen, U.K. Mudali, V.K. Mittal, H.S. Khatak, Semiconducting and passive film properties of nitrogen-containing type 316LN stainless steels, Corros. Sci. 49 (2007) 481–496.

[60]   N.B. Hakiki, S. Boudin, B. Rondot, M.D.C. Belo, The electronic structure of passive films formed on stainless steels, Corros. Sci. 37 (1995) 1809–1822.

[61]   H. Tsuchiya, S. Fujimoto, O. Chihara, T. Shibata, Semiconductive behavior of passive films formed on pure Cr and Fe–Cr alloys in sulfuric acid solution, Electrochim. Acta. 47 (2002) 4357–4366.

[62]   L. Hamadou, A. Kadri, N. Benbrahim, Impedance investigation of thermally formed oxide films on AISI 304L stainless steel, Corros. Sci. 52 (2010) 859–864.

[63]   K. Morshed-Behbahani, P. Najafisayar, M. Pakshir, M. Shahsavari, An electrochemical study on the effect of stabilization and sensitization heat treatments on the intergranular corrosion behaviour of AISI 321H austenitic stainless steel, Corros. Sci. 138 (2018) 28–41.

[64]   N.E. Hakiki, M.F. Montemor, M.G.S. Ferreira, M. da Cunha Belo, Semiconducting properties of thermally grown oxide films on AISI 304 stainless steel, Corros. Sci. 42 (2000) 687–702.

[65]   J. Amri, T. Souier, B. Malki, B. Baroux, Effect of the final annealing of cold rolled stainless steels sheets on the electronic properties and pit nucleation resistance of passive films, Corros. Sci. 50 (2008) 431–435.

[66]   D.D. Macdonald, The point defect model for the passive state, J. Electrochem. Soc. 139 (1992) 3434–3449.

[67]   N. Chandra, D.K. Singh, M. Sharma, R.K. Upadhyay, S.S. Amritphale, S.K. Sanghi, Synthesis and characterization of nano-sized zirconia powder synthesized by single emulsion-assisted direct precipitation, J. Colloid Interface Sci. 342 (2010) 327–332.

[68]   J.-B. Lee, S.-I. Yoon, Effect of nitrogen alloying on the semiconducting properties of passive films and metastable pitting susceptibility of 316L and 316LN stainless steels, Mater. Chem. Phys. 122 (2010) 194–199.

[69]   D.D. Macdonald, A. Sun, An electrochemical impedance spectroscopic study of the passive state on Alloy-22, Electrochim. Acta. 51 (2006) 1767–1779.

[70]   T. Yamamoto, K. Fushimi, S. Miura, H. Konno, Influence of substrate dislocation on passivation of pure iron in pH 8.4 borate buffer solution, J. Electrochem. Soc. 157 (2010) C231.

[71]   A. Nazarov, D. Thierry, Application of Volta potential mapping to determine metal surface defects, Electrochim. Acta. 52 (2007) 7689–7696.

[72]   J. Lv, W. Guo, T. Liang, The effect of pre-deformation on corrosion resistance of the passive film formed on 2205 duplex stainless steel, J. Alloys Compd. 686 (2016) 176–183.

[73]   D. Kong, A. Xu, C. Dong, F. Mao, K. Xiao, X. Li, D.D. Macdonald, Electrochemical investigation and ab initio computation of passive film properties on copper in anaerobic sulphide solutions, Corros. Sci. 116 (2017) 34–43.

[74]   E. Sikora, D.D. Macdonald, Defining the passive state, Solid State Ionics. 94 (1997) 141–150.

[75]   A. Fattah-Alhosseini, M.A. Golozar, A. Saatchi, K. Raeissi, Effect of solution concentration on semiconducting properties of passive films formed on austenitic stainless steels, Corros. Sci. 52 (2010) 205–209.

[76]   I. Nicic, D.D. Macdonald, The passivity of Type 316L stainless steel in borate buffer solution, J.

Nucl. Mater. 379 (2008) 54–58.

[77]   Z. Feng, X. Cheng, C. Dong, L. Xu, X. Li, Passivity of 316L stainless steel in borate buffer solution studied by Mott–Schottky analysis, atomic absorption spectrometry and X-ray photoelectron spectroscopy, Corros. Sci. 52 (2010) 3646–3653.

[78]   D. Kong, X. Ni, C. Dong, X. Lei, L. Zhang, C. Man, J. Yao, X. Cheng, X. Li, Bio-functional and anti-corrosive 3D printing 316L stainless steel fabricated by selective laser melting, Mater. Des. 152 (2018) 88–101.

[79]   C. Oernek, D.L. Engelberg, Correlative EBSD and SKPFM characterisation of microstructure development to assist determination of corrosion propensity in grade 2205 duplex stainless steel, J. Mater. Sci. 51 (2016) 1931–1948.

[80]   F. Navai, Effects of tensile and compressive stresses on the passive layers formed on a type 302 stainless steel in a normal sulphuric acid bath, J. Mater. Sci. 30 (1995) 1166–1172.

[81]   C. HAHIN, R.M. STOSS, B.H. NELSON, P.J. REUCROFT, Effect of cold work on the corrosion resistance of nonsensitized austenitic stainless steels in nitric acid, Corrosion. 32 (1976) 229–238.

Chapter 4

On Microstructure, Crystallographic Orientation, and Corrosion Properties of Wire Arc Additive Manufactured 420 Martensitic Stainless Steel: Effect of the Inter-layer Temperature [3]

Preface

The original version of this manuscript has already been published in the Journal of Additive Manufacturing. I am the first and the corresponding author of the current work. In this chapter, I, along with my colleagues, Dr. Ali Nasiri, Alireza Vahedi Nemani, Mahya Ghaffari, and Jonas Lunde, investigated the impact of interlayer deposition temperature on the microstructure, crystallographic orientation, and corrosion performance of the 420 Martensitic stainless steel, fabricated by the wire arc additive manufacturing. I was responsible for preparing methodology, experimental testing, result gathering, and drafting of the original manuscript. Subsequently, I revised the paper based on my colleagues' initial comments and the peer-review process. The co-authors contributed to the conceptualizing, project administration, supervision, and review & editing of the manuscript.

---

[3] Salahi, Salar, Alireza Vahedi Nemani, Mahya Ghaffari, Jonas Lunde, and Ali Nasiri. "On microstructure, crystallographic orientation, and corrosion properties of wire arc additive manufactured 420 martensitic stainless steel: Effect of the inter-layer temperature." *Additive Manufacturing* 46 (2021): 102157.

Abstract

In this study, the effects of inter-layer temperature variation on the microstructure, crystallographic orientation, and corrosion performance of a multilayer single-pass wall-shaped 420 stainless steel part fabricated using wire arc additive manufacturing (WAAM) were investigated. The microstructural evolution and texture formation after fabrication were analyzed using scanning electron microscopy (SEM), X-ray diffraction (XRD), and electron backscatter diffraction (EBSD) analysis. The microstructural characterization revealed the formation of a martensitic matrix with delta ferrite and retained austenite as secondary phases as a result of complex thermal history experienced by deposited layers through subsequent reheating and cooling during the fabrication process. The samples deposited at the inter-layer temperature of 200°C exhibited anisotropic crystallographic behavior, while a relatively isotropic texture was observed for the samples fabricated at the inter-layer temperature of 25°C. To characterize the electrochemical response of the fabricated samples, open circuit potential (OCP), potentiodynamic polarization (PDP), and electrochemical impedance spectroscopy (EIS) tests were conducted on the prepared samples in naturally aerated 3.5 wt.% NaCl electrolyte at ambient temperature. The volume fraction of the retained austenite phase was found to increase by increasing the inter-layer temperature from 25°C to 200°C, contributed to the enhanced corrosion performance of the fabricated wall. Localized corrosion attacks were primarily detected adjacent to the delta ferrite phase, regardless of the implemented interlayer temperature during the fabrication process.

1. Introduction

The emerging additive manufacturing (AM) technology, primarily invented by Charles W. Hull [1] and applied for the manufacturing of rapid prototypes (RP) in 1980s, has been widely adopted in the last decade for manufacturing of metallic components with intricate designs [2]. As compared to the conventional manufacturing technologies, AM implements a layer by layer deposition strategy, providing higher accuracy in the fabrication of near-net-shape products [2]. In wire arc additive manufacturing (WAAM) technology, which is a direct energy deposition (DED) process, an electric arc or plasma is used as the heat source and a wire as the feedstock material. WAAM hardware commonly includes a welding torch mounted on a multi-axis robotic arm or on a CNC system, a welding power source, and its associated wire feeding system. As the wire is fed into the electric arc at a controlled rate, it melts and is deposited on either the base plate, forming the first deposited layer, or on the previously solidified layers [3]. Compared to the other beam-based AM processes, the WAAM offers higher deposition rate (up to 8 kg/h), lower maintenance cost, accelerated lead time, and is capable of producing larger parts [4–6]. However, WAAM parts are exposed to a complex thermal treatment during the deposition process, altering localized metallurgical characteristics of the part ascribed to (*i*) frequent heating and cooling of the part, (*ii*) directional heat dissipation, (*iii*) high-temperature gradients, and (*iv*) re-melting of the previously deposited layers. Hence, the fabricated WAAM parts experience highly localized microstructural characteristics, affecting their mechanical performance and corrosion behavior [5,7–9].

As the most frequently used materials in modern industry, ferrous alloys and in particular stainless steels were also adopted as the feedstock materials for the fabrication of parts through the WAAM. Hejripour *et al.* [10] used the WAAM process to build 2209 duplex stainless parts with

different geometries, *i.e.*, tube and wall, and developed a thermal model, describing the correlation between the calculated cooling rates and the formation of different phases in the fabricated parts.

In the case of martensitic stainless steels (MSSs), there are a few studies available in the literature that characterize the microstructure and mechanical properties of the WAAM fabricated parts. Ge *et al*. [11] studied the microstructural evolution and micro-indentation properties of a WAAM 2Cr13 part and reported the formation of random crystallographic orientation in the middle region of the part and a slight fiber texture within the top layers. Alam *et al.* [12] reported anisotropic mechanical properties in the longitudinal and transverse directions for the laser-cladded and additively manufactured 420 MSS and concluded that the anisotropic issue can be resolved by applying a post-cladding heat treatment for one-hour at 565 °C.

Despite the existing a few studies on the microstructure and mechanical properties of WAAM fabricated MSSs [11,13,14], there is no study in the literature investigating the corrosion response of the fabricated MSS components. A combination of electrochemical and microstructural factors govern the localized corrosion attack (pitting corrosion) in this family of stainless steels [15]. Therefore, it is vital to understand the process-induced microstructural features of the MSSs, in order to evaluate the corrosion response and be able to predict their electrochemical stability [15]. The conventional fabrication method of MSSs consists of annealing of wrought alloy, followed by applying warm or cold deformation steps, and subsequently exposing the parts to hardening and tempering heat treatments that generate carbide particles in a ferritic/martensitic matrix [16]. The origin of the formed precipitates is highly affected by the applied heat treatment cycle's parameters. While the tempering leads to the formation of fine dissolved carbide precipitates, the annealing can form localized large spherical carbides in the microstructure [16]. Additionally, aforementioned fabrication method of the MSSs generally lead to the formation of residual delta ferrite and

unwanted retained austenite due to the applied quenching cycle subsequently after the austenitization process [16,17]. It is well stated that the high-volume fraction of the retained austenite can enhance the corrosion response and can lead to lower susceptibility to pitting corrosion for the MSSs [18]. On the other hand, the presence of delta ferrite in the microstructure with a high concentration of chromium can lead to the formation of chromium depleted zones, consequently causing susceptibility to localized corrosion [19].

Although corrosion performance of MSS is highly affected by the formation of micro-constituents during the manufacturing process, other microstructural features, such as crystallographic orientation and texture, can also play an important role in determining corrosion resistance. From the crystallographic perspective, the corrosion performance of the MSS materials is affected by two important factors. First, the formation of preferential texture during the manufacturing process, leading to the re-alignment of close-packed crystal planes with the exposed surfaces, can possibly enhance the electrochemical response by stabilizing the formed passive layer on the surface [20,21]. Second, variation in the fraction of fabrication process-induced low angle grain boundaries can directly impact the corrosion properties. Low angle grain boundaries with low energy levels can balance the diffusivity inside and along the grain boundaries [22], further contributing to the formation of more stabilized passive layer and enhanced electrochemical response of the polycrystalline materials [23].

Overall, to the best of the authors' knowledge, no study has been conducted to investigate the effects of microstructural evolution during fabrication and the crystallographic orientation on the corrosion behavior of WAAM fabricated 420 martensitic stainless steel parts. Attaining a homogenous microstructure in additively manufactured parts in the as-printed condition is essential to achieve isotropic properties. It is shown that the homogenous microstructure of WAAM parts

can be achieved through controlling the inter-layer temperature (defined as the temperature of previously deposited layer upon the deposition of the new layer), affecting the grain growth orientation and their geometry during the solidification process [24]. However, the impacts of inter-layer temperature on the crystallographic orientation, secondary phase formation, and corrosion behavior of MSSs are not known. In the present study, ER420 wire, possessing a similar chemical composition to the AISI420 martensitic stainless steel is utilized to deposit wall-shaped parts at two different inter-layer temperatures. Focusing on the aforementioned gaps, this study aims to investigate the correlations between various interlayer temperatures, microstructure, and corrosion properties in the WAAM fabricated 420 martensitic stainless steel.

2. Experimental procedure

2.1. Materials and fabrication process

In this study, ER420 feedstock wire with a diameter of 1.14 mm was used to fabricate walls of 420 stainless steel on a 20 mm thick wrought plate of 420 stainless steel through WAAM process. The chemical composition of the utilized feedstock wire and the substrate plate (AISI 420) are reported in Table 4. 1. A GMAW torch mounted on a six-axis robotic arm and an automated wire feeding system were employed to uniformly and consistently deposit the material layer-by-layer until the near-net-shape wall was fabricated. Each fabricated wall with the dimensions of 150×150×6 mm was comprised of 25 layers, deposited using a surface tension transfer (STT) mode and an all-x scanning strategy. To control the inter-layer temperature during the fabrication process, the robotic arm was equipped with a closed-loop infrared temperature measurement sensor capable of measuring the surface temperature of the underlying layer. The deposited wall with the inter-layer temperature of 25±2.5°C (denoted as the IT25 sample) was fabricated using approximately 10

minutes of dwelling time between the deposition of two consecutive layers, while for the sample with the inter-layer temperature of 200±20°C (denoted as the IT200 sample), ~ 5 min of inter-layer dwelling time was applied. To assure the accuracy of the applied IR sensor system for the interlayer temperature measurement during the fabrication process, the surface temperatures of several initial deposition points were measured using K-type high temperature thermocouple probes, and the results were compared with the acquired temperatures using the IR sensors, confirming ±10% deviations between the IR sensor measurements and the K-type probe measurements. The operating process parameters for the WAAM are summarized in Table 4. 2. The fabricated wall and a schematic illustration of the sample preparation procedure for the electrochemical testing are shown in Figure 4. 1.

Table 4. 1. The nominal chemical composition of the used material in this study (all data in wt.%).

Material	C	Cr	Mn	Si	S	P	Ni	Mo	Cu	V	Fe
ER420	0.2-0.4	11.5-13.5	0-1	0-1	0-0.04	0-0.05	0-0.6	0-0.5	0-0.4	-	Bal.
AISI420	0.15-0.46	12-14	0.3-1	0-1	0-0.04	0-0.05	-	0-0.1	-	0.3	Bal.

Table 4. 2 .The WAAM processing parameters used for the fabrication of walls in this study.

Current	Arc Voltage	Wire Feeding Rate	Scanning Rate	Argon Flow Rate	Deposition Rate
135 A	29 V	67.7 mm/s	3.6 mm/s	20 L/min	7.6 kg/h
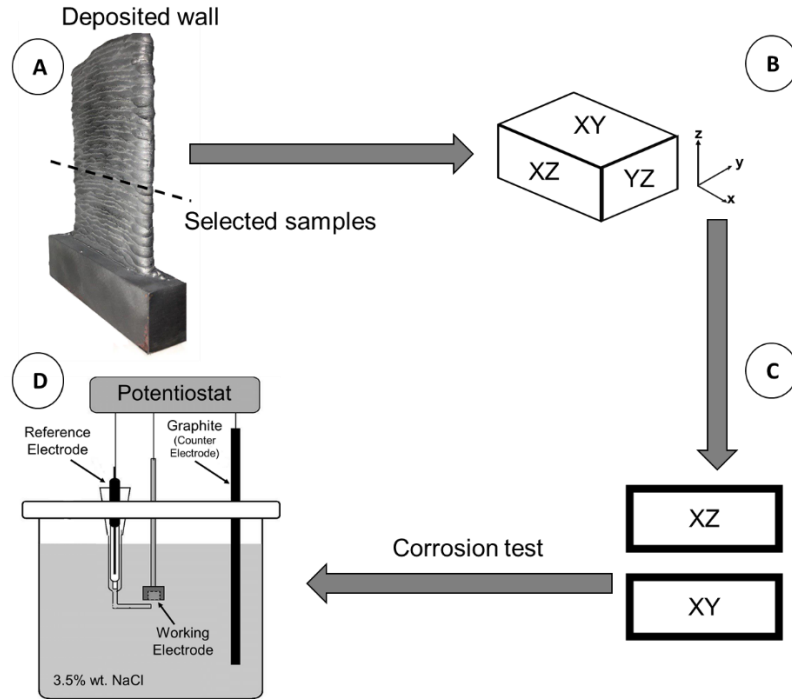
Figure 4. 1. Schematic of the sample preparation procedure for the subsequent microstructure and corrosion characterization.

2.2. Microstructural characterization

To investigate the microstructural features of the samples along the building direction (the XZ view), deposition direction (XY view), and transverse direction (YZ view), samples were cut, mounted, and prepared following recommended grinding and polishing procedures for MSS, and then etched using Villella's reagent for 20 s. Microstructural characterization of the samples were performed using a FEI MLA650F scanning electron microscope (SEM) equipped with an energy dispersive spectroscopy (EDS) detector. Electron backscatter diffraction (EBSD) analysis was also conducted using an HKL EBSD system with a tilt angle of 70° and a step size of 0.7 μm. The obtained EBSD raw data were post-processed using a Channel 5 software (from HKL Inc). To further distinguish the observed phases in the microstructure, X-ray diffraction (XRD) technique was performed using a Cu-K$_\alpha$ source at 50 kV and 30 mA.

2.3.Electrochemical analysis

The electrochemical behavior of the XZ and the XY views of the samples was examined through potentiodynamic polarization (PDP) and electrochemical impedance spectroscopy (EIS) testing. All electrochemical measurements were performed in naturally aerated 3.5 wt.% NaCl solution using an IVIUM CompactStat™ computer-controlled Potentiostat apparatus. A conventional three-electrode cell set-up, containing a saturated Ag/AgCl electrode as the reference electrode, a graphite rod as the counter electrode, and the prepared samples as the working electrode were used. As a non-invasive measurement, the open circuit potential (OCP) was also monitored for 1 h prior to each test for stabilization of the potential between the working electrode and the reference electrode. The PDP tests were conducted at the scanning rate of 0.5 mV/s in the potential range of -0.2 V up to 0.3 V versus OCP. The EIS measurements were conducted over the frequency range of 100 kHz to 10 mHz with a sinusoidal perturbation signal voltage of 10 mV. In order to ensure the reproducibility of the gathered results, The PDP and EIS experiments were repeated at least five times for each condition.

3. Results

3.1.Microstructural characterization

The three-dimensional SEM micrographs of the samples fabricated at the inter-layer temperatures of 25°C (IT25) and 200°C (IT200) are illustrated in Figures. 4. 2a and 2b, respectively, showing a columnar dendritic structure, grown along the building direction (Z-axis) parallel to the heat dissipation direction. A relatively fine lath martensitic structure (M phase) is formed in the fusion zone at both inter-layer temperatures of 25°C and 200°C, due to the fast cooling rate during solidification associated with the WAAM process [13,25,26]. Contrary to the conventionally manufactured martensitic stainless steels, a high-volume fraction of δ-ferrite (DF)

phase mainly aligned with the building direction is formed in the inter-dendritic regions, as shown in Figures. 4. 2a and 2b. The higher magnification SEM micrograph and its corresponding EDS chromium map taken from the sample fabricated at inter-layer temperature of 25°C and prepared from the side view (IT25-XZ) are shown in Figures. 4. 3a and 3b, respectively. A high volume fraction of the delta ferrite phase embedded in a martensitic matrix are observed in Figure. 4. 3a. The elemental concentration map (Figures. 4. 3b) show a high concentration of chromium in the δ-ferrite phase regions (a ferrite stabilizing element). The formation of sub-micron inter/intra-lath carbides, shown in Figure. 4. 3c and 3d, was also visible inside the martensitic matrix for both fabricated parts at inter-layer temperatures of 25°C and 200°C (IT25-XZ and IT200-XZ samples), due to the tempering effect from the deposition of subsequent layers on previously solidified tracks.

The top view of IT25 sample (IT25-XY) shows a high-volume fraction of randomly distributed delta ferrite phase having a vermicular shape morphology embedded in a martensitic matrix (Figures. 4. 2a and 3e). A comparison between Figures. 4. 3a and 3e reveal that the delta ferrite phase is relatively coarser in the side view (X-Z) as compared to that observed in the top view (X-Y).
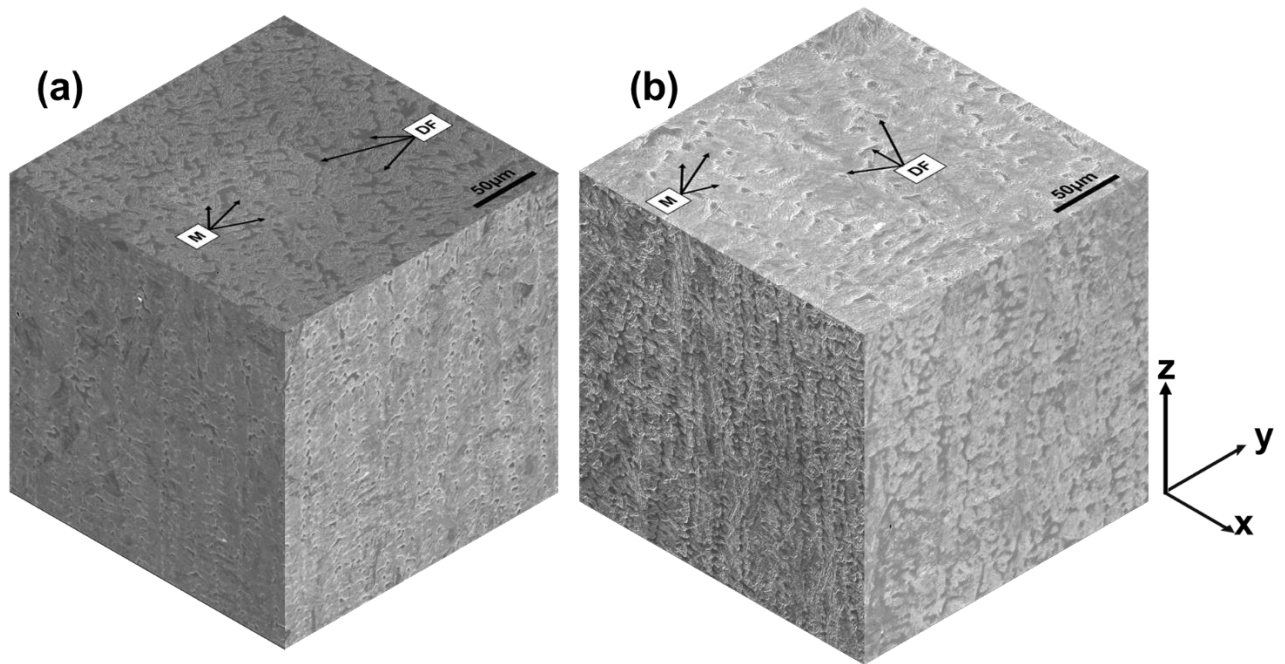
Figure 4. 2. Three-dimensional SEM micrographs taken from the WAAM-420 stainless steel samples fabricated at the inter-layer temperatures of (a) 25°C and (b) 200°C.
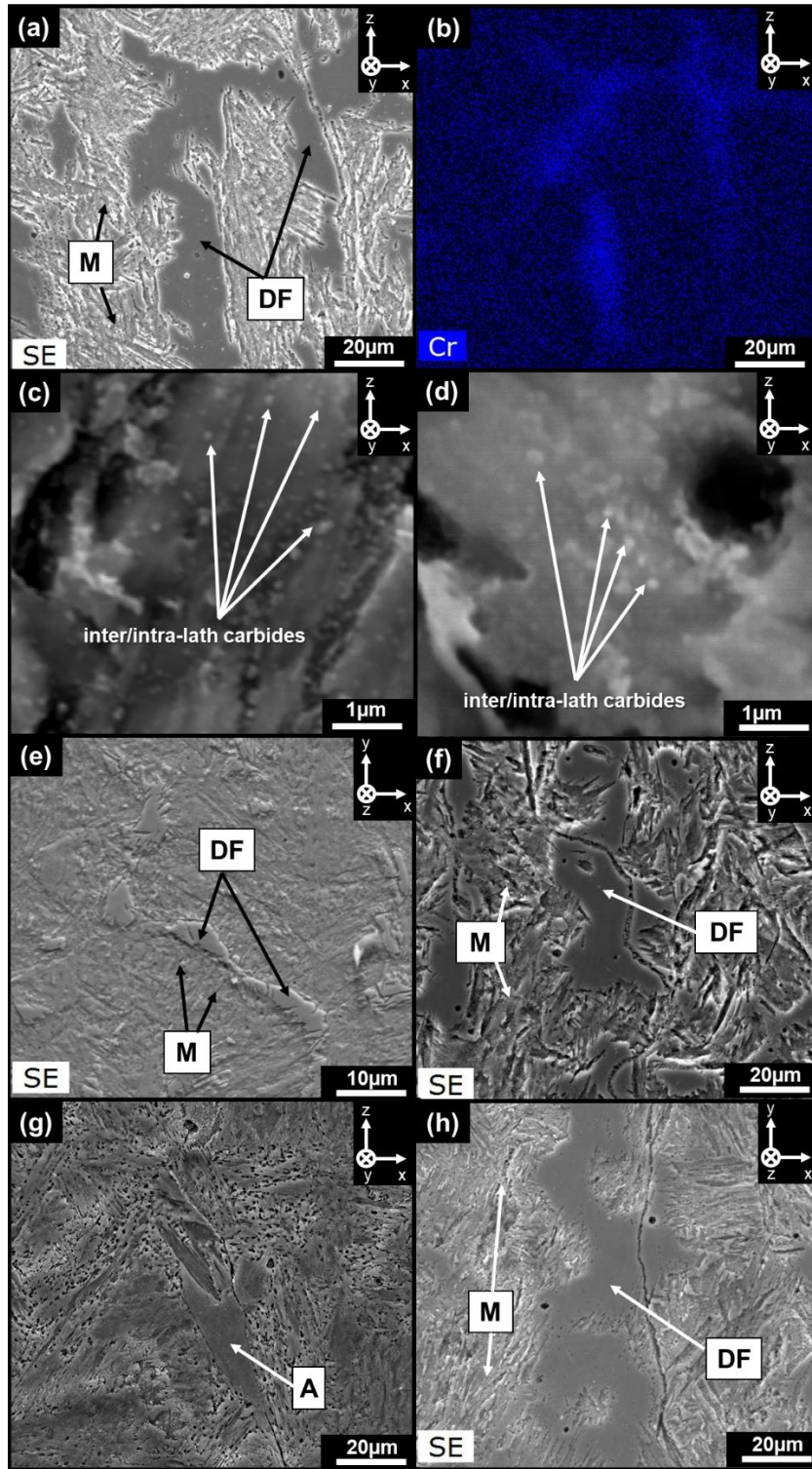
Figure 4. 3. (a) SEM micrograph of the IT25-XZ sample along with its corresponding EDS elemental maps showing (b) chromium concentration, and high magnification SEM image showing the existence of the inter/intra-lath carbides in the formed martensitic matrix in (c) IT25-XZ and (d) IT200-XZ samples, and SEM micrograph of the (e) IT25-XY and (f) IT200-XZ

samples, (g) high magnification SEM image showing the formation of retained austenite in IT200-XZ sample, and (h) SEM micrograph taken from the IT200-XY sample.

The SEM micrograph taken from the side view of the wall deposited at 200 °C inter-layer temperature (IT200-XZ) also indicates a columnar dendritic growth morphology along the building direction (Z-axis) similar to the IT25 sample, as shown in Figure. 4. 3f. Analogously, the formation of needle-shaped lath martensite as the dominant phase in the microstructure was observed at higher magnifications along with inter-dendritic δ-ferrite phase (Figure. 4. 3f).

The formation of a low volume fraction of the austenite phase was also detected in the IT200-XZ sample in tangles between martensite laths, denoted as the retained austenite (A) phase (Figure. 4. 3g). The austenite phase is formed at elevated temperatures and fully transforms into the martensite phase when exposed to high cooling rates. However, the existence of a high concentration of certain alloying elements, such as carbon or nickel, can reduce the martensite finish temperature (M_f) to temperatures lower than room temperature, causing the austenite phase stabilization at ambient temperature (known as retained austenite) [27]. A detailed description of the formation mechanism of retained austenite for the samples deposited at the inter-layer temperature of 200°C is provided in the discussion section. As shown in Figure. 4. 3h, similar to other samples, the IT200-XY sample exhibits a high fraction of randomly distributed delta ferrite islands, embedded in a martensitic matrix.

The acquired XRD spectra from the fusion zone for all samples are shown in Figure. 4. 4. Consistent with the SEM micrographs, the XRD peaks also confirmed the presence of lath martensite (M) and retained austenite (γ) phases. No peaks corresponding to the chromium carbide precipitates were identified, possibly ascribed to their lower volume fraction compared to the retained austenite and martensite phase. All samples similarly exhibit the presence of martensitic phase at (110), (200), (211), and (220) planes.

The IT200-XZ sample also exhibits a high intensity peak at 42° corresponding to (111) plane of the austenite (γ) phase, while the same peak but at lower intensity was observed for the IT25-XZ sample. The intensity of the XRD peaks can represent the volume fraction of corresponding phases. The calculated volume fraction of the austenite phase from the XRD spectra using the whole pattern fitting (WPF) procedure based on the Rietveld method [28] for the IT25-XZ and IT200-XZ samples were found to be 3% and 18%, respectively. No peaks were detected for γ (111) from the top view of both samples (IT25-XY and IT200-XY). The side view of both samples (IT25-XZ and IT200-XZ samples) also revealed a low-intensity peak of austenite phase for $(200)_\gamma$, whereas no peaks were observed for their top view counterparts.
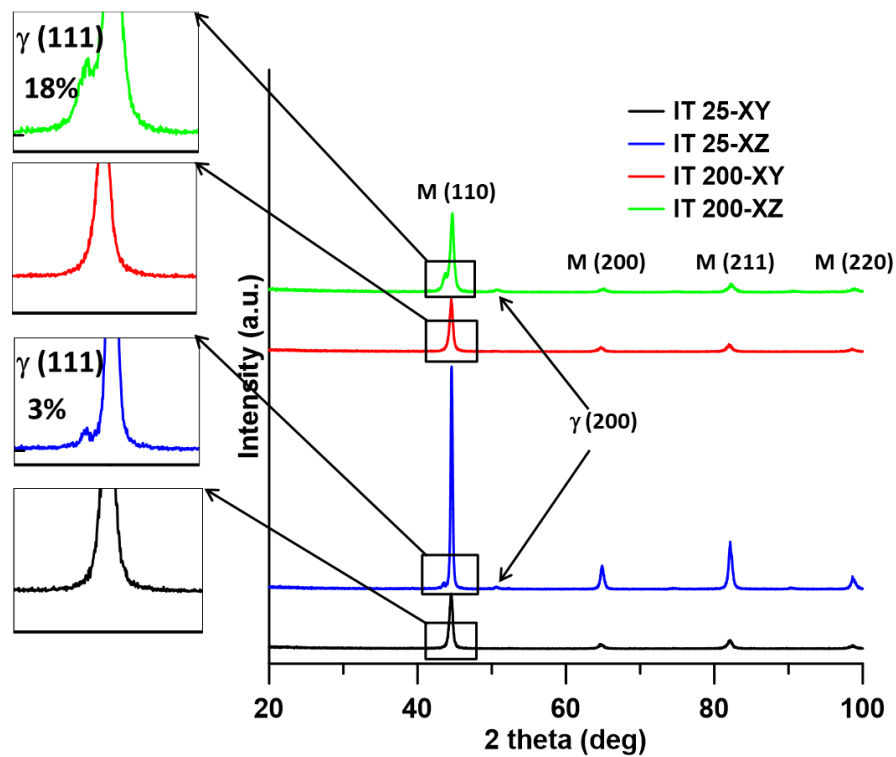
Figure 4. 4. The XRD spectra of the fabricated samples at two inter-layer temperatures of 25°C and 200°C (IT25 and IT200, respectively), acquired from the top view (XY) and the side view (XZ) of each sample.

3.2. Crystallographic orientation characterization

Figure. 4. 5 show the inverse pole Figure (IPF) maps superimposed on the lath boundaries maps for the IT25-XZ and IT25-XY samples, revealing a relatively fine lath structure (average lath size < 3 μm) for both samples. Figure. 4. 5b exhibits the phase map distribution of IT25-XZ and IT25-XY samples extracted from the EBSD results. It is observed that both IT25-XZ and IT25-XY samples possess a high fraction (97% and 99%, respectively) of body-centered cubic (BCC) crystal structure, corresponding to the martensite lath structure and delta ferrite phase. Additionally, the IT25-XZ sample contains a low volume fraction (~3%) of face-centered cubic (FCC) structure, indicating the formation of small amount of retained austenite at room temperature, consistent with the XRD spectra results (Figure. 4. 4). The FCC phase map (indicated by blue color) superimposed on the image quality (IQ) and lath boundaries maps (Figure. 4. 5c) exhibit the formation of a slight amount of austenite phase between tangles of martensite laths in IT25-XZ sample, while no retained austenite was detected in the IT25-XY sample. The crystallographic orientation of the FCC phase for the dashed rectangle area of the IT25 samples is shown in Figure 4. 5d. The hierarchical nature of the formed martensitic lath structure containing martensite lath, block, and packets is confined through the prior-austenitic grain (PAG) boundaries [29]. All austenite phases inside a PAG are expected to possess the same crystallographic orientation [29]. Accordingly, the obtained random crystallographic orientation for each detected austenite phase shown in Figure. 4. 5d indicates the randomness of the PAGs crystallographic orientation in the IT25 sample along with their relatively small size.
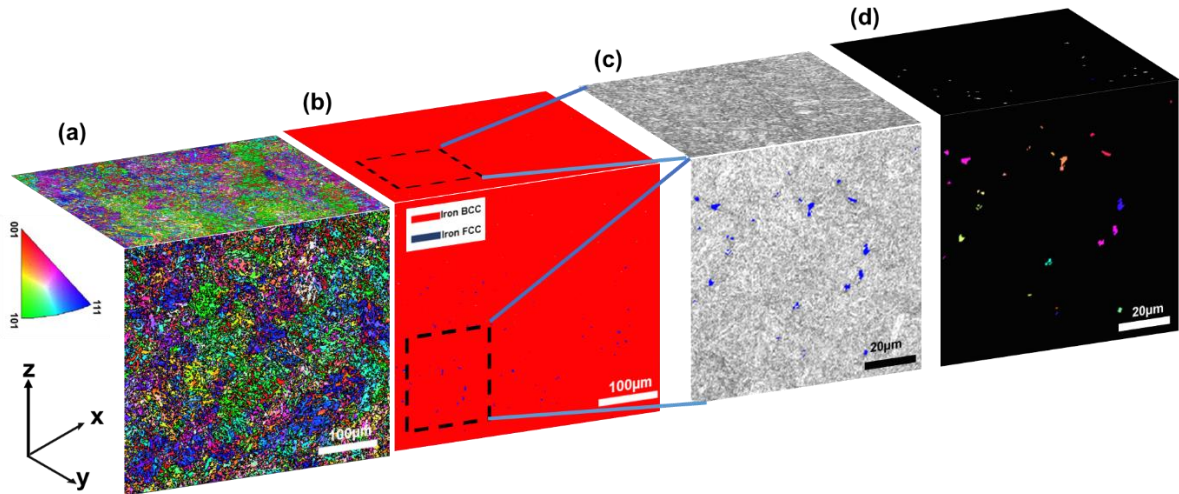
Figure 4. 5. (a) The IPF maps superimposed on the lath boundary maps (b) the EBSD phase maps: for the IT25-XY and IT25-XZ samples, (c) the IQ map superimposed on the iron-FCC phase map for the selected region, (d) the IPF map for the FCC phase of the IT25-XZ sample.

Figure. 4. 6a shows the IPF maps superimposed on the lath boundaries maps for the IT200-XZ and IT200-XY samples. Similar to the IT25 samples, IT200 samples revealed a fine lath structure with an average lath size of less than 3 μm. The average lath size was measured to be 2.24, 2.31, 2.19, and 2.13 μm, for the IT25-XY, IT25-XZ, IT200-XY, and IT200-XZ samples, respectively. Figure. 4. 6b exhibits the phase map distribution of IT200-XZ and IT200-XY samples extracted from the EBSD results. It is notable that for the IT200-XZ sample, while the BCC phase is still the dominant phase in the structure (~89 %), a relatively higher volume fraction (~11 %) of the FCC phase was detected in this sample. Contrarily, the IT25-XZ sample exhibited a lower fraction (~3 %) of the FCC phase as compared to the IT200-XZ sample. This was found to be the main noticeable difference between the microstructure of the WAAM-420 MSS fabricated with the inter-layer temperatures of 25°C and 200°C, consistent with the results obtained from the XRD analysis. The FCC phase map superimposed on the IQ and lath boundaries maps (Figure. 4. 6c) also indicates the formation of coarse retained austenite phase along the martensite laths while relatively low

fraction of fine austenite phase, similar to the one formed in the IT25-XY sample (Figure. 4. 5c) was observed in the IT200-XY sample. The crystallographic orientation of the FCC phase for the IT200 samples is shown in Figure 4. 6d. All austenite phases possessing the same crystallographic orientation were found to belong to the same PAG, defined by the white dashed lines representing the PAG boundaries (PAGBs) [29].
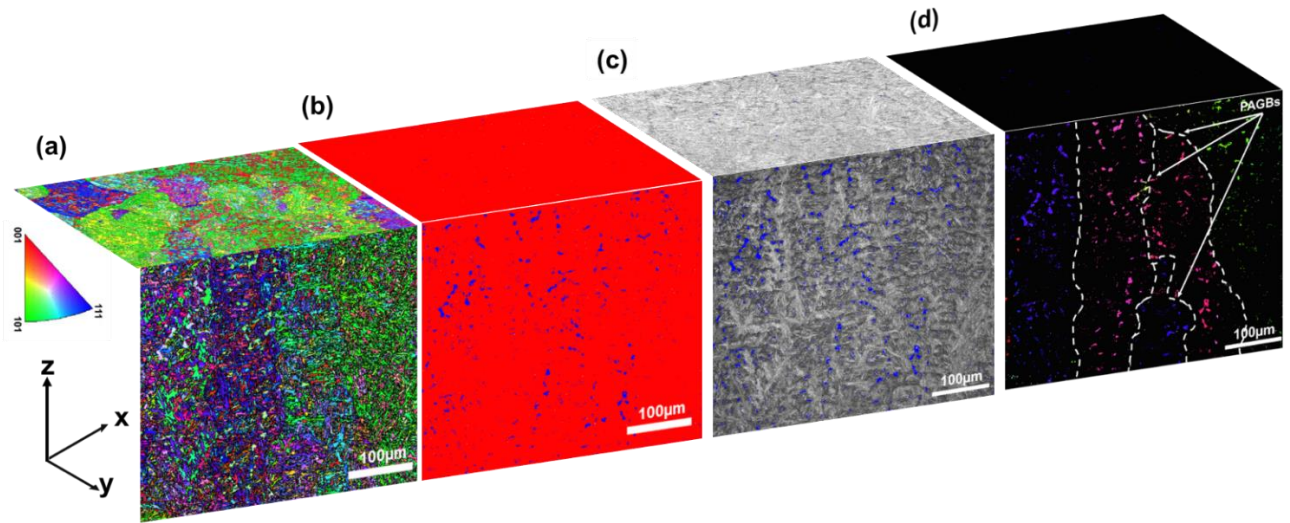
Figure 4. 6. (a) The IPF maps superimposed on the lath boundary maps (b) the EBSD phase maps: for the IT200-XY and IT200-XZ samples, (c) the IQ map superimposed on the Iron-FCC phase map for the selected region, (d) the IPF map for the FCC phase of the IT200-XZ sample.

Additionally, Figure. 4. 7 demonstrates the lath size distributions, extracted from the EBSD data, representing the size of martensite laths for fabricated samples. All samples exhibit a high fraction of relatively fine laths (lath size < 3 μm), while the IT200-XZ exhibits higher fraction of extremely fine laths (lath size < 1 μm) as compared to the other samples. Although all samples revealed a low fraction of coarser laths (lath size > 4 μm), the IT200-XZ (Figure. 4. 7d) sample exhibited a lower fraction of coarser laths as compared to the other samples (Figures. 4. 7a-7c). Figure. 4. 7e illustrates the frequency of low angle grain boundaries (LAGBs), medium-angle grain boundaries (MAGBs), and high-angle grain boundaries (HAGBs) for all deposited samples.

Generally, all samples exhibit a high fraction of LAGBs (48%-56%) and HAGBs (38%-45%), while the lowest fraction was detected for the CSL boundaries (8%-14%). It was noticed that among all samples, IT200-XZ sample possesses the highest fraction of LAGBs (~ 56%), while the highest fraction of HAGBs was observed for the IT200-XY sample (~ 45%). The effect of grain boundaries misorientation on the corrosion response will be thoroughly deliberated in the discussion section.
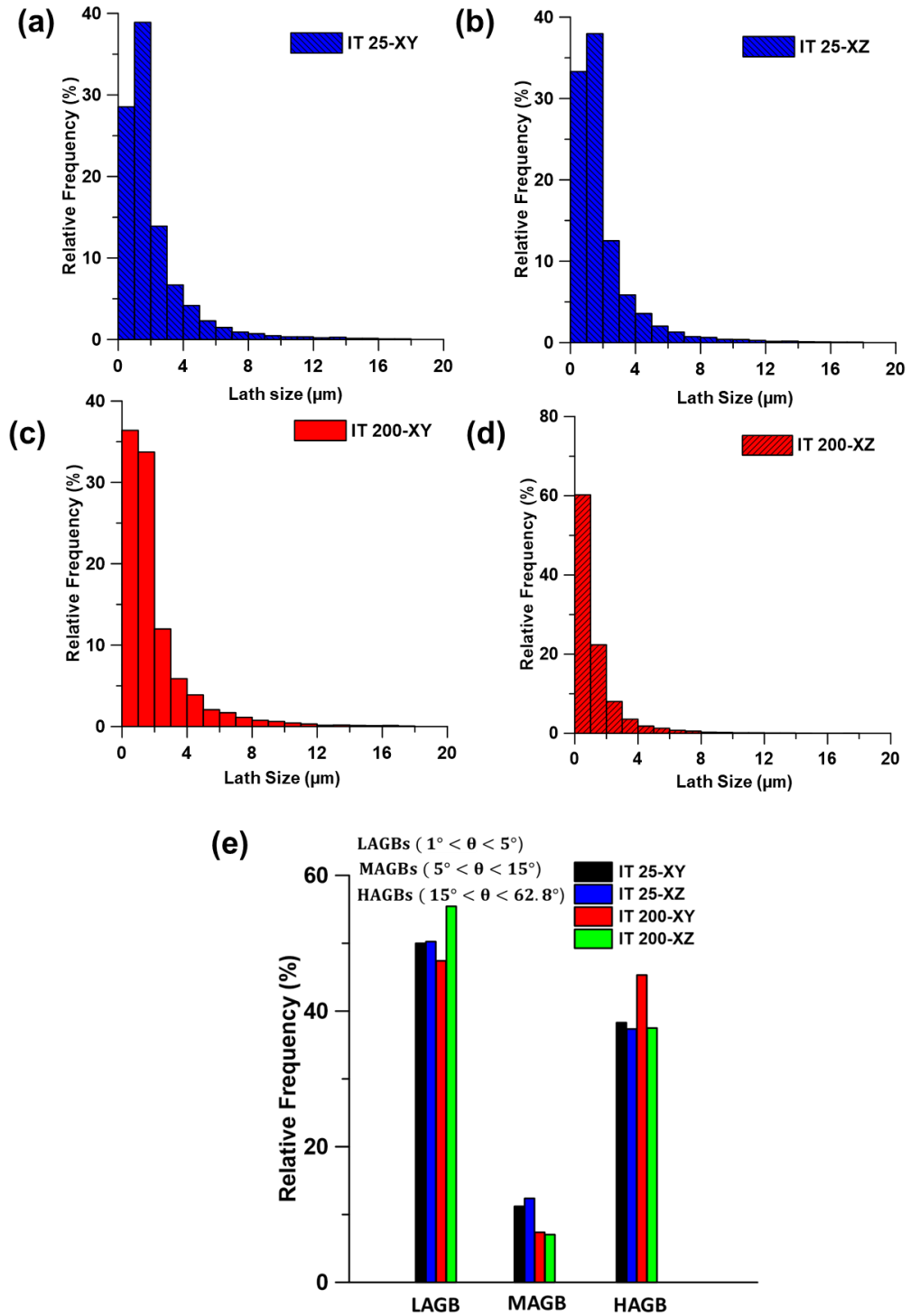
Figure 4. 7. The laths size distribution for (a) IT25-XY, (b) IT25-XZ, (c) IT200-XY, and (d) IT200-XZ, (e) grain boundaries misorientation angles distribution for the studied samples herein.

The pole figure of BCC (delta ferrite phase and martensite laths) and FCC (retained austenite) phases formed in the structure calculated from the EBSD data for {100}, {110}, and {111} families of planes are shown in Figure. 4. 8 for IT25-XY and IT25-XZ samples. Although the BCC pole figures of both IT25-XY and IT25-XZ samples exhibit relatively low intensity texture components at {100}, {110}, and {111} series of planes (Figures. 4. 8a and 8c), the IT25-XZ sample possess a slightly stronger texture component aligned with the building direction (z-axis) at {100} planes as compared to the IT25-XY sample. Stronger texture at {100} planes for the IT25-XZ sample is ascribed to directional solidification along the maximum thermal gradient direction, which is closely aligned with the z-axis [30]. The preferential grain growth direction in cubic structures is aligned with the <001> direction and leads to the formation of a strong texture in {100} series of planes in product phase [31]. It is reported that no variation is observed in the crystallographic orientation between the parent PAGs and the retained austenite phase [31]. Hence, the orientation of retained austenite phase for the IT25 sample presents the crystallographic orientation of the grains prior to phase transformation. The pole figure of the FCC phase for the IT25-XZ sample (Figure. 4. 8d) exhibits three strong cubic texture components at the {100} series of planes corresponding to the crystallographic orientation of the PAGs.

One of the most common crystallographic orientation relationships to describe the orientation relation between the parent austenite phase (γ) and product martensite phase ($\acute{\alpha}$) in plain carbon and martensitic stainless steel is known as the Kurdjumow–Sachs (K–S) and is expressed as follows [29,31]:

$$\{111\}_\gamma \,//\{110\}_{\acute{\alpha}} \quad <110>_\gamma \,//<111>_{\acute{\alpha}} \tag{1}$$

The K-S orientation relationship characterizes the coinciding planes and directions of the parent and product phases. However, the pole figure of the IT25-XY and IT25-XZ samples does

not show a coincidence between the $\{110\}_{\acute{\alpha}}$ and $\{111\}_{\gamma}$ series of planes, plausibly due to the low volume fraction of the austenite phase and the formation of a weak texture in the martensitic matrix.
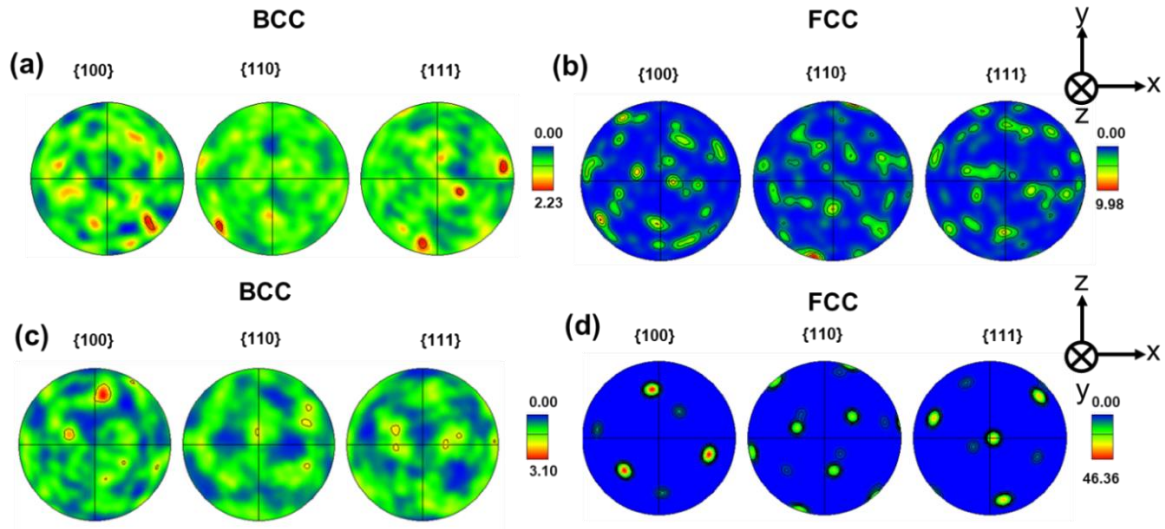
Figure 4. 8. The pole figures of the BCC and FCC phases: (a) and (b) for the IT25-XY sample, (c) and (d) for the IT25-XZ sample.

The pole figures of BCC and FCC phases for IT200-XZ and IT200-XY samples extracted from the EBSD data are shown in Figure. 4. 9. The pole figures of both IT200 samples exhibit stronger cubic texture as compared to their corresponding IT25 samples for the BCC structure (Figures. 4. 9a and 9c). Similar to the IT25 sample, the IT200 sample shows a stronger {001}<100> cubic texture on its XZ side than the XY plane. For both IT200-XY and IT200-XZ samples, the PF of the BCC structure at {110} planes ($\{110\}_{\acute{\alpha}}$) is coinciding with that of the FCC structure at {111} planes ($\{111\}_{\gamma}$), indicating the fulfillment of the K-S orientation relation between the primary austenite phase and the formed martensite laths.
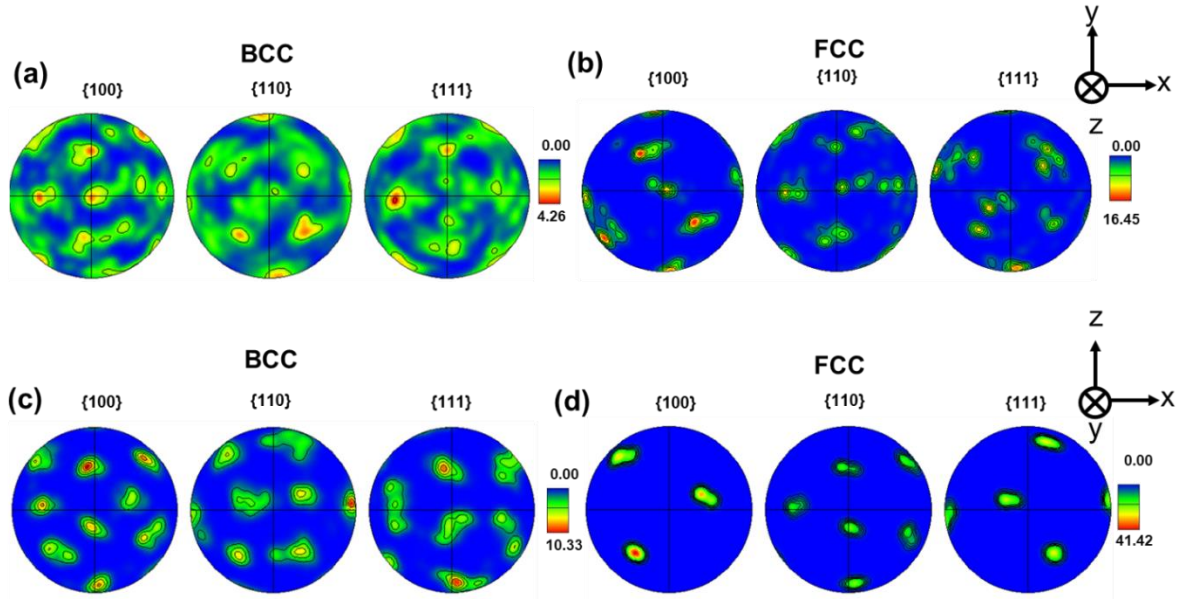
Figure 4. 9. The pole figures of the BCC and FCC phases: (a) and (b) for the IT200-XY sample, (c) and (d) for the IT200-XZ sample.

The orientation distribution function (ODF) based on the PF stereographs in different sections for all samples at φ_2=45° are shown in Figure. 4. 10 and the preferred crystallographic orientations are marked. A strong dominancy of preferential {001}<100> solidification texture is observed for the IT200-XZ sample (Figure. 4. 10d), while the IT200-XY sample exhibits {011}<111> texture component along with the{001}<100> solidification texture (Figure. 4. 10c). Weaker texture components of {011}<111> and {001}<100> were observed for the IT25-XY and IT25-XZ (Figures. 4. 10a and 10b) samples. Therefore, the fabricated samples at the inter-layer temperature of 200°C exhibited more anisotropic crystallographic behavior while relatively isotropic texture was observed for the fabricated samples at the inter-layer temperature of 25°C, suggesting a more pronounced directional solidification nature of the material along the building direction (z-axis) when fabricated at higher interlayer temperature of 200°C. Furthermore, the detected stronger texture of the fabricated samples at 200°C can be correlated to the lower cooling rate (product of temperature gradient and growth rate, G×R) of the material when deposited at higher inter-layer temperatures, leading to the formation of a coarser columnar dendritic structure grown closely

aligned with the heat dissipation direction. The coarser columnar grains of primary austenite induce a stronger texture in the solidified structure of the material [32]. Such columnar solidification mode along the building direction (z-axis) leads to the formation of strong preferential texture on the XZ view, and ultimately the anisotropic texture behavior of the IT200 sample.
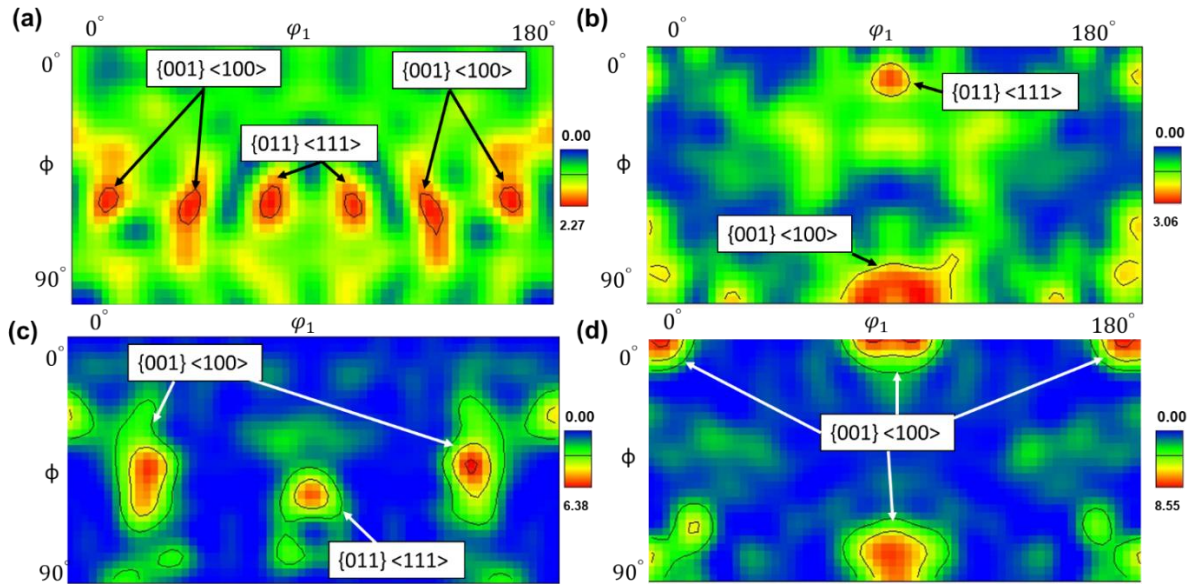
Figure 4. 10. Angular textural cross-sections of orientation distribution function at $\varphi_2=45°$ for the (a) IT25-XY, (b) IT25-XZ, (c) IT200-XY, and (d) IT200-XZ samples.

3.3.Corrosion Results

3.3.1. Open circuit potential results

The open-circuit potential (OCP) values variations versus the immersion time for the studied samples are displayed in Figure. 4. 11a. The recorded average OCP value for the IT200-XZ sample was found to be -432$\pm$17 mV$_{Ag/AgCl}$, while it decreases to -473$\pm$18 mV$_{Ag/AgCl}$, -462$\pm$15 mV$_{Ag/AgCl}$, and -511$\pm$19 mV$_{Ag/AgCl}$ for the IT25-XZ, IT200-XY, and IT25-XY samples, respectively, suggesting a lower passive film stability for the IT25 samples as well as XY views of the fabricated parts. It has been well stated that the measured value of average OCP is primarily

affected by the integrity and quality of the passive film [16]. A higher stability of the passive film is expected to be accompanied by nobler values in measured OCP.
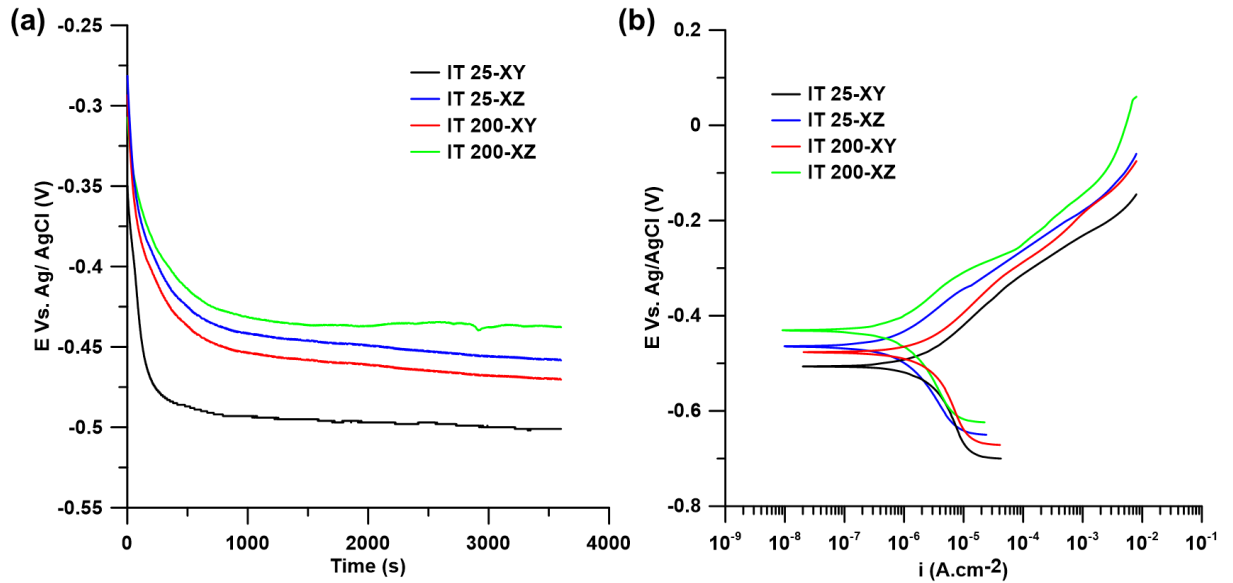
Figure 4. 11. (a) The open-circuit potential (OCP) values versus time, (b) potentiodynamic polarization graphs for the WAAM fabricated 420 stainless steel samples.

3.3.2. Potentiodynamic polarization (PDP) response results

Following the OCP measurements, the PDP experiments were conducted on the samples to characterize the electrochemical behavior in aerated 3.5 wt. % NaCl solution at 25 °C. The obtained plots of PDP are illustrated in Figure. 4. 11b. None of the studied samples has shown a clear passive region and breakdown (pitting) potential. Similarly, all samples revealed a consistent increase of the anodic current density by increasing the applied potential to values higher than the corrosion potential, suggesting a consistent dissolution of the samples into the electrolyte. However, due to the passive nature of stainless steel, such active behavior can be ascribed to the occurrence of some type of selective localized attack, such as intergranular corrosion, on the alloy's surface. The corrosion morphology assessment of the samples after the PDP testing are thoroughly elucidated in the discussion section.

157

Table 4. 3 summarizes the polarization parameters obtained from the potentiodyanmic curves. The PDP graph of the IT200-XZ sample exhibits a higher corrosion potential (E_{corr}) value (-431$\pm$15 mV$_{Ag/AgCl}$) relative to that of the IT25-XZ sample (-462$\pm$15 mV$_{Ag/AgCl}$). Additionally, the IT25-XY revealed lower corrosion potential value (-513$\pm$12 mV$_{Ag/AgCl}$) as compared to that of the IT200-XY sample (-474$\pm$13 mV$_{Ag/AgCl}$). Both samples from the XY view also showed lower corrosion potentials relative to their counterparts from the XZ view. The measured corrosion current density (i_{corr}) values of the samples were found to be inversely consistent with the measured E_{corr} trend. The corrosion current density of the IT200-XZ was the lowest (0.216$\pm$0.003 μA cm^{-2}), while it increases for the other samples in the order of IT25-XZ < IT200-XY < IT25-XY (0.224$\pm$0.005, 0.315$\pm$0.004, 0.326$\pm$0.005 μA cm^{-2}, respectively). The measured E_{corr} and i_{corr} trends are in good agreement with the OCP values reported in the previous section.

Table 4. 3 .The electrochemical parameters from the PDP curves of the WAAM fabricated 420 stainless steel.

Sample	E_{corr} (mV$_{Ag/AgCl}$)	i_{corr} (μA cm^{-2})
IT25-XY	-513$\pm$12	0.326$\pm$0.005
IT25-XZ	-462$\pm$15	0.224$\pm$0.005
IT200-XY	-474$\pm$13	0.315$\pm$0.004
IT200-XZ	-431$\pm$15	0.216$\pm$0.003

3.3.3. Electrochemical impedance spectroscopy results

The EIS tests were conducted on the samples to analyze the protectiveness and stability of the passive film on the samples' surfaces. The Nyquist plots for the as-printed samples of WAAM-420 MSS are depicted in Figure. 4. 12a. A relatively wide single capacitive loop was recorded for all samples. All samples revealed a similar semicircle capacitive loop with different sizes, ascribed to the occurrence of the same corrosion mechanism in all samples regardless of the implemented inter-layer temperature or the prepared surface orientation. It is known that the larger diameter of

the semicircle is associated with the enhanced electrochemical response of the passive film [33]. Accordingly, the larger capacitive loop of the IT200-XZ sample is associated with its higher corrosion resistance, consistent with the obtained OCP and PDP results. Contrarily, the IT25-XY sample exhibits the smallest semicircle diameter, indicating its lowest nobility against corrosion.

Figure. 4. 12b exhibits the Bode plots of the as-printed WAAM-420 MSS samples. A linear behavior over the frequency range of 10^{-1} Hz to 10^2 Hz is observed for log |Z| versus log (*frequency*) with a slope near -1, possessing a phase angle in the range of -60° to -70°, indicating the capacitive behavior of the surface. The appearance of such wide phase angle peaks is typically ascribed to the superposition of two individual peaks having non-discriminating time constants, one associated with the sealing effect of the passive film at higher frequencies and the other representing the double-layer capacitance and diffusion through the localized corroded areas at lower frequencies.

A two-time constants equivalent circuit (EC) model was used to model and fit the obtained EIS spectra, as shown in Figure. 4. 12c. In this model, constant phase elements (*CPE*) were used instead of a perfect capacitance to address the existing micro or nano surface inhomogeneities. The impedance value of the *CPE* can be described using [34]:

$$Z_{CPE} = [Y_0(j\omega)^n]^{-1} \tag{2}$$

where Y_0 is a *CPE* constant, $j = -(1)^{1/2}$, ω is the angular frequency, and n is the dispersion coefficient of the *CPE*. In the EC model, R_s is the electrolyte resistance, R_1 and R_2 are the passive film and charge transfer resistances, respectively, and *CPE$_1$* and *CPE$_2$* are the capacitance of the passive film and the double layer, respectively. The EIS fitting parameters are summarized in Table 4. 4. For all samples, n_1 values were obtained between 0.81-0.85, whereas n_2 values were between 0.80-0.91. Chi-square (χ^2) values below 1.54×10^{-6} confirmed acceptable accordance between the

fitted values and EIS spectra data. The passive film resistance and charge transfer resistance values are shown to be higher for the IT200-XZ and IT25-XZ samples than those of the XY samples, indicating a more uniform and stable nature of the passive film on the XZ surfaces. Furthermore, the IT200 samples revealed a higher R_1 and R_2 values than the IT25 samples in the same orientation. The values of the CPE_1 and CPE_2 for the IT25-XY were found to be the highest, ascribed to the formation of a more defective passive film on its surface.
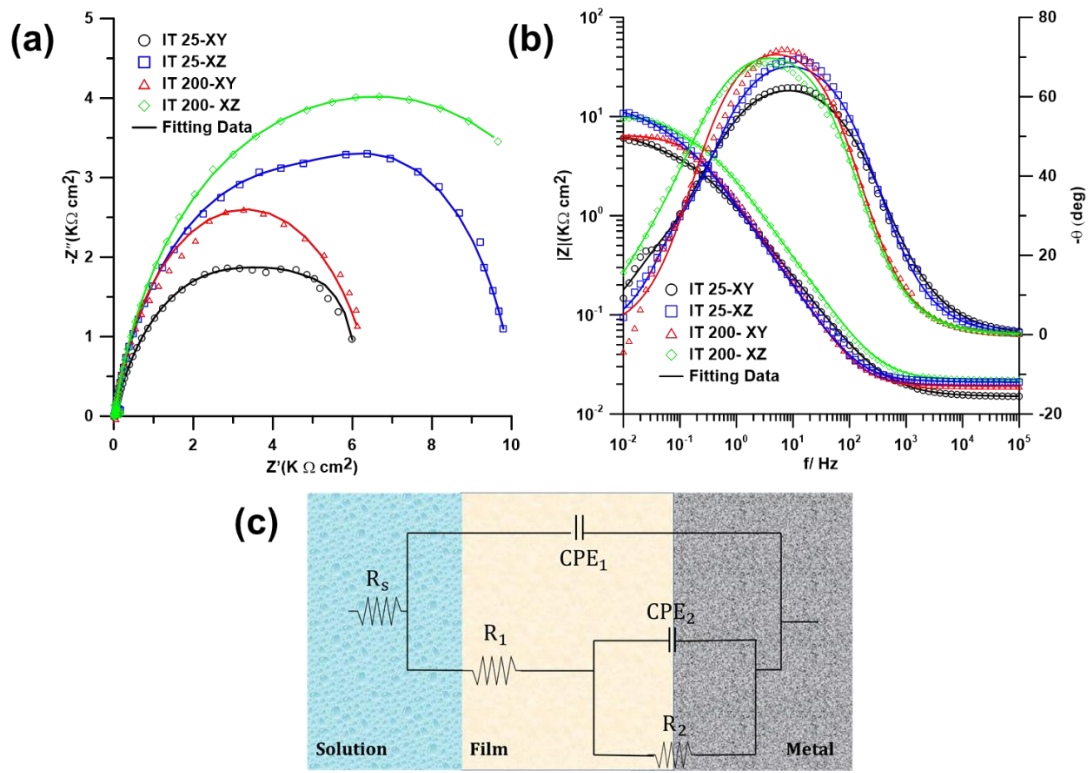
Figure 4. 12. (a) Nyquist plots and (b) Bode plots of the WAAM fabricated 420 stainless steel samples, (c) equivalent circuit model used to describe the EIS data.

Table 4. 4. The fitted EIS spectra parameters.

Sample	R_s (Ωcm^2)	CPE_1 (Ω^{-1}cm^{-2}s^n)	n_1	R_1(Ωcm^2)	CPE_2 (Ω^{-1}cm^{-2}s^n)	n_2	R_2 (Ωcm^2)	$\sum \chi^2$
IT25-XY	18	1.98×10^{-4}	0.83	5.21×10^3	9.22×10^{-3}	0.91	1.57×10^3	1.32×10^{-6}
IT25-XZ	19	1.11×10^{-4}	0.81	7.21×10^3	5.45×10^{-4}	0.86	6.14×10^3	1.27×10^{-6}
IT200-XY	19	1.48×10^{-4}	0.85	6.55×10^3	8.23×10^{-4}	0.98	3.75×10^3	1.54×10^{-6}
IT200-XZ	20	1.01×10^{-4}	0.83	8.47×10^3	4.43×10^{-4}	0.80	8.45×10^3	1.32×10^{-6}

4. Discussion

4.1. Effect of inter-layer temperature on the formation of the secondary phases in the microstructure

The dominant microstructure of all studied samples herein (Figures. 4. 3a, 3e, 3f, and 3h) revealed the formation of a lath martensitic structure along with a significant content of interdendritic delta ferrite phase. In addition, the XRD spectra and analyzed EBSD results revealed a slight fraction of retained austenite in the IT25-XZ sample (~ 3%) and a noticeably higher fraction (~ 18%) of randomly distributed retained austenite in the IT200-XZ sample. Although the formation of a fully martensitic microstructure is expected when MSSs undergo a fast cooling cycle during solidification, the fabricated MSS samples in this study revealed a substantial volume fraction of other microconstituents, *i.e.* delta ferrite, undissolved carbides, and retained austenite, due to the complex thermal history experienced by the material during the sequential heating and cooling cycles in the WAAM process. The formation of retained austenite and delta ferrite phases has been previously reported in the microstructure of additively manufactured 420 MSS parts [35]. During the cooling cycle from elevated temperatures, the 420 MSS with 0.35 wt. % carbon undergoes the following equilibrium phase transformation [27]:

$$L \rightarrow L + \delta \rightarrow \delta + \gamma + L \rightarrow \gamma \rightarrow \alpha \tag{3}$$

where L, δ, γ, and α correspond to the liquid, delta ferrite, austenite, and ferrite phases, respectively. The transformation of the delta ferrite phase into the austenite is a diffusion-controlled and time-dependent process [27]. The applied rapid cooling during the solidification process can hinder the complete transformation of the delta ferrite into the austenite due to inadequate time for diffusion. In addition, the segregation of chromium as a strong ferrite stabilizer element along the interdendritic regions can also facilitate the presence of the delta ferrite phase

at the ambient temperature. These two mentioned factors were the driving force for the formation and stabilization of the delta ferrite in the microstructure of both IT25 and IT200 samples at room temperature. It is worth noting that no significant difference in the fraction of the delta ferrite phase was observed among the samples fabricated at different inter-layer temperatures or different cross-sectional overviews of the samples. Comprehensive image analysis on the SEM micrographs taken from all the samples using the ImageJ software revealed that the fraction of the delta ferrite phase remains relatively within a constant range (~ 24%-27%), as shown in Figure. 4. 13.
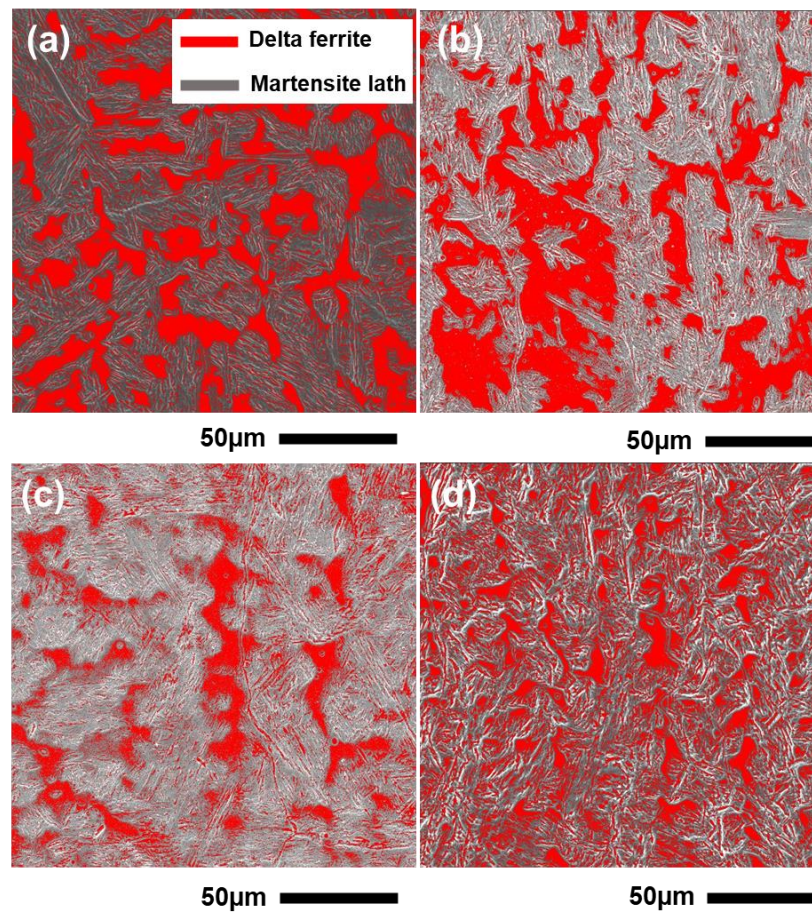
Figure 4. 13. Delta ferrite phase fraction analysis of the (a) IT25-XY, (b) IT25-XZ, (c) IT200-XY, and (d) IT200-XZ samples showing the delta ferrite phase in red and the martensite lath in grey.

As already stated, a relatively significant amount of retained austenite was formed in the IT200-XZ sample, while a lower fraction of γ was detected in the IT25-XZ sample. The

stabilization of the retained austenite at room temperature is related to the localized high concentration of austenite stabilizing elements, such as carbon, in the microstructure, which can decrease the martensite finish temperature (M_f) to a temperature lower than ambient temperature [27]. Therefore, during the solidification process of the ER420 wall, the existence of relatively high carbon content (0.35 wt. %) in the alloy has led to an incomplete martensitic transformation and retaining of the untransformed austenite phase in the structure (retained austenite). On the other hand, in the WAAM process, during the solidification of each track, the heat dissipation through the previously solidified layers has an important role in determining the final microstructure of each layer [36]. The higher volume fraction of retained austenite in IT200-XZ sample with respect to the IT25-XZ sample can be ascribed to its higher inter-layer temperature, which expedites the re-transformation of the martensite phase in the previously deposited layer to the austenite by raising the heat-affected zones' temperature to a temperature higher than the austenite formation temperature (A_s). During re-cooling cycle of each layer, the main fraction of the austenitic regions transforms to martensite and the remains retain at room temperature (also known as reversed austenite). On the contrary, the lower inter-layer temperature of the IT25 sample is plausibly not sufficient for the formation of reversed austenite during the re-heating cycle from the deposition of the subsequent layers.

Additionally, the martensite start temperature (M_s) and finish temperature (M_f) for ER420 is roughly estimated to be 210°C and 30°C, respectively [37]. Hence, prior to the deposition of a new track, the previous underlying layer at the inter-layer temperature of 200°C (between M_s and M_f temperatures) is expected to possess a martensitic microstructure containing inter-lath untransformed retained austenite. During the deposition of the next layer, the temperature of the previous underlying layer will increase to temperatures above the M_s, providing enough energy to

activate the diffusion of carbon from the supersaturated martensite phase into the austenite phase with a higher solid solubility for carbon. The higher carbon content of the austenite phase will lower both M_s and M_f temperatures and consequently stabilizes the austenite phase at ambient temperature [37]. Therefore, it can be assumed that the fabricated samples at the higher inter-layer temperature of 200°C experience a thermal history analogous to quenching and partitioning heat treatment, which is commonly applied to increase the volume fraction of the retained austenite in martensitic steels [38].

4.2. Effect of crystallographic orientation on the electrochemical response and passive film formation

The Read-Shockley equation is adopted based on the dislocation theory, in order to correlate the grain boundary energy, γ_{gb}, and the grain boundary angle (θ) [39]:

$$\gamma_{gb} = \frac{Ga\,\theta}{4\pi(1-\sigma)}(A - ln\theta) \tag{4}$$

where G is the shear modulus, a is the Burgers vector, σ is the Poisson ratio, and A is a constant approximately equal to 0.23. According to the Read-Shockley equation, the stored energy in the grain boundary is proportional to the grains' misorientation. The obtained grain boundary orientation maps from all samples (Figure. 4. 7e) confirmed that the highest fraction of LAGBs was recorded for the IT200-XZ sample. The LAGBs, possessing low energy levels, are considered as obstacles to fast diffusion and can maintain the proximity of the grain boundary diffusivity and the material's bulk diffusivity, leading to higher stability of the formed passive layer. Therefore, in the present study, the impact of LAGBs contributes to the enhanced electrochemical response of the IT200-XZ sample. On the other hand, IT200-XY sample exhibited relatively lower frequency of the LAGBs compared to the other samples, suggesting a more noticeable difference between diffusivity of the grain boundary and bulk material on its surfaces, while IT25-XY and IT25-XZ samples show relatively the same frequency of the LAGBs. The noticeably lower fraction

of the LAGBs for the IT200-XY sample can be the controlling factor contributing to its inferior electrochemical response compared to the IT25-XZ sample. Although the IT25-XY and IT25-XZ samples exhibit relatively the same density of LAGBs, the magnitude of LAGBs' impact on the electrochemical response cannot be quantified or even discriminated from the impacts of variation of other microstructural features between the samples, including the laths' size and orientation, secondary phases, and potentially process-induced residual stresses.

Speaking of the crystallographic orientation of the laths, it is well stated that the high-density close-packed crystallographic planes that coincide with the sample's exposed surface to the electrolyte exhibit better electrochemical response and higher passive layer stability [40]. The high density close-packed crystallographic plane for the polycrystalline metals with BCC structure is {110} plane. The pole figure of {110} planes for IT200-XZ sample is showing a strong texture component (high intensity of 10.33) aligned with the deposition direction (X-axis). Therefore, the surface of the fabricated sample aligned with the YZ plane is expected to contain the highest density of close-packed planes parallel to the exposed surface of the sample. Due to the similarities in the microstructure between the YZ and XZ planes, a high density of closed-packed planes is also expected on the XZ plane. Hence, the formed texture in the microstructure of IT200-XZ sample is also in favor of its superior corrosion response. On the other hand, the IT25-XY, with the lowest OCP and EIS response, exhibited a lower intensity and weaker texture for {110} planes as compared to other samples.

The corrosion mechanism in stainless steel is primarily discussed with respect to the mechanism of passive film formation and its stability. On this regard, the thickness of the passive film plays an important role on its integrity and stability [41]. According to the parallel plate

expression, the passive film thickness can be calculated using the measured EIS data as follows [21]:

$$L_{ss} = \frac{A\varepsilon\varepsilon_0}{C_f} \qquad (5)$$

where, A represents the surface area of the sample, ε is the passive film dielectric constant (~15.6 for Cr_2O_3) [21], ε_0 is the vacuum permittivity (8.854 $\times 10^{-14}$ F cm^{-1}), and C_f is the capacitance of the pure passive layer The C_f value can be estimated using:

$$C_f = \frac{(Y_0 R_{ct})^{1/n}}{R_{ct}} \qquad (6)$$

where Y_0 is the CPE constant, R_{ct} is the resistance of the charge transfer (calculated R_2 values in Table 4. 4), and n is the exponent of passive film capacitance (calculated n_2 values in Table 4. 4) [21]. The calculated passive layer thickness and pure passive layer capacitance values are shown in Table 4. 5. Apparently, the thickness of the passive layer formed on the IT200-XZ is the highest while it decreases for the other samples in the order of IT25-XZ > IT200-XY > IT25-XY, which is in good agreement with the OCP, PDP, and EIS testing results obtained in this study.

Table 4. 5. The passive layer thickness (L$_{ss}$) and corresponding pure layer capacitance values.

Sample	C_f ($\Omega^{-1}cm^{-2}s^n$)	L_{ss} (nm)
IT25-XY	1.20×10^{-2}	0.028
IT25-XZ	6.56×10^{-4}	0.52
IT200-XY	8.54×10^{-4}	0.40
IT200-XZ	6.02×10^{-4}	0.57

4.3.Effect of secondary phases formation on the corrosion behavior

The corrosion behavior of martensitic stainless steel is highly dependant on the microstructure and the formation of micro-constituents [16,42]. Corrosion behavior of the AISI 420 MSS is highly influenced by micro-galvanic coupling between the martensitic matrix as anode and existing intergranular carbides as cathode, intensifying the localized corrosion attack at the

matrix-carbides interface [16]. The formation of intergranular chromium carbides can drain the chromium from the matrix and leads to the formation of chromium depleted zones in the matrix at the periphery of the carbides, which are highly susceptible to corrosion attack [16]. As presented in this study, only a slight amount of intergranular (interlath) carbides were formed during the solidification of the WAAM samples. However, the delta ferrite phase acts nearly the same as the intergranular carbide and can adversely affect the corrosion behavior [19]. Regions containing the residual delta ferrite phase possess a high Cr concentration and thereby are surrounded by Cr-depleted zones at the martensite phase, making the interface regions between the delta ferrite and martensite phase susceptible to initiation of corrosion attack. The IT25-XY and IT25-XZ samples exhibited severe corrosion attack, as shown in Figures. 4. 14a and 15a after the PDP tests. Prior to the PDP testing, the chromium line scanning plot taken across the delta ferrite-matrix interface (the inset in Figure. 4. 14f) revealed that the Cr concentration was reduced to less than 11 wt.% adjacent to the delta ferrite phase, indicating the formation of chromium depleted region at the interface zone. Differently, after the PDP testing, the sensitized regions along the interface of the delta-ferrite phase where the initiation of localized corrosion attack was detected for the IT25-XY and IT25-XZ samples (shown in Figures. 4. 14b-d) revealed a higher concentration of chromium than that in the martensite matrix. The detected higher content of Cr element in the sensitized regions (Figure. 4. 14d) is ascribed to the preferential dissolution of Fe element (Figure. 4. 14c) from these regions during the corrosion testing in the electrolyte, while Cr element, which primarily exists in the solid-solution form in delta ferrite, does not seem to leach from the surface [20,21,43]. Therefore, the preferential depletion of Fe element from the surface leads the detected Cr-rich regions along the interface of the matrix and delta ferrite phase. Therefore, the severe corrosion attack propagated in the martensite matrix at the periphery of the delta-ferrite phase is

ascribed to the formation of micro-galvanic coupling between the cathodic delta ferrite phase with higher Cr content and the Cr-depleted martensitic matrix as the anode (shown in Figures. 4. 14b and 15b).

Unlike the sample deposited with the inter-layer temperature of 25 °C, the corrosion morphology on the IT200 sample after the PDP testing (Figure. 4. 16) exhibited the initiation stage of the intergranular corrosion and was characterized by the formation of shallow trenches at the martensite lath boundaries and the interface between the delta-ferrite phase and its surrounding matrix (indicated in Figure. 4. 16b). It is shown that the Cr-depleted regions have dissolved preferentially where the initiation of the intergranular corrosion has taken place. Similar to the IT25 sample, the martensite phase is the susceptible region to the corrosion attack and the delta ferrite phase is less prone to anodic dissolution due to the higher concentration of the chromium in this phase.

The EDX line scans shown in Figures. 4. 14e, 15d, 16d, and 17d reveal that by increasing the interlayer temperature from 25°C to 200°C the chromium content of the delta ferrite phase is decreasing from ~24 wt.% to ~17 wt.%. The lower severity of corrosion attack on the IT200-XY sample relative to that of the IT25-XY sample can be correlated to the lower chromium content of the delta-ferrite phase formed in the IT200 sample (Figures. 4. 16d and 17d) ascribed to the higher interlayer temperature used in the fabrication process of that sample. The 200 °C interlayer temperature can be sufficient to trigger the diffusion of Cr atoms from Cr-rich delta-ferrite regions to chromium-depleted zones in the previously solidified layers, slightly lowering the chromium concentration gradient and the extent of chromium depleted regions between the delta-ferrite phase and its surrounding matrix, and ultimately improving the intergranular corrosion resistance of the sample.
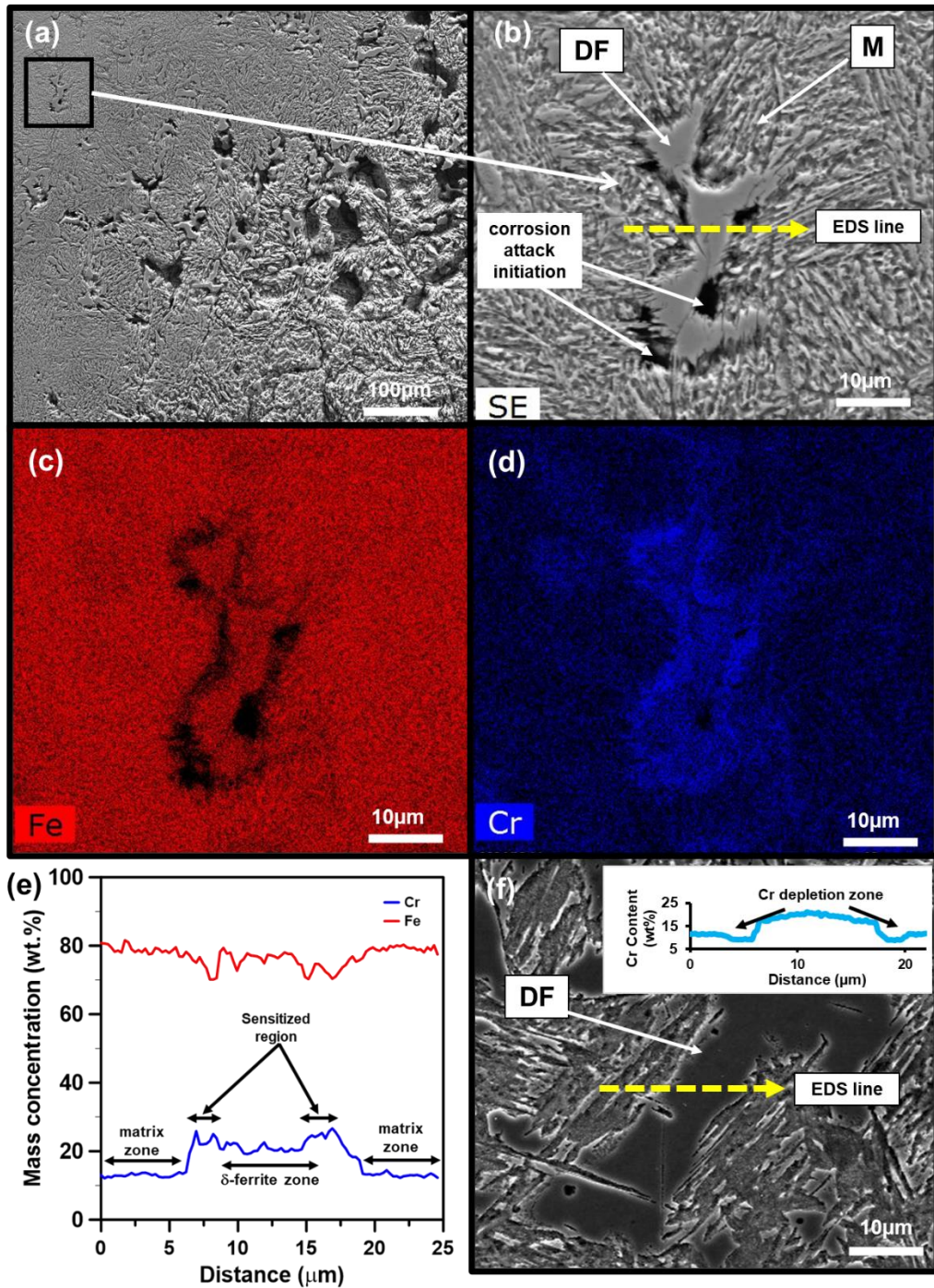
Figure 4. 14. (a) The SEM micrographs from the IT25-XY sample after polarization testing, (b) higher magnification SEM micrograph from the enclosed area in (a), (c) the corresponding EDX-Fe concentration and (d) Cr concentration maps, (e) the compositional line scan across the delta ferrite phase (along the yellow dashed arrow in (b)) after the polarization testing, and (f) SEM image and the chromium concentration line scan across the delta ferrite-matrix interface region prior to the polarization testing.
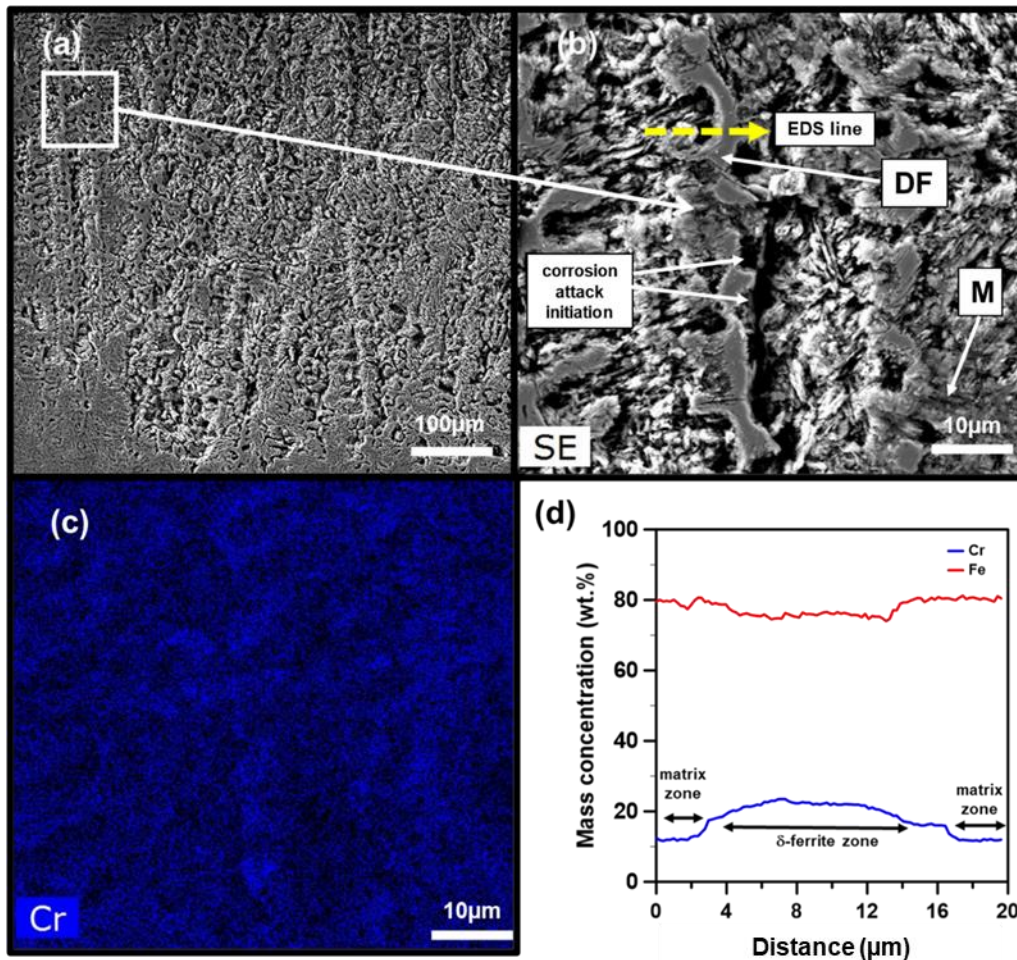
Figure 4. 15. (a) The SEM micrographs from the IT25-XZ sample after polarization testing, (b) higher magnification SEM micrograph from the enclosed area in (a), (c) the corresponding EDX-Cr concentration map, (d) compositional line scan across the delta ferrite phase.

The formed higher volume fraction of the retained austenite in the IT200-XZ sample (~ 18%) as compared to that in the IT25-XZ sample (~ 3%) also contributes to the superior corrosion response of the IT200 sample. In another study, Lei et $al.$ [44] reported that the presence of retained austenite along the martensite lath boundaries enhanced the pitting resistance of a tempered Super 13Cr alloy. Analogously, the retained austenite in the IT200 sample was primarily detected along the lath boundaries (shown in Figure. 4. 6). The presence of retained austenite is commonly detected at the chromium-depleted regions, where the austenite stabilizing elements, such as

carbon, enrich and consequently grow along the lath boundaries [25]. This is compelling evidence confirming that the formation of retained austenite can hinder the propagation of intergranular corrosion at the lath boundaries. The reversed or retained austenite can also reduce the heterogenization at the lath boundaries, leading to the enhanced stability of the boundaries, further contributing to the improved corrosion performance of the alloy by limiting the extension of intergranular corrosion [44].

Figure. 4. 18 demonstrates the schematic diagram of the intergranular corrosion mechanism at the Cr-depleted region adjacent to the delta ferrite phase in two scenarios with or without the presence of the retained austenite phase. Samples deposited at the interlayer temperature of 25°C are highly susceptible to the initiation and propagation of corrosion attack through the Cr-depleted regions adjacent to the residual delta ferrite phase with high chromium concentration (Figure. 4. 18a). Differently, the formation of high volume fraction of retained austenite along the martensite lath in the IT200-XZ can reduce the number of nucleation and propagation sites for the intergranular corrosion (Figure. 4. 18b).

As mentioned earlier, the IT25-XZ sample exhibited low volume fraction of retained austenite (~3%), while no retained austenite phase was detected in the IT200-XY. The presence of the retained austenite phase combined with the higher fraction of the LAGBs in the IT25-XZ sample can contribute to the enhanced electrochemical response of the IT25-XZ sample relative to the IT200-XY sample, despite the latter contains delta ferrite phase with lower chromium content.
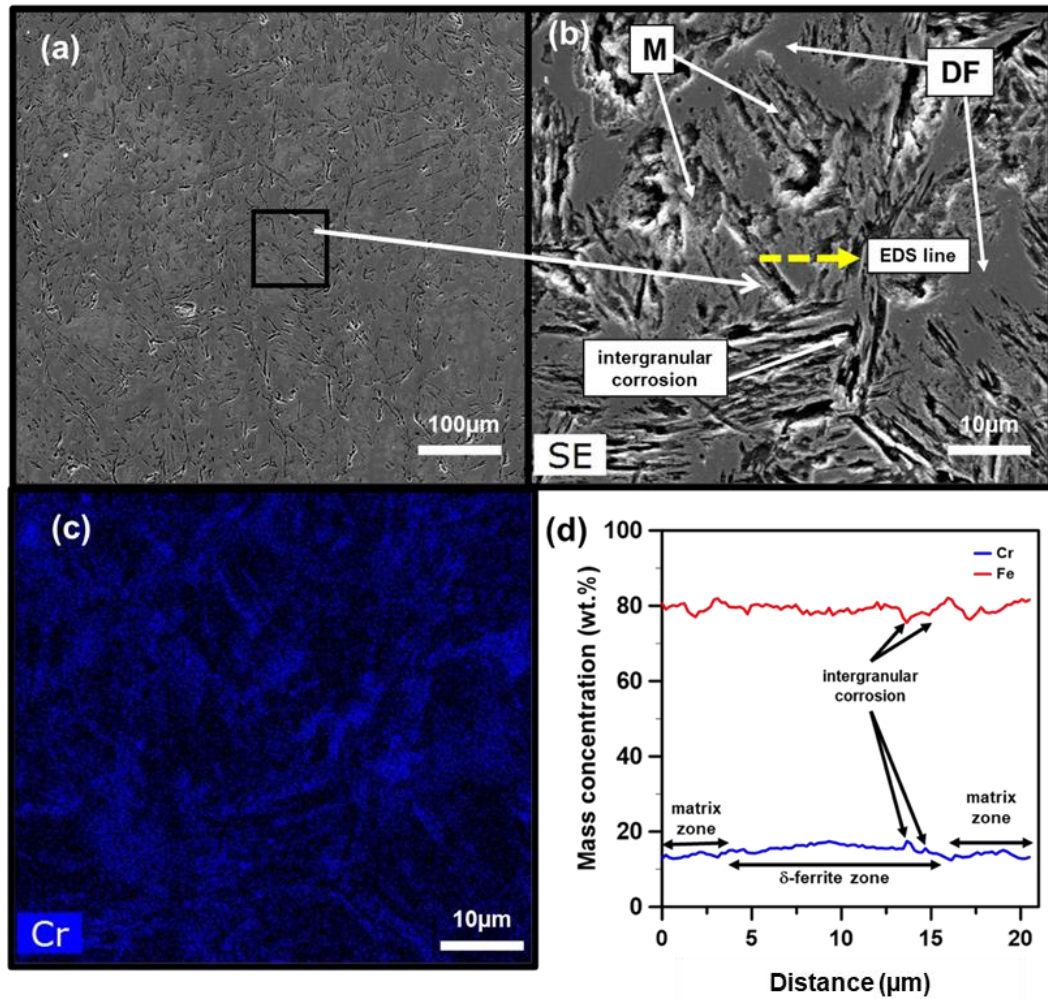
Figure 4. 16. (a) The SEM micrographs from the IT200-XY sample after polarization testing, (b) higher magnification SEM micrograph from the enclosed area in (a), (c) the corresponding EDX-Cr concentration map, (d) compositional line scan across the delta ferrite phase.
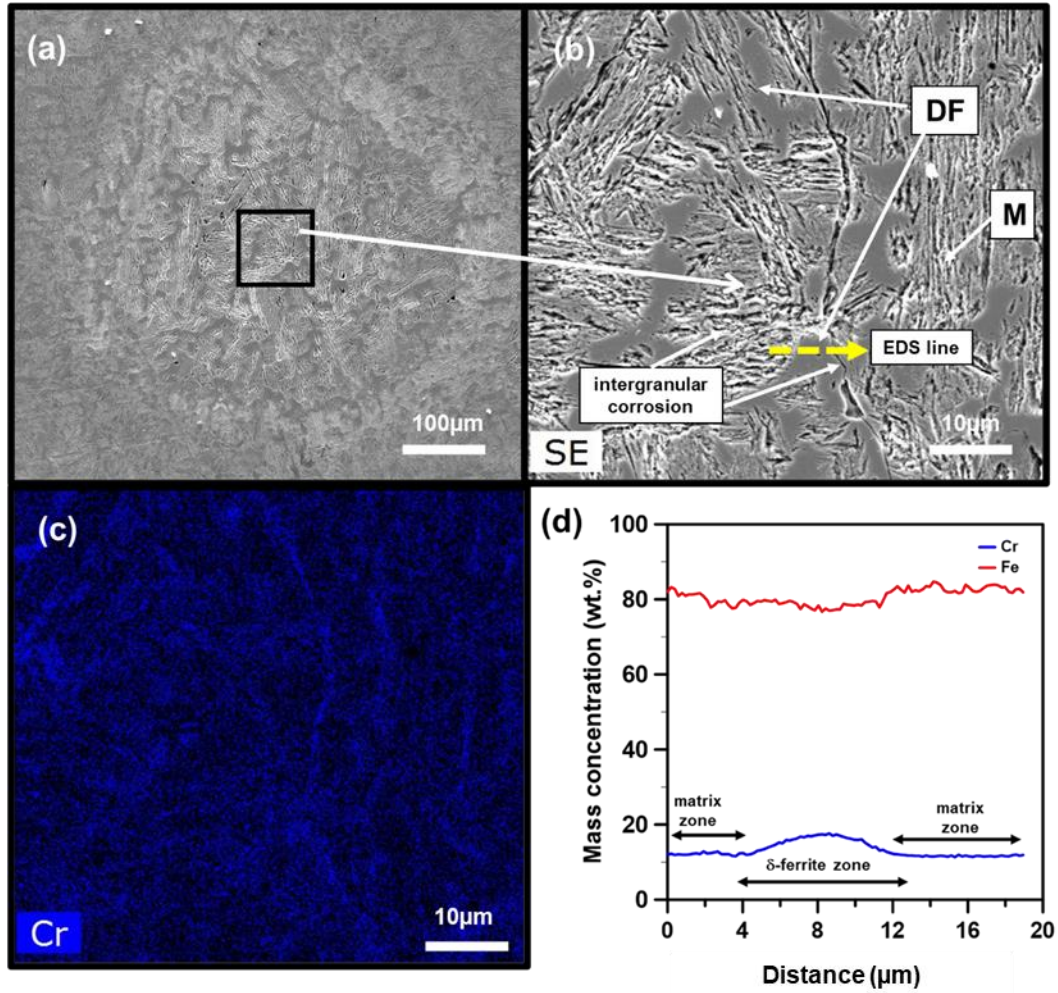
Figure 4. 17. (a) The SEM micrographs from the IT200-XZ sample after polarization testing, (b) higher magnification SEM micrograph from the enclosed area in (a), (c) the corresponding EDX-Cr concentration map, (d) compositional line scan.
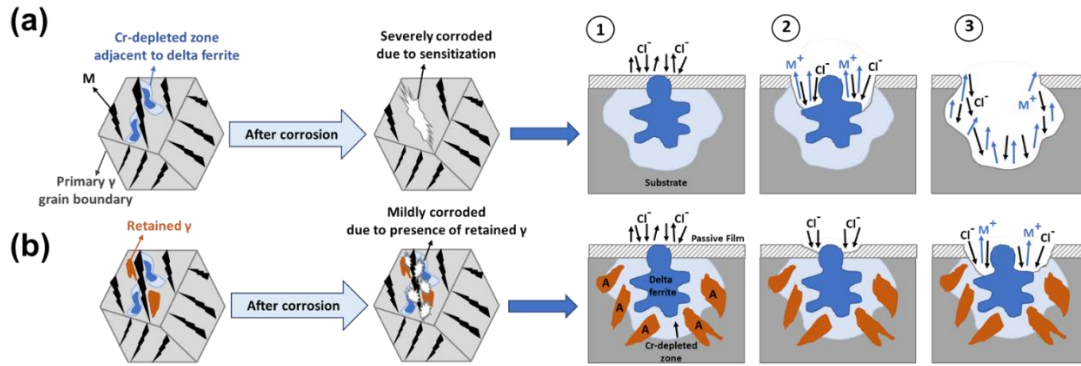
Figure 4. 18. Schematic illustration of the intergranular corrosion mechanism in WAAM fabricated 420 stainless steel: (a) in the presence of the delta ferrite and martensite laths, (b) in the presence of delta ferrite, martensite laths, and retained austenite.

5. Conclusions

In this study, the effects of the crystallographic orientation and the micro-constituents' formation on the corrosion performance of a 420 martensitic stainless steel produced by the wire arc additive manufacturing at two different inter-layer temperatures of 25 °C (IT25) and 200 °C (IT200) and from top and side views (XY and XZ views, respectively) were investigated. The following conclusions were drawn from this study:

1. The microstructure of all fabricated samples contained martensite laths with an average lath size of ~3 µm along with the delta ferrite phase. The side view of the IT200 sample (IT200-XZ) also possessed a high-volume fraction of retained austenite (~ 18%), while only 3% austenite was retained in the IT25-XZ sample.

2. The IT200 samples exhibited anisotropic crystallographic behavior, while a relatively isotropic texture was detected in the IT25 samples. Strong cubic {001}<100> solidification texture was formed in the IT200-XZ sample due to close alignment of the <001> growth direction of primary austenite grains and the sample's building direction. A Kurdjumov–Sachs orientation

relationship ($\{110\}_\alpha$//$\{111\}_\gamma$) was found between the formed retained austenite in the fabricated samples and its surrounding martensite laths.

3. The polarization results confirmed a higher corrosion potential and lower corrosion current density for the IT200-XZ and IT25-XZ samples, suggesting the better electrochemical performance of the fabricated samples on their XZ surfaces against localized corrosion attack. Additionally, the EIS data indicated higher electrochemical stability and a thicker passive film formed on the IT200XZ and IT25-XZ samples as compared to the IT25-XY and IT200-XY samples.

4. The corrosion morphology of the samples after polarization testing for the IT25-XY and IT25-XZ showed severe localized corrosion attack, while the IT200-XY and IT200-XZ samples exhibited an early stage of intergranular corrosion. The corrosion mechanism of the samples was dictated by the higher susceptibility of the delta ferrite-martensite interface to localized corrosion attack, where the Cr element was found to be depleted. The corrosion performance of the IT200-XZ sample was enhanced due to less degree of Cr-depletion from the periphery of the delta ferrite regions, higher fraction of LAGBs, and higher density of close-packed planes parallel to the exposed surface (XZ plane), along with the formation of higher concentration of retained austenite in this sample, all contributed to restraining the corrosion nucleation sites on its laths boundaries.

References

[1]   T. Horii, S. Kirihara, Y. Miyamoto, Freeform fabrication of superalloy objects by 3D micro welding, Mater. Des. 30 (2009) 1093–1097.

[2]   N. Li, J. Zhang, W. Xing, D. Ouyang, L. Liu, 3D printing of Fe-based bulk metallic glass composites with combined high strength and fracture toughness, Mater. Des. 143 (2018) 285–296.

[3]   L. Wang, J. Xue, Q. Wang, Correlation between arc mode, microstructure, and mechanical

properties during wire arc additive manufacturing of 316L stainless steel, Mater. Sci. Eng. A. (2019). https://doi.org/10.1016/j.msea.2019.02.078.

[4] M. Ghaffari, A.V. Nemani, M. Rafieazad, A. Nasiri, Effect of solidification defects and HAZ softening on the anisotropic mechanical properties of a wire arc additive-manufactured low-carbon low-alloy steel part, JOM. 71 (2019) 4215–4224.

[5] M. Rafieazad, M. Ghaffari, A.V. Nemani, A. Nasiri, Microstructural evolution and mechanical properties of a low-carbon low-alloy steel produced by wire arc additive manufacturing, Int. J. Adv. Manuf. Technol. 105 (2019) 2121–2134.

[6] A.V. Nemani, M. Ghaffari, A. Nasiri, Comparison of microstructural characteristics and mechanical properties of shipbuilding steel plates fabricated by conventional rolling versus wire arc additive manufacturing, Addit. Manuf. 32 (2020) 101086.

[7] Z. Wang, A.M. Beese, Effect of chemistry on martensitic phase transformation kinetics and resulting properties of additively manufactured stainless steel, Acta Mater. 131 (2017) 410–422.

[8] A. Vahedi Nemani, M. Ghaffari, A. Nasiri, On the Post-Printing Heat Treatment of a Wire Arc Additively Manufactured ER70S Part, Materials (Basel). 13 (2020) 2795.

[9] A.V. Nemani, M. Ghaffari, S. Salahi, A. Nasiri, Effects of post-printing heat treatment on the microstructure and mechanical properties of a wire arc additive manufactured 420 martensitic stainless steel part, Mater. Sci. Eng. A. (2021) 141167.

[10] F. Hejripour, F. Binesh, M. Hebel, D.K. Aidun, Thermal modeling and characterization of wire arc additive manufactured duplex stainless steel, J. Mater. Process. Technol. 272 (2019) 58–71.

[11] J. Ge, J. Lin, H. Fu, Y. Lei, R. Xiao, A spatial periodicity of microstructural evolution and anti-indentation properties of wire-arc additive manufacturing 2Cr13 thin-wall part, Mater. Des. 160 (2018) 218–228. https://doi.org/10.1016/j.matdes.2018.09.021.

[12] M.K. Alam, M. Mehdi, R.J. Urbanic, A. Edrisy, Mechanical behavior of additive manufactured AISI 420 martensitic stainless steel, Mater. Sci. Eng. A. 773 (2020) 138815.

[13] M. Ghaffari, A.V. Nemani, A. Nasiri, Interfacial bonding between a wire arc additive manufactured 420 martensitic stainless steel part and its wrought base plate, Mater. Chem. Phys. (2020) 123199.

[14] A.V. Nemani, M. Ghaffari, S. Salahi, J. Lunde, A. Nasiri, Effect of interpass temperature on the formation of retained austenite in a wire arc additive manufactured ER420 martensitic stainless steel, Mater. Chem. Phys. (2021) 124555.

[15] A.J. Sedriks, Corrosion of stainless steel, 2, (1996).

[16] K.H. Anantha, C. Ornek, S. Ejnermark, A. Medvedeva, J. Sj, Correlative Microstructure Analysis and In Situ Corrosion Study of AISI 420 Martensitic Stainless Steel for Plastic Molding, 164 (2017) 85–93. https://doi.org/10.1149/2.0531704jes.

[17] Y. Cao, H. Di, R.D.K. Misra, X. Yi, J. Zhang, T. Ma, On the hot deformation behavior of AISI 420 stainless steel based on constitutive analysis and CSL model, Mater. Sci. Eng. A. 593 (2014) 111–119.

[18] M. Kimura, Y. Miyata, T. Toyooka, Y. Kitahaba, Effect of retained austenite on corrosion performance for modified 13% Cr steel pipe, Corrosion. 57 (2001) 433–439.

[19] B.T. Lu, Z.K. Chen, J.L. Luo, B.M. Patchett, Z.H. Xu, Pitting and stress corrosion cracking behavior in welded austenitic stainless steel, Electrochim. Acta. 50 (2005) 1391–1403. https://doi.org/10.1016/j.electacta.2004.08.036.

[20] S. Salahi, M. Kazemipour, A. Nasiri, Effect of Uniaxial Tension-Induced Plastic Strain on the Microstructure and Corrosion Behavior of 13Cr Martensitic Stainless Steel, CORROSION. (2020).

[21] S. Salahi, M. Kazemipour, A. Nasiri, Effects of microstructural evolution on the corrosion properties of AISI 420 martensitic stainless steel during cold rolling process, Mater. Chem. Phys. 258 (2021). https://doi.org/10.1016/j.matchemphys.2020.123916.

[22] X. Ren, K. Sridharan, T.R. Allen, Effect of grain refinement on corrosion of ferritic–martensitic steels in supercritical water environment, Mater. Corros. 61 (2010) 748–755.

176

[23] L. Tan, X. Ren, K. Sridharan, T.R. Allen, Corrosion behavior of Ni-base alloys for advanced high temperature water-cooled nuclear plants, Corros. Sci. 50 (2008) 3056–3062.

[24] J. Wang, Q. Luo, H. Wang, Y. Wu, X. Cheng, H. Tang, Microstructure characteristics and failure mechanisms of Ti-48Al-2Nb-2Cr titanium aluminide intermetallic alloy fabricated by directed energy deposition technique, Addit. Manuf. (2019) 101007.

[25] M. Kazemipour, J.H. Lunde, S. Salahi, A. Nasiri, On the Microstructure and Corrosion Behavior of Wire Arc Additively Manufactured AISI 420 Stainless Steel, in: TMS 2020 149th Annu. Meet. Exhib. Suppl. Proc., Springer, 2020: pp. 435–448.

[26] J. Lunde, M. Kazemipour, S. Salahi, A. Nasiri, Microstructure and Mechanical Properties of AISI 420 Stainless Steel Produced by Wire Arc Additive Manufacturing, in: TMS 2020 149th Annu. Meet. Exhib. Suppl. Proc., Springer, 2020: pp. 413–424.

[27] J.C. Lippold, D.J. Kotecki, Welding metallurgy and weldability of stainless steels, Weld. Metall. Weldability Stainl. Steels, by John C. Lippold, Damian J. Kotecki, Pp. 376. ISBN 0-471-47379-0. Wiley-VCH, March 2005. (2005) 376.

[28] P. Scardi, L. Lutterotti, A. Tomasi, XRD characterization of multilayered systems, Thin Solid Films. 236 (1993) 130–134.

[29] H. Kitahara, R. Ueji, N. Tsuji, Y. Minamino, Crystallographic features of lath martensite in low-carbon steel, Acta Mater. 54 (2006) 1279–1288.

[30] J. Li, C. Yuan, Q. Qi, X. Bao, X. Gao, Effect of Initial Oriented Columnar Grains on the Texture Evolution and Magnetostriction in Fe–Ga Rolled Sheets, Metals (Basel). 7 (2017) 36.

[31] L.A.I. Kestens, H. Pirgazi, Texture formation in metal alloys with cubic crystal structures, (2016).

[32] T. Nagase, T. Hori, M. Todai, S.-H. Sun, T. Nakano, Additive manufacturing of dense components in beta-titanium alloys with crystallographic texture from a mixture of pure metallic element powders, Mater. Des. 173 (2019) 107771.

[33] A. Kocijan, D.K. Merl, M. Jenko, The corrosion behaviour of austenitic and duplex stainless steels in artificial saliva with the addition of fluoride, Corros. Sci. 53 (2011) 776–783.

[34] D. Wallinder, J. Pan, C. Leygraf, A. Delblanc-Bauer, EIS and XPS study of surface modification of 316LVM stainless steel after passivation, Corros. Sci. 41 (1998) 275–289.

[35] M.K. Alam, M. Mehdi, R.J. Urbanic, A. Edrisy, Mechanical behavior of additive manufactured AISI 420 martensitic stainless steel, Mater. Sci. Eng. A. (2019) 138815.

[36] A. Caballero, J. Ding, S. Ganguly, S. Williams, Wire+ Arc Additive Manufacture of 17-4 PH stainless steel: Effect of different processing conditions on microstructure, hardness, and tensile strength, J. Mater. Process. Technol. 268 (2019) 54–62.

[37] K.W. Andrews, Empirical formulae for the calculation of some transformation temperatures, J. Iron Steel Inst. (1965) 721–727.

[38] S.-Y. Lu, K.-F. Yao, Y.-B. Chen, M.-H. Wang, N. Chen, X.-Y. Ge, Effect of quenching and partitioning on the microstructure evolution and electrochemical properties of a martensitic stainless steel, Corros. Sci. 103 (2016) 95–104.

[39] W.T. Read, W. Shockley, Dislocation models of crystal grain boundaries, Phys. Rev. 78 (1950) 275.

[40] B.R. Kumar, R. Singh, B. Mahato, P.K. De, N.R. Bandyopadhyay, D.K. Bhattacharya, Effect of texture on corrosion behavior of AISI 304L stainless steel, Mater. Charact. 54 (2005) 141–147.

[41] H. Luo, C.F. Dong, K. Xiao, X.G. Li, Characterization of passive film on 2205 duplex stainless steel in sodium thiosulphate solution, Appl. Surf. Sci. 258 (2011) 631–639.

[42] L. Pan, C.T. Kwok, K.H. Lo, Enhancement in hardness and corrosion resistance of AISI 420 martensitic stainless steel via friction stir processing, Surf. Coatings Technol. 357 (2019) 339–347.

[43] M. Kazemipour, S. Salahi, A. Nasiri, Box-Behnken design approach toward predicting the corrosion response of 13Cr stainless steel, Corrosion. 76 (2020). https://doi.org/10.5006/3429.

[44] X. Lei, Y. Feng, J. Zhang, A. Fu, C. Yin, D.D. Macdonald, Impact of reversed austenite on the pitting corrosion behavior of super 13Cr martensitic stainless steel, Electrochim. Acta. 191 (2016) 640–650.

Chapter 5

Effects of Secondary-phase Formation on the Electrochemical Performance of a Wire Arc Additive Manufactured 420 Martensitic Stainless Steel under Different Heat Treatment Conditions [4]

Preface

The original version of this manuscript has already been published in the Journal of Materials Engineering and Performance (JMEP). I am the first and the corresponding author of the current work. In this chapter, I and my colleagues, Dr. Ali Nasiri, Alireza Vahedi Nemani, and Mahya Ghaffari, investigated the impact of secondary phase formation on the electrochemical performance of a wire arc additive manufactured 420 martensitic stainless steel under two different heat treatment conditions. I was responsible for preparing methodology, experimental testing, result gathering, and drafting of the original manuscript. Subsequently, I revised the paper based on my colleagues' initial comments and the peer-review process. The co-authors contributed to the conceptualizing, project administration, supervision, and review & editing of the manuscript

---

[4] Salahi, Salar, Mahya Ghaffari, Alireza Vahedi Nemani, and Ali Nasiri. "Effects of Secondary-Phase Formation on the Electrochemical Performance of a Wire Arc Additive Manufactured 420 Martensitic Stainless Steel under Different Heat Treatment Conditions." *Journal of Materials Engineering and Performance* (2021): 1-12.

Abstract

This study aims to investigate the effects of annealing, quenching and tempering (Q&T) heat treatments on the microstructure, crystallographic orientation, and electrochemical performance of a wall shaped 420 martensitic stainless steel part fabricated by wire arc additive manufacturing (WAAM) technology. The formation of a martensitic matrix with delta ferrite in the as-printed sample, islands of spherical chromium carbides embedded in a ferritic matrix in annealed sample, and intergranular chromium-rich carbides along the primary austenite grain boundaries in addition to intra-lath Fe-rich carbides in the Q&T heat treated sample were detected. To characterize the corrosion performance of the fabricated samples, open circuit potential (OCP), potentiodynamic polarization (PDP), and electrochemical impedance spectroscopy (EIS) tests were performed on all samples in aerated 3.5 wt% NaCl electrolyte at room temperature. The corrosion morphology of the as-printed sample was characterized by localized corrosion attacks adjacent to the delta ferrite phase, while severe pitting occurred in the annealed sample due to the high susceptibility of ferritic matrix-carbide interface to pitting. In contrast to the as-printed and annealed sample, the electrochemical performance of the Q&T samples was found to be significantly improved, ascribed to the elimination of the chromium-depleted regions adjacent to the delta ferrite phase and enhanced protectiveness of the passive film on the alloy's surface.

1. Introduction

Martensitic stainless steels (MSSs) are broadly used in automotive, aerospace, medical, and marine industries due to their excellent combination of mechanical properties and corrosion performance [1]. Unlike the ferritic and austenitic stainless steels, both mechanical and corrosion performance of the MSSs can be controlled by applying proper heat treatments, leading to their expanded demands for structural applications in harsher environments [2]. Most commercial sheets of MSSs are available in the soft annealed condition with islands of spherical carbides embedded in a ferritic matrix, possessing high ductility and relatively lower strength, leading to their outstanding formability [3]. MSSs can also be heat treated through a Q&T cycle, in which newly-precipitated carbides form in a martensitic matrix, resulting in a higher hardness and strength [4,5]. Among all MSSs, AISI 420 MSS with 13 wt% chromium is commonly used for plastic molding applications, where sufficient corrosion and wear resistance is required [6]. Conventional manufacturing techniques, such as forming and casting, have been used for the fabrication of 420 MSS, while several in-service defects, including edge deterioration, diggings, and dents, have been reported for dies fabricated through aforementioned techniques [6]. Recently, additive manufacturing (AM) technology has been adopted for the fabrication of 420 MSS with improved mechanical properties and minimum process-induced defects [1,7]. In a recent study, Alam *et al.* [1] implemented a laser-based AM technique for the fabrication of 420 MSS and reported comparable mechanical properties for the fabricated part relative to its conventionally fabricated counterpart.

Considering the recent COVID-19 outbreak and its impact on the supply chain for many industries, AM technology is suggesting promising on-site production engineering routes for the post-COVID-19 era, especially for the manufacturing sectors [8]. In general, due to the layer-by-

layer construction fashion and other unique process aspects, metal AM can facilitate building complex parts in a timely manner with less material waste than traditional metal manufacturing methods [9]. As one of the fastest evolving metal AM technologies, WAAM technology implements an electric arc or plasma as the heat source to fabricate medium to large-scale metal parts using a continuous wire as the feedstock material [10]. In the authors' previous works [11,12], the fabrication feasibility of 420 MSS parts using the WAAM technique and the preliminary mechanical properties and corrosion performance of the alloy in as-printed condition were reported. Rapid solidification and complex heating and cooling cycles associated with the WAAM process lead to the formation of a non-homogeneous microstructure containing non-equilibrium micro-constituents [6]. The presence of secondary non-equilibrium micro-constituents can adversely impact the corrosion performance of the as-printed samples [12]. Hence, developing a systematic post-printing heat treatment cycle is required to eliminate the formation of unfavorable micro-constituents and enhance the mechanical and corrosion performance of the WAAM part. Furthermore, the variation of crystallographic orientation (texture) during post-printing heat treatment can also contribute to the overall corrosion resistance of the alloy either by formation of a preferential texture during the heat treatment process or altering the misorientation nature of grain boundaries [4,13]. Therefore, this study aims to characterize the effect of different post-printing heat treatments, *i.e.* annealing and quenching and tempering, on the corrosion performance of a WAAM fabricated 420 MSS with respect to the micro-constituents' evolution and texture annihilation during heat treatment.

2.   Experimental procedure

WAAM technology was adopted to fabricate a wall of 420 MSS on a 30 mm thick base plate of AISI 420 stainless steel using ER420 feedstock wire. The chemical composition of both ER420 wire and AISI 420 substrate are reported in Table 5. 1. As shown in Figure 5. 1, a gas metal arc welding (GMAW) torch mounted on a robotic arm, along with an automated wire feeding system were employed to fabricate a 25-layer wall with the dimensions of $160 \times 160 \times 6$ mm^3 using an all-x scanning strategy and the inter-layer temperature of 100 °C (attained by ~ 7 min of dwelling time between the deposition of two consecutive layers). The implemented WAAM process parameters are summarized in Table 5. 2. To eliminate the process-induced microstructural inhomogeneities and unfavorable phases, the as-printed samples were exposed to annealing and Q&T heat treatments. For annealing, the as-printed sample was held at 850°C for 120 min, followed by cooling to room temperature in the furnace. For Q&T, the as-printed sample was first austenitized for 30 min at 1150°C and then quenched in the air to room temperature. After a detailed investigation on the effect of several tempering temperatures on the electrochemical response of the samples (to be reported by the authors in another study), 400°C was selected as the optimum tempering temperature. The as-quenched sample was then subjected to a 4 h tempering cycle at 400°C, followed by air cooling.
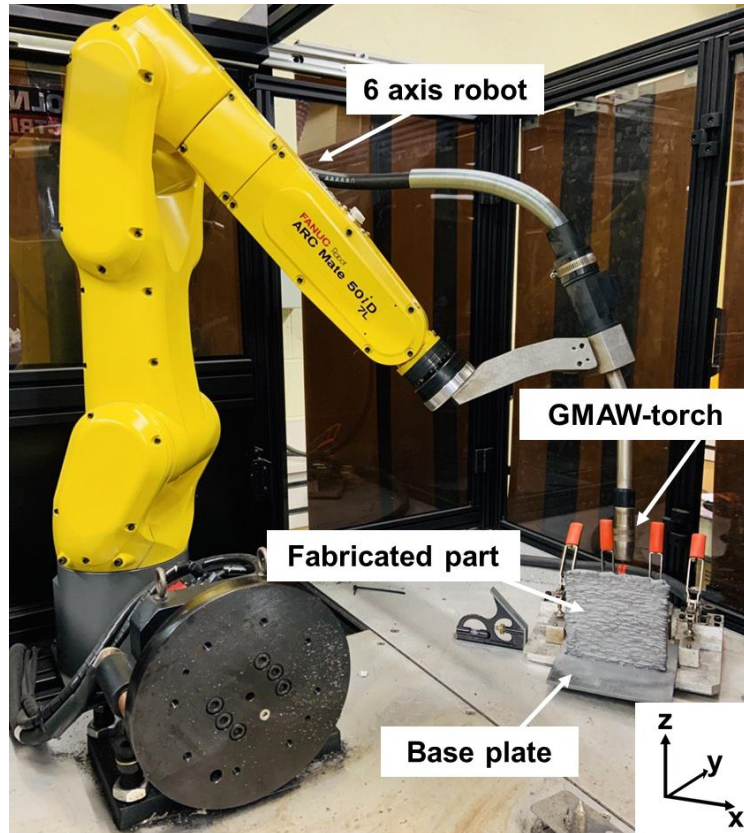
Figure 5. 1. The WAAM platform used for the fabrication of 420 MSS walls in this study.

Table 5. 1. The nominal chemical composition of the used materials in this study (all data in wt.%).

Material	C	Cr	Mn	Si	S	P	Ni	Mo	Cu	V	Fe
ER420	0.3-0.4	12-14	0-1	0-1	0-0.03	0-0.04	0-0.5	0-0.5	0-0.5	-	Bal.
AISI420	0.15-0.46	12-14	0.4-1	0-1	0-0.03	0-0.04	-	0-0.1	-	0.3	Bal.

Table 5. 2. The WAAM process parameters used for the fabrication of AISI 420 MSS wall in this study.

Current	Arc Voltage	Wire Feeding Rate	Scanning Rate	Ar Flow Rate
135 A	29 V	67.7 mm/s	3.6 mm/s	20 L/min

For microstructural characterizations, samples were cut, mounted, and prepared following standard grinding and polishing procedures for stainless steels, and then etched using Villella's reagent for 20 s. The microstructural characteristics of the samples were studied using an FEI MLA 650F scanning electron microscope (SEM) equipped with an energy-dispersive X-ray

spectroscopy (EDS) detector. Electron backscatter diffraction (EBSD) analysis was also conducted using an HKL EBSD system at the step size of 0.5 μm. X-ray diffraction (XRD) analysis was also performed using a Cu-K$_\alpha$ source at 40 kV and 30 mA.

The electrochemical behavior of the samples was examined through OCP and PDP testing. The EIS testing was also conducted to measure and analyze the electronic properties of the passive film formed on all samples. Electrochemical measurements were performed in aerated 3.5 wt% NaCl solution using an IVIUM CompactStat™ computer-controlled Potentiostat apparatus. A conventional three-electrode cell set-up, containing a saturated Ag/AgCl electrode as the reference electrode, a graphite rod as the counter electrode, and the prepared samples as the working electrode were used. Prior to each PD and EIS experiments, the OCP values were also monitored for 1 h for stabilization. Separately,the OCP measurements were conducted over 14 h to analyze the electrochemical stability of samples over a longer period of time. The PDP tests were conducted at the scanning rate of 0.4 mV/s in the potential range of -0.2 V up to 0.5 V versus OCP. The EIS measurements were conducted over the frequency range of 10^5 Hz to 10^{-2} Hz with a sinusoidal perturbation signal voltage of 10 mV after 1 h and 120 h of immersion time. All electrochemical experiments for each condition were repeated at least five times to ensure the reproducibility of the results.

3.   Results

3.1.Microstructural characterization:

The low and high magnification SEM images of the as-printed sample and its corresponding EDS elemental maps of iron and chromium are illustrated in Figure 5. 2a-2c. The low magnification micrograph of the as-printed sample (Figure 5. 2a) exhibits a columnar dendritic structure, grown along the building direction (Z-axis) parallel to the heat dissipation direction. As shown in Fig. 2b,

a fine lath martensitic structure (M phase) along with a high-volume fraction (~20%) of δ-ferrite (DF) phase are formed in the as-printed part. While the formation of a martensitic structure containing δ-ferrite phase is not expected according to the pseudo-binary phase diagram of 420 MSS alloy [3], a martensitic matrix in the as-printed sample has formed due to the non-equilibrium solidification condition with relatively high cooling rate associated with the WAAM process [6]. Moreover, the stabilization of the δ-ferrite phase at ambient temperature is correlated to the high chromium content of the alloy (Figure 5. 2c), as a ferrite stabilizing element, accompanied by the rapid solidification nature of process that hinders the diffusion-controlled transformation of δ-ferrite to austenite at ~1400 °C [6]. On the other hand, the Cr-EDX line scan analysis along the delta ferrite-matrix interface (Figure 5. 2c) revealed that in the area adjacent to the delta ferrite-matrix interface, Cr concentration reduced to less than 11 wt.%, confirming formation of Cr depleted region at the interface in the as-printed sample.

Figure 5s. 2d-2f exhibit the SEM micrographs of the annealed sample and the corresponding EDS elemental maps of iron, chromium, and carbon elements. The annealed sample (Figure 5s. 2d and 2e) revealed the suggested microstructure by the pseudo-binary phase diagram of 420 MSS alloy with islands of spherical chromium carbides embedded in a ferritic matrix [3]. The EDS elemental map of the annealed sample (Figure 5. 2f) shows enrichment in chromium and carbon and depletion in iron, indicating the formation of chromium-rich carbides.

SEM micrographs of the Q&T sample at three different magnifications are shown in Figure 5s. 2g-2i. The formation of a fully martensitic matrix without any undissolved carbides (coarse spherical carbides) and dissolution of δ-ferrite phase were detected in the as-quenched sample before tempering, indicating the samples' proper austenitization at 1150 °C . Austenite grains are formed through austenitization and transformed on cooling, while the segregation of chromium

carbides at the prior austenite grain boundaries (PAGBs) (see Figure 5. 2h) and the formation of sub-micron intra-lath chromium carbides occurred during the tempering process (Figure 5. 2i). Previous studies on the MSS with 13 wt% chromium content [14,15] suggested that the intra-lath carbides formed at low tempering temperatures (~400 °C) were mainly characterized as nano-sized M_3C type carbides with similar Cr-concentration to the martensitic matrix
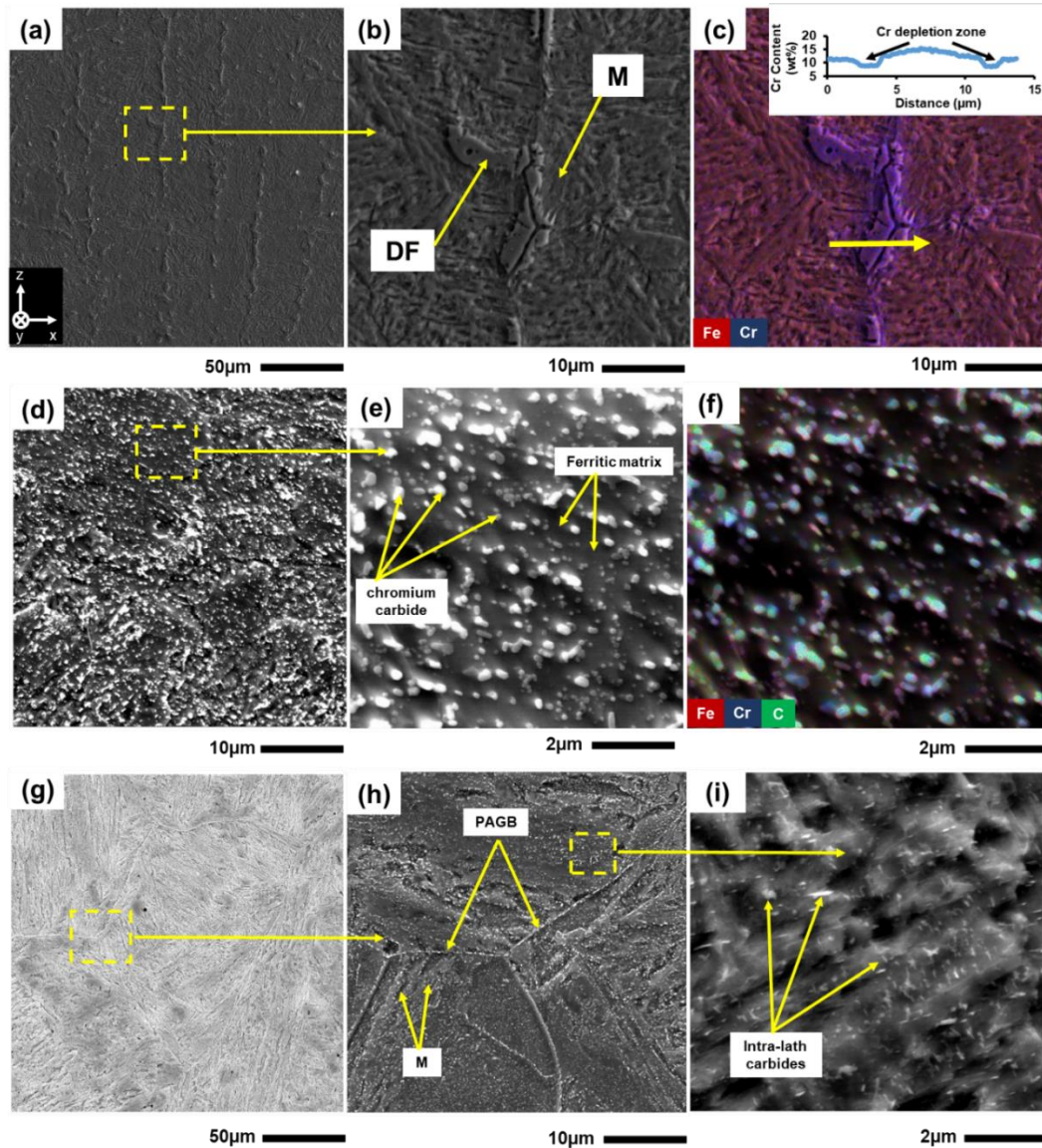
Figure 5. 2. (a) Low magnification SEM micrograph of the as-printed sample along with (b) its high magnification SEM showing the formation of the δ-ferrite phase and (c) its corresponding EDS elemental map and line scan showing high concentration of Cr in the δ-ferrite phase, (d and

e) multi-scale SEM micrographs of the annealed sample showing islands of spherical carbides in a ferritic matrix and (f) its corresponding EDS elemental map showing high concentration of Cr and C in the spherical carbides, (g) low magnification SEM micrograph of the Q&T and (f) high magnification SEM showing PAGBs, intergranular carbides, and martensitic phase, and (i) formation of intra-lath carbides in the martensitic phase.

The XRD patterns of the as-printed, annealed, and the Q&T samples are shown in Figure 5. 3. The XRD spectra of the as-printed sample exhibits the presence of martensitic phase at (110), (200), (211), and (220) planes along with low-intensity peaks of austenite phase (γ) at (111) and (200) planes. Presence of $(111)_\gamma$ and $(200)_\gamma$ peaks indicates the formation of retained austenite phase through the solidification process due to the sequential heating and cooling cycles associated with the WAAM process and also the noticeable content of carbon as an austenite stabilizing element in the alloy [6,12]. The formation mechanism of the retained and reversed austenite in the WAAM-420 stainless steel is thoroughly explained in the authors' previous works [11,12]. No δ-ferrite peaks were distinguished on the XRD spectra due to only minor variation of lattice parameters between martensite and δ-ferrite phases (10^{-4}-10^{-5}nm) [16]. The XRD spectra of the annealed and Q&T samples show the same ferritic/martensitic peaks as the as-printed sample, while the $(111)_\gamma$ and $(200)_\gamma$ are disappeared after annealing and tempering cycles. During the Q&T heat treatment process, the sample experiences a single fast cooling cycle from the austenitizing temperature, and the tempering temperature (400 °C) is not sufficient to activate the reversed austenite formation. On the other hand, during the annealing process, the diffusional segregation of carbon element from the austenite phase to the ferritic matrix eliminates the retained austenite phase from the as-printed structure.
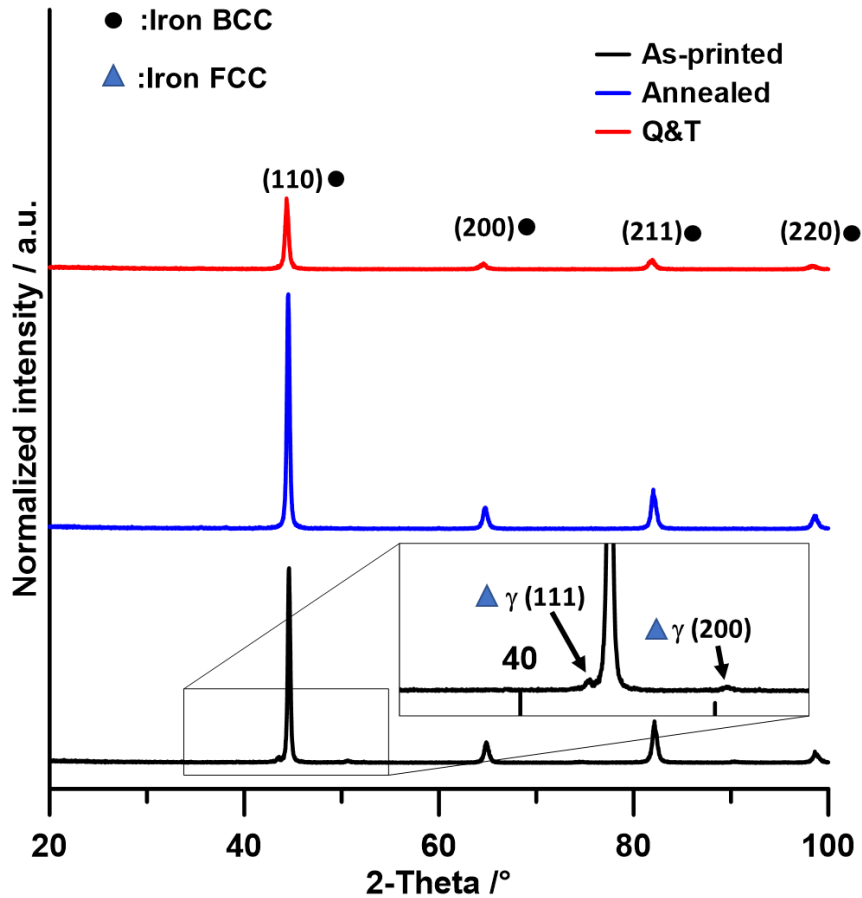
Figure 5. 3. The XRD results of the as-printed, annealed, and Q&T samples.

3.2.Crystallographic orientation characterization:

Figure 5. 4a-4c illustrate the inverse pole figure (IPF) maps superimposed on the grain boundaries maps for the as-printed, annealed, and the Q&T samples, respectively. The IPF of the as-printed sample reveals a fine martensitic lath structure formed within the coarse primary austenite grains (marked with black lines) with several crystallographic orientations normal to {001}, {101}, and {111} planes. Unlike the as-printed sample, the IPF map of the annealed sample (Figure 5. 4b) reveals an equiaxed and coarser grain structure. Moreover, as shown in Figure 5. 4c, the IPF of the Q&T sample exhibits a tempered martensitic structure, characterized by a three-level hierarchy within its morphology, *i.e.*, martensite lath, block, and packet, confined within the PAGBs (marked with black lines). Distribution of low angle grain boundaries (LAGBs), medium

angle grain boundaries (MAGBs), and high angle grain boundaries (HAGBs), for the as-printed, annealed, and Q&T samples are exhibited in Figure 5. 4d-4f. It is notable that the distributions of the LAGBs and HAGBs remain relatively the same for the as-printed and the Q&T samples, while the annealed sample exhibits a significantly lower fraction of LAGBs and a higher fraction of HAGBs. Statistical illustration of the misorientation angle distribution at Figure 5. 4j reveals that the fraction of the LAGBs for the annealed sample is ~11%, while this fraction is ~51 % and ~56 % for the as-printed and Q&T samples, respectively. Additionally, Figure 5. 4g-4i illustrate the grain and lath size distributions, extracted from the EBSD data, representing the size of martensite laths for the as-printed and Q&T samples and the ferrite grain size for the annealed sample. Both as-printed and Q&T samples exhibit a high fraction of relatively fine lath structure (average lath size ~ 2.50 μm), while the annealed sample exhibits relatively coarser grain structure with an average grain size of ~ 5.25 μm.
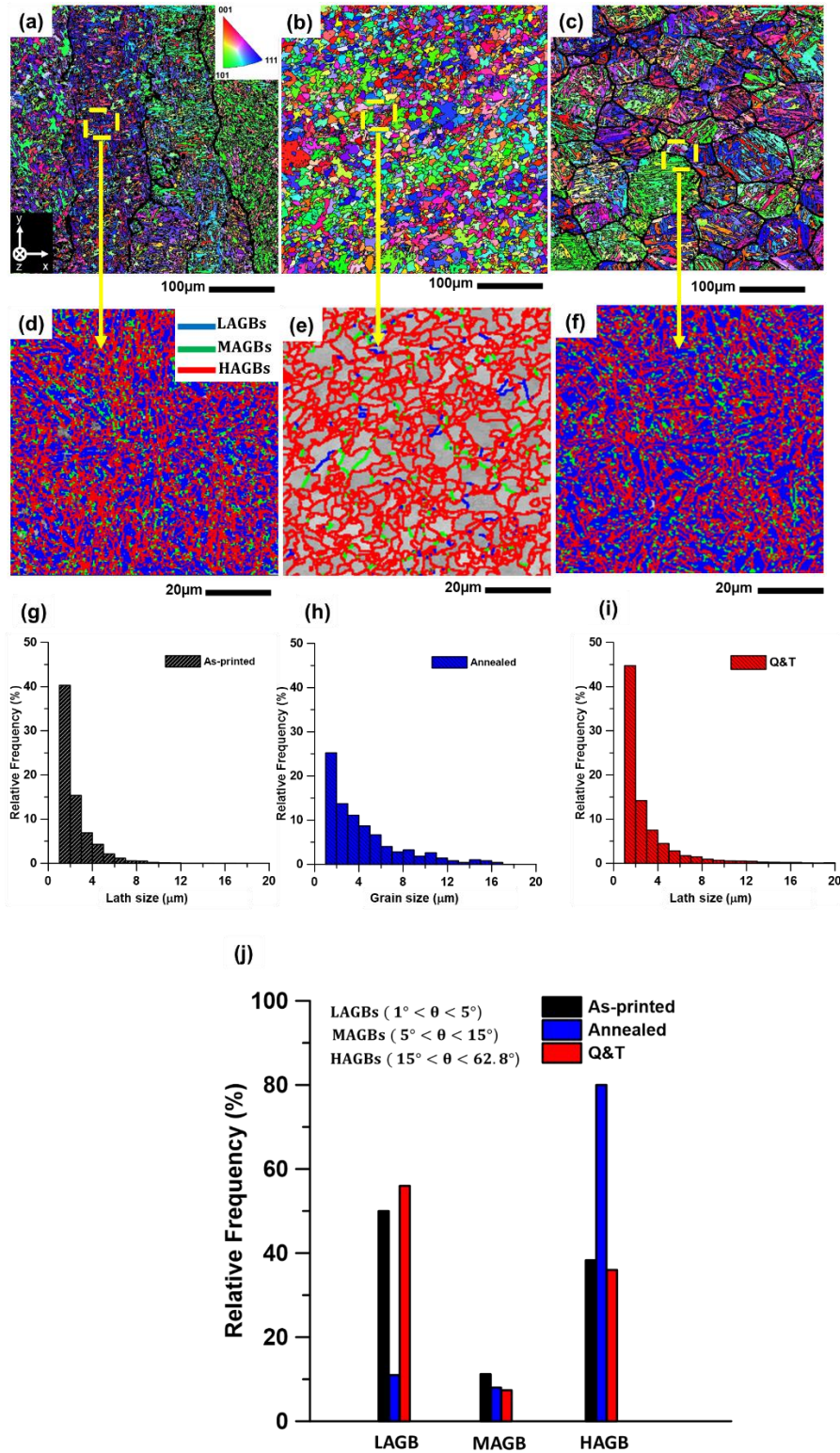
Figure 5. 4. (a-c) The IPF maps superimposed on the grain boundary maps for the as-printed, annealed, and the Q&T samples, respectively, (d-f) the corresponding grain boundaries

misorientation maps, (g-i) grain size distribution plots, and (j) grain boundaries misorientation angles distributions for the studied samples.

The pole figures (PFs) of the as-printed, annealed, and Q&T samples at {100}, {110}, and {111} planes are demonstrated in Figure 5. 5 and the building direction (BD) and the deposition direction (DD) are marked as well . The PF of the as-printed sample (Figure 5. 5a) exhibits a strong cubic texture at {100} planes (maximum intensity of ~4.22 MUD), ascribed to the directional solidification along the maximum thermal gradient direction [7]. Contrarily, the pole figures of annealed and Q&T samples (Figure 5. 5b and 5c) exhibit relatively weaker texture, ascribed to the elimination of solidification texture during recrystallization (in the annealed sample) or austenitization (for the Q&T sample). The orientation distribution function (ODF) maps based on the PF stereographs at $\varphi_2=45°$ associated with the detailed crystallographic orientation of each texture component and their corresponding 3D plots are shown in Figure 5. 6. Figure 5. 6a and 6b exhibit a strong dominancy of preferred columnar {001}<100> solidification texture combined with {111}<110> texture component with the maximum intensity of 6.52, while significantly weaker columnar {001}<100> texture is observed for the heat-treated samples (Figure 5. 6c-6f). The annealed sample exhibits {111}<110> and {011}<111> texture components along with full elimination of {001}<100> solidification texture (Figure 5. 6c), ascribed to occurrence of severe recrystallization during annealing, while weak {001}<100> and {011} <111> texture components are observed for the Q&T sample (Figure 5. 6e).
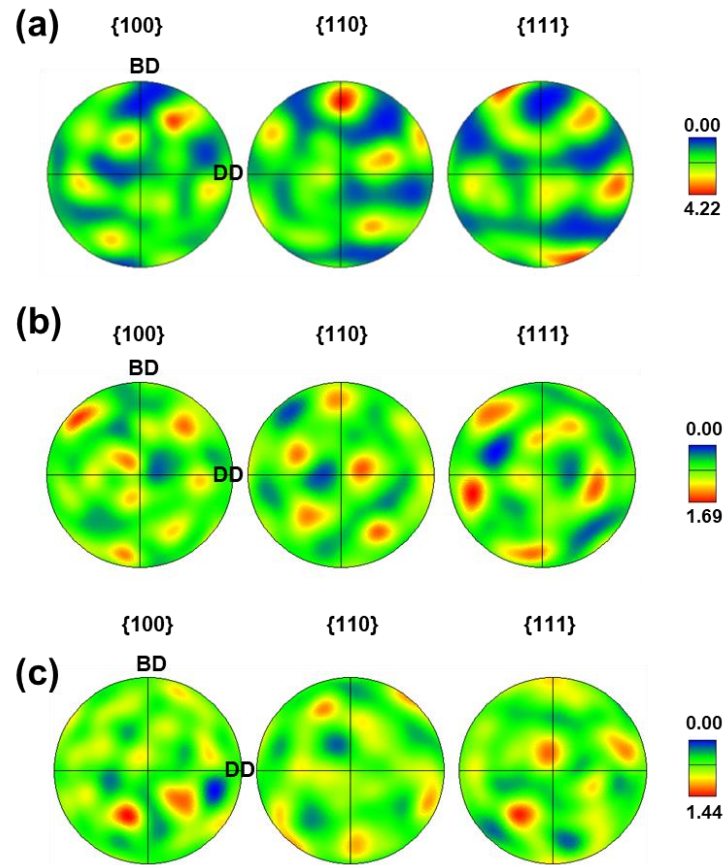
Figure 5. 5. EBSD pole figure maps of (a) the as-printed, (b) annealed, and (c) the Q&T samples.
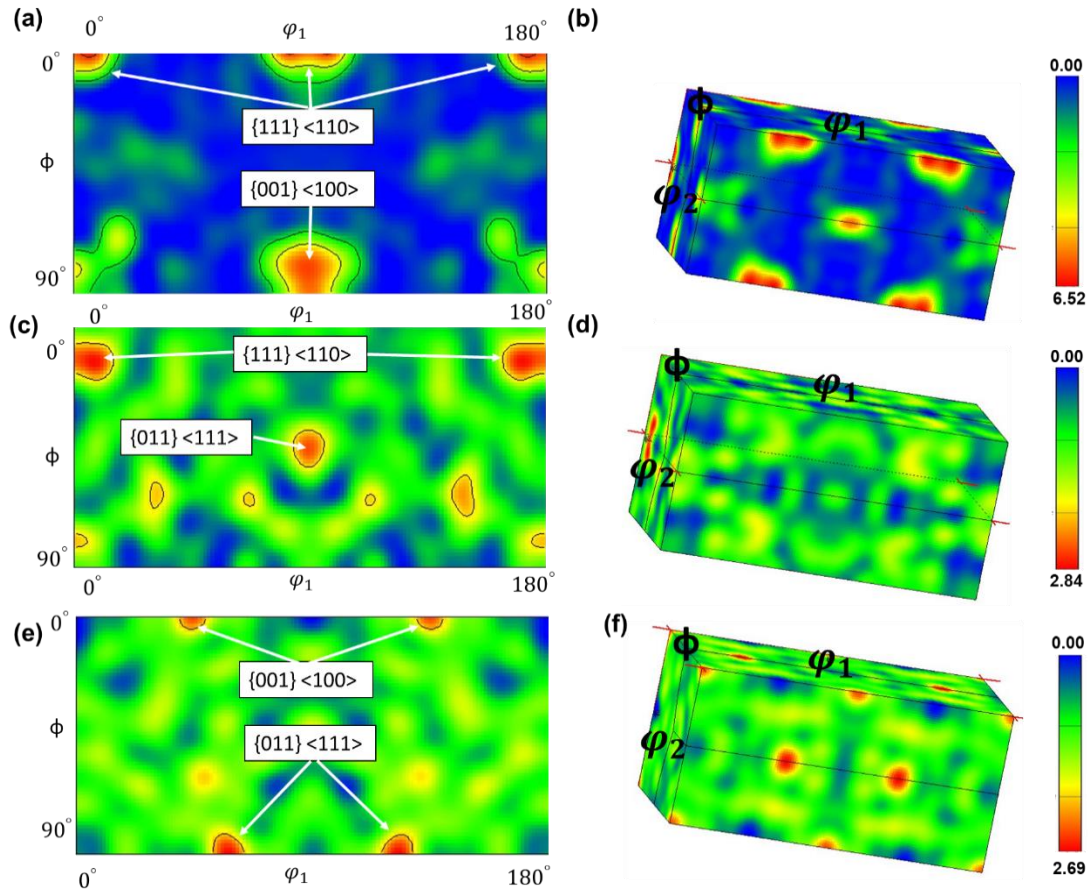
Figure 5. 6. Angular textural cross-sections of orientation distribution function at $\varphi_2=45°$ and their corresponding 3D-plots for (a and b) the as-printed, (c and d) annealed, and (e and f) the Q&T samples

3.3. Corrosion results:

The OCP values variations over 14 h in aerated 3.5 wt% NaCl solution for the as-printed and heat-treated samples are displayed in Figure 5. 7a. The OCP trend relatively stabilized after nearly 9.7 h, and the average stabilized OCP value for the as-printed sample was found to be -390$\pm$20 mV$_{Ag/AgCl}$, while it increases to -365$\pm$15 mV$_{Ag/AgCl}$ and -315$\pm$25 mV$_{Ag/AgCl}$ for the annealed and Q&T samples, respectively. Severe fluctuations were observed in the OCP values of the annealed and Q&T samples at the initial monitoring times (immersion time $\leq 10^4$ s), possibly ascribed to continuous metastable pitting or some type of localized attack on the samples surfaces [3] that eventually decreases the OCP value at immersion times higher than 10^4 s.

Following the OCP measurements, the PDP experiments were conducted to characterize the electrochemical behavior of the samples, as shown in Figure 5. 7b. The obtained electrochemical parameters from the PDP graphs, *i.e.* corrosion current density (i_{corr}), corrosion potential (E_{corr}), pitting potential (E_{pit}), and passivation current density (i_p) are summarized in Table 5. 3. A wide passive region with clear breakdown potential was observed for the Q&T sample, while an active-like behavior, characterized by a rapid increase of the anodic current density at potentials higher than E_{corr}, was detected for the as-printed and annealed samples, suggesting the continuous occurrence of severe localized corrosion attacks that hinder the formation of an intact passive film on the samples' surfaces. The observed fluctuations in the anodic branch for the Q&T sample also correspond to metastable pitting [3]. The Q&T sample exhibited higher E_{corr} and lower i_{corr} values as compared to the as-printed and annealed samples, indicating its lower corrosion susceptibility and higher electrochemical stability, consistent with the OCP trends.
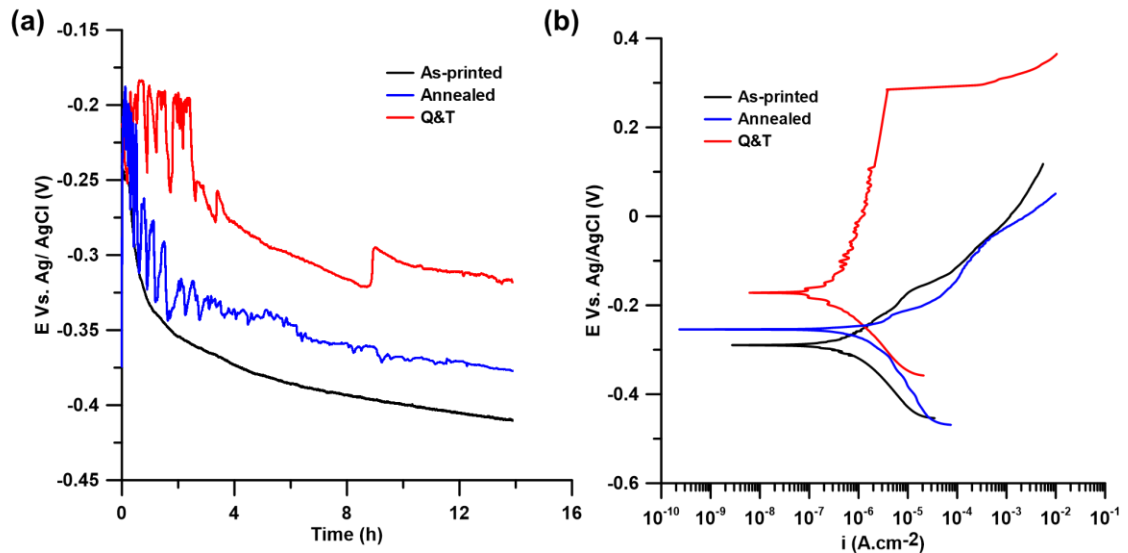
Figure 5. 7. (a) The open-circuit potential (OCP) values versus time, (b) potentiodynamic polarization curves for the as-printed, annealed, and the Q&T samples in aerated 3.5 wt.% NaCl solution

Table 5. 3. The electrochemical parameters extracted from the PDP graphs in aerated 3.5 wt.% NaCl solution at room temperature.

Sample	E_{corr} (mV$_{Ag/AgCl}$)	i_{corr} (μA cm^{-2})	i_p (μA cm^{-2})	E_{pit} (mV$_{Ag/AgCl}$)
As-printed	-293±12	0.62±0.05	-	-
Annealed	-258±15	0.44±0.03	-	-
Q&T	-176±13	0.21±0.04	8.256±0.04	302±15

In order to analyze the protectiveness and stability of the passive film on the samples' surfaces, the EIS experiments were conducted in aerated 3.5 wt% NaCl electrolyte. Figure 5. 8 shows the obtained Nyquist diagrams for the as-printed and heat-treated samples, after 1 h and 120 h of immersion times. Nyquist diagrams of all samples exhibited one broad capacitive semicircle as a result of the superposition of two individual peaks with neutral time constants for both immersion times [13]. The significantly larger semicircle curves in the Nyquist diagrams for the Q&T sample at both immersion times as compared to the other two samples confirm the more protective nature of the passive film formed on the Q&T sample [13], consistent with the observed trend in the PDP results. After the longer immersion time of 120 h, a significant reduction in the radius of the Nyquist curves was detected, ascribed to the continuous dissolution of the passive layer into the solution over time, causing severe deterioration in the electrochemical stability [13]. As shown in Figure 5. 8a, a simplified equivalent circuit (SEC) was fitted to the EIS data to quantitatively analyze the passive film evolution on the samples' surfaces. The obtained fitted results are also plotted on the Nyquist diagrams (Figure 5. 8a and 8b). In the used SEC model, R_s corresponds to the electrolyte resistance, CPE_p and R_p represent the capacitance and the resistance of the passive film, CPE_{dl} and R_{ct} correspond to the double layer constant phase element (CPE) and its charge transfer resistance, respectively [4]. The impedance value of the CPE can be described as: $Z_{CPE} = [Y_0(j\omega)^n]^{-1}$, where Y_0 is the CPE constant, ω is the angular frequency, n is the dispersion

coefficient of the *CPE, and* $j = -(1)^{1/2}$ [4]. The fitting parameters obtained from the EIS results are summarized in Table 5. 4. At both immersion times of 1 h and 120 h, the Q&T sample showed higher R_{ct} and lower CPE_{dl} values as compared to the other two samples, revealing the more protective nature of the passive layer against localized attack on the Q&T sample. Significantly lower R_{ct} and R_p values at 120 h as compared to the samples immersed for 1 h indicate the reduced stability of the passive film at longer immersion times in the electrolyte. The obtained lower R_{ct} values than their corresponding R_p values for the as-printed and annealed samples at both immersion times confirms the active-like behavior of the samples' surfaces, while an opposite trend ($R_p < R_{ct}$) was detected for the Q&T sample, indicating its clear passive behavior.
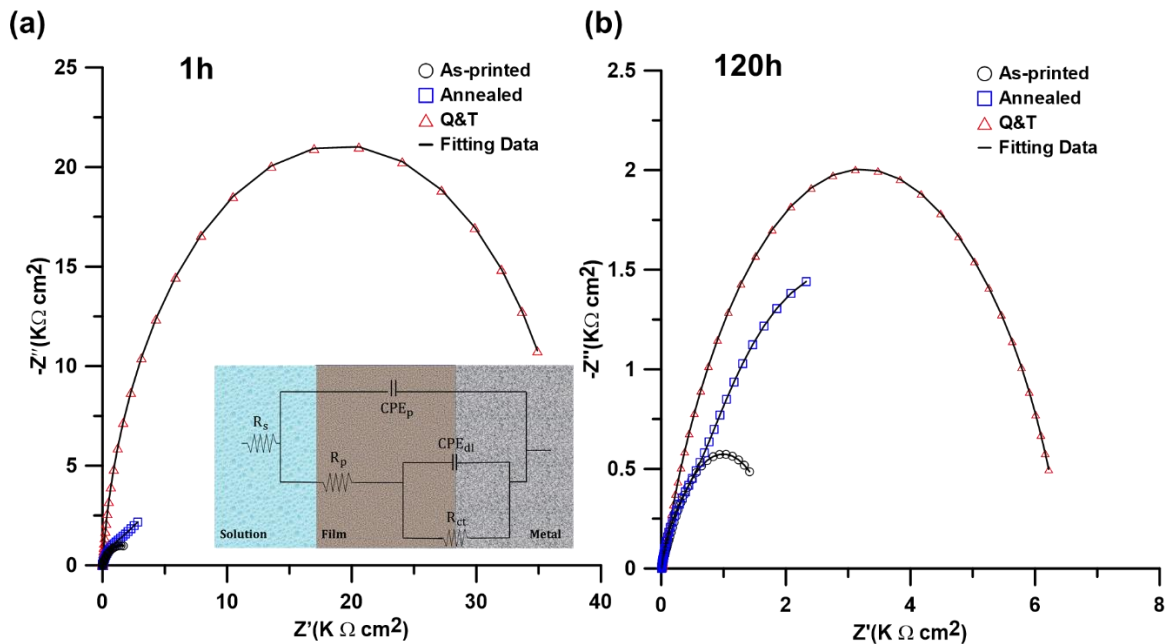
Figure 5. 8. Nyquist plots and the corresponding equivalent circuit model used to describe the EIS data at immersion times of (a)1 h, (b) 120 h.

The power-law model developed by Hirschorn *et al.* [17], is used as a practical technique to analyze the CPE parameters in terms of passive film thickness and resistance. In this model [17],

the C_{eff} is described as: $C_{eff} = gQ(\rho_\delta \varepsilon_0 \varepsilon)^{1-n}$, where ε is the passive film dielectric constant

(~15.6 for Cr_2O_3), ε_0 is the vacuum permittivity (8.854×10^{-14} Fcm^{-1}) [18], g is a function of n

($g = 1 + 2.88(1 - n)^{2.375}$), and ρ_δ is the passive layer resistance at its maximum thickness. The

passive layer thickness in steady-state condition (L_{ss}) can be estimated based on the EIS data and

using the plate capacitor relationship as suggested in [13,19]: $L_{SS} = \frac{\varepsilon \varepsilon_0 A}{C_{eff}}$, where A is the is the

surface area of the corroded sample. The calculated L_{ss} and C_{eff} values for the samples, presented

in Table 5. 5, confirmed a higher passive layer thickness for the Q&T sample, while it decreases

for the other samples in the order of annealed sample > as-printed sample, consistent with the OCP,

PDP, and EIS results.

Table 5. 4. The fitted electrochemical parameters for the EIS spectra.

Immersion Time (h)	Sample	R_s (Ωcm^2)	CPE_p (Ω^{-1}cm^{-2}s^n)	n_1	R_p (Ωcm^2)	CPE_{dl} (Ω^{-1}cm^{-2}s^n)	n_2	R_{ct} (Ωcm^2)	$\sum \chi^2$
1	As-printed	3.54	1.75×10^{-4}	0.89	1.40×10^4	1.33×10^{-4}	0.88	1.89×10^2	1.27×10^{-5}
	annealed	3.56	6.82×10^{-5}	0.96	2.60×10^4	5.74×10^{-5}	0.94	1.93×10^3	1.64×10^{-5}
	Q&T	3.58	9.27×10^{-6}	0.94	1.19×10^2	2.62×10^{-5}	0.86	1.90×10^5	1.62×10^{-5}
120	As-printed	3.54	9.94×10^{-4}	0.89	6.04×10^3	1.83×10^{-4}	0.83	1.03×10^2	1.52×10^{-5}
	annealed	3.58	4.23×10^{-4}	0.88	1.74×10^3	1.25×10^{-3}	0.84	1.24×10^3	1.47×10^{-5}
	Q&T	3.65	8.24×10^{-5}	0.87	1.12×10^2	2.71×10^{-2}	0.98	7.5×10^3	1.25×10^{-5}

Table 5. 5. The calculated capacitance (C_{eff}) and passive layer thickness (L_{ss}).

Immersion Time (h)	Sample	C_{eff} (Fcm^{-2})	L_{ss} (nm)
1	As-printed	6.52×10^{-4}	0.52
	annealed	4.06×10^{-4}	1.07
	Q&T	1.45×10^{-5}	61.23
120	As-printed	8.24×10^{-4}	0.25
	annealed	6.03×10^{-4}	0.43
	Q&T	4.62×10^{-5}	18.05

4.   Discussion

It is well-known that the electrochemical response of MSSs is highly dependent on the formation of micro-constituents, where micro-galvanic coupling between the anodic martensitic/ferritic matrix and cathodic carbides (mostly chromium carbides) governs the localized corrosion attack [3]. The same scenario can be seen in the WAAM 420 MSS, where δ-ferrite phase possessing a high content of chromium, plays the same role as cathodic intergranular carbides and can adversely impact the corrosion performance [12]. Regions at the periphery of the δ-ferrite phase are mostly chromium depleted (shown in Figure 5. 2c), since the Cr-rich δ-ferrite phase drains the chromium element from its adjacent matrix, causing the susceptibility of the δ-ferrite/martensite interface to initiation of corrosion attack [12]. Such corrosion attack initiation sites were observed at the interface of the δ-ferrite phase and martensitic matrix in the as-printed sample, after the PDP test, as shown in Figure 5. 9a, and 9b. The EDS elemental maps (Figure 5. 9c and 9d) revealed the sensitized regions with high concentration of chromium at the δ-ferrite/matrix interface due to the preferential dissolution of Fe element (Figure 5. 9c) during the corrosion testing, while Cr element does not seem to leach from the surface [4,13]. The presence of a high fraction of δ-ferrite phase (~20%) in the microstructure of the as-printed sample provokes the occurrence of micro-galvanic coupling between the cathodic delta ferrite phase and the Cr-depleted martensitic matrix and acts as the main factor for deterioration of the electrochemical response and active-like behavior of this sample [11]. Similarly, the active behavior of the annealed sample through the PDP test is ascribed to the high volume fraction of intergranular chromium carbides at the ferritic matrix and higher susceptibility of matrix/carbide interface to the pitting initiation [4,5]. The corrosion morphology of the annealed sample (Figure 5. 9e and 9f) revealed stable pit growth on its surface, characterized

by the formation of propagated pitting sites resulted from continuous growth and coalescence of the pits as the corrosion progresses. The EDS mapping from one of the surface pits revealed selective dissolution of Fe element from the pit and its border, creating a Cr-rich band along its periphery (Figure 5. 9g and 9h). As shown in Figure 5. 9i-9l, the corrosion mechanism of the Q&T sample is controlled by the intergranular corrosion at the PAGBs, where a chromium depleted region is formed through precipitation of the intergranular carbides adjacent to the high energy grain boundaries. Interestingly, it is observed that the martensitic matrix in the interior of PAGs is highly resistant to localized corrosion, possibly attributed to the chemical composition of the intra-lath carbides (see Figure 5. 2i) [14,15]. Previous studies have revealed that the morphology, size, and chemical composition of tempered carbides are highly dependent on the tempering temperature [14,15]. The intra-lath carbides formed at 400 °C are mostly nano-sized M_3C type carbides with chemical composition and chromium concentration similar to the martensitic matrix [14,15], hindering the micro-galvanic coupling effect at their interface with the matrix, leading to the formation of a uniform passive layer on the Q&T sample.

In addition to the impact of secondary phases as the dictating factor that controls the corrosion behavior of the studied alloy, the distribution of grain boundary misorientation maps for the as-printed and heat-treated samples herein (Figure 5. 4j) revealed that the annealed sample possesses a significantly lower fraction of LAGBs and higher fraction of HAGBs, while the fractions of LAGBs and HAGBs are relatively constant for the as-printed and the Q&T sample. According to the Read-Shockley equation [20], the amount of stored energy in the grain boundaries is proportional to the grain boundaries misorientation angle with some exceptions, such as twin boundaries. Although not significant, this can be considered as a minor contributing factor to the reduced corrosion performance of the annealed sample with a high fraction of high energy HAGBs,

where fast diffusion paths can be easily activated [21]. The noticeable higher fraction of LAGBs in the Q&T sample can support the formation of a more uniform passive film on its surface resulted from the proximity of the grain boundary diffusivity and the material's bulk diffusivity [21].
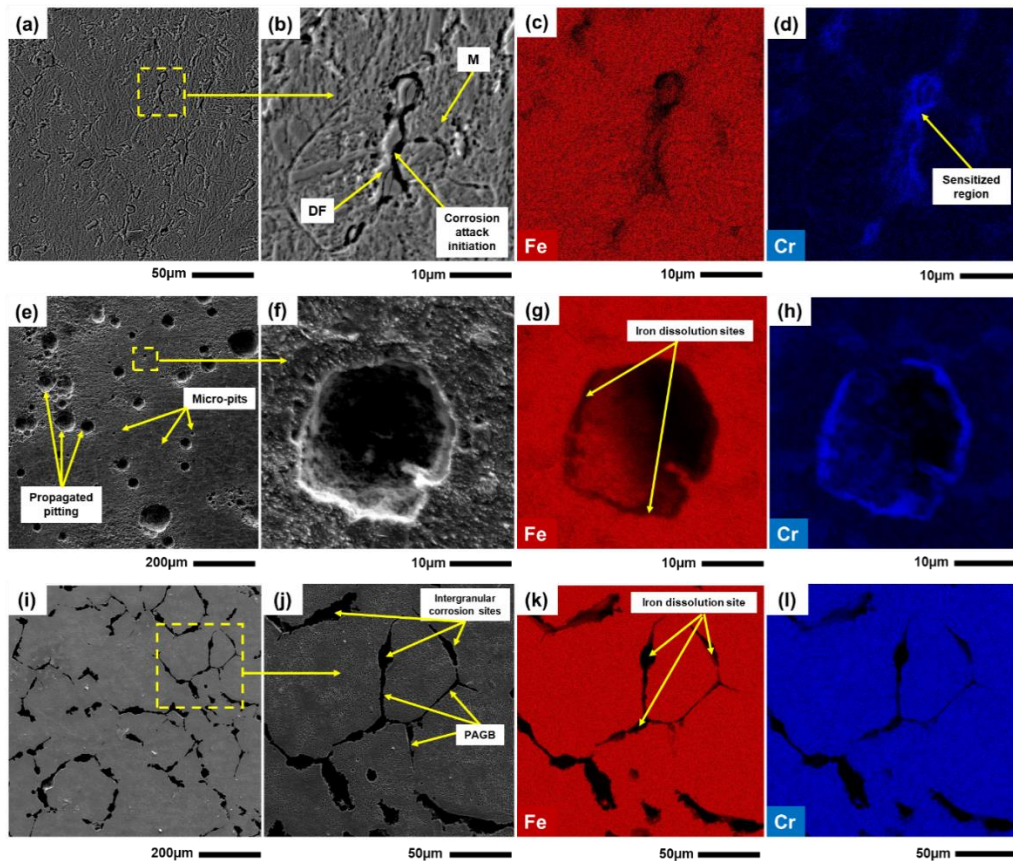
Figure 5. 9. (a) The SEM micrographs from the as-printed sample after polarization testing, (b) higher magnification SEM micrograph from the enclosed area in (a), (c and d) the corresponding EDX-Fe and EDX-Cr concentration maps, respectively, (e) the SEM micrographs from the annealed sample after polarization testing, (f) higher magnification SEM micrograph from the enclosed area in (f) showing the micro-pit formation, (g and h) the corresponding EDX-Fe and EDX-Cr concentration maps, respectively, (i) the SEM micrographs from the Q&T sample after polarization testing, (j) higher magnification SEM micrograph from the enclosed area in (i), and (k and l) the corresponding EDX-Fe and EDX-Cr concentration maps, respectively.

5.   Conclusions

In this study, the effects of different heat treatment processes, *i.e.* annealing and quenching & tempering (Q&T) cycles, on the electrochemical stability of a WAAM fabricated 420 MSS were investigated. The microstructure of the as-printed sample contained martensite laths with an average lath size of ~2.5 µm along with the delta ferrite phase. The annealed sample exhibited islands of spherical chromium carbides embedded in a ferritic matrix, while the Q&T sample showed intergranular carbides precipitated at the PAGBs, and sub-micron intra-lath carbides. While the as-printed sample exhibited strong {001}<100> solidification texture, the annealed and Q&T samples showed relatively weaker texture components, ascribed to the elimination of solidification texture during phase transformations. The PDP and EIS testing revealed the formation of a uniform passive film on the Q&T sample, while an active-like behavior was observed for the as-printed and annealed samples. The higher corrosion potential and lower corrosion current density of the Q&T sample consistent with its Nyquist's larger capacitive loop confirmed its better electrochemical response as compared to the other two samples. The corrosion morphology of the samples after the PDP test revealed severe localized corrosion attack on the as-printed sample, severe localized pitting on the annealed sample, and early stage of intergranular corrosion at the PAGBs on the Q&T sample. The superior corrosion response of the Q&T sample was attributed to the formation of intra-lath M_3C type carbides with similar chemical composition to the matrix and lack of sensitized regions on its surface.

References

[1]   M.K. Alam, M. Mehdi, R.J. Urbanic, A. Edrisy, Mechanical behavior of additive manufactured AISI 420 martensitic stainless steel, Mater. Sci. Eng. A. 773 (2020) 138815.

[2]   A.N. Isfahany, H. Saghafian, G. Borhani, The effect of heat treatment on mechanical properties and corrosion behavior of AISI420 martensitic stainless steel, J. Alloys Compd. 509 (2011) 3931–3936.

[3]   K.H. Anantha, C. Ornek, S. Ejnermark, A. Medvedeva, J. Sj, Correlative Microstructure Analysis and In Situ Corrosion Study of AISI 420 Martensitic Stainless Steel for Plastic Molding, 164 (2017) 85–93. doi:10.1149/2.0531704jes.

[4]   S. Salahi, M. Kazemipour, A. Nasiri, Effect of Uniaxial Tension-Induced Plastic Strain on the Microstructure and Corrosion Behavior of 13Cr Martensitic Stainless Steel, CORROSION. (2020).

[5]   S. Salahi, M. Kazemipour, A. Nasiri, Effects of microstructural evolution on the corrosion properties of AISI 420 martensitic stainless steel during cold rolling process, Mater. Chem. Phys. 258 (2021). doi:10.1016/j.matchemphys.2020.123916.

[6]   M. Ghaffari, A.V. Nemani, A. Nasiri, Interfacial bonding between a wire arc additive manufactured 420 martensitic stainless steel part and its wrought base plate, Mater. Chem. Phys. (2020) 123199.

[7]   F. Khodabakhshi, M.H. Farshidianfar, A.P. Gerlich, M. Nosko, V. Trembošová, A. Khajepour, Effects of laser additive manufacturing on microstructure and crystallographic texture of austenitic and martensitic stainless steels, Addit. Manuf. 31 (2020) 100915.

[8]   H. Chae, E.-W. Huang, W. Woo, S.H. Kang, J. Jain, K. An, S.Y. Lee, Unravelling thermal history during additive manufacturing of martensitic stainless steel, J. Alloys Compd. (2020) 157555.

[9]   M. Rafieazad, M. Ghaffari, A.V. Nemani, A. Nasiri, Microstructural evolution and mechanical properties of a low-carbon low-alloy steel produced by wire arc additive manufacturing, Int. J. Adv. Manuf. Technol. 105 (2019) 2121–2134.

[10]   A. Vahedi Nemani, M. Ghaffari, A. Nasiri, On the Post-Printing Heat Treatment of a Wire Arc Additively Manufactured ER70S Part, Materials (Basel). 13 (2020) 2795.

[11]   J. Lunde, M. Kazemipour, S. Salahi, A. Nasiri, Microstructure and Mechanical Properties of AISI 420 Stainless Steel Produced by Wire Arc Additive Manufacturing, in: TMS 2020 149th Annu. Meet. Exhib. Suppl. Proc., Springer, 2020: pp. 413–424.

[12]   M. Kazemipour, J.H. Lunde, S. Salahi, A. Nasiri, On the Microstructure and Corrosion Behavior of Wire Arc Additively Manufactured AISI 420 Stainless Steel, in: TMS 2020 149th Annu. Meet. Exhib. Suppl. Proc., Springer, 2020: pp. 435–448.

[13]   S. Salahi, M. Kazemipour, A. Nasiri, Effects of Microstructural Evolution on the Corrosion Properties of AISI 420 Martensitic Stainless Steel during Cold Rolling Process, Mater. Chem. Phys. (2020) 123916.

[14]   S.K. Bonagani, V. Bathula, V. Kain, Influence of tempering treatment on microstructure and pitting corrosion of 13 wt.% Cr martensitic stainless steel, Corros. Sci. (2018). doi:10.1016/j.corsci.2017.12.012.

[15]   S.-Y. Lu, K.-F. Yao, Y.-B. Chen, M.-H. Wang, X. Liu, X. Ge, The effect of tempering temperature on the microstructure and electrochemical properties of a 13 wt.% Cr-type martensitic stainless steel, Electrochim. Acta. 165 (2015) 45–55.

[16]   J. Ge, J. Lin, Y. Chen, Y. Lei, H. Fu, Characterization of wire arc additive manufacturing 2Cr13 part: Process stability, microstructural evolution, and tensile properties, J. Alloys Compd. 748 (2018) 911–921.

[17]   B. Hirschorn, M.E. Orazem, B. Tribollet, V. Vivier, I. Frateur, M. Musiani, Constant-phase-element behavior caused by resistivity distributions in films: I. Theory, J. Electrochem. Soc. 157

(2010) C452.

[18] A. Fattah-Alhosseini, M.A. Golozar, A. Saatchi, K. Raeissi, Effect of solution concentration on semiconducting properties of passive films formed on austenitic stainless steels, Corros. Sci. 52 (2010) 205–209.

[19] M. Rafieazad, M. Mohammadi, A. Gerlich, A. Nasiri, Enhancing the corrosion properties of additively manufactured AlSi10Mg using friction stir processing, Corros. Sci. 178 (n.d.) 109073.

[20] W.T. Read, W. Shockley, Dislocation models of crystal grain boundaries, Phys. Rev. 78 (1950) 275.

[21] H. Luo, X. Wang, C. Dong, K. Xiao, X. Li, Effect of cold deformation on the corrosion behaviour of UNS S31803 duplex stainless steel in simulated concrete pore solution, Corros. Sci. 124 (2017) 178–192.

Chapter 6

Microstructural Evolution and Electrochemical Performance of the Interfacial Region between a Wrought and a Wire Arc Additive Manufactured 420 Martensitic Stainless Steel[5]

Preface

The original version of this manuscript has already been submitted to the Journal of Materials Characterization. I am the first and the corresponding author of the current work. In this chapter, along with my colleagues, Dr. Ali Nasiri, Alireza Vahedi Nemani, and Mahya Ghaffari, I characterize the microstructure and electrochemical performance of the interface between a wrought and wire arc additively manufactured 420 martensitic stainless steel. I was responsible for preparing methodology, experimental testing, result gathering, and drafting of the original manuscript. Subsequently, I revised the paper based on my colleagues' initial comments and peer review process feedback. The co-authors contributed to the conceptualizing, project administration, supervision, and review & editing of the manuscript

---

[5]Salahi, Salar, Mahya Ghaffari, Alireza Vahedi Nemani, and Ali Nasiri. "Microstructural Evolution and Electrochemical Performance of the Interfacial Region between a Wrought and a Wire Arc Additive Manufactured 420 Martensitic Stainless Steel. Submitted to the " *Journal of Materials Characterization* .

Abstract

In this study, the interfacial microstructure and corrosion resistance between a wrought-AISI420 substrate plate and a wire arc additive manufactured 420 stainless steel were studied. Formation of four distinct microstructural regions, including (i) far heat-affected zone (HAZ), (ii) close HAZ, (iii) partially melted zone (PMZ), and (iv) fusion zone was disclosed following the characterization of the interfacial bonding region. In the as-printed sample, the formation of chromium-depleted regions adjacent to the residual delta ferrite phase led to the occurrence of localized corrosion attacks, remarkably diminishing the electrochemical stability of the alloy. The electrochemical response of the interfacial bonding region revealed intense degradation close to the PMZ and fusion zone, potentially ascribed to the formation of several distinctive microstructural regions with high susceptibility to localized corrosion attacks in the interface of the aforementioned regions. The onset of localized corrosion attack in the interfacial bonding region was mostly initiated along the primary austenite grain boundaries (PAGBs), where segregation of chromium carbides was detected. Compared to the as-printed and interfacial bonding samples, the substrate alloy exhibited a better electrochemical response ascribed to the absence of susceptible regions to localized corrosion attack, leading to the formation of a continuous protective passive film on its surface.

1. Introduction

Repair and restoration as a value-adding strategy have been extensively implemented to broaden the in-service life cycle of components in the automotive, maritime, and aerospace industries [1]. These restoration policies assure the reversion of a used or even failed component to its initial service performance with minimum waste of material and maximum efficiency rate [2]. Conventional repair and restoration techniques involve remanufacturing of failed parts by the adoption of localized arc or laser-based welding and pinning processes to cover the cracked or failed surfaces [3]. Automated restoration techniques, such as state-of-the-art additive manufacturing processes, are foreseen to be a fast-growing alternative to manual methods [4]. This adoption can be further promoted and accelerated by the incremental growth in raw materials consumption within the last two decades, which is becoming an alarming threat for the supply chain management of non-renewable resources [5]. Moreover, the recent novel Covid-19 outbreak has extensively influenced the global supply chain for the manufacturing section, arising a need for on-site manufacturing and remanufacturing methods as an alternative production technique and repair strategy for unprecedented situations and the post-Covid-19 era [6].

Metal additive manufacturing (AM) technology, as a resilient fabrication method for in-house production, can facilitate fabricating complex metal parts with high accuracy and low manufacturing waste rate [7]. As a fast-growing metal 3D-printing method, wire arc additive manufacturing (WAAM) can produce large-scale near-net-shape components by implementing plasma or electric arc as the heat source and metal wire as the feedstock material [8]. Hitherto, a variety of feedstock materials have been adopted for fabrication through the WAAM process, including aluminum, titanium, steel, copper, brass, and nickel alloys [9]. Among ferrous alloys,

the fabrication feasibility of multiple grades of austenitic stainless steels, duplex steels, as well as martensitic stainless steels (MSSs) has been proven [10–13].

WAAM can also be employed as an on-site repairing and remanufacturing technique for parts exposed to in-service malfunctioning [14], leading to an extended service life span of the parts [15]. Through the implementation of the WAAM process as a restoration technique, controlling the exposed complex thermal cycles associated with the process and prevention of the inhomogeneities and anomalies formation at the interfacial bonding between the substrate and the deposited layers are of great importance [8].

420 Martensitic stainless steel (420 MSS), possessing high wear and corrosion resistance, is widely used for plastic molding fabrication [16]. Frequent in-service failures have been reported for the plastic molds ascribed to their harsh working environment and inherent manufacturing-related defects [17]. Extending the service life of 420 MSS molding casts through their repair using the WAAM process is a cost-effective alternative to the costly replacement of the defected molds [15]. Although WAAM-420 MSS alloy is primarily characterized by having a martensitic lath structure, meta-stable micro-constituents, such as undissolved carbides, residual delta ferrite, and retained austenite, can also form in the as-printed structure of the alloy as a result of non-equilibrium solidification and complex thermal history of deposited layers [18–20]. These microstructural features can adversely impact the electrochemical response of the deposited layers [19,21]. Controlling the heat input of the process, in particular through optimization of the fabrication process parameters, has been proven to eliminate the residual delta ferrite constituents, which are known to be susceptible sites to micro-galvanic corrosion attack, from the microstructure of additively manufactured MSS components [19]. Further studies are required to characterize the feasibility of controlling the formation of other non-equilibrium

microconstituents, such as retained austenite and chromium carbides, at the interfacial bonding

region through the WAAM process without applying any extra post-fabrication heat treatment

cycle. On the other hand, complicated thermal exposure of HAZ, the formation of brittle

intermetallic particles at the interfacial region, and the electro-potential difference between the

substrate and the deposited layers can influence the electrochemical performance of the interfacial

bonding of the repaired 420 MSS parts by WAAM process [15,22]. Moreover, the formation of a

preferred crystallographic orientation through the manufacturing or solidification process can lead

to substantial variation in the crystallographic criteria, *i.e.*, misorientation boundaries distribution,

lath size, grain size, and close-packed plane arrangement, significantly impacting the corrosion

resistance of the 420 MSS [16,23]. Hence, characterizing the microstructural evolution and

crystallographic orientation of the interfacial region between the 420 MSS substrate and WAAM

deposited layers is highly crucial.

Although a few studies have been conducted on the microstructure and corrosion

performance characterization of the as-printed 420 MSS parts fabricated via the WAAM process

[15,24], a comprehensive investigation on the adoption feasibility of WAAM technology as a

repair and restoration alternative for defected 420 stainless steel parts is lacking. Heretofore, no

study has been conducted to correlate the microstructural features and crystallographic orientation

of the metallurgical bonding between the wrought substrate and deposited WAAM-420 MSS with

its electrochemical response. In this paper, for the first time, the authors investigated the effect of

microstructural variations on the corrosion performance of the interfacial bonding between the

wrought-AISI420 MSS substrate and the additively manufactured layers. In addition, the corrosion

response of the interfacial region was compared with the wrought-AISI420 MSS and as-printed

WAAM-420 MSS, and the governing factors controlling the overall corrosion performance were discussed comprehensively.

2. Experimental procedure

2.1.Materials and fabrication process

In this study, a six-axis WAAM robot equipped with a gas metal arc power supply was adopted to produce a wall-shaped part ($\sim160\times160\times6$ mm^3) using an all-x scanning strategy and the optimum process parameters presented in the authors' previous work [18]. A standard AISI420 MSS wrought plate was used as the substrate, and the feedstock material was a commercial ER420 wire with a diameter of 1.14 mm. The nominal chemical compositions of the substrate and feedstock wire are presented in Table 6.1. In order to control the temperature distribution through the deposition process of each layer, an infrared-based closed-loop sensor was used to measure the surface temperature of the last deposited layer, assuring the inter-layer temperature was constant through the deposition process and adjusted to be 100±2.5°C. To prevent oxidation and environmental contamination, Argon gas with 99.9% purity was used to shield the fusion zone throughout the deposition process. The fabricated wall and the schematic illustration of the deposition process are shown in Figure 6. 1a and 1b.

Table 6. 1. The nominal chemical compositions of the used materials in this study (wt.%).

Material	C	Cr	Mn	Si	S	P	Ni	Mo	Cu	V	Fe
ER420	0.3	13	0.5	0.5	0.02	0-0.05	0.3	0.25	0.2	-	Bal.
AISI420	0.15-0.46	12-14	0.3-1	0-1	0-0.04	0-0.05	-	0-0.1	-	0.3	Bal.
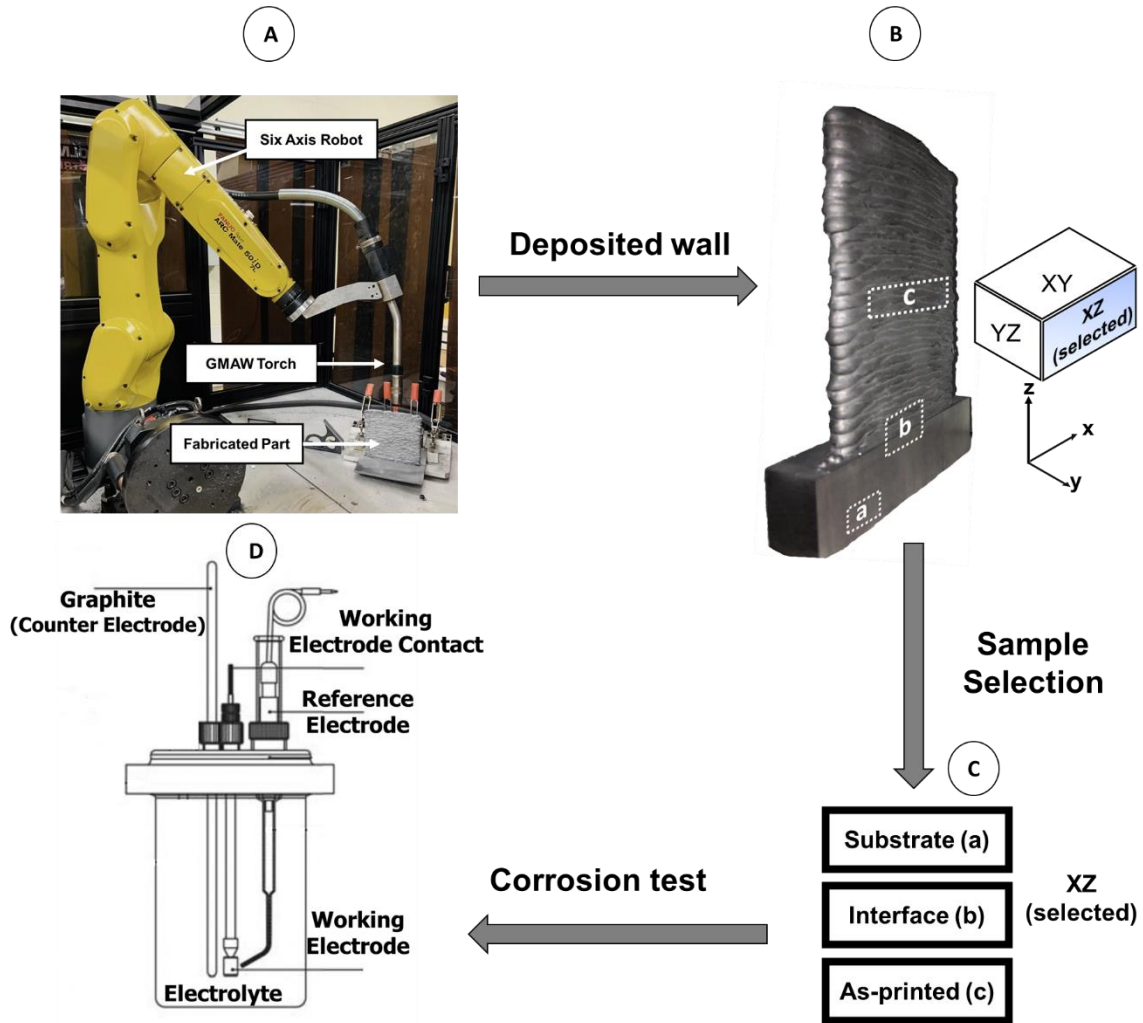
Figure 6. 1. Schematic illustration of the 420 WAAM wall fabrication and subsequent sample preparation steps for microstructural and corrosion analysis.

2.2. Microstructural characterizations

As shown in Figure 6. 1b, to characterize the microstructural features, different samples from the as-printed part, interfacial bonding zone, and the wrought-420 MSS plate were cut, hot mounted, and prepared through recommended grinding and polishing procedures for MSSs using a Tegramin-30 Struers grinder and polisher, and then etched using Villella's reagent for 20 s. The optical microscopy (OM) characterization was performed using a Nikon-Eclipse 50i instrument. For elemental composition analysis, and also to characterize the existence of different micro-

constituents formed in the structure of each sample, an energy dispersive spectroscopy (EDS) detector integrated into a scanning electron microscope (SEM) was applied. Electron Backscatter Diffraction (EBSD) technique was used to characterize the crystallographic orientation of studied samples herein using an Oxford Symmetry S2$^®$ detector with a step size of 0.5 μm and tilt angle of 70°. To characterize the nature of formed secondary phases in more detail, X-ray diffraction (XRD) technique was conducted at the angle range of 20°–100° and an accelerating voltage of 42 kV and the current value of 35 mA.

2.3.Electrochemical analysis

The same samples being prepared for microstructural characterizations were also used for electrochemical analysis. The open-circuit potential (OCP), potentiodynamic polarization (PDP), electrochemical impedance spectroscopy (EIS), and Mott-Schottky measurements were conducted to examine the samples' electrochemical behavior in aerated 3.5 wt.% NaCl-solution at the ambient temperature. As schematically shown in Figure 6. 1d, a standard three-electrode cell apparatus containing a graphite rod as the counter electrode, the prepared 420 MSS samples as the working electrode, and a saturated silver-silver chloride (Ag/AgCl) electrode as the reference electrode were implemented. To investigate the electrochemical stability of the samples over a prolonged immersion time, the OCP variations were monitored for 14 h. The PDP measurements were conducted with a scanning rate of 0.1 mV/s commencing at -0.2 V versus OCP and the test was interrupted at the current density threshold of 10^{-2} A.cm^{-2}. The EIS experiments were conducted using a sinusoidal perturbation signal at the voltage value of 10 mV and frequency range of 100 kHz to 10 mHz. Mott-Schottky examinations were conducted at the scanning rate of 40 mV/step, frequency of 1000 Hz, the amplitude of 5 mV, and ranging potential of -1000 to 1000 mV$_{Ag/AgCl}$.

To validate the accuracy of the conducted electrochemical experiments, all tests for each condition were repeated at least five times.

3. Results and Discussion

3.1.Microstructural characterizations

The SEM micrographs taken from the wrought-AISI420 MSS substrate at high and low magnifications and their corresponding EDS elemental maps of iron, chromium, and carbon are shown in Figure 6. 2a-2e. Chromium carbides were detected in both spherical and vermicular-shaped morphologies (see Figure 6. 1a and 1b) and were generated through the annealing heat treatment process of the substrate. Additionally, it can be noticed that carbides were formed both along the grain boundaries (intergranular carbides) and embedded in the ferritic matrix (intragranular carbides), as illustrated in Figure 6. 1b. The EDS elemental maps of the wrought-420 MSS sample (Figure 6. 2c-2e) depict the chromium-rich nature of carbides, indicating depletion in iron and enrichment in chromium and carbon.

The SEM micrograph images of the as-printed sample at low and high magnifications and its corresponding EDS elemental maps are illustrated in Figure 6. 2f-2j. Formation of columnar dendritic structure parallel to the building direction (Z-axis) and along the thermal gradient path is observed for the as-printed sample, as shown in Figure 6. 2f. The microstructure of the as-printed sample consists of a relatively high-volume fraction of residual delta ferrite (DF) phase (~20%) embedded in a fine lath martensitic structure. Due to the high cooling rate and non-equilibrium nature of solidification during the WAAM process, the metastable martensitic structure was formed in the as-printed alloy. Likewise, the stability of residual delta ferrite phase at the ambient temperature (see Figure 6. 2f and 2g) is attributed to the disturbance of highly time-dependent (diffusion-controlled) transformation of delta ferrite phase to austenite at ~1400°C, analogously

caused by the high cooling rate during solidification [8]. Furthermore, the high chromium content of 420 MSS (~13 wt.%) as a ferrite stabilizing alloying element (see Figures 6. 2i and 2j) can promote the stability of residual delta ferrite at room temperature [25]. It should be noted that the formation of delta ferrite phase with higher chromium concentration (~16%) compared to the matrix can lead to chromium depletion in the areas adjacent to the delta ferrite/matrix interface (with Cr content ≤ 11 wt.%), confirmed by the EDS line scanning results measured across the delta ferrite phase in the as-printed sample in Figure 6. 2j.
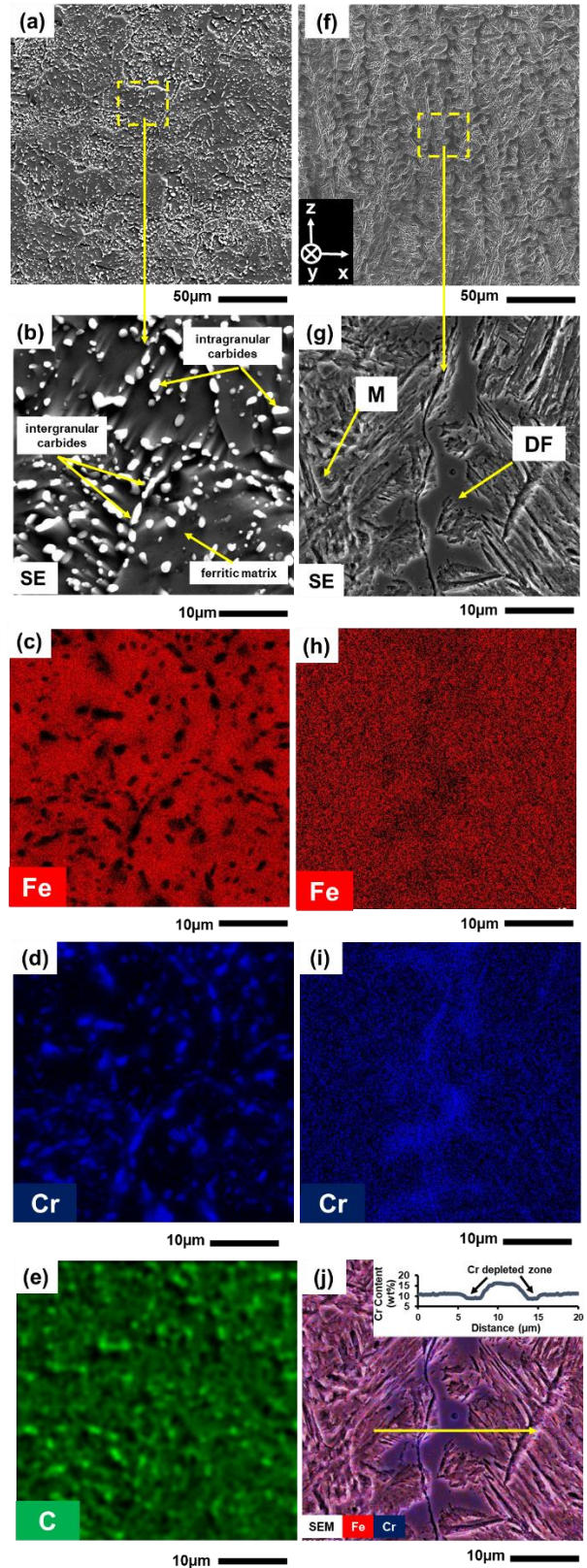
Figure 6. 2. SEM micrographs of the wrought-420 MSS substrate at (a) low magnification (b) high magnification showing the existence of intergranular and intragranular chromium carbides

along with its corresponding elemental maps indicating the concentration of (c) iron, (d) chromium, and (e) carbon, (f) SEM micrograph of the as-printed 420 MSS sample at low magnification, (g) high magnification along with its corresponding elemental maps showing the concentration of (h) iron, (i) chromium, and (j) EDS elemental line scanning showing the Cr concentration across the delta ferrite phase.

The low magnification optical micrograph of the interfacial bonding zone between the wrought-420 MSS substrate and deposited WAAM-420 alloy (see Figure 6. 3a) indicates the formation of four distinct regions, *i.e.*, fusion zone, partially melted zone (PMZ), close heat-affected zone (HAZ), and the far HAZ. The formation of different zones with distinct microstructural features can be attributed to different thermal histories experienced by each zone. High magnification SEM images from the entire HAZ (see Figure 6. 3b-3e) imply the formation of two distinct sub-zones, *i.e.*, the area close to the fusion zone with higher thermal exposure (close HAZ) and the region far from the fusion zone with less thermal exposure (far HAZ). Due to the higher thermal exposure, the close HAZ experiences a temperature raise up to the austenite stability region for 420 MSS alloy (~1100–1350°C) followed by fast air cooling, leading to the formation of martensitic structure in the matrix (see Figure 6. 3c) and partial dissolution of pre-existing carbides into the martensitic matrix [15]. Contrarily, the far HAZ consists of a ferritic matrix structure due to the lower thermal exposure and lower temperature-rise (~600–1000°C) during the WAAM deposition process, hindering the partial transformation of ferrite to austenite in the matrix. The temperature rise during the deposition of initial layers can facilitate the nucleation and growth of new carbides in the far HAZ region while pre-existing carbides remain undissolved due to the short exposure time to the high temperatures. This leads to a higher volume fraction of chromium-rich carbides in far HAZ compared to the wrought-420 MSS substrate [15]. A relatively thin PMZ was formed (see Figures 6. 3a and 4a), where thermal exposure was high enough to reach the stability region of delta ferrite, austenite, and liquid, expected to be in the

range of ~1350–1450°C according to the pseudo-binary phase diagram of 420 MSS alloy [26]. Accordingly, PMZ consists of the martensitic matrix with a high-volume fraction of residual delta ferrite phase, retained austenite, and fine chromium carbides, as shown in the SEM micrographs of PMZ at higher magnifications (see Figure 6. 4b-4g). Formation of fine chromium-rich carbides (see Figures 6. 4b and 4c) in PMZ is attributed to the partial dissolution of large undissolved carbides during the deposition of the first WAAM-420 MSS track and also subsequent nucleation of finer carbides through the recurrence of heating and cooling cycles by the deposition of next WAAM tracks [16]. The complete transformation of the delta ferrite phase to the austenite is hindered due to the rapid cooling experienced in PMZ. Moreover, dissolution of the pre-existing chromium-rich carbides at elevated temperatures and segregation of chromium as a ferrite stabilizer element at PMZ can facilitate the formation of the delta ferrite phase at the ambient temperature [24,27], as shown in Figures 6. 4d and 4e. The stabilization of the austenite phase at the ambient temperature (retained austenite formation) in PMZ (see Figure 6. 4g) is related to the localized increase in the chromium and carbon content in this region as a result of the dissolution of pre-existing chromium-rich carbides, decreasing the martensite start (M_s) temperature and promoting the stability of retained austenite at room temperature [24]. It is worth noting that the primary austenite grain boundaries (PAGBs) are also discernible in PMZ, as shown in Figures 6. 4d and 4g. PAGBs are formed through rapid austenitization, while the precipitation of chromium carbides along the PAGBs (see Figure 6. 4g) occurs during the recurring heating and cooling cycles associated with depositing the subsequent layers [8].
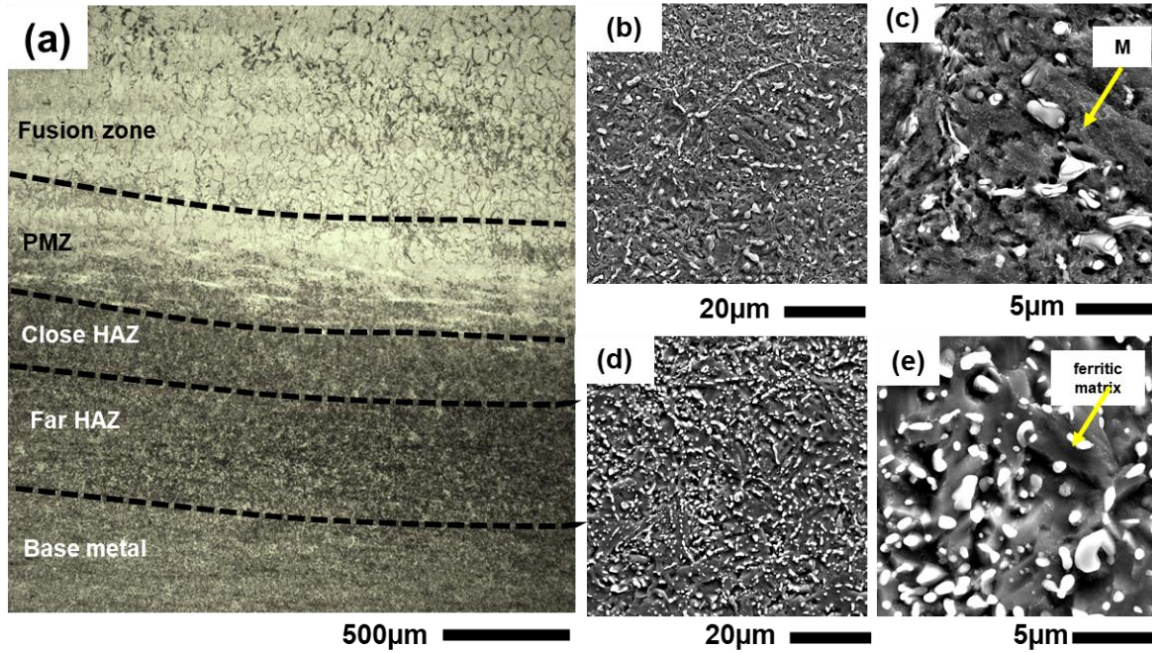
Figure 6. 3. (a) The OM micrograph of the interfacial region, (b) and (c) SEM micrographs of the close HAZ, and (d) and (e) far HAZ.

The microstructure of the fusion zone consists of a martensitic structure, PAGBs, and inter-dendritic residual delta ferrite phase (see Figures 6. 4h and 4i) generated along the building direction parallel to the heat dissipation direction during the solidification.
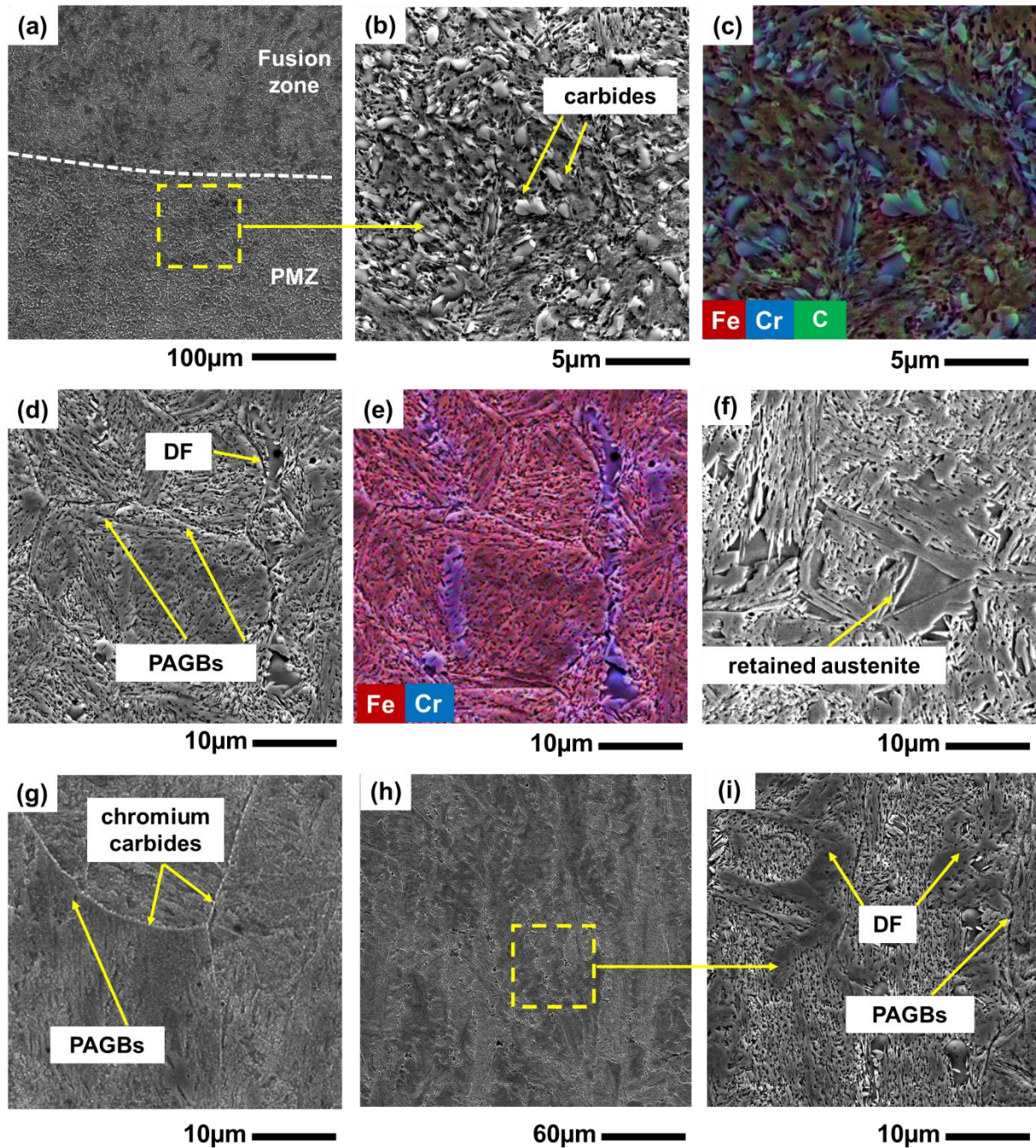
Figure 6. 4. (a) Low magnification SEM micrograph showing the transition from PMZ to the fusion zone, and high magnification SEM micrograph of (b) PMZ consisting of chromium carbides and (c) its corresponding elemental map, (d) SEM micrograph taken from a different location of PMZ consisting of delta ferrite and PAGBs and (e) its corresponding elemental map, (f) the formed retained austenite phase in PMZ, (g) the formation of carbides along the PAGBs, (h) low magnification SEM micrograph of the fusion zone, and (i) high magnification SEM micrograph from the fusion zone showing the formation of PAGBs and delta ferrite phase.

The XRD patterns of the wrought-420 MSS substrate, as-printed sample, and interfacial bonding zone are illustrated in Figure 6. 5. The XRD spectra of the 420 MSS substrate depicts the BCC phases at (110), (200), (211), and (220) planes along with some low-intensity peaks for chromium-rich carbides of $M_{23}C_6$ and M_7C_3, confirming the observation of the carbides embedded in the ferritic matrix from the SEM micrographs of the wrought-420 MSS. Through the post-rolling annealing heat treatment of the wrought-AISI420 MSS, the retained austenite phase can be removed from the microstructure of conventionally hot-rolled sample via the diffusional segregation of carbon element from the austenite phase to the matrix [16,28]. The BCC peaks at (110), (200), (211), and (220) planes are observed for the as-printed sample along with a high-intensity austenitic phase (γ) peak at (111) plane in addition to the low-intensity peak of austenite phase at (200) plane. Presence of high density $(111)_\gamma$ phase is in good agreement with the observations from the SEM micrographs of the as-printed sample (Figures 6. 2f and 2g), confirming the formation of high volume fraction of retained austenite due to recurrence of heating and cooling cycles through the WAAM deposition process and the existence of a significant amount of carbon as an austenite stabilizer element in the deposited sample [12]. It is notable that a slight change of lattice parameters between the delta ferrite and martensite phases (10^{-4}-10^{-5} nm) made it impossible to differentiate between these two phases using the XRD data [12]. The XRD spectra of the interfacial region exhibit formation of the same FCC peaks at $(111)_\gamma$ and $(200)_\gamma$ along with two new austenite peaks at $(220)_\gamma$ and $(311)_\gamma$, while the existence of the martensitic/ferritic peaks are observed at (110), (200), (211), and (220) planes as well. The Rietveld method [29], based on the whole pattern fitting (WPF) procedure, was used to calculate the volume fraction of the formed austenite phase. The obtained volume fraction of the retained austenite phase [29] for the as-printed sample and interfacial bonding region were found to be 15%±0.1 and 23%±0.1,

respectively. Existence of higher-intensity peaks of $(111)_\gamma$ and $(200)_\gamma$, and new peaks of $(220)_\gamma$ and $(311)_\gamma$ planes in the interface sample are attributed to the formation of the high-volume fraction of retained austenite phase in PMZ.

The XRD spectra results can be used to calculate the dislocation density defined as the length of dislocation lines per unit volume (denoted by δ) for the observed martensitic phases by applying the following equation [30]:

$$\delta = \frac{1}{L^2} \tag{1}$$

where L is the crystal size and can be calculated using two different approaches, *i.e.*, Scherrer and Cauchy equations [31].

Scherrer equation shall be used to calculate the average grain diameter (crystal size) [31]:

$$L = \frac{D\lambda}{\beta \cos\theta} \tag{2}$$

where D is the unity shape factor, L is the crystal size, θ is the Bragg angle, β is the breadths of the same Bragg peak from the XRD spectra, and λ is the X-ray wavelength (for Cu-K$_\alpha$ radiation = 1.54056 Å).

For the Cauchy approach, it is assumed that the crystal size (L) and lattice strain (e) follow a linear pattern as follows [32]:

$$\beta \cos\theta = \frac{\lambda}{L} + 4e \sin\theta \tag{3}$$

The average grain diameter (crystallite size) can be calculated from the slope of the $\beta \cos\theta$ versus $\sin\theta$ graph and the ordinate-intersection of the developed Cauchy equation. Table 6. 2 presents the modeled dislocation density values, using the Scherrer and Cauchy equations based on the XRD spectra data for the (110), (200), (211), (220) intensity peaks. Expectedly, the as-printed and

220

interface samples seem to contain a higher dislocation density compared to the wrought-420 MSS, attributed to the existence of martensitic matrix with highly strained structure, which can significantly promote the dislocation formation in the as-printed and interface samples [33]. The interface sample possessing higher volume fraction of ferritic phase with strain-free structure in the HAZ was characterized with a lower dislocation density as compared to the fully martensitic as-printed sample [33,34].
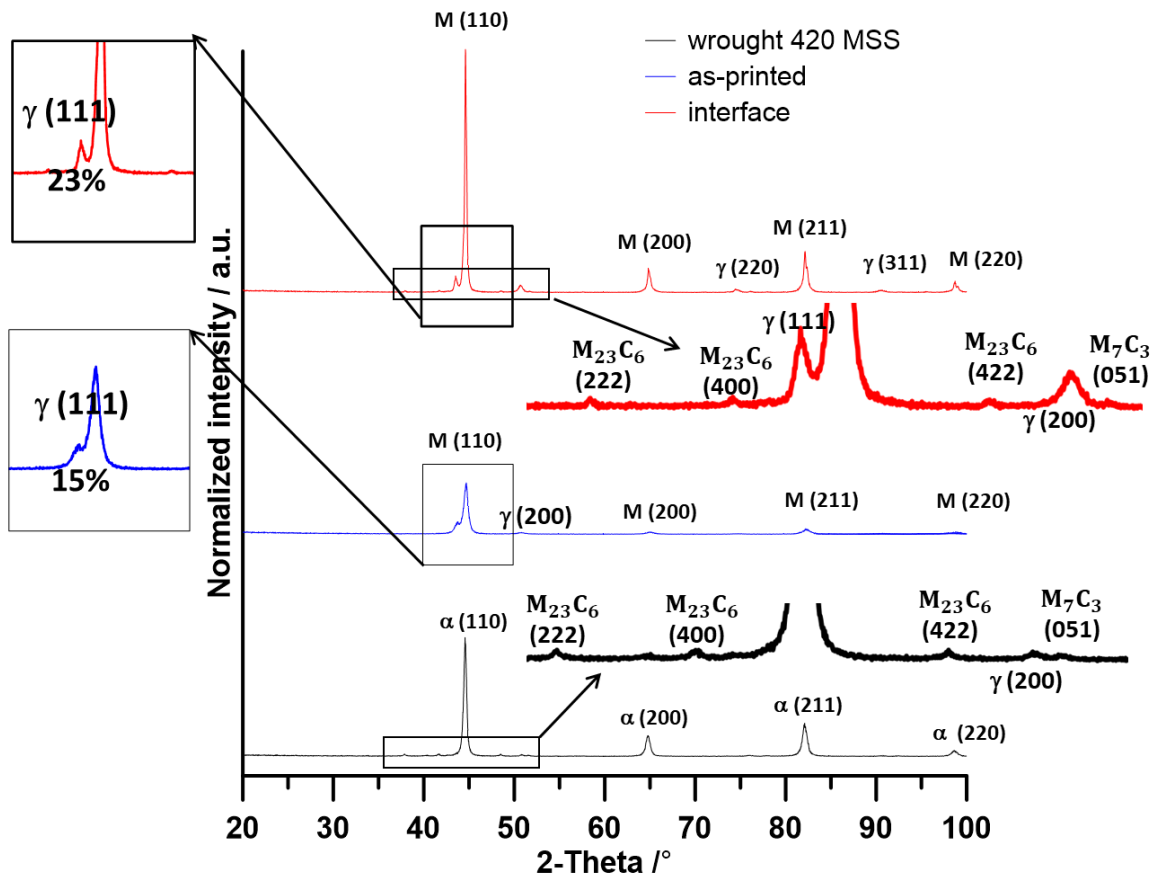
Figure 6. 5. The XRD spectra results of the wrought-420 MSS, as-printed, and the interface samples.

Table 6. 2. The obtained dislocation density (δ) values for the substrate, as-printed, and the interface samples.

Sample	$\delta/1.nm^{-2}$ (Scherrer)				$\delta/1.nm^{-2}$ (Cauchy)			
	(110)	(200)	(211)	(220)	(110)	(200)	(211)	(220)
Wrought-420 MSS	0.003	0.49	0.01	0.003	0.03	0.54	0.01	0.003
As-printed	0.02	1.56	0.42	0.012	0.02	1.56	0.42	0.012
Interface	0.01	1.28	0.33	0.005	0.01	1.23	0.31	0.005

3.2.Crystallographic orientation characterization

The inverse pole figure (IPF) maps for the wrought 420 MSS and as-printed samples with superimposed grain/lath boundaries maps are shown in Figures 6. 6a and 6b, respectively. The IPF map of the wrought-420 MSS substrate (Figure 6. 6a) depicts an equiaxed and relatively coarse grain structure (average grain size ~ 8 μm). Unlike the wrought-420 MSS substrate, the IPF of the as-printed sample (see Figure 6. 6b) shows a fine martensitic lath structure (lath size < 3 μm), formed within the coarse primary austenite grains (average size ~ 50 μm). Figures 6. 6c and 6d demonstrate the phase map distribution for the wrought-420 MSS substrate and as-printed samples. The wrought-420 MSS shows a dominant volume fraction of BCC phase (~99%) with no FCC structure formed, attributed to the presence of a ferritic matrix. On the other hand, the as-printed sample was characterized by a high-volume fraction of FCC phase (~15%) alongside the BCC phase, corresponding to the formed retained austenite phase in the as-printed sample and in good agreement with findings from the XRD spectra. Grain boundaries misorientation maps for the wrought-420 MSS and as-printed WAAM-420 samples are shown in Figures 6. 6e and 6f, respectively.
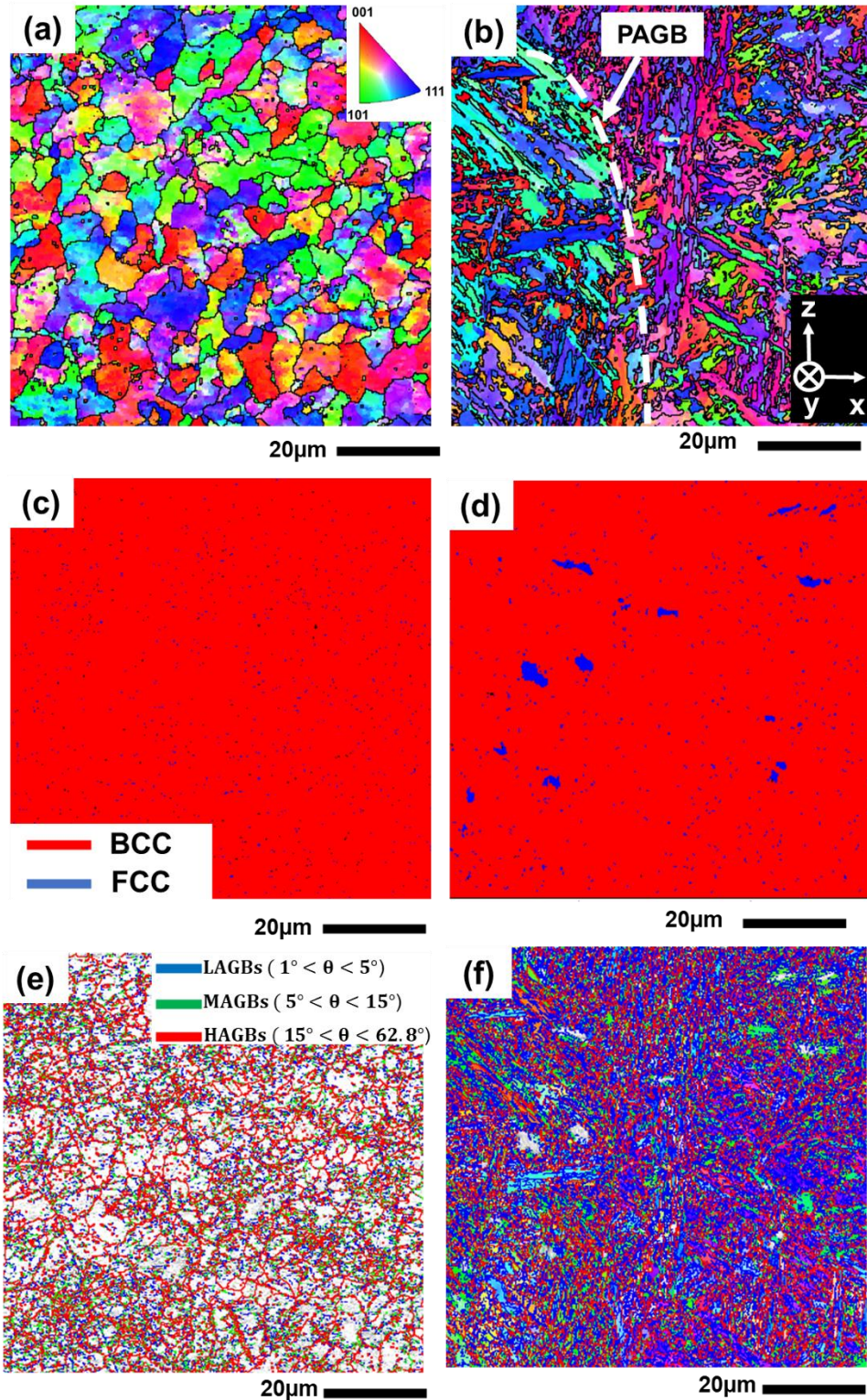
Figure 6. 6. (a) and (b) IPF maps for the wrought-420 MSS and as-printed WAAM-420 samples, (c) and (d) their corresponding phase maps, (e) and (f) their corresponding grain boundaries misorientation maps, respectively.

223

Figure 6. 7a-7c show the IPF, phase map, and grain boundaries misorientation map for the interfacial bonding region, distinguishing close HAZ, PMZ, fusion zone, and subsequently deposited tracks of WAAM-420. As shown in Figure 6. 7a, a fine lath structure was formed in PMZ region (average lath size < 3 μm), while a coarser lath martensitic structure (average lath size ~ 10 μm) confined within the PAGBs is noticed in the fusion zone. Moreover, the formation of the high-volume fraction of FCC structure (retained austenite phase) is confirmed in PMZ as shown in Figure 6. 7b, which is in good agreement with the obtained XRD spectra and SEM micrographs from the interface sample. Interestingly, the fusion zone adjacent to PMZ is showing the dominance of BCC structure (martensite phase) with low volume fraction of FCC structure, correlated to the high cooling rate of the first deposited layer due to the high heat dissipation through the substrate during its solidification. The formation of a high-volume fraction of retained austenite (FCC structure) is also observed in the subsequently deposited layers, confirming the observed XRD results for the as-printed sample. The formation of highly populated but fine austenite phase in PMZ (see in Figure 6. 7b) is ascribed to the nucleation of the austenite grains on the high angle boundaries of the primary austenite grains through heating cycles associated with the deposition of the subsequent layers [22,35]. It should be mentioned that the martensitic lath structure possesses a hierarchical pattern with martensite blocks and packets surrounded by PAGBs [36]. After the deposition of the first track, an untempered martensitic structure forms in PMZ adjacent to the fusion zone, introducing a high density of high angle grain boundaries as the PAGBs, packet boundaries, and block boundaries. Through the deposition of the next tracks, the new austenite grains nucleate at the high angle boundaries, specially PAGBs. As the number of deposited tracks increases, the recurring heating cycles lead to the formation of more nucleated

austenite grains at the prior martensitic structure, resulting in a finer austenitic structure in PMZ [22,37].

Figure 6. 7d shows the distribution of LAGBs, medium angle grain boundaries (MAGBs), and HAGBs for the wrought-420 MSS substrate, the as-printed, and interface samples. As can be seen, the wrought-420 MSS sample exhibits a noticeably higher fraction of HAGBs and a lower fraction of LAGBs as compared to both as-printed and interface samples. In particular, the fraction of LAGBs for the as-printed and interface samples are 50% and 57%, respectively, while this fraction reduces to 11% for the substrate. Generally, lath boundaries are considered as LAGBs [22,38]. The higher fraction of LAGBs for both the interface and as-printed samples is related to the formation of martensitic lath structure possessing low angle boundaries (≤5°) as lath boundaries [38].
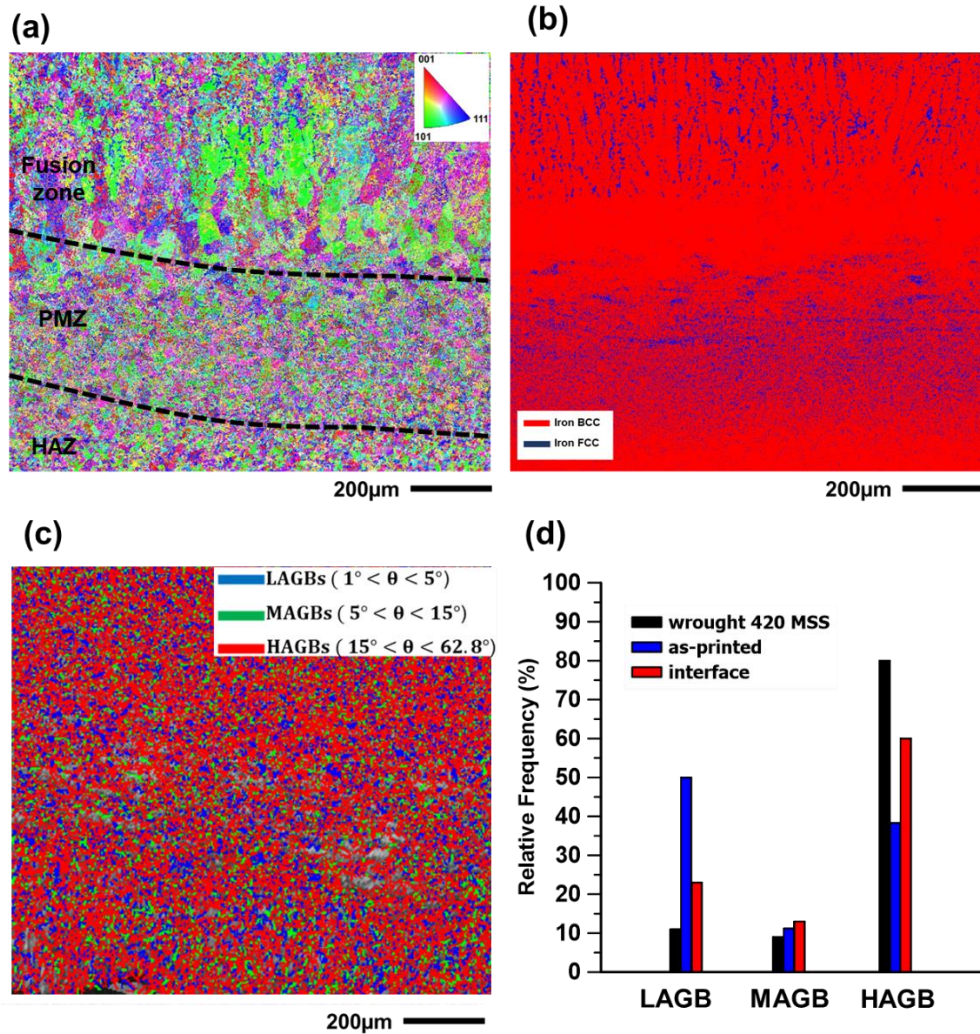
Figure 6. 7. IPF of the interfacial region and its corresponding (b) phase map and (c) grain boundaries misorientation map, and (d) statistical distribution of misorientation angles for all samples.

The pole figures (PFs) of the substrate, as-printed sample, and the interfacial bonding region (at PMZ and fusion zone) for {100}, {110}, and {111} planes are illustrated in Figure 6. 8a-8e. The PF of the substrate (see Figure 6. 8a) exhibits a weak texture (maximum intensity of ~2.16 MUD), ascribed to the dislocation annihilation and grain recrystallization of wrought-420 MSS through the annealing process. Recrystallization through the annealing process is the main reason for higher fraction of HAGBs and low fraction of LAGBs for the wrought-420 MSS as well.

Contrarily, the as-printed sample shows a strong {100} solidification texture (maximum intensity of ~7.72 MUD), formed through the directional solidification aligned with the thermal gradient and building direction [39]. The PFs of PMZ for both BCC and FCC phases (Figures 6. 8d and 8e) exhibit relatively weaker texture than those of the as-printed sample, ascribed to the complex thermal history of the region with successive tempering effect from subsequent heating cycles by the next layers' deposition, leading to the formation of fine carbide precipitates, nucleation of new non-directional austenite grains, and random distribution of delta ferrite phase throughout the region [18,24]. According to the obtained PF maps shown in Figure 6. 8, the crystallographic orientation relationship between the parent primary austenite phase (γ) and the formed final martensite phase ($\acute{\alpha}$) in both as-printed sample and PMZ of the interface sample can be defined as follows [36,40]:

$$\{111\}_{\gamma} // \{110\}_{\acute{\alpha}} \quad < 110 >_{\gamma} // < 111 >_{\acute{\alpha}} \tag{4}$$

This orientation relationship is known as of the variants of the Kurdjumov–Sachs (K–S) orientation relationship [36].
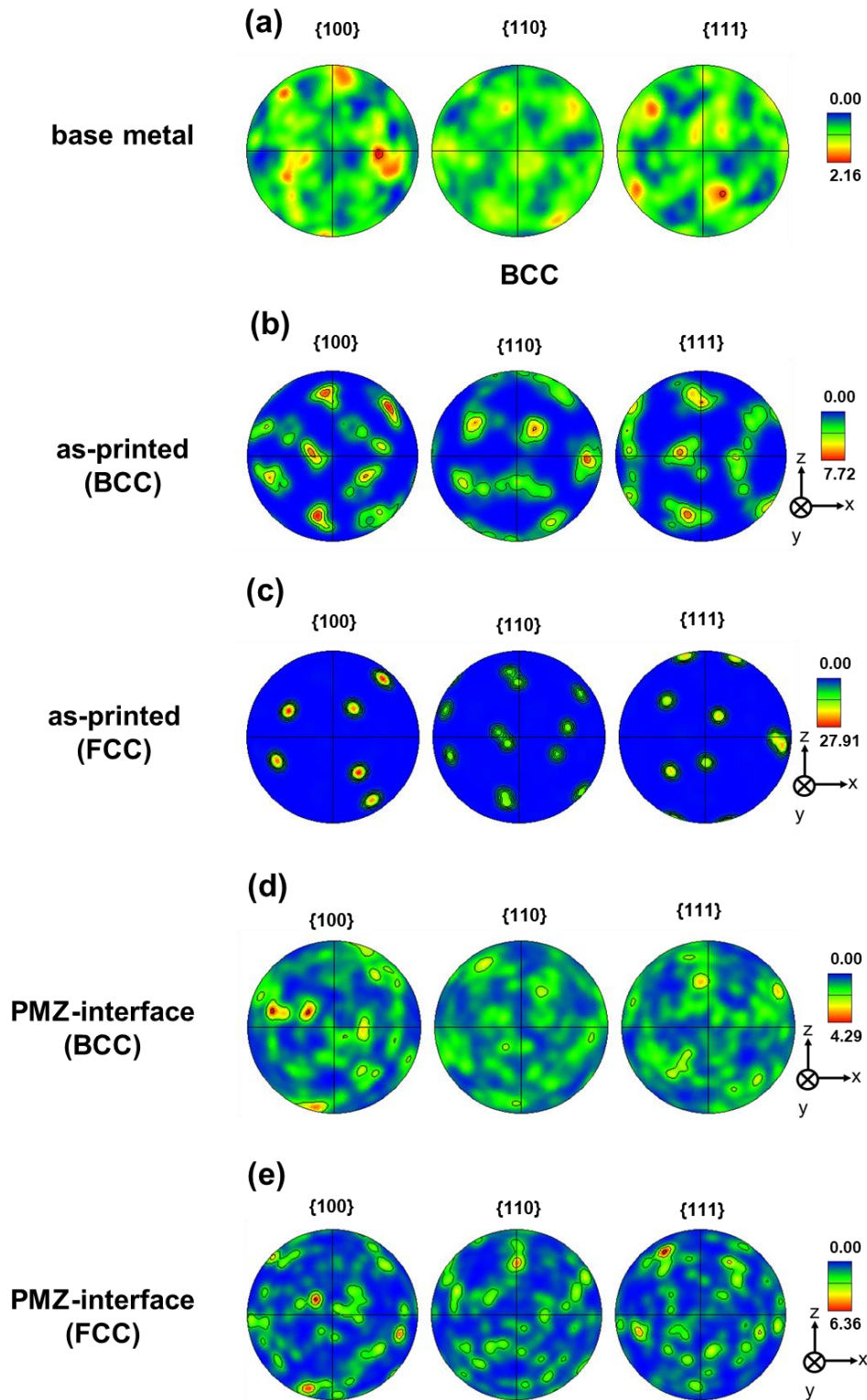
Figure 6. 8. The PFs of the BCC and FCC phases taken from: (a) the substrate, (b) and (c) as-printed sample, (d) and (e) PMZ in the interfacial bonding zone.

Figure 6. 9a-9f illustrates the orientation distribution function (ODF) maps at φ₂=45° along with the detailed crystallographic direction and plane of each observed component associated with their corresponding 3D plots. The wrought-420 MSS substrate exhibits weak {111}<110> and {011}<111> texture components (Figures 6. 9a and 9b), while the as-printed sample shows strong dominancy of preferential columnar {111}<110> texture component with the maximum intensity of 11.24 (see Figures 6. 9c and 9d). The interfacial bonding region depicts noticeably weaker columnar solidification texture at {111}<110> as compared to the as-printed sample, which agrees with the PF results.

The severity of the major texture components can be calculated using the *J*-index value as an alternative approach. A complete random crystallographic orientation is characterized by a *J*-index value of one, while the higher values of *J*-index close to infinite value present the existence of strong texture components close to single crystal material [39]. The *J*-index value, possessing a dimensionless nature, can be calculated using the following equation [39]:

$$j - index = \int f\,(g)^2\,d_g \qquad (5)$$

where *f (g)* is the ODF density at the orientation of *g*. Also, the variation in orientation (d$_g$) can be estimated using the following equation [39]:

$$d_g = d_{\varphi 1} d_\phi d_{\varphi 2} \frac{sin\phi}{8\pi^2} \qquad (6)$$

where φ$_1$, ϕ, and φ$_2$ are the Euler angles, characterizing the crystallographic relationships in a coordinate system. Hence, the *J*-index values can be correlated to the maximum textural intensity values in the PFs. Higher values of *J*-index present the existence of the strong dominant textural component with higher intensity of PF. Moreover, the *J*-index can assess the preferential orientation in a quantitative manner through the material [39]. The calculated *J*-value for the wrought-420 MSS was 2, while it increased up to 3.17 for the interfacial bonding region sample

and up to 13.25 for the as-printed sample, indicating significantly stronger texture formation in the as-printed sample.
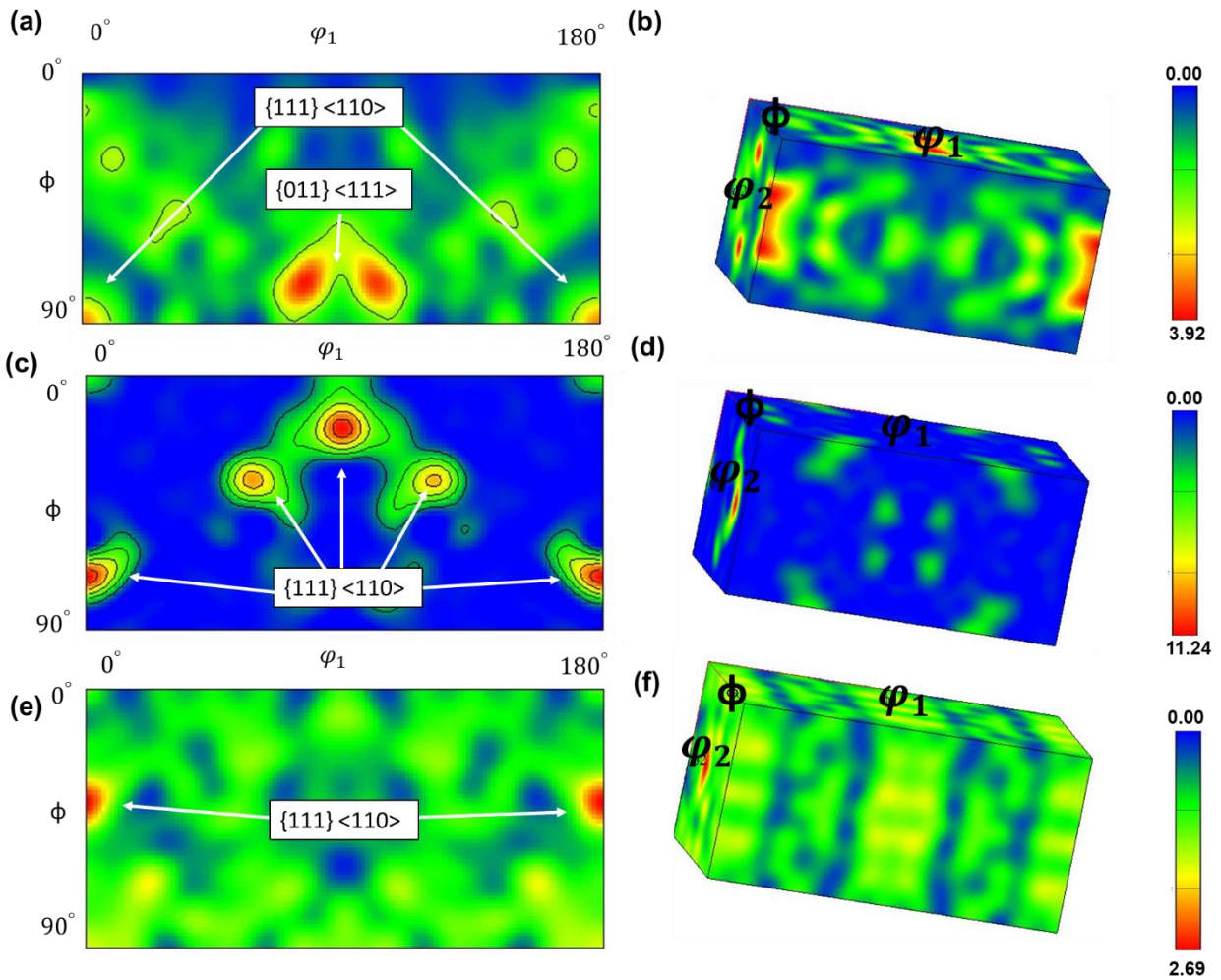
Figure 6. 9. The orientation distribution function (ODF) maps at $\varphi_2=45°$ and their corresponding 3D-plots for (a) and (b) the wrought-420 MSS, (c) and (d) as-printed, and (e) and (f) the interface samples.

3.3.Corrosion Results

3.3.1. *Open circuit potential and potentiodynamic polarization (PDP) response results*

The monitored OCP values, and the PDP experiments results for the wrought-420 MSS substrate, interface, and as-printed samples are respectively shown in Figures 6. 10a and 10b. The interface sample exhibited a lower OCP value, as compared to the as-printed and the wrought-420 MSS samples, suggesting its higher corrosion susceptibility and lower electrochemical stability. Severe fluctuations were observed in the OCP values of the as-printed sample at the initial immersion time up to 2×10^4 s, potentially related to the localized attack occurrence on the surface of the sample [24]. Several drop-offs were also observed through the OCP monitoring for the wrought-420 MSS, ascribed to continuous metastable pitting on the sample's surface [26].
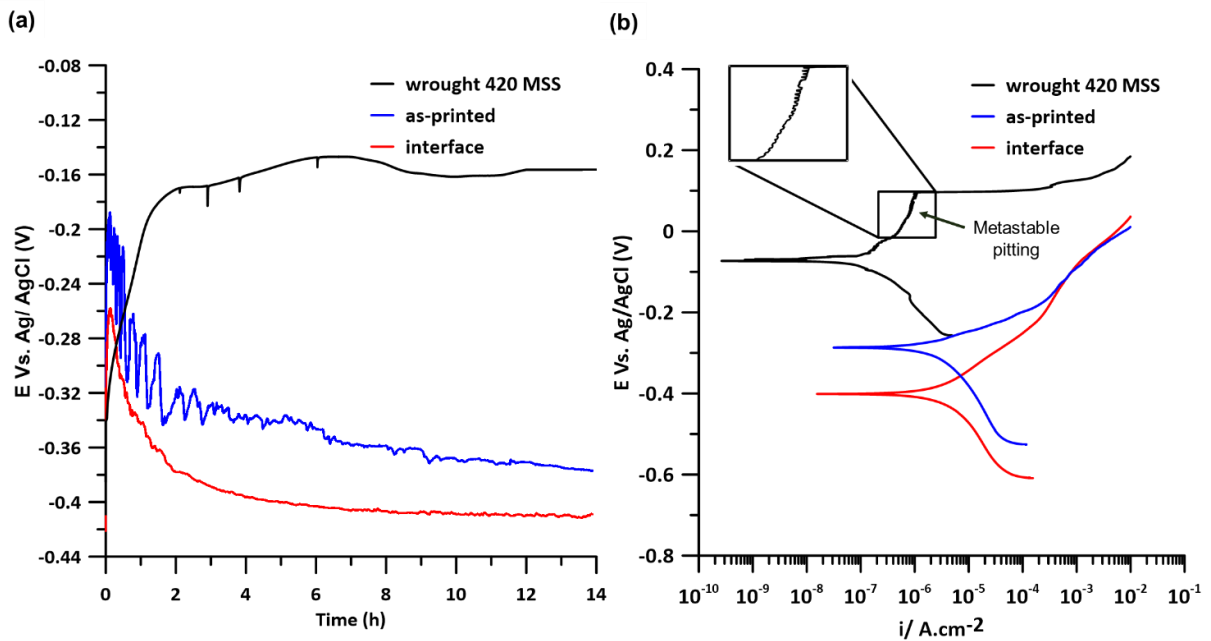
Figure 6. 10. (a) The OCP values versus time and (b) PDP graphs.

The PDP tests were run following the OCP tests to examine the corrosion performance of the samples in aerated 3.5 wt.% NaCl-solution at 25°C, as shown in Figure 6. 10b. Table 6. 3 depicts the obtained electrochemical parameters from the PDP experiments. The PDP curve of the wrought 420 MSS sample showed a passive behavior with a distinct breakdown potential, while an active-like behavior, characterized by a rapid increase of the current density at the anodic branch for potentials higher than corrosion potential ($E>E_{corr}$) with no clear breakdown potential, was detected for the as-printed and interface samples. This active-like behavior possibly indicates the constant occurrence of the localized corrosion attacks, hindering the formation of a stable passive film on samples' surfaces. The metastable pitting occurrence was also observed in the anodic branch (see Figure 6. 10b) for the wrought 420 MSS sample [26]. The interfacial bonding sample exhibited lower E_{corr} and higher corrosion current density (i_{corr}) values as compared to the as-printed and wrought-420 MSS samples, suggesting its higher electrochemical susceptibility and lower corrosion resistance, in agreement with the observed OCP trends.

Table 6. 3. The corrosion parameters obtained from the PDP graphs.

Sample	E_{corr} (mV$_{Ag/AgCl}$)	i_{corr} (µA cm^{-2})	i_p (µA cm^{-2})	E_{pit} (mV$_{Ag/AgCl}$)
Wrought-420 MSS	-293±12	0.21±0.04	8.256±0.04	123±15
As-printed	-358±15	0.44±0.03	-	-
Interface	-396±13	0.51±0.04	-	-

3.3.2. EIS results

To assess the long-term integrity and protectiveness of the formed passive layer on the surface of wrought-420 MSS, as-printed WAAM-420 MSS, and interfacial bonding region samples, EIS experiments were performed in aerated 3.5% NaCl-solution at 25°C. To examine the stability of the formed passive film for different samples, the EIS results after 1h of immersion time were compared with those conducted after 5-days of immersion time. The obtained Bode plots and Nyquist diagrams after 1h and 5-days of immersion time are demonstrated in Figure 6. 11a-11d.

The ohmic drop at high frequencies on the Bode plots corresponds to the low electrolyte resistance values, whereas the absolute impedance values at low to medium frequencies represent the integrity of the passive film on the surface of the samples. At both immersion times of 1h and 5-days, the wrought-420 MSS sample is showing noticeably higher absolute impedance value at medium and low frequencies (see Figure 6. 11a and 11c) as compared to the as-printed WAAM-420 and interface samples, indicating significantly slower kinetics for the corrosion reactions on the surface of the wrought-420 MSS substrate. Extremely smaller capacitive semi-circle radius of Nyquist plots for the interface and as-printed samples, compared to the large capacitive radius of the wrought-420 MSS sample at both immersion times of 1h and 5-days (see Figure 6. 11b and 11d), also confirm the less stable and protective nature of the passive film on the surface of the interface and as-printed samples [41], in harmony with the observed OCP and PDP trends. A significant decrease in the absolute impedance values at medium and high frequencies for Bode plots, and also significant reduction on the capacitive semi-circle radius for all samples immersed for longer time (5-days), compared to the samples immersed for 1h, is ascribed to the dissolution of passive film into the electrolyte solution, decreasing the electrochemical resistance over the time [16,41].

The phase angle diagram of the wrought-420 MSS sample exhibits two wide individual peaks in the range of −60° to −80° after 1h of immersion time (Figure 6. 11a). The first peak is attributed to the impact of passive layer sealing at higher frequencies and the second one represents diffusion through the susceptible regions to the localized corrosion and the double-layer capacitance at medium and lower frequencies [24]. The same trend is observed for the as-printed sample after 5-days of immersion time, while other samples are showing wide phase angle peaks over the varying

frequencies, potentially attributed to the superposition of two distinct peaks possessing two non-discriminating time constants [24].

To elucidate the passive layer characteristics formed on each sample in a quantitative way, a simplified equivalent circuit (SEC), as shown in Figure 6. 11e, was utilized to fit the experimental EIS results. The modeled data are also reflected on the Bode and Nyquist plots (Figure 6. 11a-11d). In the applied SEC model, R_s represents the resistance of the solution, CPE_p and R_p correspond to the capacitance and the resistance of the passive film, CPE_{dl} and R_{ct} represent the double layer constant phase element (CPE) and its charge transfer resistance, respectively [28].

The absolute impedance value of the constant phase element can be determined by the following equation:

$$Z_{CPE} = [Q(i\omega)^n]^{-1} \tag{7}$$

where Q is the CPE constant, ω is the angular frequency, n is the dispersion coefficient of the constant phase element, and i is an imaginary unit (i = $-(1)^{1/2}$) [24].

Table 6. 4 presents the deducted electrochemical parameters from the EIS experiments. The as-printed and interface samples after both immersion times of 1h and 5-days exhibited noticeably lower charge transfer resistance and higher double-layer constant phase element values as compared to those of the wrought-420 MSS, affirming less protective nature of their passive film against localized corrosion attacks. Lower R_p and R_{ct} values for samples immersed for 5-days compared to the samples immersed for 1h reveal the deterioration of the passive layer's electrochemical stability over time [42].

At both immersion times, lower R_{ct} values were observed compared to their corresponding R_p values ($R_p > R_{ct}$) for the as-printed and interface samples, confirming the active-like behavior of the

exposed samples' surfaces, while higher charge transfer resistance values than the passive film resistance (R_p<R_{ct}) was detected for the wrought-420 alloys, indicating its clear passive behavior.

The thickness of the passive layer can be estimated by a mathematical model developed by Hirschorn *et al.* [42]. In this model, the effective capacitance (C_{eff}) is determined using the following equation [42]:

$$C_{eff} = gQ(\rho_\delta \varepsilon_0 \varepsilon)^{1-n} \tag{8}$$

where g is a function of n ($g = 1 + 2.88(1-n)^{2.375}$), ρ_δ is the maximum resistance of the passive layer, ε_0 is the vacuum permittivity (8.854×10^{-14} Fcm^{-1}), and ε is the passive film dielectric constant (~15.6 for Cr_2O_3) [18,43]. After calculating the effective capacitance, the thickness of the passive film can be found by applying the following equation [16,41]:

$$L_{ss} = \frac{\varepsilon \varepsilon_0 A}{C_{eff}} \tag{9}$$

where A is the surface area of the exposed samples to the corrosive electrolyte. The fitted effective capacitance and passive film thickness values are presented in Table 6. 5. The passive film thickness for the as-printed and interface samples is significantly lower than that for the wrought-420 MSS sample, well-aligned with the attained electrochemical analysis results in the current study.
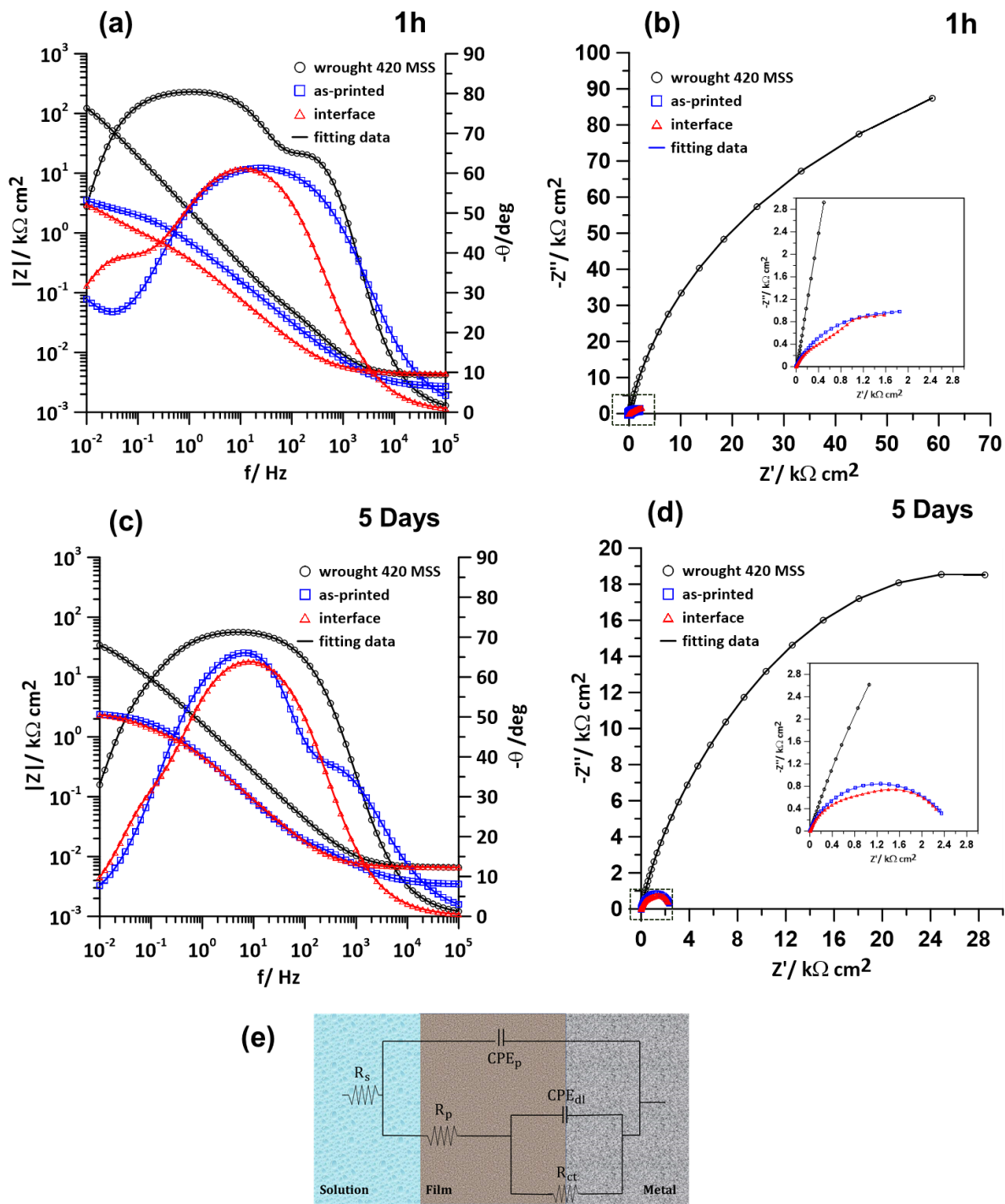
Figure 6. 11. The Bode and Nyquist plots of samples after (a) and (b) 1h, (c) and (d) 5-days of immersion time, (e) the used equivalent circuit fitted to the EIS data.

Table 6. 4. The deducted electrochemical parameters from the EIS experiments and the applied model.

Immersion Time	Sample	R_s (Ωcm^2)	CPE_p ($\Omega^{-1}cm^{-2}s^n$)	n_1	R_p (Ωcm^2)	CPE_{dl} ($\Omega^{-1}cm^{-2}s^n$)	n_2	R_{ct} (Ωcm^2)	$\sum \chi^2$
1 h	As-printed	3.54	1.75×10^{-4}	0.89	1.40×10^4	1.33×10^{-4}	0.88	1.89×10^2	1.27×10^{-5}
	Interfacial bonding	3.56	6.82×10^{-5}	0.96	2.60×10^4	5.74×10^{-5}	0.94	1.93×10^3	1.64×10^{-5}
	Wrought-420 MSS	3.58	9.27×10^{-6}	0.94	1.19×10^2	2.62×10^{-5}	0.86	1.90×10^5	1.62×10^{-5}
5-Days	As-printed	3.54	9.94×10^{-4}	0.89	6.04×10^3	1.83×10^{-4}	0.83	1.03×10^2	1.52×10^{-5}
	Interfacial bonding	3.58	4.23×10^{-4}	0.88	1.74×10^3	1.25×10^{-3}	0.84	1.24×10^3	1.47×10^{-5}
	Wrought-420 MSS	3.65	8.24×10^{-5}	0.87	1.12×10^2	2.71×10^{-2}	0.98	7.5×10^3	1.25×10^{-5}

Table 6. 5 The effective capacitance *(C_eff)* and passive film thickness (L_{ss}) calculated for each sample at different immersion times.

Immersion Time	Sample	C_{eff} (Fcm^{-2})	L_{ss} (nm)
1h	Wrought-420 MSS substrate	1.23×10^{-5}	62.34
	as-printed	6.52×10^{-4}	0.52
	interface	6.97×10^{-4}	0.48
5-Days	Wrought-420 MSS substrate	5.63×10^{-5}	34.46
	as-printed	8.24×10^{-4}	0.25
	interface	9.69×10^{-4}	0.21

3.3.3. Mott-Schottky analysis

Mott-Schottky measurements were conducted to characterize the semi-conductive characteristics of the samples in the applied electrolyte. Mott-Schottky plots for the 420 MSS substrate, as-printed, and the interfacial region samples are shown in Figure 6. 12a-12c. Based on the Mott-Schottky equation, the applied potential value (E) and the measured electrode capacitance (C) are correlated as follows [44]:

$$\frac{1}{C^2} = \frac{1}{C_H^2} + \frac{1}{C_{SC}^2} = \frac{1}{C_H^2} + \frac{2}{e.N_q.\varepsilon.\varepsilon_0}\left(E - E_{FB} - \frac{kT}{e}\right) \tag{10}$$

where C_H is the Helmholtz capacitance, C_{SC} is the space charge capacitance of the passive film, e is the electron charge (1.6×10^{-19} C), N_q is the doping density, ε is the relative dielectric constant for the passive layer ($\varepsilon = 15.6$ for martensitic stainless steel), ε_0 is the vacuum permittivity, k is Boltzmann's constant (8.16×10^{-5} eV/K), E_{FB} is the flat band potential, and T is the absolute temperature. The linear portion of C^{-2} vs E graph can be used to calculate the N_q and E_{FB} by implementing the intercept and slop technique and by considering the kT/e value close to zero [44].

Three distinct zones with different slopes were detected from the Mott-Schottky graphs for the studied samples. The left zone with a negative slope possesses p-type semiconductor behavior in which the major defect formation factor in the passive film is the cation vacancies [45]. The formed oxide layer through the p-type semiconductor zone for martensitic stainless steel is primarily chromium oxide (Cr_2O_3), which contains a higher number of holes in the valence band of the oxide film as compared to the number of electrons in the conduction band [16,46]. The middle region with a positive slope possesses n-type semiconductor behavior, in which major defect formation factors in the passive film are oxygen vacancies and interstitial cations [46] . Based on the electron band theory, it can be inferred that the formed oxide layer through the n-type transition for a 420 MSS alloy is considered to be an iron oxide (Fe_2O_3), since the number of the holes in its valence band is less than the number of electrons in its conduction band. For martensitic stainless steels possessing a high content of iron and chromium, it is frequently reported that the observed duplex semiconductor behavior is caused by the formation of an internal chromium oxide passive film with p-type behavior containing metal vacancies as acceptor states, along with an external iron oxide passive layer, possessing n-type semiconductor characteristics, which contains oxygen vacancies as donor states [16]. The region with the negative slope on the right side of the curve where E $\geq$ 0.2 V is attributed to the formation of an inversion layer where no reasonable

relationship can be correlated between the semiconductor behavior and charge carriers due to the high density of holes in the valence band [24,44].

The calculated donor density (N_D) and acceptor density (N_A) values, using equation 6 and the slope of the M-S curves for the wrought-420 MSS, as-printed WAAM-420 MSS, and interfacial bonding regions are shown in Figure 6. 12d, where only a single donor level was identified. Although the obtained N_D and N_A values with the order of 10^{17}-10^{18} cm^{-3} in magnitude imply the existence of severely disordered passive layer on all samples' surfaces, significantly higher donor and acceptor density values were observed in the interfacial bonding region followed by the as-printed sample, while the N_D and N_A values were the lowest for the wrought-420 MSS substrate. The stability of the passive layer is highly disturbed by the high donor and acceptor density due to the significant increase in the occurrence of the electrochemical reactions at the metal/passive film interface [16,44,45]. Higher N_D is also a major sign of increased susceptibility for the pitting nucleation and localized attack initiation on the sample's surface, due to the increased adsorption affinity of chloride ions in the passive layer [47]. Thus, the passive film of the interfacial bonding and as-printed samples potentially can have easier chloride ions adsorption, and simultaneously this can accelerate the reaction between oxygen vacancies in the passive film and chloride ions [47].

As discussed earlier, the dislocation densities of interfacial bonding region and as-printed WAAM-420 MSS samples were estimated to be significantly higher than that of the wrought-420 MSS sample after the process-induced martensite transformation through WAAM, as summarized in Table 6. 2. Considering the M-S curves of the samples, in the WAAM-420 MSS, the doping concentration significantly increases as a result of the formation of a highly strained martensitic structure, which can also reflect on the susceptibility to localized corrosion attack [48]. As

suggested by the point defect model, the cation vacancies' formation is commonly expected to occur at the passive film/electrolyte interface, while oxygen vacancies and cation interstitials generally nucleate at the interface of the passive layer and metal, which can initiate the severe propagation of localized attacks and deterioration of the passive film [49].

Martensite formation-induced dislocations can potentially contribute to the formation of the passive layer at the interface of the metal and passive film through the reaction below [50]:

$$M + T \rightarrow M + \frac{x}{2} V_o^{\cdot\cdot} + xe^{'} \qquad (11)$$
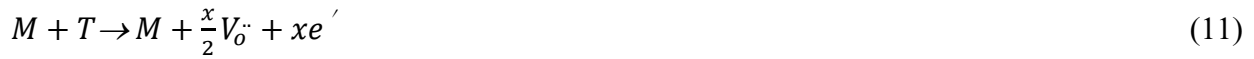
where M represents the metal (420 MSS in this study), T is defined as the process-induced dislocation formed at the interface of the metal and passive layer, $e^{'}$ is the transferred electron, and $V_o^{\cdot\cdot}$ is the oxygen vacancy. According to reaction (11), one mole of the dislocation formed through the martensitic phase transformation herein, can produce $\frac{x}{2}$ mole of oxygen vacancies at the passive layer [48]. Hence, an increased dislocation density through the martensitic phase transformation for the as-printed and interface sample can stimulate more oxygen vacancies in the passive layer and break down the protective nature of the passive film [16]. Furthermore, the diffusion-controlled process of vacancies transition into the passive layer can be facilitated by the martensite-induced dislocations, acting as a supplementary factor for facilitating the deterioration of the passive film formed on the interface and as-printed samples of WAAM-420 MSS [50].
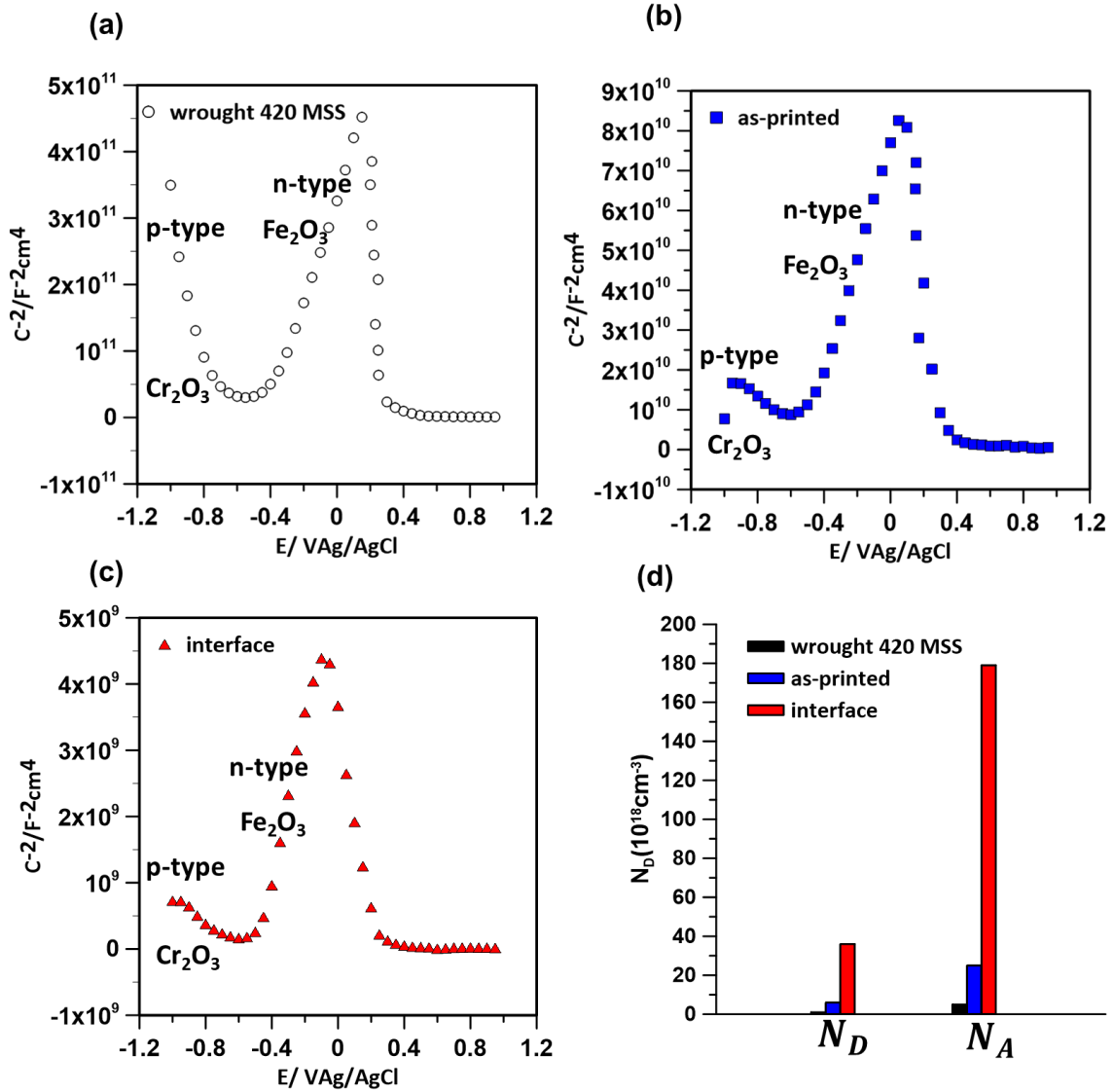
Figure 6. 12. The Mott-Schottky curves of the passive film formed on the (a) wrought-420 MSS substrate, (b) as-printed sample, and (c) the interface sample, (d) the variations of the donor and acceptor densities.

3.4. Electrochemical response interpretation

The correlation between the grain boundary energy (γ_{gb}) and grain boundary misorientation angle (θ) can be explained by the Read-Shockley equation as follows [51]:

$$\gamma_{gb} = \frac{Ga\,\theta}{4\pi(1-\sigma)}(A - ln\theta) \qquad (12)$$

where A is a constant approximately equal to 0.23, G is the shear modulus, σ is the Poisson ratio, and a is the Burgers vector. This relationship confirms that the amount of energy stored in the grain boundaries is highly dependent on the grain's crystallographic misorientation degree. As discussed in section 3.2, a high fraction of HAGBs was detected in PMZ and fusion zone of the interfacial bonding region through the formation of the PAGBs and also nucleation of new austenite grains through the cyclic heating while depositing the subsequent tracks of WAAM-420 MSS. The HAGBs formed in the austenite boundaries in the interface sample possess high energy levels and are considered as easy paths for fast diffusion, deviating the grain boundary diffusivity far away from bulk material's diffusivity, further contributing to the deterioration of the passive layer electrochemical stability [28].

Previous studies have confirmed that the corrosion performance of the wrought-420 MSS alloy is highly related to the microstructural features, *i.e.*, primary micro-constituents, secondary phase formation, and particularly micro-galvanic coupling effect between the cathodic chromium-rich carbides, such as $M_{23}C_6$ and M_7C_3, and anodic ferritic matrix [26]. The corrosion morphology of wrought-420 MSS substrate after the PDP test revealed the nucleation (formation of micro-pits), growth, and propagation of pitting (constant coalescence of the pits) at the susceptible regions to pitting corrosion (see Figure 6. 13a and 13b). These pits were mostly located at the ferrite grain boundaries (see Figure 6. 13b), where a high-volume fraction of chromium-rich carbides were formed, making the matrix/intergranular carbide interface susceptible sites to chromium depletion and pitting corrosion. The dissolution of the iron element from the surface through the PDP test forms a Cr-rich zone along the initiated micro-pits' periphery (see Figure 6. 13c and 13d). The same micro-galvanic coupling effect can have a detrimental impact on the electrochemical response of the as-printed WAAM-420 MSS sample, where non-equilibrium and chromium-rich

residual delta ferrite phase (see Figure 6. 13e-13h) drains the chromium out of its adjacent martensitic regions and act as the cathode, while the martensitic matrix/delta ferrite interface plays the role of the anode, making the entire region susceptible to initiation of localized corrosion attack (Figure 6. 13e-13h) [24]. The formation of high amount of the residual delta ferrite can intensify the micro-galvanic coupling at the martensite/delta ferrite interface and significantly deteriorate the electrochemical performance of the as-printed sample through localized corrosion attack initiation [16].
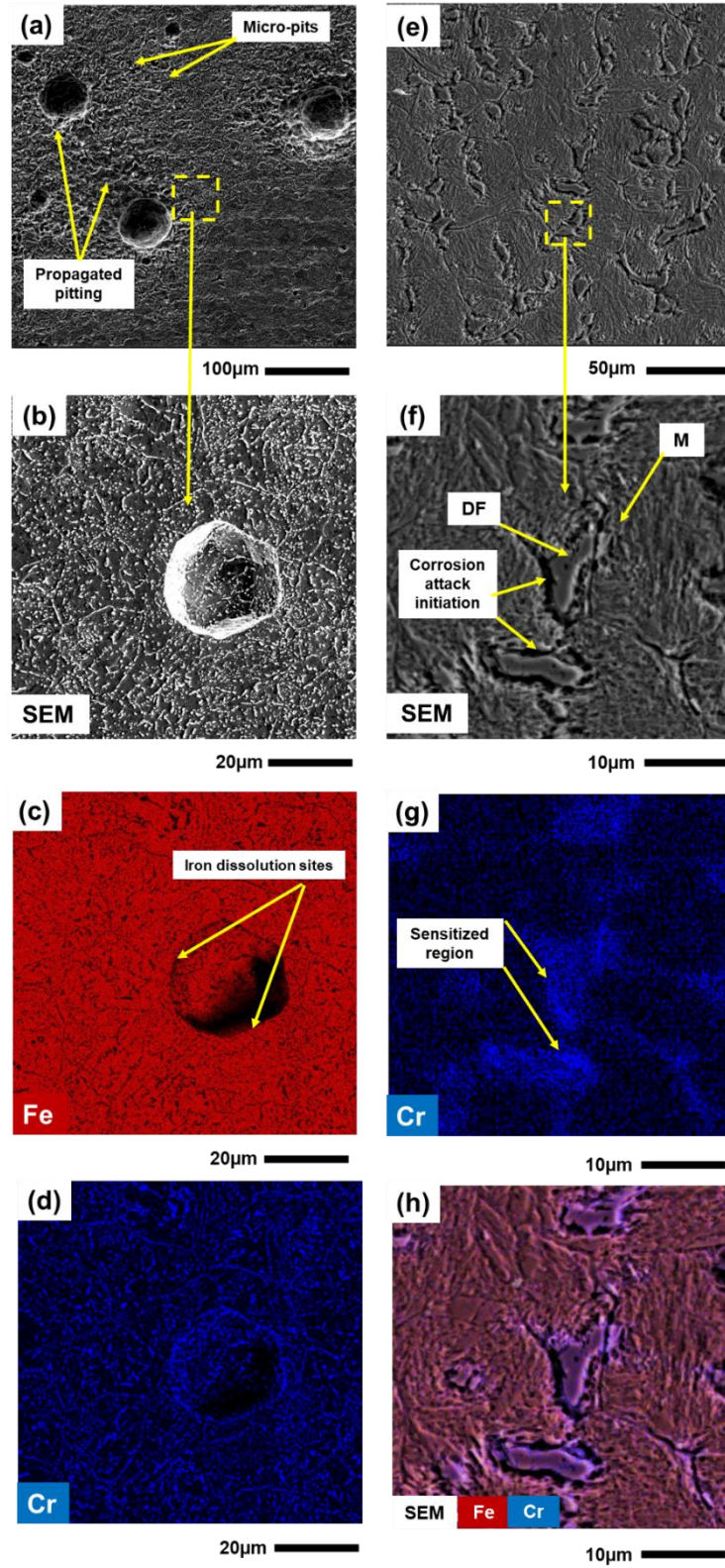
Figure 6. 13. (a) SEM micrograph of the wrought-420 MSS sample showing the corrosion morphology after the PDP test, (b) SEM image at higher magnification showing a micro-pit

initiation site, (c) and (d) the elemental maps for iron and chromium, respectively, (e) and (f) morphology of corroded as-printed sample after the PDP test, and (g) and (h) the corresponding elemental maps for iron and combined iron and chromium, respectively.

SEM micrograph of interfacial bonding region after the PDP experiments is illustrated in Figure 6. 14a. To characterize the corrosion onset and most susceptible sites to localized corrosion, the PDP test has paused at corrosion current density value of 30 μAcm^{-2}. It is observed that the localized corrosion onset occurs mostly at the PAGBs formed in PMZ and fusion zone. Higher magnification SEM micrographs of both PMZ and fusion zone (Figures 6. 14b and 14e) illustrate the intergranular corrosion initiated at the PAGBs, while sensitized regions are characterized by the EDS elemental maps of iron and chromium elements (see Figure 6. 14c-14g). PAGBs possessing high energy levels are susceptible regions to initiation of localized corrosion. As discussed earlier, due to the complex thermal exposure associated with the deposition of successive layers, new austenite grains can form through the high angle boundaries of PAGs, refining the austenite structure in PMZ and fusion zone, and providing more susceptible zones to localized corrosion attack. This can lead to severe deterioration of the electrochemical stability of the interface region through the initiation of intergranular corrosion at the formed PAGBs and refined austenite boundaries [52,53]. Moreover, the complex microstructural features in PMZ with a high volume fraction of fine chromium-rich carbides and residual delta ferrite can intensify the micro-galvanic coupling effect by introducing more susceptible regions with high chromium depletion around the chromium-rich micro-constituents [16]. On the other hand, precipitation of fine chromium carbides along the austenite grain boundaries can intensify the corrosion susceptibility of these regions and shift the corrosion morphology towards intergranular corrosion (see Figures 6. 14b and 14d). The schematic illustrations of the corrosion mechanism and passive/active characteristics for the wrought-420 MSS, as-printed, and the interfacial bonding samples are shown in Figure 6. 15. As schematically illustrated, the active-like behavior of the interface and

as-printed samples and the formation of intact passive layer on the wrought-420 MSS sample are

dictated by the mentioned microstructural features in each sample. Superior electrochemical

response and passive behavior of the wrought-420 MSS substrate are primarily attributed to the

elimination of the susceptible regions to localized corrosion attack, in particular the PAGBs.
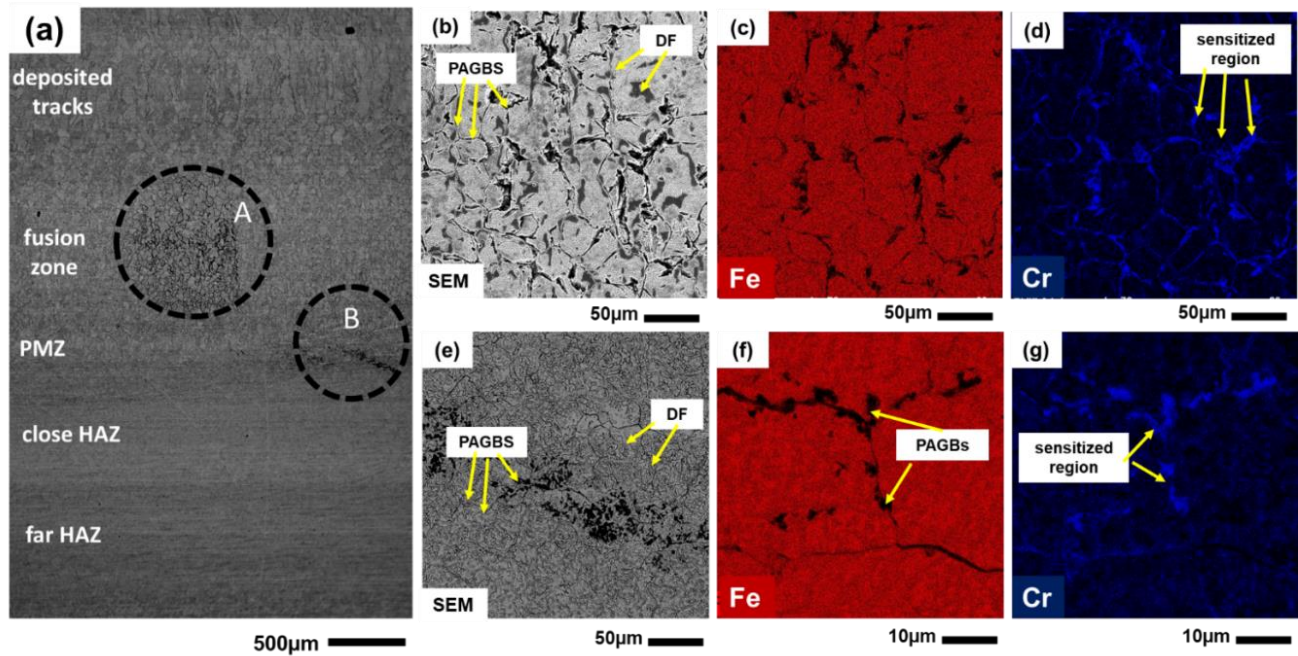
Figure 6. 14. (a) The low-magnification SEM micrograph of the interface region showing the morphology of corroded zone after the PDP test, (b) SEM image at higher magnification from the fusion zone, (c) and (d) the elemental maps for iron and chromium, respectively, (e) SEM micrograph of corroded PMZ, and (f) and (g) the elemental maps for iron and chromium, respectively.
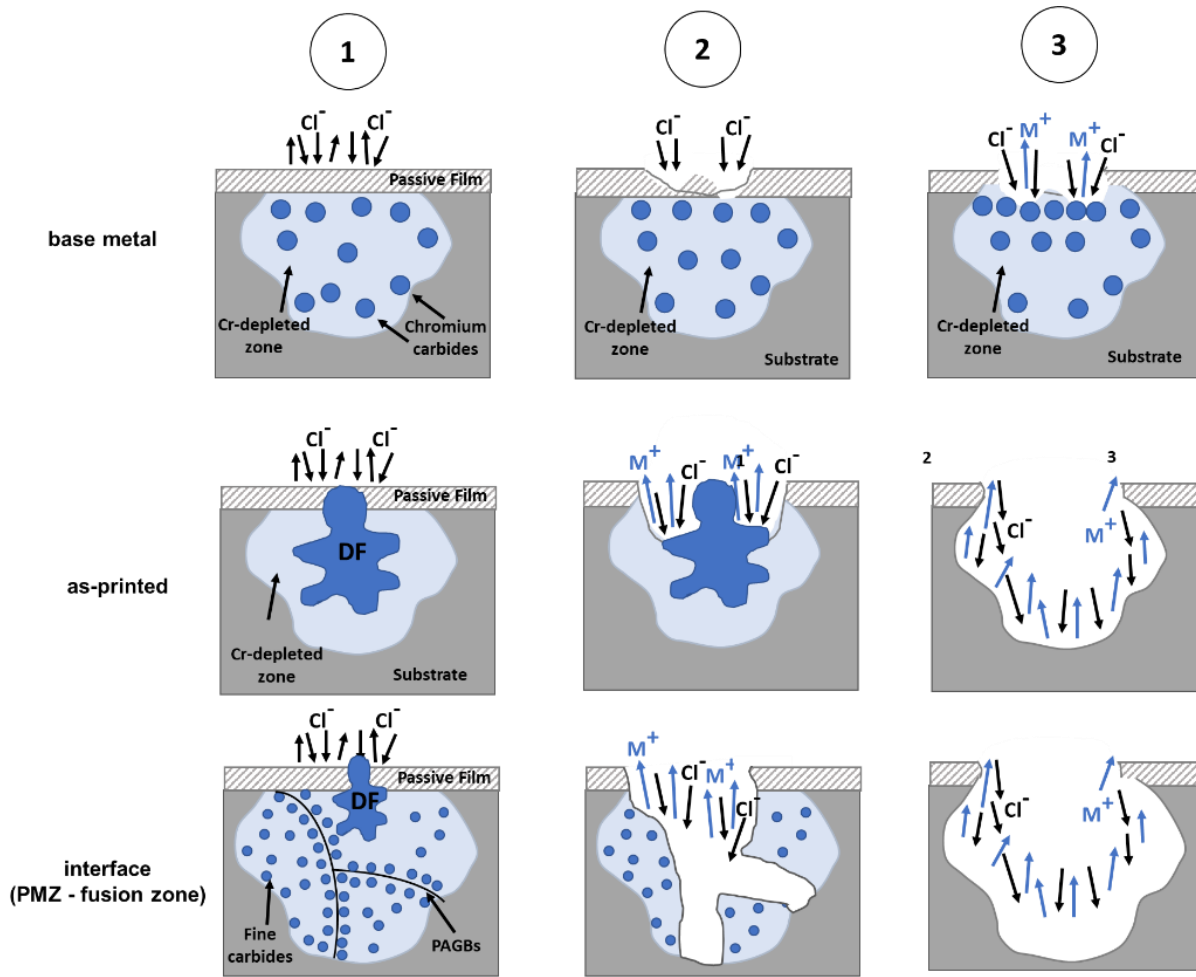
Figure 6. 15. Schematic illustration of the corrosion morphology for the wrought-420 MSS, as-printed WAAM-420 MSS, and the interface region.

4. **Conclusions**

In this article, the interfacial microstructure and corrosion response between a wrought-AISI420 substrate and a wire arc additive manufactured 420 stainless steel were correlated. The electrochemical response of the interfacial region unveiled intense deterioration adjacent to the partially melted zone and fusion zone, ascribed to the existence of a high fraction of primary austenite grain boundaries (PAGBs) as susceptible sites to localized corrosion attack. The onset of localized corrosion attack in the interfacial region was mainly initiated at the fusion zone and the PAGBs, due to the formation of chromium depleted zones at the interface of the PAGBs and the

martensitic matrix. Severe deterioration of the corrosion performance for the as-printed WAAM-420MSS was ascribed to the intensified micro-galvanic coupling effect at the delta ferrite/martensitic matrix interface, while superior electrochemical response and the passive behavior of the wrought-AISI420 substrate was correlated to the elimination of the susceptible regions to localized corrosion attacks, *i.e.*, PAGBs.

Data availability

The raw/processed data required to reproduce these findings cannot be shared at this time due to technical or time limitations.

References

[1]   G.S. San, I.N. Pujawan, Remanufacturing of the short life-cycle products, Oper. Supply Chain Manag. An Int. J. 7 (2014) 13–22.

[2]   A.M. Benoy, L. Owen, M. Folkerson, Triple win-the social, economic and environmental case for remanufacturing, All-Party Parliam. Sustain. Resour. Gr. All-Party Parliam. Manuf. Group, London. (2014).

[3]   S.M. Mirhedayatian, S.E. Vahdat, M.J. Jelodar, R.F. Saen, Welding process selection for repairing nodular cast iron engine block by integrated fuzzy data envelopment analysis and TOPSIS approaches, Mater. Des. 43 (2013) 272–282.

[4]   J. Gardan, Additive manufacturing technologies: state of the art and trends, Addit. Manuf. Handb. (2017) 149–168.

[5]   H. Sun, C. Liu, J. Chen, M. Gao, X. Shen, A novel method of sustainability evaluation in machining processes, Processes. 7 (2019) 275.

[6]   V. Tambrallimath, R. Keshavamurthy, A. Badari, L. Ramesh, G. Raj, Emergence of Additive Manufacturing in global scale during the crisis of 2019-nCoV (novel corona virus), Mater. Today Proc. (2021).

[7]   X. Tang, S. Zhang, C. Zhang, J. Chen, J. Zhang, Y. Liu, Optimization of laser energy density and scanning strategy on the forming quality of 24CrNiMo low alloy steel manufactured by SLM, Mater. Charact. 170 (2020) 110718.

[8]   A.V. Nemani, M. Ghaffari, S. Salahi, A. Nasiri, Effects of post-printing heat treatment on the microstructure and mechanical properties of a wire arc additive manufactured 420 martensitic stainless steel part, Mater. Sci. Eng. A. (2021) 141167.

[9]   S.W. Williams, F. Martina, A.C. Addison, J. Ding, G. Pardal, P. Colegrove, Wire + Arc Additive Manufacturing, Mater. Sci. Technol. 32 (2016) 641–647. doi:10.1179/1743284715Y.0000000073.

[10]   C. V Haden, G. Zeng, F.M. Carter, C. Ruhl, B.A. Krick, D.G. Harlow, Wire and arc additive manufactured steel: Tensile and wear properties, Addit. Manuf. 16 (2017) 115–123. doi:https://doi.org/10.1016/j.addma.2017.05.010.

[11]   X. Chen, J. Li, X. Cheng, B. He, H. Wang, Z. Huang, Microstructure and mechanical properties of

the austenitic stainless steel 316L fabricated by gas metal arc additive manufacturing, Mater. Sci. Eng. A. 703 (2017) 567–577. doi:https://doi.org/10.1016/j.msea.2017.05.024.

[12] J. Ge, J. Lin, Y. Chen, Y. Lei, H. Fu, Characterization of wire arc additive manufacturing 2Cr13 part: Process stability, microstructural evolution, and tensile properties, J. Alloys Compd. 748 (2018) 911–921.

[13] A.T. Polonsky, M.P. Echlin, W.C. Lenthe, R.R. Dehoff, M.M. Kirka, T.M. Pollock, Defects and 3D structural inhomogeneity in electron beam additively manufactured Inconel 718, Mater. Charact. 143 (2018) 171–181.

[14] N.A. Kistler, D.J. Corbin, A.R. Nassar, E.W. Reutzel, A.M. Beese, Effect of processing conditions on the microstructure, porosity, and mechanical properties of Ti-6Al-4V repair fabricated by directed energy deposition, J. Mater. Process. Technol. 264 (2019) 172–181.

[15] M. Ghaffari, A.V. Nemani, A. Nasiri, Interfacial bonding between a wire arc additive manufactured 420 martensitic stainless steel part and its wrought base plate, Mater. Chem. Phys. (2020) 123199.

[16] S. Salahi, M. Kazemipour, A. Nasiri, Effects of microstructural evolution on the corrosion properties of AISI 420 martensitic stainless steel during cold rolling process, Mater. Chem. Phys. 258 (2021). doi:10.1016/j.matchemphys.2020.123916.

[17] A. Persson, S. Hogmark, J. Bergström, Thermal fatigue cracking of surface engineered hot work tool steels, Surf. Coatings Technol. 191 (2005) 216–227.

[18] S. Salahi, M. Ghaffari, A.V. Nemani, A. Nasiri, Effects of Secondary-Phase Formation on the Electrochemical Performance of a Wire Arc Additive Manufactured 420 Martensitic Stainless Steel under Different Heat Treatment Conditions, J. Mater. Eng. Perform. (2021) 1–12.

[19] B. Zhu, J. Lin, Y. Lei, Y. Zhang, Q. Sun, S. Cheng, Additively manufactured δ-ferrite-free 410 stainless steel with desirable performance, Mater. Lett. 293 (2021) 129579.

[20] Z. Lyu, Y.S. Sato, S. Tokita, Y. Zhao, J. Jia, A. Wu, Microstructural evolution in a thin wall of 2Cr13 martensitic stainless steel during wire arc additive manufacturing, Mater. Charact. 182 (2021) 111520.

[21] J. Moon, H.-Y. Ha, T.-H. Lee, Corrosion behavior in high heat input welded heat-affected zone of Ni-free high-nitrogen Fe–18Cr–10Mn–N austenitic stainless steel, Mater. Charact. 82 (2013) 113–119.

[22] M. Shojaati, S.F.K. Bozorg, M. Vatanara, M. Yazdizadeh, M. Abbasi, The heat affected zone of X20Cr13 martensitic stainless steel after multiple repair welding: Microstructure and mechanical properties assessment, Int. J. Press. Vessel. Pip. 188 (2020) 104205.

[23] Y. Zhang, F. Cheng, S. Wu, Improvement of pitting corrosion resistance of wire arc additive manufactured duplex stainless steel through post-manufacturing heat-treatment, Mater. Charact. 171 (2021) 110743.

[24] S. Salahi, A.V. Nemani, M. Ghaffari, J. Lunde, A. Nasiri, On Microstructure, Crystallographic Orientation, and Corrosion Properties of Wire Arc Additive Manufactured 420 Martensitic Stainless Steel: Effect of the Inter-layer Temperature, Addit. Manuf. (2021) 102157.

[25] A. Vahedi Nemani, M. Ghaffari, A. Nasiri, On the Post-Printing Heat Treatment of a Wire Arc Additively Manufactured ER70S Part, Materials (Basel). 13 (2020) 2795.

[26] K.H. Anantha, C. Ornek, S. Ejnermark, A. Medvedeva, J. Sj, Correlative Microstructure Analysis and In Situ Corrosion Study of AISI 420 Martensitic Stainless Steel for Plastic Molding, 164 (2017) 85–93. doi:10.1149/2.0531704jes.

[27] A.V. Nemani, M. Ghaffari, S. Salahi, J. Lunde, A. Nasiri, Effect of interpass temperature on the formation of retained austenite in a wire arc additive manufactured ER420 martensitic stainless steel, Mater. Chem. Phys. (2021) 124555.

[28] S. Salahi, M. Kazemipour, A. Nasiri, Effect of Uniaxial Tension-Induced Plastic Strain on the Microstructure and Corrosion Behavior of 13Cr Martensitic Stainless Steel, CORROSION. (2020).

[29] H.M. Rietveld, Line profiles of neutron powder-diffraction peaks for structure refinement, Acta

Crystallogr. 22 (1967) 151–152.

[30] M. Dongol, A. El-Denglawey, A.F. Elhady, A.A. Abuelwafa, Structural properties of nano 5, 10, 15, 20-Tetraphenyl-21H, 23H-porphine nickel (II) thin films, Curr. Appl. Phys. 12 (2012) 1334–1339.

[31] R.A. Varin, J. Bystrzycki, A. Calka, Effect of annealing on the microstructure, ordering and microhardness of ball milled cubic (L12) titanium trialuminide intermetallic powder, Intermetallics. 7 (1999) 785–796.

[32] A.A. Al-Ghamdi, S.A. Khan, A. Nagat, M.S. Abd El-Sadek, Synthesis and optical characterization of nanocrystalline CdTe thin films, Opt. Laser Technol. 42 (2010) 1181–1186.

[33] T. Shintani, Y. Murata, Evaluation of the dislocation density and dislocation character in cold rolled Type 304 steel determined by profile analysis of X-ray diffraction, Acta Mater. 59 (2011) 4314–4322.

[34] M.R. Jandaghi, H. Pouraliakbar, Elucidating the microscopic origin of electrochemical corrosion and electrical conductivity by lattice response to severe plastic deformation in Al-Mn-Si alloy, Mater. Res. Bull. 108 (2018) 195–206.

[35] J. Hidalgo, M.J. Santofimia, Effect of prior austenite grain size refinement by thermal cycling on the microstructural features of as-quenched lath martensite, Metall. Mater. Trans. A. 47 (2016) 5288–5301.

[36] H. Kitahara, R. Ueji, N. Tsuji, Y. Minamino, Crystallographic features of lath martensite in low-carbon steel, Acta Mater. 54 (2006) 1279–1288.

[37] N. Nakada, T. Tsuchiyama, S. Takaki, N. Miyano, Temperature dependence of austenite nucleation behavior from lath martensite, ISIJ Int. 51 (2011) 299–304.

[38] S. Chen, Q. Yu, The role of low angle grain boundary in deformation of titanium and its size effect, Scr. Mater. 163 (2019) 148–151.

[39] F. Khodabakhshi, M.H. Farshidianfar, A.P. Gerlich, M. Nosko, V. Trembošová, A. Khajepour, Effects of laser additive manufacturing on microstructure and crystallographic texture of austenitic and martensitic stainless steels, Addit. Manuf. 31 (2020) 100915.

[40] G.L. Liu, S.W. Yang, W.T. Han, P.P. Yan, M. Wang, Q. Hu, R.D.K. Misra, C.J. Shang, F.R. Wan, The simultaneous occurrence of Kurdjumov-Sachs and irrational orientation relationships between delta-ferrite and austenite phase in a 17Cr–5Ni stainless steel, Mater. Sci. Eng. A. 798 (2020) 140122.

[41] M. Rafieazad, M. Mohammadi, A. Gerlich, A. Nasiri, Enhancing the corrosion properties of additively manufactured AlSi10Mg using friction stir processing, Corros. Sci. 178 (n.d.) 109073.

[42] B. Hirschorn, M.E. Orazem, B. Tribollet, V. Vivier, I. Frateur, M. Musiani, Constant-phase-element behavior caused by resistivity distributions in films: I. Theory, J. Electrochem. Soc. 157 (2010) C452.

[43] A. Fattah-Alhosseini, M.A. Golozar, A. Saatchi, K. Raeissi, Effect of solution concentration on semiconducting properties of passive films formed on austenitic stainless steels, Corros. Sci. 52 (2010) 205–209.

[44] H. Luo, X. Wang, C. Dong, K. Xiao, X. Li, Effect of cold deformation on the corrosion behaviour of UNS S31803 duplex stainless steel in simulated concrete pore solution, Corros. Sci. 124 (2017) 178–192.

[45] L. V Taveira, M.F. Montemor, M.D.C. Belo, M.G. Ferreira, L.F.P. Dick, Influence of incorporated Mo and Nb on the Mott–Schottky behaviour of anodic films formed on AISI 304L, Corros. Sci. 52 (2010) 2813–2818.

[46] S.R. Morrison, Electrochemistry at semiconductor and oxidized metal electrodes, (1980).

[47] D.G. Li, Y.R. Feng, Z.Q. Bai, J.W. Zhu, M.S. Zheng, Influence of temperature, chloride ions and chromium element on the electronic property of passive film formed on carbon steel in bicarbonate/carbonate buffer solution, Electrochim. Acta. 52 (2007) 7877–7884.

[48] M. Talha, Y. Ma, Y. Lin, Y. Pan, X. Kong, O.P. Sinha, C.K. Behera, Corrosion performance of cold deformed austenitic stainless steels for biomedical applications, Corros. Rev. 37 (2019) 283–

306.

[49] A. Fattah-Alhosseini, F. Soltani, F. Shirsalimi, B. Ezadi, N. Attarzadeh, The semiconducting properties of passive films formed on AISI 316 L and AISI 321 stainless steels: A test of the point defect model (PDM), Corros. Sci. 53 (2011) 3186–3192.

[50] D.J. Sprouster, W.S. Cunningham, G.P. Halada, H. Yan, A. Pattammattel, X. Huang, D. Olds, M. Tilton, Y.S. Chu, E. Dooryhee, Dislocation microstructure and its influence on corrosion behavior in laser additively manufactured 316L stainless steel, Addit. Manuf. 47 (2021) 102263.

[51] W.T. Read, W. Shockley, Dislocation models of crystal grain boundaries, Phys. Rev. 78 (1950) 275.

[52] I.G.R. Santos, F.F. de Assis, R. Silva, G. Zepon, C.A.D. Rovere, Corrosion resistance of UNS S41426 stainless steel in acid media and its relation to chemical partition and austenite fraction, Corros. Sci. 188 (2021) 109519.

[53] P. Ganesh, R. Giri, R. Kaul, P.R. Sankar, P. Tiwari, A. Atulkar, R.K. Porwal, R.K. Dayal, L.M. Kukreja, Studies on pitting corrosion and sensitization in laser rapid manufactured specimens of type 316L stainless steel, Mater. Des. 39 (2012) 509–521.

Chapter 7

Electrochemical Performance of the Interfacial Region between an AISI 420 and a Wire Arc Additive Manufactured PH 13–8Mo Martensitic Stainless Steel[6]

Preface

The original version of this manuscript has already been prepared for submission to the Journal of Additive manufacturing. I am the first and the corresponding author of the current work. In this chapter, along with my colleagues, Dr. Ali Nasiri, Alireza Vahedi Nemani, and Mahya Ghaffari, I characterize the microstructure and electrochemical performance of the interface between a wrought 420 MSS substrate and wire arc additively manufactured PH 13–8Mo Martensitic Stainless steel. I was responsible for preparing methodology, experimental testing, result gathering, and drafting of the original manuscript. Subsequently, I revised the paper based on my colleagues' initial comments and peer-review process feedback. The co-authors contributed to the conceptualizing, project administration, supervision, and editing of the manuscript

---

[6] Salahi, Salar, Mahya Ghaffari, Alireza Vahedi Nemani, and Ali Nasiri. " Electrochemical Performance of the Interfacial Region between an AISI 420 and a Wire Arc Additive Manufactured PH 13–8Mo Martensitic Stainless Steel. Prepared for the " *Journal of Additive Manufacturing*.

Abstract

In this study, the electrochemical response of the interfacial region between an AISI 420 martensitic stainless-steel (MSS) substrate and a wire arc additive manufactured PH 13-8Mo MSS part was investigated. The complicated thermal cycle through the deposition of the PH 13-8Mo part led to the formation of distinct zones, including far heat-affected zone (FHAZ), close heat-affected zone (CHAZ), partially melted zone (PMZ), and fusion zone (FZ) at the interfacial bonding region. The formation of an austenitic structure with coarse grains was observed in the PMZ and FZ. The corrosion performance of the interface sample was degraded significantly, attributed to the formation of highly populated fine chromium-rich carbides. The corrosion onset at the interface region was initiated at the carbide/matrix interface in the CHAZ and PMZ regions, where chromium depleted regions adjacent to the carbides intensify the micro-galvanic coupling effect. The corrosion resistance of the as-printed PH 13-8Mo sample was remarkably higher than the 420 MSS and interface samples, supported by the formation of an intact passive film on the samples' surfaces. The formation of a uniform lath martensitic structure with low energy levels at lath boundaries and the absence of metastable chromium-rich micro-constituents, such as carbides, due to the low carbon content of the PH 13-8Mo MSS alloy, contributed to its superior electrochemical performance.

1. Introduction

Metal additive manufacturing (AM), also known as metal 3D printing, is a promising alternative to conventional manufacturing for fabricating customized and highly complex metallic components [1]. Considering the current disruption on the global supply chain for the manufacturing sector, the AM processes can offer more versatile inventory management for the post-Covid era by providing on-site manufacturing options and less material waste as compared to the conventional fabrication methods [2,3]. Among various AM techniques, wire arc additive manufacturing (WAAM) is considered a highly efficient AM method for the production of large-scale metal components due to its high deposition rate (~3–8 kg/h) [4]. WAAM can also be implemented for rapid restoration and remanufacturing of defected or even failed components [5,6]. In the WAAM process, the feedstock wire is continuously fed into an electric arc or plasma while it is translated along the deposition direction using a 6-axis robotic arm or a computerized numerically controlled system [7,8]. Among the adopted heating sources for the WAAM process, the use of gas metal arc (GMA) based WAAM process has been extensively investigated to fabricate metallic components from various feedstock alloys, such as steels, aluminum, titanium, brass, and nickel alloys [9,10]. Fabrication feasibility of ferrous alloys through WAAM process has been thoroughly examined for austenitic stainless steels [11,12], duplex steels [13], martensitic stainless steels [14], and precipitation hardened martensitic stainless steels (PHMSS) [15].

On the other hand, the application of the wire arc additive manufacturing process is not only restricted to the fabrication of large-scale metallic components. Recently, several studies have

explored new techniques for implementing the WAAM as a micro-scale restoration method, especially in the manufacturing industry, where part replacement is costly and requires service interruption [6,16,17]. For instance, AISI 420 martensitic stainless steel (420 MSS) containing 13 wt.% chromium with a great combination of high strength, suitable wear and creep resistance, and acceptable corrosion performance is widely used for plastic molding applications [18]. Implementing conventional manufacturing techniques to fabricate these molds generally end up with recurring failures during service [19]. A localized and automated restoration process by implementing the WAAM technique can expand the in-service life of the 420 MSS molds and delay the part replacement in critical situations [20]. Considering the formation of martensitic lath structure and the high tensile strength of the 420 MSS parts fabricated by the WAAM process, implementing the similar 420 MSS track as the restoration material can be favorable in terms of mechanical response [8]. However, the electrochemical performance of the 420 MSS track can be challenging due to the formation of residual metastable phases with high chromium and high carbon content at the interface region [25,26]. Hence, applying a dissimilar restoring track with acceptable mechanical performance and higher corrosion response compared to the 420 MSS components can be reasonable. Unlike the martensitic stainless steels (MSS), PH-MSS alloys, such as 17-4 PH, 15-5 PH, and PH 13-8Mo alloys, possess a low carbon content ($\leq$0.07 wt.%), which hinders the formation of carbon-rich secondary phases and leads to superior corrosion performance as compared to the WAAM 420 MSS [15,21]. Hence, applying the as-printed PH-MSS tracks as the localized repairing alternative for the 420 MSS casting molds is potentially more viable than the similar 420 WAAM tracks, considering the superior corrosion performance.

As the first step to analyze the application feasibility of the WAAM PH-MSS alloys as a restoration alternative, it is crucial to explore the performance of the fabricated parts with other

accessible AM techniques. Several studies have been conducted to investigate the fabrication possibility of PH-MSS alloys via additive manufacturing techniques. Asghari and Mohammadi [22] have successfully fabricated stainless steel CX alloy with a similar composition to PH 13-8Mo alloy, implementing powder-based direct metal laser sintering (DMLS) process and reported a low level of porosity formation and high tensile strength for as-printed parts. Shahriari *et al.* [21] implemented the laser-powder bed fusion (L-PBF) technique for fabricating maraging stainless steel Corrax® with similar chemical composition to PH 13-8Mo stainless steel. The anisotropic electrochemical response was reported for the as-printed sample on the top versus the side planes, plausibly attributed to the different thermal history experienced by the surfaces and variation in residual stress level [21].

In case PH13-8Mo stainless steel samples fabricated by the AM technology exhibit superior corrosion response relative to the conventional AISI 420 MSS, it can be considered as a promising choice for repair and restoration of Oil Country Tubular Goods (OCTG) materials used in extremely harsh and corrosive environments, where high corrosion performance is required for the restored components [18,23]. On the other hand, the electrochemical performance of the interfacial region between the 420 MSS and WAAM PH 13-8Mo stainless steel is of crucial importance. The formation of micro-constituents at the interfacial region and the microstructural variations combined with the Volta potential difference between the substrate and the deposited tracks can adversely impact this dissimilar metal combination [24–26]. Although a few studies have focused on the electrochemical performance characterization of the PH13-8Mo stainless steel parts fabricated by various AM techniques [21,27], there is a knowledge gap on the corrosion response of the interfacial region between a 420 MSS substrate and WAAM deposited PH13-8Mo

stainless steel. Focusing on this gap, this study investigates the microstructural evolution and the electrochemical performance of the interfacial region in a 420 MSS substrate repaired with WAAM deposited PH13-8Mo stainless steel. Detailed comparisons have been made with the properties of individual alloys.

2. Experimental procedure

2.1.Materials and the sample fabrication process

This study implemented a robotic wire arc additive manufacturing platform equipped with a GMA power supply with a surface tension transfer (STT) mode and an all-x scanning strategy to fabricate a wall-shaped piece with an approximate dimension of $160 \times 160 \times 6$ mm^3. The studied samples herein were fabricated using AISI 420 MSS as the substrate plate and the commercial PH 13–8Mo wire with a diameter of 1.143 mm (0.045 in) as the feedstock material. The nominal chemical composition of used materials in this study is presented in Table 7.1. The optimum process parameters for the fabrication of sound defect-free parts are summarized in Table 7.2. The inter-layer temperature prior to the deposition of a new layer was monitored using an infrared-based closed-loop sensor and kept constant at 100 ± 2.5 °C throughout the fabrication process. A commercial shielding gas containing a mixture of 90% pure argon, 7.5% pure helium, and 2.5% carbon dioxide was applied to protect the fusion zone and eliminate oxidation and contamination through the deposition process. An illustration of the used GMA-WAAM system and the fabricated wall are shown in Fig. 7. 1 a and 7. 1.b.

Table 7. 1. The nominal chemical composition of the PH 13–8Mo feedstock wire and 420 MSS (data in wt.%).

Material	C	Cr	Mn	Si	S	P	Ni	Mo	Al	Cu	V	Fe
PH 13–8Mo feedstock wire	0.05	12.5-13.5	0.1	0.1	0-0.04	0-0.05	7.5-8.5	2-2.5	0.9-1.35	0-0.4	-	Bal.
AISI420	035	12-14	0.5	0.3	0-0.04	0-0.05	-	0-0.1	-	-	0.3	Bal.

Table 7. 2. The applied GMA-WAAM processing parameters for fabrication the PH 13–8Mo wall

Current	Arc Voltage	Wire Feeding Rate	Scanning Rate	Argon Flow Rate
130 A	28 V	67 mm/s	4.2 mm/s	25 L/min
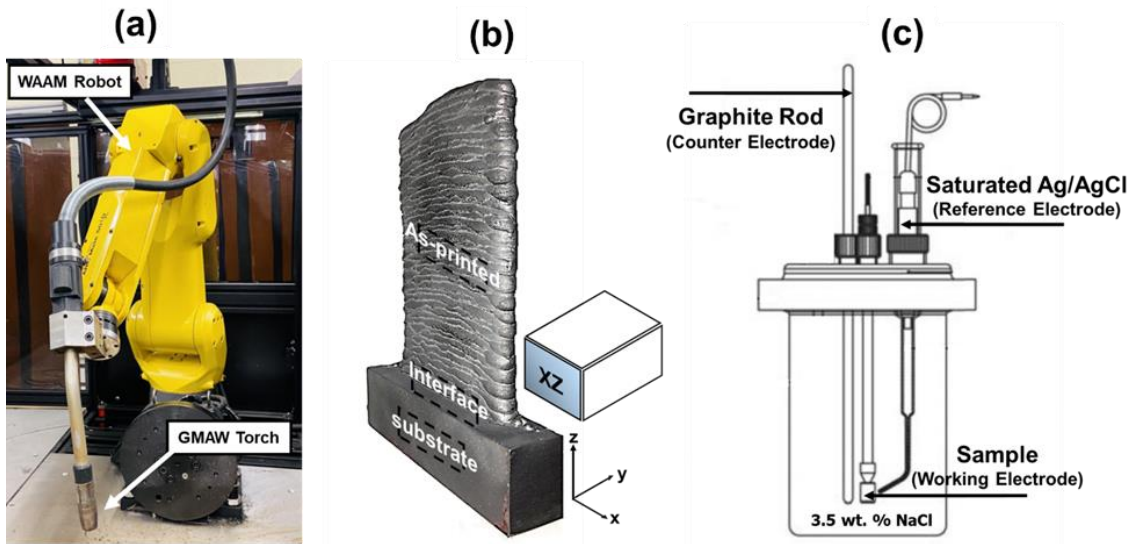
Figure 7. 1. (a) Automated WAAM robot, (b) fabricated wall and the selected samples' location and surface for electrochemical analysis, and (c) illustration of the experimental setup for electrochemical tests.

2.2.Microstructural characterization

The standard grinding and polishing procedure for stainless steel was applied to prepare samples for microstructural characterization. The 420 MSS sample was then etched with Villella's reagent for 20 s, while the interface sample and the as-printed WAAM PH 13–8Mo sample's microstructure were revealed after etching in Fry's reagent for 5 s. To characterize the formation

of possible phases, the X-ray diffraction (XRD) technique at the range of 20°–100° was conducted by implementing a Cu-K$_\alpha$ X-ray source at a voltage exposure rate of 52 kV and the current value of 25 mA. To further investigate the microstructural evolution, grain size distribution, and crystallographic orientation of samples, A FEI MLA650F scanning electron microscope (SEM) equipped with both energy dispersive spectroscopy (EDS) and electron backscattered diffraction (EBSD) detectors were used. The EBSD data was gathered at the sample's tilt angle of 70° and a step size of 0.5 μm and then post-processed using an HKL EBSD software. In addition, to reveal the possible formation of particles and secondary phases at nano-scale, transmission electron microscopy (TEM) samples were prepared using a focused ion beam (FIB) system and in-situ lift-out technique and analyzed with a Talos 200X TEM apparatus at an accelerating voltage of 200 kV.

2.3. Electrochemical analysis

Samples from the interface region, 420 MSS substrate, and WAAM side were prepared with polished surfaces for the electrochemical analysis. All electrochemical measurements were conducted in naturally-aerated 3.5 wt.% NaCl solution at room temperature. A standard three-electrode corrosion cell apparatus was used with configuration as shown in Fig. 1c. The OCP measurements were performed for 14 h to analyze the impact of the prolonged immersion time on the OCP stability. The cyclic potentiodynamic polarization (CPP) tests were run at the scanning rate of 0.1 mV/s commencing at -0.4 V versus OCP. The EIS measurements were conducted over the frequency range of 100 kHz to 10 mHz with a sinusoidal perturbation signal voltage of 10 mV. Mott-Schottky examinations were conducted with a frequency of 1000 Hz, amplitude of 5 mV, a scanning rate of 40 mV/step, and a ranging potential of −1000 to 1000 mV$_{Ag/AgCl}$. All corrosion experiments for each sample were repeated at least five times to ensure the reproducibility of the

results. Following the CPP experiments, a VK-X1000 confocal laser scanning microscope (CLSM) was also implemented to quantify the pit/localized corrosion depth formed on the samples and to evaluate the extent of corrosion damage.

3. Results and Discussion

3.1.Microstructural characterization

The optical micrograph taken from the 420 MSS substrate is shown in Figure. 7. 2a. Figures. 7. 2b-2e exhibits the SEM micrograph of the 420 MSS and its corresponding EDS elemental maps of iron, chromium, and carbon. Chromium-rich carbides with vermicular and spherical shapes (see Figure. 7. 2b and 7. 2c) are formed through the grain boundaries (intergranular carbides) of the ferritic matrix and also embedded inside the matrix (intragranular carbides).

The SEM micrograph of the as-printed PH 13–8Mo samples at low and high magnification and its corresponding EDS elemental maps are illustrated in Figures. 7. 2f-2j. It is observed that directional columnar grain growth occurs parallel to the heat dissipation direction, approximately aligned with the building direction (z-axis). Moreover, relatively coarse (~40–200 μm) and epitaxial grains were found to grow along each deposited track. As shown in the high magnification SEM micrograph in Figure. 7. 2g, the microstructure of the as-printed WAAM PH 13–8Mo sample at ambient temperature consists of lath martensitic structure (M) and residual delta ferrite phase (δ). EDS elemental maps (Figures. 7. 2h and 2i) confirmed high chromium concentration and nickel depletion where the delta ferrite phase was formed. To better understand the formed microstructure at ambient temperature, the phase(s) transition sequence for a PH-MSS alloy should be considered as follows [28]:

$$L \rightarrow L + \delta \rightarrow \delta \rightarrow \delta + \gamma \rightarrow \delta + \gamma + M \rightarrow \delta + M \qquad (1)$$

The formation of the martensitic structure is related to the rapid cooling through the non-equilibrium solidification of the WAAM process, which leads to the shear-based transformation of the austenite phase (γ) to metastable martensite structure at room temperature [29]. On the other hand, the diffusion-based transformation of the delta ferrite phase to austenite at a high temperature can also be hindered via a fast cooling rate associated with the nature of the WAAM process, leaving a significant amount of delta ferrite phase untransformed [15]. This justifies the formation and stability of the residual delta ferrite phase at room temperature. However, the existence of ferrite stabilizer elements, such as chromium at high concentration (~13 wt.%), can also contribute to the retainment of remnant delta ferrite at ambient temperature [7]. Moreover, the EDS elemental mapping reveals the formation of a few spherical aluminum-rich inclusions (Figure. 7. 2j) in the microstructure [30].

TEM analysis was also used to characterize the microstructure of the as-printed PH 13–8Mo sample. According to the lower magnification bright-field TEM image (Fig. 7. 3a), the predominant microstructure can be characterized as a lath martensitic structure. However, the higher magnification TEM image along with its corresponding selected area electron diffraction (SAED) pattern, revealed the formation of retained austenite in the as-printed PH 13–8Mo sample (see Figure. 7. 3b-3d). Although the formation of retained austenite was not expected in the as-printed PH 13–8Mo sample as its M_f is higher than room temperature, the sequential heating, and cooling cycles during the fabrication process resulted in the formation and stability of retained austenite in the as-printed microstructure.
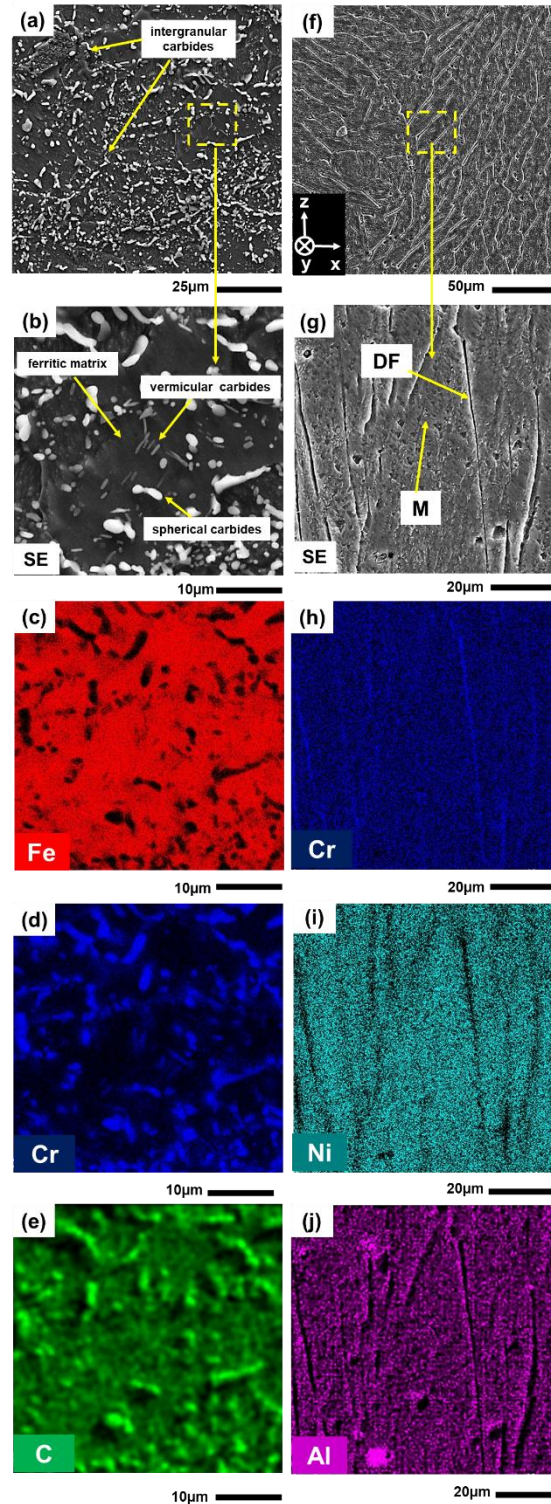
Figure 7. 2. SEM micrograph of the 420 MSS substrate at (a) low magnification showing the intergranular carbides, (b) high magnification showing vermicular and spherical carbides along with its corresponding EDX elemental concentration maps exhibiting: (c) iron concentration, (d) chromium concentration, and (e) carbon concentration, (f) low magnification SEM micrograph

of the as-printed PH 13–8Mo sample, (g) high magnification SEM micrograph of as-printed PH 13–8Mo sample representing martensitic matrix and residual delta ferrite formation accompanied by its EDX elemental concentration maps including (h) chromium concentration, (i) nickel concentration, and (j) aluminum concentration.
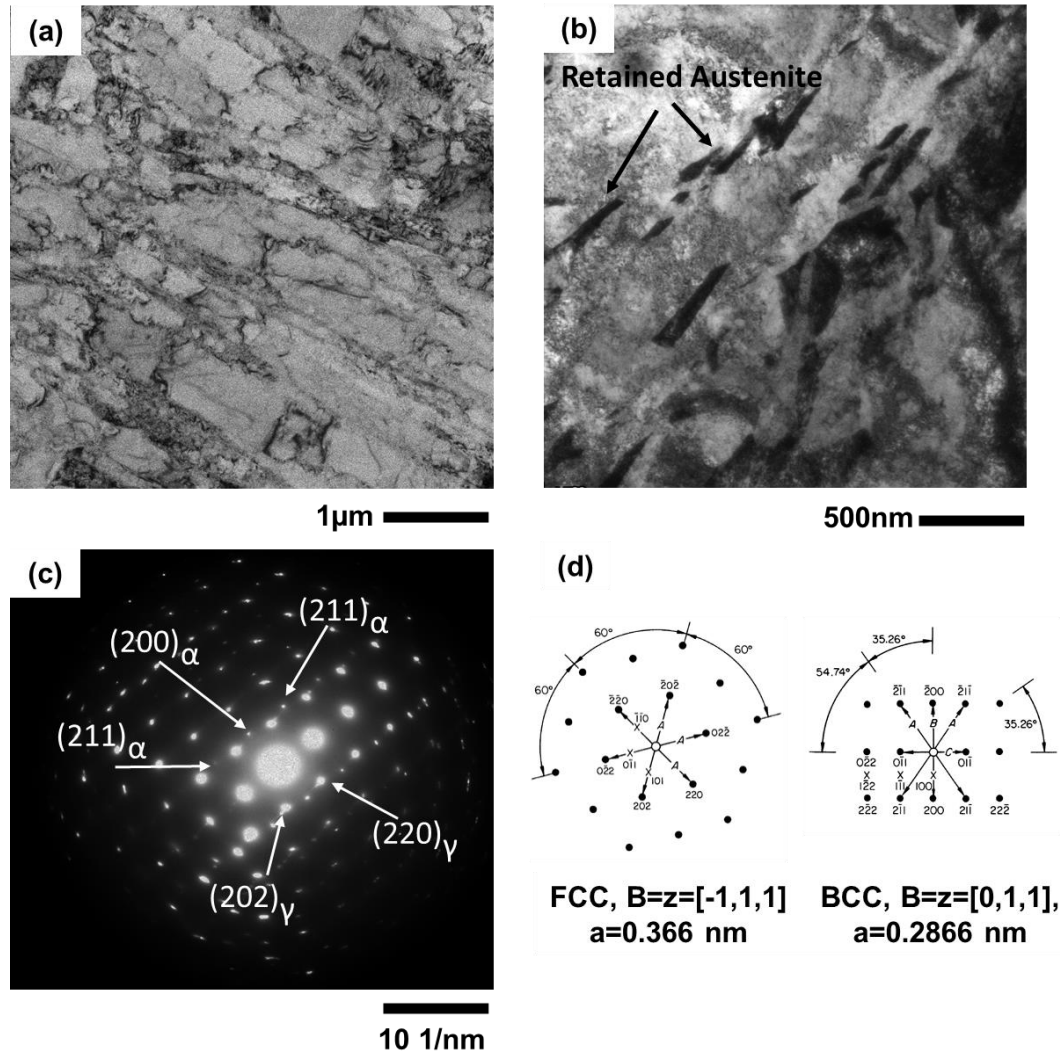
Figure 7. 3. (a) Bright-field TEM image of the as-printed PH 13-8Mo sample, (b) high magnification TEM image showing the existence of the retained austenite, and (c and d) the corresponding SAED pattern confirming the co-existence of martensite and retained austenite in the microstructure.

The optical micrograph of the interfacial bonding zone between the 420 MSS substate and the additively manufactured PH 13–8Mo alloy (Figure. 7. 4a) reveals the formation of four different zones, *i.e.*, far heat affected zone (FHAZ), close heat affected zone (CHAZ), partially

melted zone (PMZ), and fusion zone (FZ). Each zone is formed as a result of distinct thermal history, leading to the existence of different micro-constituents in each zone. By deposition of the first few layers of the WAAM PH 13–8Mo alloy, the underlying regions of the 420 MSS substrate far from the fusion line experience a lower thermal exposure in the range of 600–1000 °C, not high enough for the austenitic phase transformation [25]. Hence, the microstructure of the FHAZ remains ferritic upon cooling (see Figure. 7. 4b). Moreover, the short exposure time to high temperature mainly hinders the dissolution of pre-existing carbides in FHAZ, while a temperature rise up to the annealing temperature (600–800 °C) potentially expedites the nucleation of chromium-rich carbides in the HAZ [25]. This can justify the formation of more refined with a higher volume fraction of carbides in FHAZ compared to the 420 MSS substrate (see Figures. 7. 4b and 4c). Contrarily, the CHAZ experiences a higher thermal exposure as high as the austenitic stability region (~1100–1350 °C) followed by rapid cooling, forming a martensitic structure and leading to the partial dissolution of chromium-rich carbides (see Figures. 7. 4d and 4e) [25].
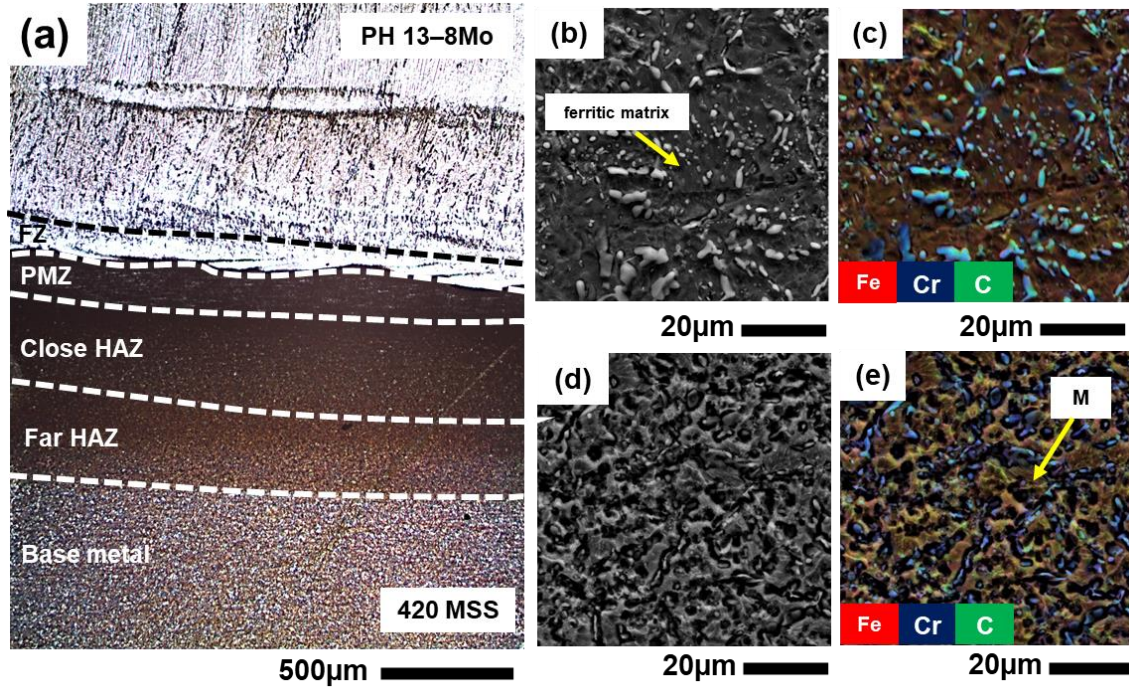
Figure 7. 4. (a) The OM macrograph of deposited PH 13–8Mo wall and its interfacial region, (b and c) SEM micrographs of the FHAZ, and (d and e) CHAZ

In the regions adjacent to the CHAZ and under the fusion line (shown by the dashed line in Figure. 7. 5a), significantly higher thermal exposure raises the temperature to the stability region of delta ferrite, austenite, and liquid, leading to the formation of a narrow partially melted zone (PMZ). Upon cooling, the microstructure of PMZ consists of a martensitic structure with a high-volume fraction of fine chromium-rich carbides (see Figures. 7. 5b and 5c). The EDX elemental maps and the line scanning over the formed micro-constituents (see Figures. 7. 5d-5f) exhibit higher concentrations of chromium and carbon, confirming the chromium carbide nature of these particles. These fine carbides possibly form through the initial dissolution of pre-existing coarse carbides and following the nucleation of finer carbides through sequential thermal cycles associated with the deposition of the following tracks [18].

In the region above the PMZ, the fusion zone of the first deposited layer consists of a considerable amount of retained austenite (see Figure. 7. 5b). Through the deposition of the first track at the fusion zone, the transformation of the austenite to the martensite phase can be hindered due to the existence of high content of the nickel (see combined EDX elemental mapping at Figure. 7. 5c) as an austenite promoter element. High nickel content can decrease the martensite start (M_s) temperature and leave a substantial amount of austenite at room temperature (retained austenite formation) [15]. On the other hand, high thermal exposure in this region can facilitate the dissolution of carbides from the substrate into the fusion line and lead to a sudden increase of the carbon content (see Figure. 7. 5c), which can act as an austenite stabilizer in the FZ, as well [7].
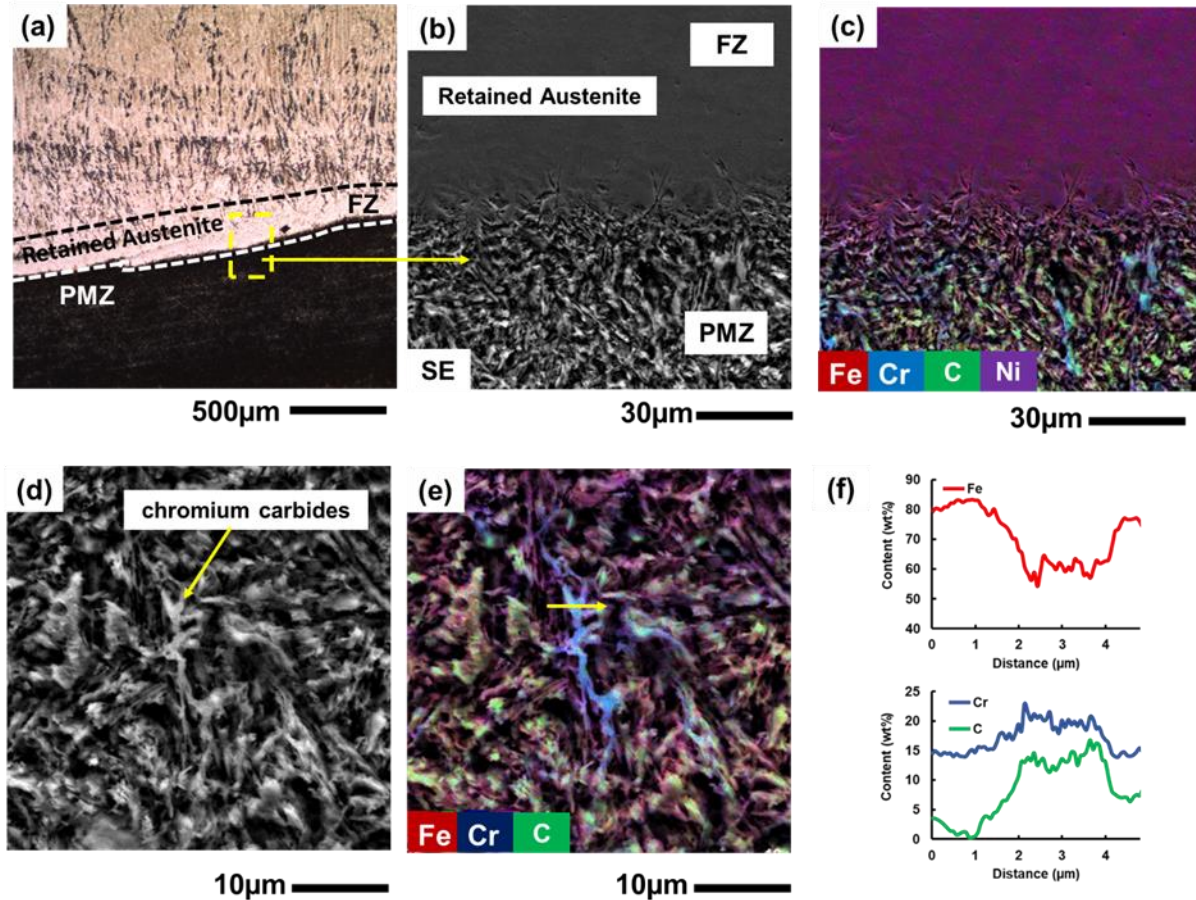
Figure 7. 5. (a) SEM micrograph of the PMZ and FZ at low magnification, (b) SEM micrograph at high magnification for the PMZ and FZ showing the formation of retained austenite at the FZ, and (c) its superimposed EDX elemental maps of iron, chromium, carbon, and nickel, (d) high magnification SEM micrograph exhibiting the formation of chromium carbides, (e) EDX elemental mapping of the area shown in (d), (f) EDX line scanning across the carbide shown in (e)

Figure. 7. 6 demonstrates the obtained XRD spectra for the 420 MSS substrate, interface region, and the as-printed PH 13–8Mo sample. The XRD spectra of the 420 MSS substrate confirmed the observations from the SEM micrographs, showing the existence of ferrite peaks at (110), (200), (211), and (220) planes, along with peaks for M_7C_3 and $M_{23}C_6$ carbides. No austenitic peaks were detected for the 420 MSS substrate, potentially due to the elimination of this phase through the annealing heat treatment of the as-received material [31]. For the as-printed PH 13–

8Mo sample, martensitic peaks at (110), (200), (211), and (220) along with low-intensity austenitic peaks of $(111)_\gamma$ and $(200)_\gamma$ were detected. The XRD spectra of the interfacial bonding sample revealed the formation of high-intensity austenitic peaks at (111), (200), (220), and (311) planes, confirming the findings of the SEM analysis, which exhibited the formation of a high-volume fraction of retained austenite in the fusion zone.
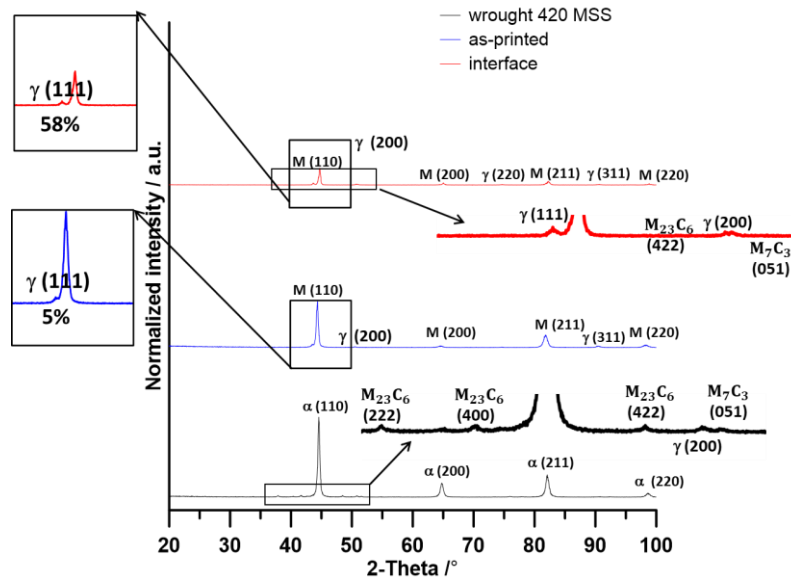
Figure 7. 6. The XRD spectra results of the 420 MSS substrate, as-printed PH 13–8Mo, and the interface samples.

The dislocation formation can potentially contribute to the corrosion response of the samples, which will be elaborated later. Hence, the XRD spectra results were used to calculate the dislocation density of each sample for the detected martensitic phases by implementing the following Scherrer equations [32]:

$$\delta = \frac{1}{L^2} \tag{2}$$

$$L = \frac{D\lambda}{\beta \, cos\theta} \tag{3}$$

where δ is the length of dislocation lines per unit volume (dislocation density), L is the average diameter of the crystallites (crystal size), D is the unity shape factor, θ is the Bragg angle, β is the breadths of the same Bragg peak from the XRD spectra, and λ is the X-ray wavelength (for Cu-K$_\alpha$ radiation = 1.54056 Å) [33].

The calculated dislocation values for the martensitic/ferritic (110), (200), (211), (220) intensity peaks are presented in Table 7. 3. The 420 MSS substrate expectedly exhibits the lowest dislocation density compared to the a-printed PH 13–8Mo and interface sample, attributed to the annealing impact of the pre-deposition heat treatment. The as-printed sample contained the highest dislocation density, ascribed to the formation of a highly-strained martensitic structure [34]. In contrast, the interface sample with strain-free ferritic structure at the FHAZ possessed a lower dislocation density [35].

Table 7. 3. Calculated dislocation density values for the 420 MSS substrate, as-printed PH 13–8Mo, and the interfacial bonding samples.

Sample	δ/1.nm^{-2} (Sherrer)			
	(110)	(200)	(211)	(220)
420 MSS Substrate	0.003	0.49	0.01	0.003
As-printed PH 13–8Mo	0.05	2.16	0.62	0.018
Interface	0.01	1.37	0.39	0.008

3.2.Crystallographic orientation characterization

To characterize the crystallographic orientation of the samples, inverse pole figure (IPF) map superimposed on the grain/lath boundaries map and the phase map along the building direction (z-axis), covering various observed zones with distinct microstructure, are shown in Figures. 7. 7a and 7. 7b. The IPF, phase, and grain misorientation maps of each distinct zone are

shown in more details and higher magnifications in Figures. 7. 8 and 7. 9, as well. The equiaxed grains are clearly observed in the 420 MSS substrate, also called base metal (BM), FHAZ, and CHAZ, while a drastic change in the grain size distribution over these zones is observed (see Figures. 7. 7a, 8a-8c). Although the dominant crystallographic phase formed in the wrought 420 MSS and the FHAZ is the BCC phase (see Figure. 7. 7b, 7. 8d and 7. 8e), a relatively low volume fraction of FCC phase (~4 %) was detected in the CHAZ, as shown in Figure. 8f. The formation of retained austenite phase in the CHAZ is potentially attributed to the high thermal exposure of this region during WAAM (close to the austenite transformation temperature), followed by its fast-cooling to room temperature that can sustain the formed austenite phase to some extent in CHAZ [36].

The misorientation angle grain boundaries maps of the substrate, FHAZ, and CHAZ (Figures. 7. 8g-8i) show that the fraction of high angle grain boundaries (HAGBs) decreases moving from the substrate toward the CHAZ due to the nucleation of new grain boundaries with lower misorientation angles (LAGBs) at the primary ferrite boundaries of the 420 MSS [37]. Moving closer to the CHAZ, the fraction of nucleation increases dominated by the higher thermal exposure at a longer time [38], leading to a higher fraction of LAGBs, and a lower fraction of HAGBs for the CHAZ and FHAZ as compared to the 420 MSS substrate. The grain/lath size distribution of different zones and statistical illustration of the misorientation angle boundaries are shown in Fig. 7. 10, as well. It is observed that moving from the 420 MSS substrate to the FHAZ, and CHAZ, the average ferritic grain size decreases from 8.04 µm for substrate to 6.45 µm and 4.02 µm for FHAZ and CHAZ, respectively. This reduction in grain size is attributed to the nucleation and grain recrystallization via the exposed thermal experience in these regions, which is more severe in CHAZ compared to the FHAZ.

The IPF and phase maps of the PMZ (Figures. 7. 9a and 9d) exhibited the formation of fine equiaxed ferritic grains (average grain size < 5 μm) along with relatively coarse austenitic grains with the average size of 6.25 μm. The phase map of the PMZ relevels the existence of a significant volume fraction of the FCC phase (~15%) along the BCC structure. The IPF and phase maps of the FZ (Figures. 7. 9b and 7. 9e) reveal the formation of a bimodal structure with coarse austenitic grains with an average size of 8.54 μm along with fine martensitic lath structure (average lath size < 1 μm). The high-volume fraction of the FCC phase (~61%), representing the austenite, is observed on the phase map of the FZ, which is in great accordance with the observed retained austenite phase in the SEM micrographs of the interfacial bonding region and detected austenitic peaks on the XRD spectra. As shown in Figure. 7. 9h, the retained austenite phase is characterized by having high angle grain boundaries (AGB≥15°), while the fine martensitic laths expectedly nucleate with low misorientation angles relative to their parent austenite grains (AGB≤5°)[39,40]. As shown in Figures. 7. 9c and 7. 9f, the as-printed sample (AP) exhibited the dominancy of fine martensitic lath structure (average lath size < 4 μm) with a low fraction of FCC structure (~6%), which is also in good agreement with SEM and TEM micrograph observations and XRD spectra findings. Contrarily to the FZ, the as-printed sample exhibits a higher fraction of LAGBS (~20%), potentially related to the higher volume fraction of lath martensitic structure possessing low angle boundaries (≤5°) as lath boundaries [41]. In general, the 420 MSS substrate was characterized by coarse grains with a significantly higher fraction of HAGBs, possibly attributed to the prolonged exposure to the recrystallization and subsequent grain growth through the heat treatment prior to the WAAM. In contrast, during the WAAM deposition process, the experienced high thermal exposure leads to a higher fraction of LAGBs at the FHAZ, CHAZ, PMZ, and AP. The FZ

possessing a coarse austenitic structure with high energy levels at grain boundaries is an exception

and has a higher fraction of HAGBs (82%) than the other subsections.
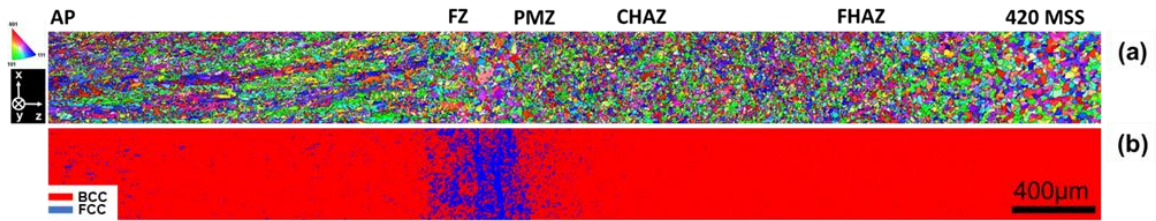
Figure 7. 7. (a) Inverse pole figure (IPF) map superimposed on the lath/grain boundary map across the interfacial bonding zone and (b) its corresponding phase map.
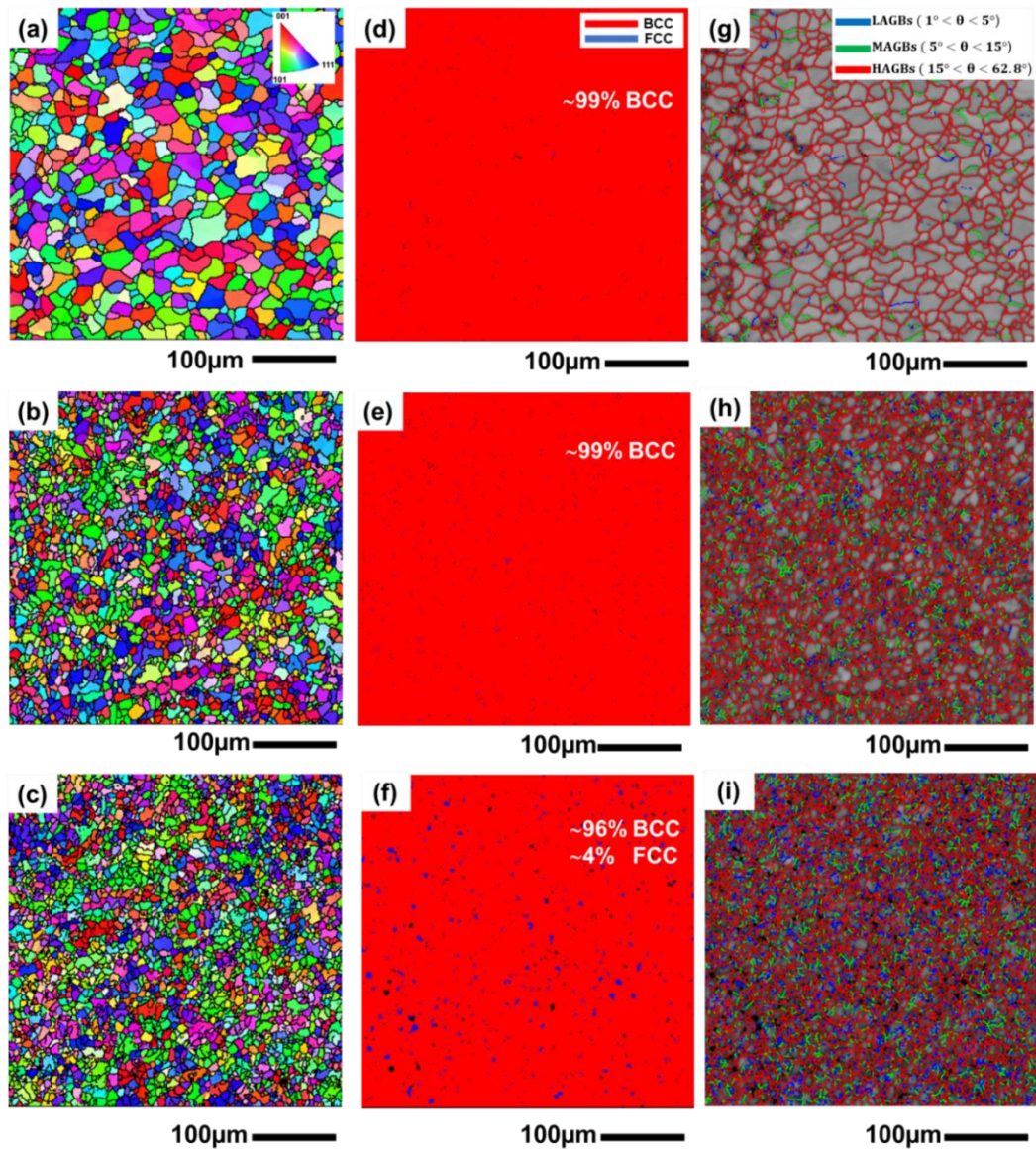
Figure 7. 8. Fig. 8. (a), (b), and (c) IPF maps, (d), (e), and (f) their corresponding phase maps, (g), (h), and (i) their corresponding grain boundaries misorientation maps for the 420 MSS substrate, FHAZ, and CHAZ, respectively.
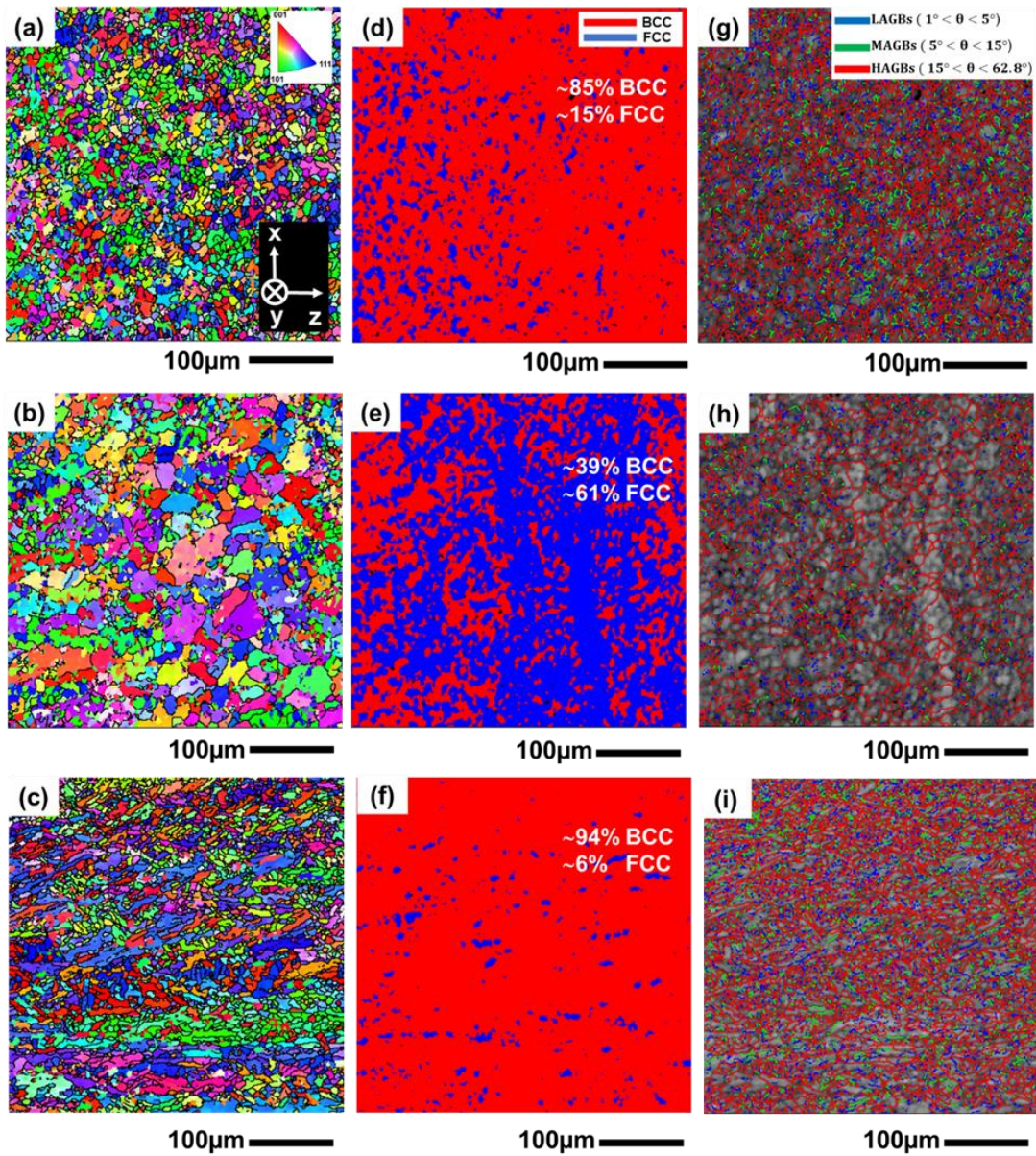
Figure 7. 9. (a), (b), and (c) IPF maps for the PMZ, FZ, and as-printed PH 13–8Mo, (d), (e), and (f) their corresponding phase maps, (g), (h), and (i) their corresponding grain boundaries misorientation maps, respectively.
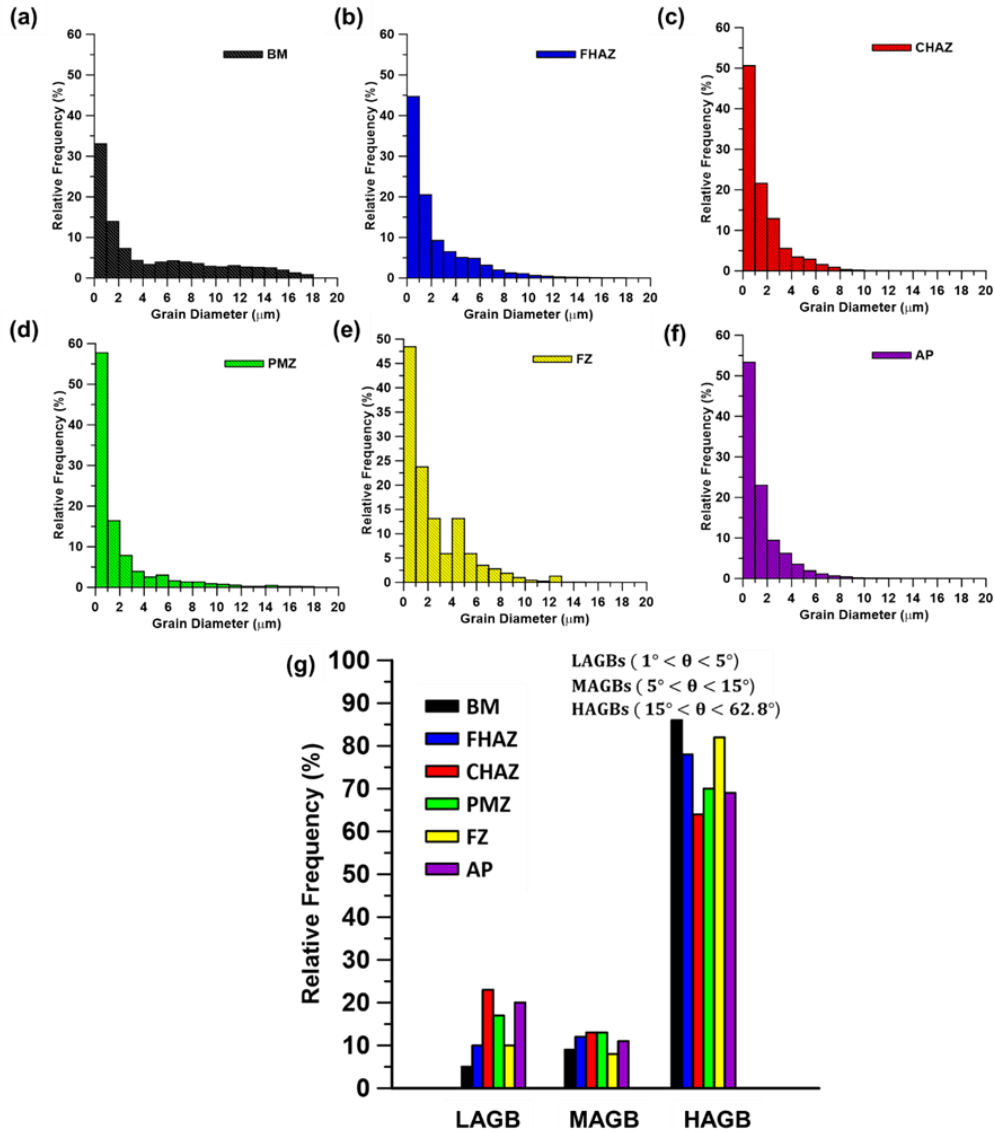
Figure 7. 10. (a-f) grain/lath size distribution of the subzones and (g) their corresponding statistical grain boundaries misorientation angles distributions.

The orientation distribution function (ODF) maps at $\varphi_2=45°$ corresponding to all subzones, *i.e.*, 420 MSS substrate, FHAZ, CHAZ, PMZ, FZ, and the as-printed sample along with the detailed crystallographic direction, planes, and the 3D representations are exhibited in Figure. 11. The 420 MSS substrate, FHAZ, CHAZ, and PMZ exhibited weak texture components with maximum intensities of ~2.25, 1.18, 2.19, 2.75MUD, respectively, potentially attributed to the dislocation

annihilation and recurring recrystallization through the pre-WAAM annealing process for the substrate as well as the tempering effect of WAAM process on the FHAZ, CHAZ, and PMZ. Contrarily, the fusion zone exhibit strong {011}<111> texture components with maximum intensities of ~5.63. The {011}<111> texture component is known as the parent martensite component for the observed austenite structure in the FZ. The crystallographic relationship between the final martensite structure ($\acute{\alpha}$) and the primary austenite phase (γ) can be explained by the Kurdjumow–Sachs (K–S) approach as follows [42]:

$$\{111\}_\gamma \ //\{110\}_{\acute{\alpha}} \quad <110>_\gamma \ //<111>_{\acute{\alpha}} \tag{4}$$

The coinciding and formation direction of the parent and final phases can be characterized by the K-S orientation relationship. The formation of strong {011}<111> components in the FZ confirmed the fulfillment of the K-S orientation relation between the austenite phase and the observed final martensitic lath structure [7,43].

On the other hand, the as-printed PH 13–8Mo (AP) sample exhibits a strong preferential solidification texture component of {001}<100> (maximum intensity of 6.16 MUD). Through the deposition of initial tracks, primary delta ferrite grains formed at higher temperatures experience a competitive growth upon solidification along the <100> direction (known as the preferential growth direction for the cubic structure) coinciding with the heat dissipation direction (z-axis) parallel to the {001} planes [44]. Through the deposition of subsequent layers, the epitaxial growth mechanism resumes on the columnar grains of the previous track, maintaining strong directional texture throughout the whole deposited wall [15].

The J-index concept is used herein to calculate the severity and strength of texture components. The *J*- index as a dimensionless value is defined as unity for a fully randomized crystallographic

orientation, whereas the values close to infinity exhibit a single crystal structure. The *J*-index value

can be calculated using the following equations [45]:

$$J - index = \int f\,(g)^2\,dg \tag{5}$$

$$dg = d\varphi_1\,d\phi\,d\varphi_2\,\frac{sin\phi}{8\pi^2} \tag{6}$$

where φ_1, ϕ, and φ_2 are the Euler angles, characterizing the crystallographic relationships in a

coordinate system, *f (g)* is the ODF density at the orientation of *g*, and *dg* is the variation in

orientation. Consequently, the maximum textural strength can be indicated by a *J*-index value. In

addition, *J*-index is a strong tool as a quantitative illustration of materials' preferential orientation

[45]. The calculated *J*-value for substrate, FHAZ, CHAZ, PMZ, FZ, and the AP sample are 2, 2.25,

2.45, 3.25, 5.16, and 12.25, respectively, affirming the formation of a stronger texture in the as-

printed PH 13-8Mo sample.
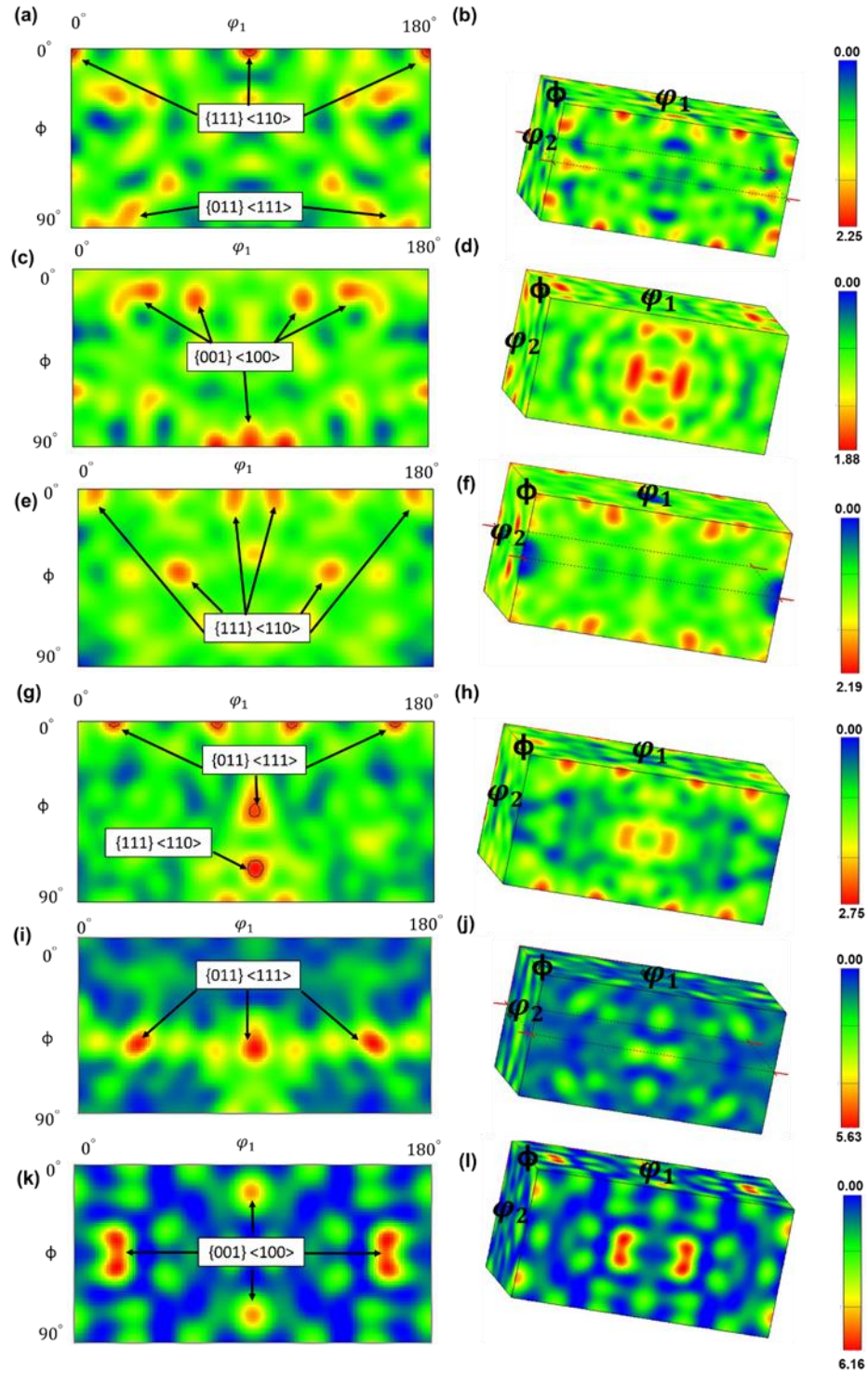
Figure 7. 11. The ODF maps at $\varphi_2=45°$ and their corresponding 3D-plots for (a) and (b) the 420 MSS substrate, (c) and (d) FHAZ, (e) and (f) CHAZ, (g) and (h) PMZ, (i) and (j) FZ, and (k) and (l) as-printed PH 13-8Mo sample, respectively.

3.3.Corrosion Results

3.3.1. *Open circuit potential and cyclic potentiodynamic polarization results*

The variations of the OCP over a long immersion time (14 h) for the 420 MSS, as-printed PH 13–8Mo, and the interface samples in an aerated 3.5 wt.% NaCl solution are shown in Figure. 12. The 420 MSS substrate exhibits an average OCP value of -25 mV±5, where a slight increase in the OCP trend is demonstrated over time (t≤10h), while OCP stabilization is observed after 10 h of immersion, possibly attributed to the improved passivation ability of the alloy over the specified immersion time [23]. On the other hand, intermittent spikes of the OCP values, representing rapid fall followed with a sudden increase back to the baseline, are observed, especially at the onset of the immersion (t≤2h) for the 420 MSSsubstrate sample, which can be related to the initiation, growth, and subsequent re-passivation of meta-stable pits on the sample's surface [46]. Differently, the as-printed PH 13–8Mo sample shows a higher OCP value (average OCP ~ +38 mV±2) compared to the 420 MSS and interface samples, with an increasing trend over time, indicating its high passivation ability. The detected fluctuations in the OCP over the entire immersion time for the as-printed PH 13–8Mo sample imply the recurrence of the micro-pits formation followed by their re-passivation. The interface sample show the lowest OCP (average OCP ~ -415 mV±2) and a reducing trend at longer immersion times, possibly correlating to consistent dissolution of its passive film in the electrolyte over time.
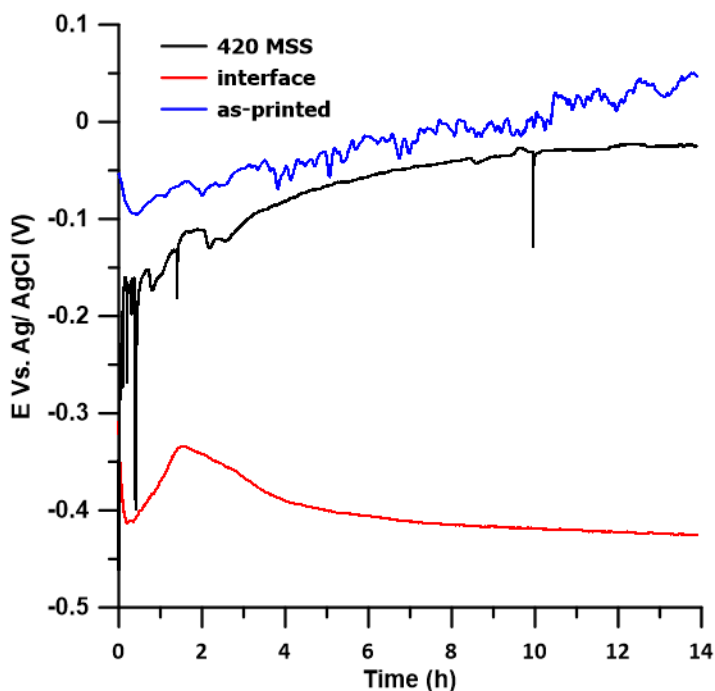
Figure 7. 12. The OCP variation versus the monitoring time for the 420 MSS substrate, as-printed PH 13–8Mo, and the interface samples in an aerated 3.5 wt.% NaCl solution at room temperature.

The cyclic potentiodynamic polarization (CPP) test was also conducted on the samples after immersion periods of 1 h, 3 days, and 5 days to examine the electrochemical stability of samples over time, and the obtained graphs are illustrated in Figure 7. 13. The obtained electrochemical parameters from the CPP tests are summarized in Table 7. 4. The 420 MSS substrate exhibited a passive behavior with a comparatively wide passivation range over the anodic branch at all immersion times (see Figures. 7. 13a-13c). The pitting potential (E_{pit}) remains relatively constant at the longer immersion times, while higher passivation current density (i_p) indicates a slight deterioration of the passive film on the surface of the 420 MSS sample over time. The as-printed PH 13–8Mo sample exhibits strong passive behavior with a distinct breakdown potential (E_{pit}) accompanied with a high re-passivation potential (E_{rep}) at various immersion times (see Figure. 7. 13d-13f), suggesting the formation of an intact passive film and stabilization of the

passive layer over the extended immersion time. In harmony with the OCP trends, the interface sample exhibits lower electrochemical stability and corrosion resistance compared to the as-printed and 420 MSS substrate samples, as evidenced by its low corrosion potential (E_{corr}) and E_{pit} values after 1 h of immersion time (see Figure. 7. 13g) and passivation occurring at higher corrosion current density (higher i_p) after 3-days and 5-days of immersion periods (Figure. 7. 13h and 13i).
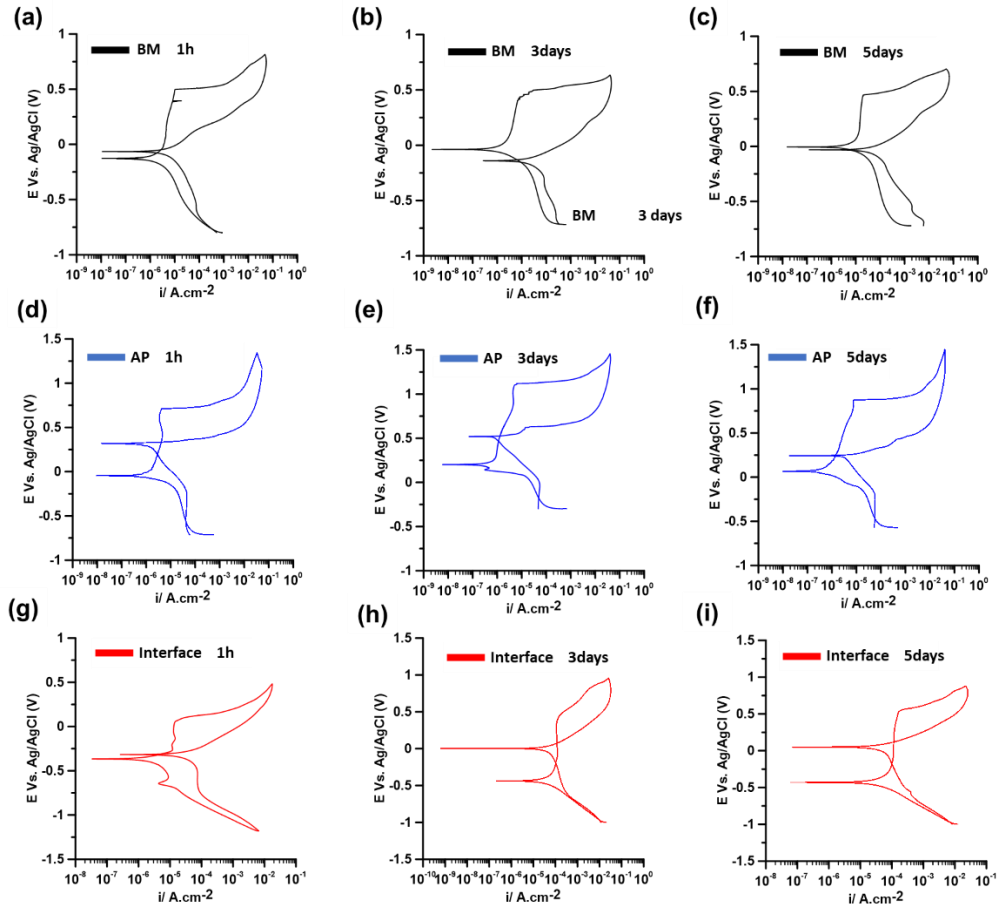
Figure 7. 13. The CPP graphs of (a-c) 420 MSS, (d-f) as-printed PH 13–8Mo, and (g-i) interface samples over 1 h, 3-days, and 5-days of immersion times, respectively.

.

Table 7. 4. The electrochemical parameters obtained from the CPP graphs.

Immersion Time	Sample	E_{corr} $(mV_{Ag/AgCl})$	i_{corr} $(\mu A\ cm^{-2})$	i_p $(\mu A\ cm^{-2})$	E_{pit} $(mV_{Ag/AgCl})$	E_{rep} $(mV_{Ag/AgCl})$
1 h	as-printed	-50±5	0.85±0.05	3.05±0.04	710±35	335±20
	interface	-380±15	1.50±0.05	15.25±0.05	80±5	-
	420 MSS	-120±15	0.80±0.03	5.25±0.05	490±15	-70±5
3-days	as-printed	215±25	0.25±0.01	3.15±0.05	1150±50	550±40
	interface	-450±25	20±-1	200±10	460±20	50±5
	420 MSS	-30±15	1.05±0.02	6.25±0.05	450±20	-
5-days	as-printed	100±10	0.35±0.03	8.25±0.05	870±50	250±35
	interface	-410±25	25±1	150±10	510±20	15±2
	420 MSS	-5±1	2.10±0.02	15.25±0.05	470±30	-

3.3.2. Electrochemical impedance spectroscopy results

EIS experiments were carried out for each sample after 1 h, 3-days and 5-days of immersion periods in 3.5 wt.% NaCl solution at 25 °C to characterize the passive layer's protective nature over time. The obtained absolute values of ohmic resistance at low to medium frequency range of the Bode plots can represent the integrity of the passive layer on the samples' surfaces (Figures. 7. 14a and 7. 14c). Apparently, at various immersion times, the as-printed sample exhibited significantly higher ohmic resistance values at low frequencies compared to the 420 MSS substrate and interface samples, suggesting the formation of a more stable passive film and noticeably slower kinetics of corrosion reactions on its surface.

From the Nyquist plots, a significantly smaller semi-circle radius for the interface sample is observed as compared to that of the as-printed PH 13–8Mo sample (see Figures. 7. 14b, 14d, and 14f), at various immersion times, confirming the less protective nature of the passive film on the interfacial region [46], aligned with the obtained OCP and CPP results. Contrarily, the as-printed sample after 3 days of immersion time showed higher absolute values of impedance at low

frequencies and larger capacitive radius compared to the sample immersed for 1 h, suggesting the formation of a more stable and thicker passive layer on its surface over time. However, a slight reduction in both impedance values and capacitive semicircle diameter was observed after five days of immersion for the as-printed sample. The 420 MSS substrate exhibited significantly lower impedance values and a drastic reduction of the capacitive semi-circle radius over the 3-days and 5-days immersion times, potentially ascribed to the dissolution of passive film into the electrolyte solution, leading to the decreased electrochemical resistance of the alloy over time [46]. Despite lower ohmic resistance at low frequencies over the various immersion times compared to the other samples, the interface sample immersed for 5 days exhibited a larger capacitive radius compared to the interface samples immersed for 1 h and 3 days, indicating relative improvement in terms of passive film protectiveness, in good accordance with findings of the CPP tests for this sample at different immersion periods.

On the other hand, the phase angle versus frequencies diagrams for the interface and 420 MSS substrate samples exhibit two broad individual peaks in the range of $-60°$ to $-80°$ after 3-days and 5-days of immersion times, attributed to the diffusion through the susceptible regions to localized corrosion attack and the double-layer capacitance at lower frequencies [7]. On the other hand, the as-printed sample exhibits broader phase angle peaks over the varying frequencies at various immersion times, possibly related to the superposition of two distinct peaks with two non-discriminating time constants [7].

To better understand and quantify the characteristics of the formed passive film on the surface of the samples, experimental data were modeled using a simplified equivalent circuit (SEC), as shown in Figure. 7. 14a. R_s represents the resistance of the solution, CPE_p and R_p correspond to the capacitance and the resistance of the passive film, CPE_{dl} and R_{ct} represent the

double layer constant phase element (CPE) and its charge transfer resistance, respectively [23]. The electrochemical parameters deducted from the modeled SEC are presented in Table 7. 5. After various immersion times, the as-printed sample exhibited higher R_{ct} and lower CPE_{dl} values compared to the 420 MSS substrate and interface samples, confirming the formation of a more intact passive film against corrosion on its surface. High R_{ct} and low CPE_{dl} values were still observed for the as-printed sample after 3-days and 5-days of immersion times, suggesting better stabilization of the passive layer on its surface over time. On the other hand, the interface sample exhibits significantly lower charge transfer resistance and higher double-layer constant phase element values at various immersion times, confirming the less protective nature of the passive film at the interfacial bonding. Moreover, higher charge transfer resistance values than the passive film resistance ($R_p<R_{ct}$) for the samples implies their clear passivation behavior.

The thickness of the passive layer for each sample at various immersion times (presented in Table 7. 6) was calculated using the following equations [47]:

$$C_{eff} = gQ(\rho_\delta \varepsilon_0 \varepsilon)^{1-n} \tag{7}$$

$$L_{ss} = \frac{\varepsilon \varepsilon_0 A}{C_{eff}} \tag{8}$$

where C_{eff} is the effective capacitance, g is a function of n ($g = 1 + 2.88(1 - n)^{2.375}$), ρ_δ is the maximum resistance of the passive layer, ε_0 is the vacuum permittivity (8.854×10^{-14} Fcm^{-1}), ε is the passive film dielectric constant (~15.6 for Cr_2O_3), L_{ss} is the thickness of the passive film, and A is the surface area of the exposed samples [2,48]. The interface sample's calculated passive film thickness is significantly lower than the 420 MSS substrate and as-printed sample. In contrast, the thickness of the passive film for the as-printed sample increases after 3-days of immersion time, indicating improved passive film stabilization/thickening on the as-printed sample over time, consistent with the obtained corrosion results in this study.
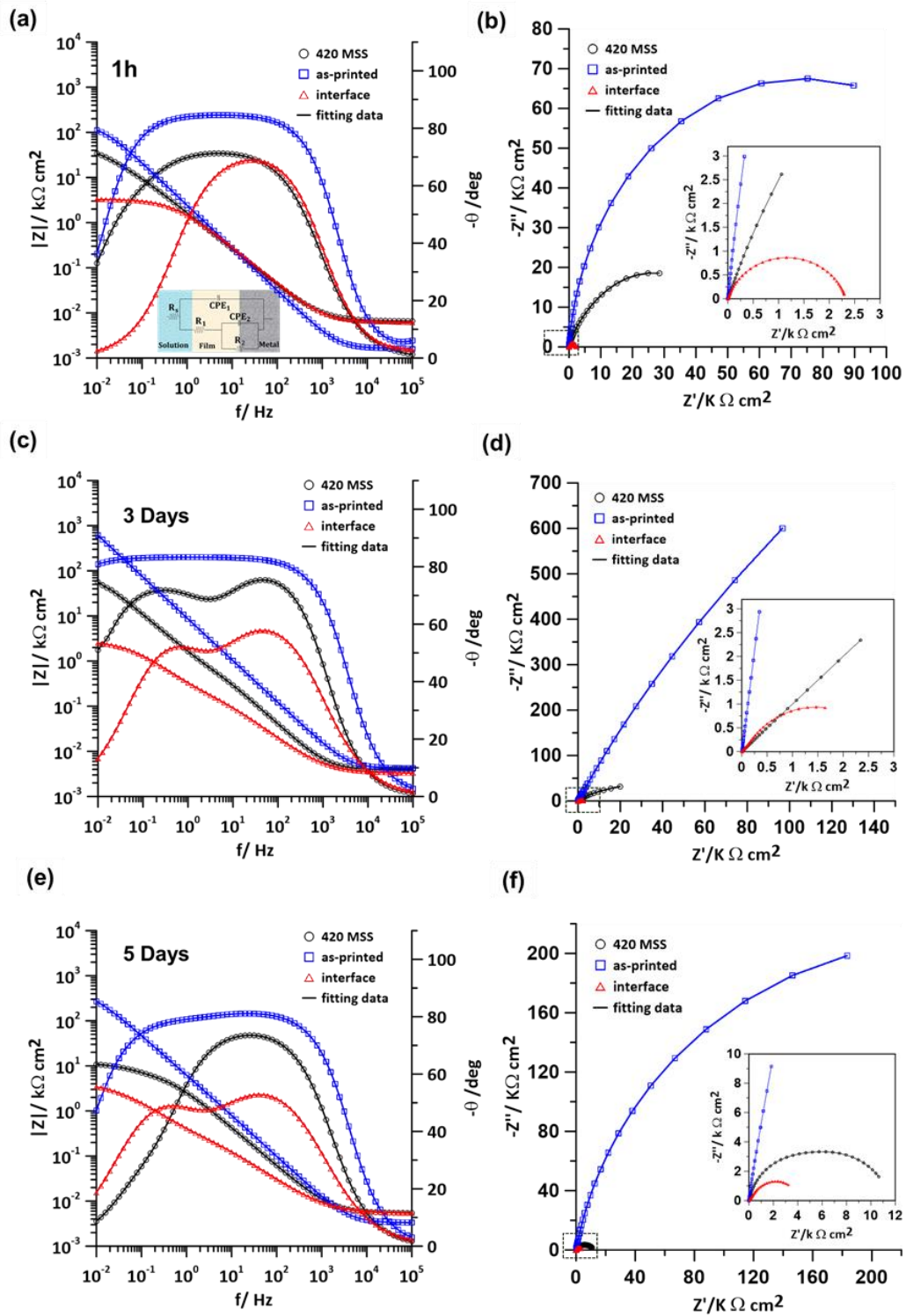
Figure 7. 14. The Bode and Nyquist plots of samples after (a) and (b) 1h, (c) and (d) 3-days, (e) and (f) of 5-days immersion time

Table 7. 5. The fitted electrochemical parameters for the EIS spectra.

Immersion Time	Sample	R_s (Ωcm^2)	CPE_p ($\Omega^{-1}cm^{-2}s^n$)	n_1	R_p (Ωcm^2)	CPE_{dl} ($\Omega^{-1}cm^{-2}s^n$)	n_2	R_{ct} (Ωcm^2)	$\sum \chi^2$
1h	as-printed	3.54	8.44×10^{-7}	0.88	1.19×10^2	6.56×10^{-6}	0.88	2.18×10^6	1.37×10^{-5}
	interface	3.56	6.22×10^{-4}	0.97	5.72×10^3	5.62×10^{-4}	0.94	4.60×10^4	1.44×10^{-5}
	420 MSS	3.58	9.27×10^{-6}	0.95	1.24×10^2	2.62×10^{-5}	0.86	1.90×10^5	1.23×10^{-5}
3-days	as-printed	3.54	4.23×10^{-7}	0.88	1.09×10^2	4.16×10^{-6}	0.83	4.45×10^6	1.32×10^{-5}
	interface	3.58	9.62×10^{-4}	0.88	3.62×10^3	7.48×10^{-4}	0.84	3.57×10^4	1.54×10^{-5}
	420 MSS	3.65	1.27×10^{-6}	0.84	1.17×10^2	8.62×10^{-5}	0.98	7.56×10^4	1.76×10^{-5}
5-days	as-printed	3.55	6.83×10^{-7}	0.95	1.12×10^2	5.66×10^{-6}	0.86	3.15×10^6	1.42×10^{-5}
	interface	3.64	2.45×10^{-4}	0.88	9.75×10^3	1.46×10^{-4}	0.83	6.59×10^4	1.74×10^{-5}
	420 MSS	3.58	8.24×10^{-5}	0.84	1.12×10^2	2.71×10^{-2}	0.98	7.50×10^3	1.96×10^{-5}

Table 7. 6. The effective capacitance *(C_{eff})* and passive film thickness (L_{ss}), calculated for each sample at different immersion times.

Immersion Time	Sample	C_{eff} (Fcm^{-2})	L_{ss} (nm)
1h	Wrought-420 MSS substrate	1.23×10^{-5}	62.34
	as-printed	4.12×10^{-6}	126.75
	interface	6.87×10^{-4}	0.68
3-Days	Wrought-420 MSS substrate	2.63×10^{-5}	45.87
	as-printed	1.15×10^{-6}	143.54
	interface	7.47×10^{-4}	0.58
5-Days	Wrought-420 MSS substrate	5.63×10^{-5}	38.46
	as-printed	2.24×10^{-6}	134.25
	interface	6.95×10^{-4}	0.63

3.3.3. Mott-Schottky analysis

The semiconductive characteristics of the passive layer formed on the samples were analyzed by carrying out the Mott-Schottky measurements in aerated 3.5 wt.% sodium chloride solution at room temperature. The obtained Mott-Schottky graphs are presented in Figure. 7. 15a-15c. According to the Mott-Schottky equation, the applied potential value (*E*) and the measured electrode capacitance (*C*) are correlated as follows [49]:

$$\frac{1}{C^2} = \frac{1}{C_H^2} + \frac{1}{C_{SC}^2} = \frac{1}{C_H^2} + \frac{2}{e.N_q.\varepsilon.\varepsilon_0}(E - E_{FB} - \frac{kT}{e}) \qquad (9)$$

where C_H is the Helmholtz capacitance, C_{SC} is the space charge capacitance of the passive film, e is the electron charge (1.6×10^{-19} C), N_q is the doping density, ε is the relative dielectric constant for the passive layer ($\varepsilon = 15.6$ for martensitic stainless steel), ε_0 is the vacuum permittivity, k is Boltzmann's constant (8.16×10^{-5} eV/K), E_{FB} is the flat band potential, and T is the absolute temperature. The linear portion of the C^{-2} *vs* E graph can calculate the N_q and E_{FB} by implementing the intercept and slope technique and considering the kT/e value close to zero [49].
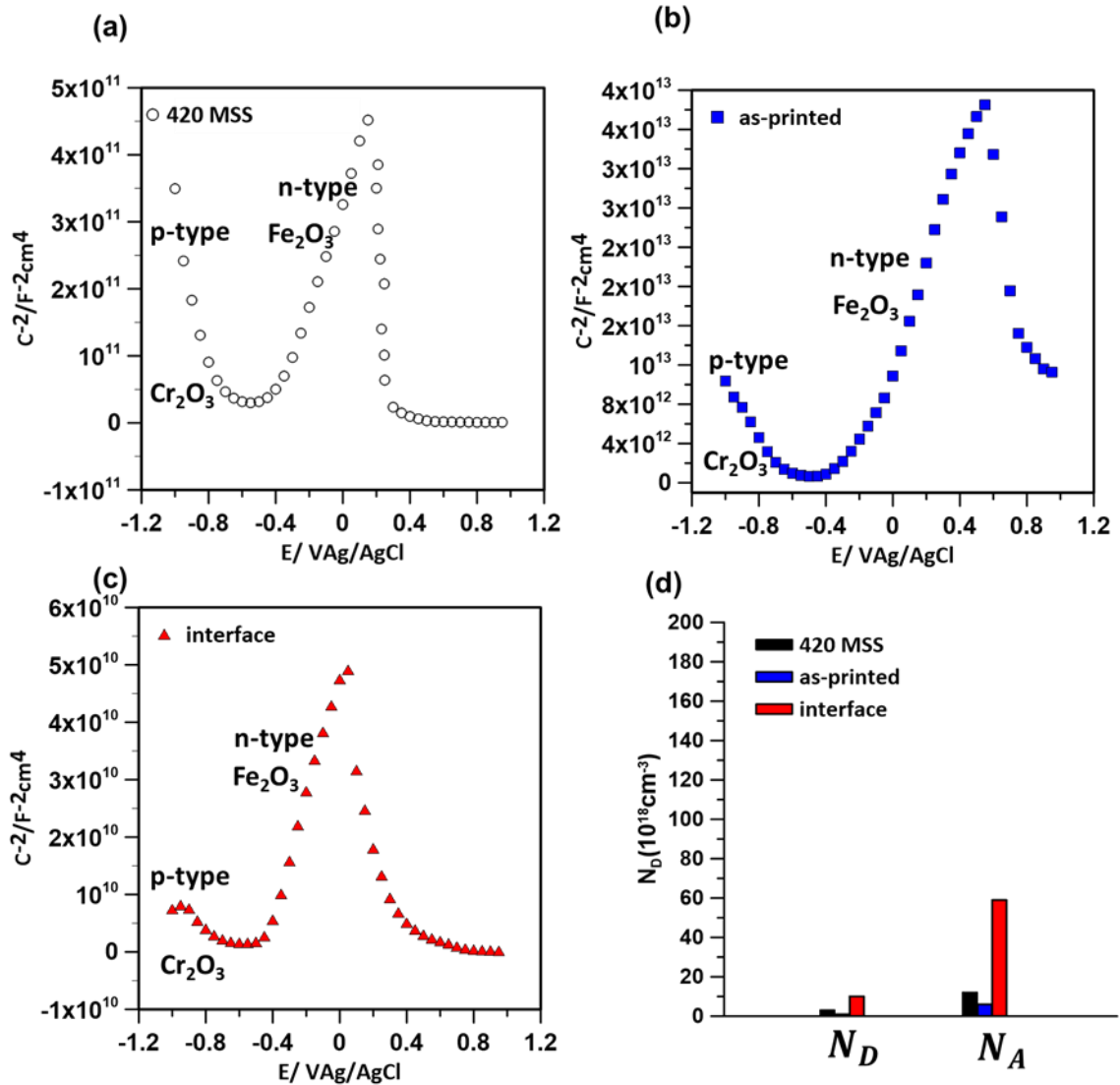
Figure 7. 15. The Mott-Schottky curves of the passive film for the (a) base metal, (b) as-printed sample, and (c) interface sample, (d) the variations of the donor and acceptor densities.

A zone with p-type semiconductor behavior (left side of the graphs) confirms the formation of chromium oxide (Cr_2O_3) as the primary content of the passive film in all samples, in which the number of holes in the valence band of the oxide film is higher than the number of electrons in the conduction band [50]. On the other hand, an n-type semiconductor behavior, characterized by the positive slope on the M-S plots, was also detected, suggesting oxygen vacancies and interstitial

cations as the major defects in the formed passive film. Through the n-type transition, it is believed that the oxide layer primarily consists of iron oxide (Fe_2O_3) since the number of holes in its valence band is less than the number of electrons in its conduction band [50].

The donor density and acceptor density values, N_D and N_A, respectively, calculated from the M-S equation for samples, are shown in Figure. 7. 15d. High values of the N_D and N_A imply the formation of disordered passive film on the samples' surfaces. The interface sample has a significantly higher donor and acceptor density values as compared to the as-printed PH 13–8Mo, and substrate 420 MSS samples, indicating the stability disturbance of the passive film for the interface region, ascribed to the significant increase in recurring electrochemical reactions at the metal/passive film interface [18,51]. Higher donor density of the passive layer can potentially increase the chloride ion's adsorption affinity, leading to a higher susceptibility to the pitting nucleation and corrosion initiation [51]. Hence, the interface sample with a passive film containing a high donor density can promote the accelerated reaction between the oxygen vacancies and chloride ions due to the easier ions adsorption [51].

As discussed earlier, the dislocation density of the as-printed PH 13–8Mo sample was estimated to be significantly higher than that of the 420 MSS and interface sample after the process-induced martensite transformation through WAAM, as summarized in Table 2. However, considering the semiconductive characteristics of the as-printed PH 13–8Mo sample, the highly strained martensitic structure has not led to a drastic increase in doping density. Hence, the high dislocation density of the as-printed samples does not reflect the susceptibility to localized corrosion attack [48], and potentially other factors govern this sample's corrosion response, which will be elaborated later on.

3.4.Electrochemical response interpretation and morphology of corroded samples

Previous studies have shown that the electrochemical response of the 420 martensitic alloy was adversely impacted by the formation of chromium-rich carbides, provoking the micro-galvanic coupling effect between anodic ferritic matrix and cathodic carbide particles [52]. The corrosion morphology of the 420 MSS sample after the CPP test (see Figure. 7. 16a- 16d) reveals that micro-pitting at the ferrite grain boundaries, where a high-volume fraction of chromium rich-carbides form (promoting the micro-galvanic coupling), is the dominant localized attack on this sample. On the other hand, the corrosion morphology of the as-printed PH 13-8Mo sample depicts the formation of randomly distributed pits on the samples' surface (see Figure. 7. 16e-14h), where iron dissolution occurs at the pitting sites, possibly attributed to the constant recurrence of the re-passivation, pit nucleation, and subsequent pitting coalescence. The corrosion response of the as-printed PH 13-8Mo sample was significantly higher than the other samples, potentially related to the elimination of chromium carbides and the existence of a uniform martensitic structure, hindering the micro-galvanic effect at the early stages of passivation. Due to the lower carbon content of the PH 13-8Mo feedstock material compared to the 420 MSS sample, the formation of carbides in the as-printed condition was not detected. Furthermore, the low volume fraction (6-15%) of the formed delta ferrite phase in the as-printed sample inherently generates a weaker micro-galvanic coupling effect due to its lower chromium content as compared to that in chromium carbides [7].

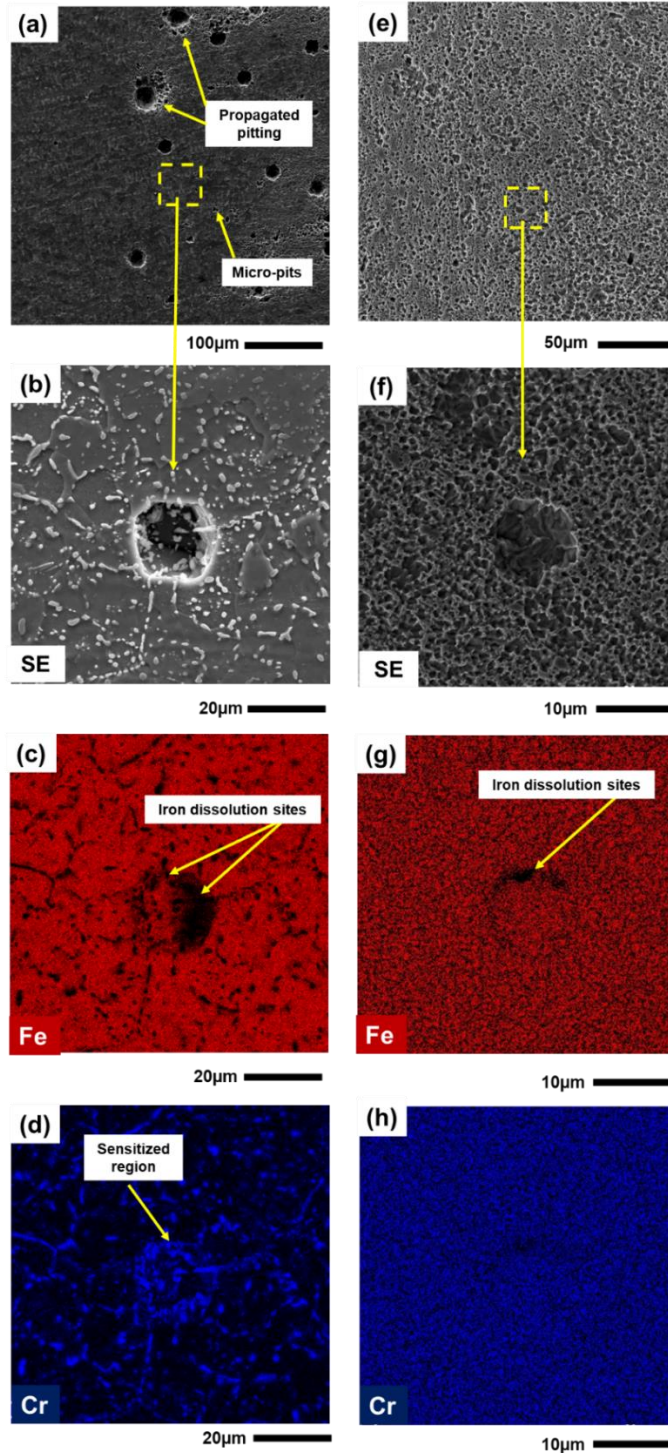Figure 7. 16. (a) SEM micrograph of the 420 MSS sample showing the corrosion morphology after the CPP test, (b) SEM image at higher magnification showing a micro-pit initiation site, (c) and (d) the elemental maps for iron and chromium, respectively, (e) and (f) corrosion morphology of the as-printed PH 13-8Mo sample after the CPP test, and (g) and (h) its corresponding elemental maps for iron and chromium, respectively.

The corrosion morphology on the interface region after the CPP test is exhibited in Figure. 7. 17a. To distinguish the electrochemical attack onset and the most susceptible areas to corrosion at the interfacial bonding region, the CPP test was paused on the advancing side at corrosion current density of 3 $\mu A/cm^2$. The onset of corrosion occurred at the CHAZ and especially at the PMZ, while the fusion zone remained uncorroded at the specified corrosion current density. The formation of a high-volume fraction of corrosion product (possibly Cr_2O_3) is confirmed with iron depletion and higher concentration of chromium and oxygen (Figures. 7. 17b-17e), supporting the increased susceptibility of this region to corrosion. The PMZ possesses a high fraction of fine chromium carbides, which are susceptible regions to micro-galvanic coupling. The chromium depletion can occur at the carbide/martensitic matrix interface, providing susceptible regions for localized corrosion, as shown in Figures. 7. 17f and 17g.

Similarly, the formed fine chromium-rich carbides in the martensitic matrix of the CHAZ can potentially intensify the micro-galvanic coupling at the interface of matrix/carbides and deteriorate the corrosion performance in this region, as shown in Figures. 7. 17h and 17i. The formed retained austenite phase at the fusion zone tends to nucleate and grow along the enriched regions with the austenite stabilizer element Ni, where the chromium is mostly depleted [53,54]. Moreover, the Cr concentration at the austenite phase is close to the one in the martensitic lath structure. This can reduce the heterogeneity at the formed martensitic lath boundaries and enhance the corrosion performance of the fusion zone [7,54]. Consequently, it is expected that the galvanic coupling effect in the macro-scale between the fusion zone and the PMZ (anodic 420 MSS side and cathodic PH 13-8Mo side) intensifies the corrosion susceptibility in this region [23,55].

The pitting depth can be used as a vital tool for quantifying the degree of corrosion damage on various subzones [56]. The scanning depth profiles of the interfacial bonding region after the

CPP test and corrosion product removal are characterized using the confocal microscopy technique and are shown in Figures. 7. 17j and 17k. The pits depth in the order of 1 µm was measured along the PMZ and CHAZ (spots highlighted with dark blue and black), while no significant corrosion damage is observed on the PH 13-8Mo side of the PMZ. This can support the previous finding of this study, affirming the lower electrochemical stability at the 420 MSS side of the interface. From the confocal microscopy graphs herein, a more aggressive and localized corrosion damage is observed in the CHAZ compared to the uniform general corrosion attack in the PMZ, potentially attributed to the less uniform distribution of chromium carbide particles with coarser structure, which can inherently intensify the galvanic coupling effect in the CHAZ.

The stored energy at the grain boundaries depends on the grain misorientation angle. A high fraction of HAGBs with higher energy levels was detected in the fusion zone and partially in the PMZ region, where coarse austenite grains were formed through the complex thermal history during the WAAM process. These high-energy level austenite grain boundaries are considered the accessible routes for diffusion, leading to deviation of the grain boundary diffusivity from the bulk diffusivity and deteriorating the electrochemical response of the passive layer for the interface sample [23]. On the other hand, the martensitic lath structure of the as-printed PH 13–8Mo sample with a high fraction of low angle grain boundaries can be the major factor contributing to the superior electrochemical response of this sample since LAGBs are considered less susceptible to corrosion as they possess lower energy levels [23]. In general, the inferior electrochemical response of the interface sample and high electrochemical stability of the as-printed sample can be related to the microstructural induced factors, as mentioned. The superior corrosion performance of the PH 13-8Mo sample compared to the interface and 420 MSS sample can be correlated to the absence of chromium-rich carbides in this sample. Overall, the superior electrochemical response

of the WAAM fabricated side of the PH 13-8Mo – 420 MSS dissimilar metal combination attests on the improved corrosion behavior and, ultimately, the service life of the PH 13-8Mo coated 420 MSS components, showcasing the capability of WAAM as a directed energy deposition process for coating deposition, repair, and restoration applications.
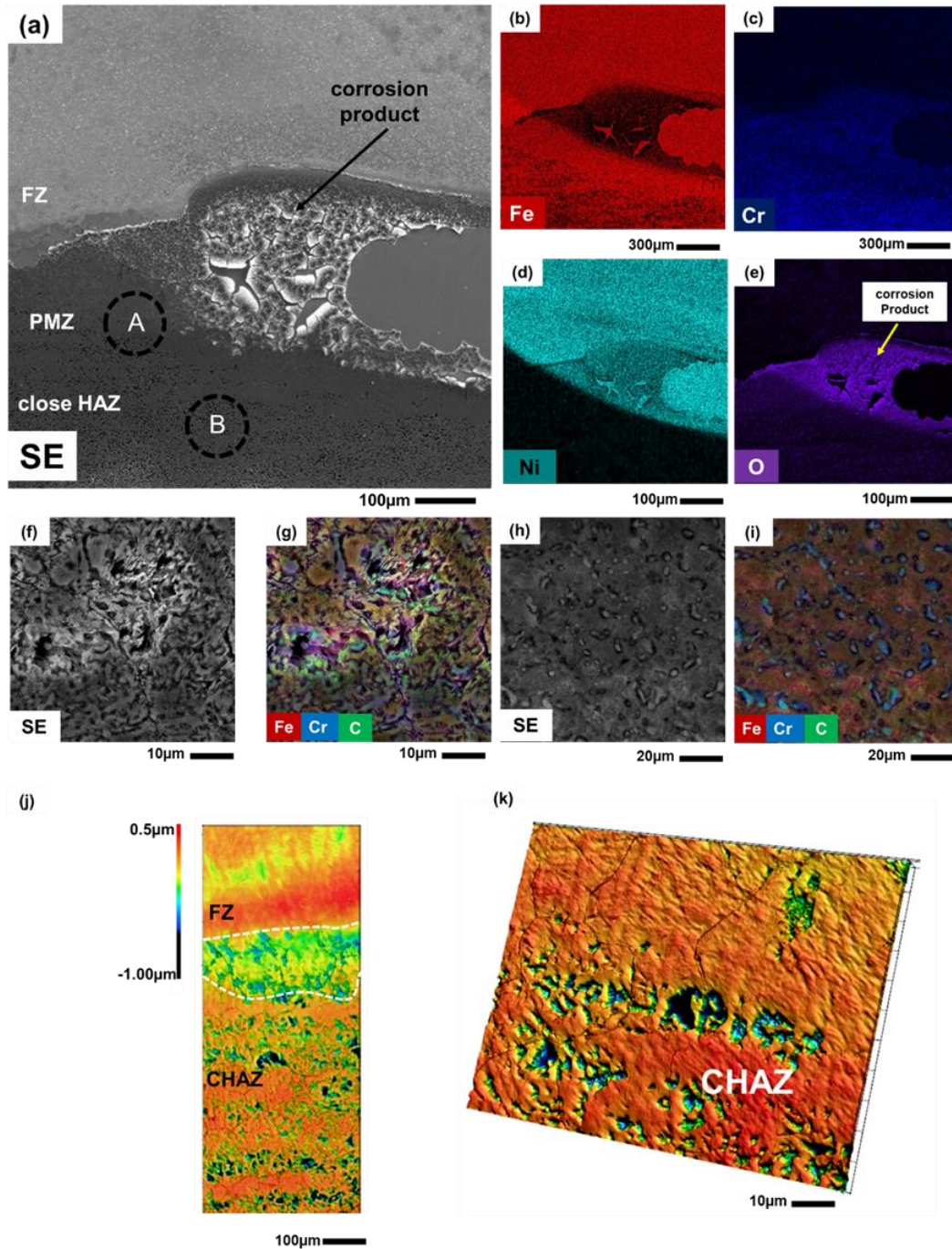
Figure 7. 17. (a) The low magnification SEM micrograph of the interfacial bonding region after the CPP test, and (b-e) the corresponding EDX elemental mappings of iron, chromium, nickel, and oxygen, (f) high magnification SEM micrograph of the PMZ after the CPP test, and (g) its corresponding combined elemental mapping, (h) high magnification SEM micrograph of the corroded CHAZ area after the CPP test and (i) its corresponding combined elemental mapping, (j and k) depth-profiles of the localized corrosion at interfacial bonding in two various locations.

4. Conclusions

In this study, the interfacial microstructure and corrosion performance between a 420 martensitic stainless-steel substrate and a wire arc additive manufactured PH 13-8Mo part are investigated. The interfacial bonding region experienced a complex thermal cycle, leading to the formation of multiple distinct regions, including the far heat affected zone (FHAZ), close heat affected zone (CHAZ), partially melted zone (PMZ), and fusion zone (FZ). The interfacial region exhibited weaker corrosion performance with intense degradation on the PMZ and CHAZ, ascribed to the formation of fine chromium-rich carbides that promoted the micro-galvanic coupling effect along the carbide/martensite interface, leading to the onset of localized corrosion attack from these regions. The superior corrosion resistance of the as-printed PH 13-8Mo and the protective nature of the passive film formed on this alloy were correlated to the dominancy of uniform lath martensitic structure characterized by primarily grains with low misorientation angles along with the absence of chromium-rich carbides in this alloy.

References

[1]   D. Herzog, V. Seyda, E. Wycisk, C. Emmelmann, Additive manufacturing of metals, Acta Mater. 117 (2016) 371–392.

[2]   S. Salahi, M. Ghaffari, A.V. Nemani, A. Nasiri, Effects of Secondary-Phase Formation on the Electrochemical Performance of a Wire Arc Additive Manufactured 420 Martensitic Stainless Steel under Different Heat Treatment Conditions, J. Mater. Eng. Perform. (2021) 1–12.

[3]   H. Sun, C. Liu, J. Chen, M. Gao, X. Shen, A novel method of sustainability evaluation in machining processes, Processes. 7 (2019) 275.

[4]   C.R. Cunningham, J.M. Flynn, A. Shokrani, V. Dhokia, S.T. Newman, Invited review article: Strategies and processes for high quality wire arc additive manufacturing, Addit. Manuf. 22 (2018) 672–686. https://doi.org/10.1016/j.addma.2018.06.020.

[5]   N.A. Kistler, D.J. Corbin, A.R. Nassar, E.W. Reutzel, A.M. Beese, Effect of processing conditions on the microstructure, porosity, and mechanical properties of Ti-6Al-4V repair fabricated by directed energy deposition, J. Mater. Process. Technol. 264 (2019) 172–181.

[6]   M. Vishnukumar, R. Pramod, A.R. Kannan, Wire arc additive manufacturing for repairing aluminium structures in marine applications, Mater. Lett. 299 (2021) 130112.

[7]   S. Salahi, A.V. Nemani, M. Ghaffari, J. Lunde, A. Nasiri, On Microstructure, Crystallographic Orientation, and Corrosion Properties of Wire Arc Additive Manufactured 420 Martensitic Stainless Steel: Effect of the Inter-layer Temperature, Addit. Manuf. (2021) 102157.

[8]   A.V. Nemani, M. Ghaffari, S. Salahi, A. Nasiri, Effects of post-printing heat treatment on the microstructure

and mechanical properties of a wire arc additive manufactured 420 martensitic stainless steel part, Mater. Sci. Eng. A. (2021) 141167.

[9]   C. Dharmendra, A. Hadadzadeh, B.S. Amirkhiz, G.D.J. Ram, M. Mohammadi, Microstructural evolution and mechanical behavior of nickel aluminum bronze Cu-9Al-4Fe-4Ni-1Mn fabricated through wire-arc additive manufacturing, Addit. Manuf. 30 (2019) 100872.

[10]   A.V. Nemani, M. Ghaffari, S. Salahi, J. Lunde, A. Nasiri, Effect of interpass temperature on the formation of retained austenite in a wire arc additive manufactured ER420 martensitic stainless steel, Mater. Chem. Phys. (2021) 124555.

[11]   V. Laghi, M. Palermo, L. Tonelli, G. Gasparini, L. Ceschini, T. Trombetti, Tensile properties and microstructural features of 304L austenitic stainless steel produced by wire-and-arc additive manufacturing, Int. J. Adv. Manuf. Technol. 106 (2020) 3693–3705.

[12]   D.T. Sarathchandra, M.J. Davidson, G. Visvanathan, Parameters effect on SS304 beads deposited by wire arc additive manufacturing, Mater. Manuf. Process. 35 (2020) 852–858. https://doi.org/10.1080/10426914.2020.1743852.

[13]   V. A Hosseini, M. Högström, K. Hurtig, M.A. Valiente Bermejo, L.E. Stridh, L. Karlsson, Wire-arc additive manufacturing of a duplex stainless steel: thermal cycle analysis and microstructure characterization, Weld. World. 63 (2019) 975–987. https://doi.org/10.1007/s40194-019-00735-y.

[14]   J. Lunde, M. Kazemipour, S. Salahi, A. Nasiri, Microstructure and Mechanical Properties of AISI 420 Stainless Steel Produced by Wire Arc Additive Manufacturing, 2020. https://doi.org/10.1007/978-3-030-36296-6_39.

[15]   M. Ghaffari, A.V. Nemani, A. Nasiri, Microstructure and mechanical behavior of PH 13–8Mo martensitic stainless steel fabricated by wire arc additive manufacturing, Addit. Manuf. (2021) 102374.

[16]   P.C. Priarone, G. Campatelli, A.R. Catalano, F. Baffa, Life-cycle energy and carbon saving potential of Wire Arc Additive Manufacturing for the repair of mold inserts, CIRP J. Manuf. Sci. Technol. 35 (2021) 943–958.

[17]   Y. Zhuo, C. Yang, C. Fan, S. Lin, C. Chen, X. Cai, Microstructure and mechanical properties of wire arc additive repairing Ti–5Al–2Sn–2Zr–4Mo–4Cr titanium alloy, Mater. Sci. Technol. 36 (2020) 1712–1719.

[18]   S. Salahi, M. Kazemipour, A. Nasiri, Effects of microstructural evolution on the corrosion properties of AISI 420 martensitic stainless steel during cold rolling process, Mater. Chem. Phys. 258 (2021). https://doi.org/10.1016/j.matchemphys.2020.123916.

[19]   A. Persson, S. Hogmark, J. Bergström, Thermal fatigue cracking of surface engineered hot work tool steels, Surf. Coatings Technol. 191 (2005) 216–227.

[20]   T.D. Ngo, A. Kashani, G. Imbalzano, K.T.Q. Nguyen, D. Hui, Additive manufacturing (3D printing): A review of materials, methods, applications and challenges, Compos. Part B Eng. (2018). https://doi.org/10.1016/j.compositesb.2018.02.012.

[21]   A. Shahriari, L. Khaksar, A. Nasiri, A. Hadadzadeh, B.S. Amirkhiz, M. Mohammadi, Microstructure and corrosion behavior of a novel additively manufactured maraging stainless steel, Electrochim. Acta. 339 (2020) 135925. https://doi.org/10.1016/j.electacta.2020.135925.

[22]   H. Asgari, M. Mohammadi, Microstructure and mechanical properties of stainless steel CX manufactured by Direct Metal Laser Sintering, Mater. Sci. Eng. A. 709 (2018) 82–89. https://doi.org/10.1016/j.msea.2017.10.045.

[23]   S. Salahi, M. Kazemipour, A. Nasiri, Effect of Uniaxial Tension-Induced Plastic Strain on the Microstructure and Corrosion Behavior of 13Cr Martensitic Stainless Steel, CORROSION. (2020).

[24]   M. Shojaati, S.F.K. Bozorg, M. Vatanara, M. Yazdizadeh, M. Abbasi, The heat affected zone of X20Cr13 martensitic stainless steel after multiple repair welding: Microstructure and mechanical properties assessment, Int. J. Press. Vessel. Pip. 188 (2020) 104205.

[25]   M. Ghaffari, A.V. Nemani, A. Nasiri, Interfacial bonding between a wire arc additive manufactured 420 martensitic stainless steel part and its wrought base plate, Mater. Chem. Phys. (2020) 123199.

[26]   C. Dharmendra, S. Shakerin, G.D.J. Ram, M. Mohammadi, Wire-arc additive manufacturing of nickel aluminum bronze/stainless steel hybrid parts–Interfacial characterization, prospects, and problems, Materialia. 13 (2020) 100834.

[27]   A. Shahriari, M. Ghaffari, L. Khaksar, A. Nasiri, A. Hadadzadeh, B.S. Amirkhiz, M. Mohammadi, Corrosion resistance of 13wt.% Cr martensitic stainless steels: Additively manufactured CX versus wrought Ni-containing AISI 420, Corros. Sci. 184 (2021) 109362.

[28]   J. Wan, H. Ruan, J. Wang, S. Shi, The Kinetic diagram of sigma phase and its precipitation hardening effect on 15Cr-2Ni duplex stainless steel, Mater. Sci. Eng. A. 711 (2018) 571–578.

[29] J. Ge, J. Lin, Y. Chen, Y. Lei, H. Fu, Characterization of wire arc additive manufacturing 2Cr13 part: Process stability, microstructural evolution, and tensile properties, J. Alloys Compd. 748 (2018) 911–921.

[30] X. Zhang, K. Wang, Q. Zhou, Y. Peng, J. Kong, Y. Huang, D. Yang, System study of the formability, nitrogen behaviour and microstructure features of the CMT wire and arc additively manufactured high nitrogen Cr-Mn stainless steel, Mater. Today Commun. 27 (2021) 102263.

[31] W.J. Oh, Y. Son, S.Y. Cho, S.W. Yang, G.Y. Shin, D.S. Shim, Solution annealing and precipitation hardening effect on the mechanical properties of 630 stainless steel fabricated via laser melting deposition, Mater. Sci. Eng. A. 794 (2020) 139999.

[32] A. Milev, M. Wilson, G.S.K. Kannangara, N. Tran, X-ray diffraction line profile analysis of nanocrystalline graphite, Mater. Chem. Phys. 111 (2008) 346–350.

[33] M. Dongol, A. El-Denglawey, M.S. Abd El Sadek, I.S. Yahia, Thermal annealing effect on the structural and the optical properties of Nano CdTe films, Optik (Stuttg). 126 (2015) 1352–1357.

[34] F. Christien, M.T.F. Telling, K.S. Knight, Neutron diffraction in situ monitoring of the dislocation density during martensitic transformation in a stainless steel, Scr. Mater. 68 (2013) 506–509.

[35] D.C. Saha, E. Biro, A.P. Gerlich, Y. Zhou, Martensite tempering kinetics: Effects of dislocation density and heating rates, Mater. Charact. 168 (2020) 110564.

[36] M. Sharifitabar, A. Halvaee, Resistance upset butt welding of austenitic to martensitic stainless steels, Mater. Des. 31 (2010) 3044–3050.

[37] A.A. Saleh, E. V Pereloma, A.A. Gazder, Texture evolution of cold rolled and annealed Fe–24Mn–3Al–2Si–1Ni–0.06 C TWIP steel, Mater. Sci. Eng. A. 528 (2011) 4537–4549.

[38] L.Y. Zhao, H. Yan, R.S. Chen, E.-H. Han, Oriented nucleation causing unusual texture transition during static recrystallization annealing in cold-rolled Mg–Zn–Gd alloys, Scr. Mater. 188 (2020) 200–205.

[39] S. Morito, H. Yoshida, T. Maki, X. Huang, Effect of block size on the strength of lath martensite in low carbon steels, Mater. Sci. Eng. A. 438 (2006) 237–240.

[40] H. Beladi, G.S. Rohrer, A.D. Rollett, V. Tari, P.D. Hodgson, The distribution of intervariant crystallographic planes in a lath martensite using five macroscopic parameters, Acta Mater. 63 (2014) 86–98.

[41] S. Chen, Q. Yu, The role of low angle grain boundary in deformation of titanium and its size effect, Scr. Mater. 163 (2019) 148–151.

[42] H. Kitahara, R. Ueji, N. Tsuji, Y. Minamino, Crystallographic features of lath martensite in low-carbon steel, Acta Mater. 54 (2006) 1279–1288.

[43] J. Lunde, M. Kazemipour, S. Salahi, A. Nasiri, Microstructure and Mechanical Properties of AISI 420 Stainless Steel Produced by Wire Arc Additive Manufacturing, in: TMS 2020 149th Annu. Meet. Exhib. Suppl. Proc., Springer, 2020: pp. 413–424.

[44] S. Paul, J. Liu, S.T. Strayer, Y. Zhao, S. Sridar, M.A. Klecka, W. Xiong, A.C. To, A Discrete Dendrite Dynamics Model for Epitaxial Columnar Grain Growth in Metal Additive Manufacturing with Application to Inconel, Addit. Manuf. 36 (2020) 101611.

[45] F. Khodabakhshi, M.H. Farshidianfar, A.P. Gerlich, M. Nosko, V. Trembošová, A. Khajepour, Effects of laser additive manufacturing on microstructure and crystallographic texture of austenitic and martensitic stainless steels, Addit. Manuf. 31 (2020) 100915.

[46] Y.Z. Li, X. Wang, G.A. Zhang, Corrosion behaviour of 13Cr stainless steel under stress and crevice in 3.5 wt.% NaCl solution, Corros. Sci. 163 (2020) 108290.

[47] B. Hirschorn, M.E. Orazem, B. Tribollet, V. Vivier, I. Frateur, M. Musiani, Constant-phase-element behavior caused by resistivity distributions in films: I. Theory, J. Electrochem. Soc. 157 (2010) C452.

[48] A. Fattah-Alhosseini, M.A. Golozar, A. Saatchi, K. Raeissi, Effect of solution concentration on semiconducting properties of passive films formed on austenitic stainless steels, Corros. Sci. 52 (2010) 205–209.

[49] H. Luo, X. Wang, C. Dong, K. Xiao, X. Li, Effect of cold deformation on the corrosion behaviour of UNS S31803 duplex stainless steel in simulated concrete pore solution, Corros. Sci. 124 (2017) 178–192.

[50] L. V Taveira, M.F. Montemor, M.D.C. Belo, M.G. Ferreira, L.F.P. Dick, Influence of incorporated Mo and Nb on the Mott–Schottky behaviour of anodic films formed on AISI 304L, Corros. Sci. 52 (2010) 2813–2818.

[51] J. Amri, T. Souier, B. Malki, B. Baroux, Effect of the final annealing of cold rolled stainless steels sheets on the electronic properties and pit nucleation resistance of passive films, Corros. Sci. 50 (2008) 431–435.

[52] K.H. Anantha, C. Ornek, S. Ejnermark, A. Medvedeva, J. Sj, Correlative Microstructure Analysis and In Situ Corrosion Study of AISI 420 Martensitic Stainless Steel for Plastic Molding, 164 (2017) 85–93.

https://doi.org/10.1149/2.0531704jes.

[53]   C. Man, C. Dong, D. Kong, L. Wang, X. Li, Beneficial effect of reversed austenite on the intergranular corrosion resistance of martensitic stainless steel, Corros. Sci. 151 (2019) 108–121.

[54]   X. Lei, Y. Feng, J. Zhang, A. Fu, C. Yin, D.D. Macdonald, Impact of reversed austenite on the pitting corrosion behavior of super 13Cr martensitic stainless steel, Electrochim. Acta. 191 (2016) 640–650.

[55]   A. Venugopal, K. Sreekumar, V.S. Raja, Effect of repair welding on electrochemical corrosion and stress corrosion cracking behavior of TIG welded AA2219 aluminum alloy in 3.5 wt pct NaCl solution, Metall. Mater. Trans. A. 41 (2010) 3151–3160.

[56]   J. Samei, H. Asgari, C. Pelligra, M. Sanjari, S. Salavati, A. Shahriari, M. Amirmaleki, M. Jahanbakht, A. Hadadzadeh, B.S. Amirkhiz, A Hybrid Additively Manufactured Martensitic-Maraging Stainless Steel with Superior Strength and Corrosion Resistance for Plastic Injection Molding Dies, Addit. Manuf. (2021) 102068.

Chapter 8

Summary, Recommendations, and Future works

1. Summary

This thesis investigated the impact of the process-induced microstructural evolution and texture variation on the electrochemical performance of 420 martensitic stainless steel. Specifically, the effect of two deformation techniques (uniaxial tension and cold rolling), a novel additive manufacturing process, and post-fabrication heat treatments on the corrosion response of 420 MSS was characterized using microstructural features and crystallographic variation.

First, the impact of the uniaxial tension on the corrosion performance of 420 MSS was investigated. A higher fraction of LAGBs and a strong {110} texture was observed for the fractured sample compared to the base metal. It was noticed that the corrosion performance of the samples deteriorated significantly as the deformation level increased. Micro-pit formation was observed in the matrix and coarse chromium carbides interface. A higher fraction of susceptible regions to initiation and propagation of pitting in deformed samples were observed, where the elongation provided vast sensitized regions at the periphery of the precipitates. Consequently, the corrosion resistance of the alloy was found to deteriorate by increasing the applied plastic strain.

Secondly, the effect of cold rolling on the microstructure and corrosion resistance of 420 MSS was investigated. The cold-rolling process led to a slight refinement in lath size, the fragmentation of pre-existing large carbide precipitates, and an increased fraction of LAGBs. The applied cold deformation also resulted in the formation of a stronger {111}<112> texture component aligned with the ND in the 50% rolled sample. It was found that by increasing the

samples' deformation level, the corrosion resistance decreased, suggesting the reduced stability of the protective passive film on the deformed samples against corrosion attacks. At higher deformation levels, the micro-galvanic coupling effect was provoked at the carbide/matrix interface, where precipitates' fragmentation resulted from the cold deformation provided more susceptible regions for corrosion.

Thirdly, the effects of the crystallographic orientation and the secondary phase formation on the electrochemical performance of a 420 martensitic stainless steel produced by the wire arc additive manufacturing at two different inter-layer temperatures were investigated. The microstructure of as-printed WAAM 420 MSS contained martensite laths with an average lath size of ~3 µm along with the delta ferrite phase and a high-volume fraction of retained austenite at the side view. Strong cubic {001}<100> solidification texture was formed in the side view of the sample with an interlayer temperature of 200°C, due to close alignment of the <001> growth direction of primary austenite grains and the sample's building direction. The corrosion mechanism for all samples was governed by the localized corrosion attack at the delta ferrite/ martensite interface, where chromium depletion was significant.

Fourthly, the effects of different heat treatment processes, *i.e.* annealing and quenching & tempering (Q&T) cycles, on the corrosion performance of a WAAM fabricated 420 MSS were investigated. Islands of spherical chromium carbides embedded in a ferritic matrix were observed for the annealed sample, while the Q&T sample showed intergranular carbides precipitated at the PAGBs and sub-micron intra-lath carbides. The weak texture was observed for the annealed and Q&T samples, ascribed to the elimination of solidification texture during phase transformations. A uniform passive film formation on the Q&T sample was observed after the PDP and EIS tests, while the annealed sample exhibited active-like behavior. The corrosion morphology of the

annealed samples revealed localized pitting formation, while an early stage of intergranular corrosion at the PAGBs was observed for the Q&T sample. The superior corrosion response of the Q&T sample was related to the formation of intra-lath M_3C type carbides with similar chemical composition to the matrix and a lack of sensitized regions on its surface.

Fifthly, the interfacial microstructure and corrosion response were characterized between a wrought-AISI420 substrate and a wire arc additive manufactured 420 stainless steel. The corrosion response of the interface region was affected adversely by the high-volume fraction of primary austenite grain boundary formation at the partially melted and fusion zones with increased susceptibility to localized corrosion attack. The onset of localized corrosion attack at the interfacial region was mainly initiated at the fusion zone and the PAGBs, due to the formation of chromium depleted zones at the interface of the PAGBs and the martensitic matrix.

Finally, the feasibility of implementing PH 13-8Mo WAAM track as a repairing alternative for the 420 martensitic stainless steel was examined. The interface region experienced a complicated thermal cycle, leading to multiple distinct regions. The corrosion performance of the interfacial region exhibited intense degradation at the 420 MSS side of the PMZ and HAZ, potentially attributed to the formation of fine chromium-rich carbides. The corrosion onset initiated at the interface of the fine chromium carbides and martensitic matrix.

2. Concluding Remarks

I. The corrosion performance of the 420 MSS received from the industrial partner and the uniaxial tension's impact on the samples' corrosion response were investigated in chapter 1. However, since the 420 MSS alloy received from the industrial partner was exposed to multiple heat treatment cycles, the initial microstructure was not uniform along the pipeline. It was difficult to generalize the observed results concisely and correlate the results herein for all deformation techniques. Hence, cold rolling at more severe deformation levels was conducted to as-annealed samples of 420 MSS alloy with a uniform and single-phase heat treatment cycle, which facilitated the correlation of the observed electrochemical behavior to the applied deformation technique. In general, it was noted that the applied plastic deformation could adversely impact the corrosion performance of the 420 MSS alloy with different microstructural features, attributed to the formation of susceptible regions with chromium depletion adjacent to the chromium carbides.

II. As the impact of the plastic deformation on the corrosion performance of the 420 MSS alloy was revealed, the characterization of other process-induced features' impact on the alloy's electrochemical performance was vital. Considering the on-site manufacturing features, acceptable part quality, and low waste rate, the WAAM process was selected to fabricate the 420 MSS alloy as a novel technique. For the first time, the corrosion performance of the as-printed 420 MSS parts fabricated by the WAAM process with a complex experienced thermal history was characterized. The as-printed samples exhibited lower corrosion resistance as compared to the available commercial 420 MSS parts, ascribed to the existence of a non-equilibrium delta ferrite phase.

III. Since the as-printed samples exhibited weak corrosion performance, post-fabrication heat treatment was required to eliminate the delta ferrite phase and improve the corrosion response. After examining two different heat treatment cycles, the quenching and tempering (Q&T) heat treatment with specified parameters in chapter 5 was found to be an effective method to eliminate the meta-stable microconstituents and improve the corrosion response of the as-printed 420 MSS samples fabricated by the WAAM process. By implementing the WAAM process and applying appropriate heat treatments, 420 MSS parts with higher corrosion performance compared to the conventional techniques (described in Chapters 2 and 3) and with lower waste rate and energy consumption were fabricated.

IV. After successfully adopting the WAAM process for the fabrication of 420 MSS parts, it is important to explore the viability of applying the process for repairing purposes of 420 MSS alloy, considering the current need for on-site restoration of critical components to the disruption in the global supply chain. Initially, a similar 420 MSS wire was used as the repairing track for the 420 MSS, and the electrochemical performance of the track was investigated in chapter 6. However, the corrosion resistance of the interfacial region between the substrate 420 MSS and the repairing track was below expectation, use to the formation of multiple chromium depleted regions at the interface. Hence, a PH 13-8Mo wire with higher corrosion performance compared to the 420 MSS wire was used as h repairing track in Chapter 7. Overall, a superior electrochemical response was observed for the as-printed side of the PH 13-8Mo – 420 MSS dissimilar metal combination, certifying the acceptable corrosion performance of the 420 MSS components coated with the PH 13-

8Mo and the capability of the developed process herein for repair, and restoration applications.

3. Recommendation and future works

The following topics are suggested for future research:

I. In the current thesis, the electrochemical behavior of 420 MSS samples was investigated in naturally aerated 3.5 wt.% NaCl solution at room temperature. Further studies can be conducted to investigate the corrosion performance of the alloy in other corrosive environments such as low concentration H_2SO_4 solutions and combined HCl+HF acidic environments. The impact of the testing conditions, i.e., temperature, conductivity, type of ions, and pH value, can also be characterized.

II. In the current thesis, the impact of plastic deformation techniques such as uniaxial tension and cold rolling was investigated on the corrosion performance of 420 MSS. The severe plastic deformation techniques such as equal channel angular pressing (ECAP) have been implemented for steels toward grain refinement and mechanical performance enhancement. The effect of the ECAP process on the corrosion response of 420 MSS samples can be investigated in future studies.

III. The electrochemical response of the interfacial region between 420 MSS substrate and the deposited wire arc additive manufactured tracks of ER420 and PH 13-8Mo was below the expectations. The post-fabrication heat treatment cycles should be designed and implemented on repairing tracks, and electrochemical analysis of the heat-treated samples can be a subject for future studies.

IV. For further grain refinement and improving microstructure uniformity, the addition of nano-particles to the metal feedstock can be considered as a new approach for the fabrication of wire arc additive manufacturing parts. The impact of novel nano-particles on the electrochemical performance of 420 MSS can be investigated in future studies.